



The University of
Nottingham

**Constraints on the Operation of a DI Diesel
Engine in Partially-premixed Combustion Mode**

Benjamin Keeler, MEng. (Hons)

*Thesis submitted to The University of Nottingham
for the degree of Doctor of Philosophy*

May 2009

ABSTRACT

CONSTRAINTS ON THE OPERATION OF A DI DIESEL ENGINE IN PARTIALLY-PREMIXED COMBUSTION MODE

Benjamin Keeler, 2009

Partially-premixed Charge Compression Ignition (PCCI) combustion is defined by increased levels of premixed charge whilst retaining control over combustion through injection timing. An experimental investigation has been carried out on a current generation DI diesel engine, equipped with High Pressure Common Rail (HPCR) fuel injection equipment and an external Exhaust Gas Recirculation (EGR) system. The aims of the investigation were to determine the constraints imposed on operating a PCCI combustion strategy with the aim of simultaneously reducing engine-out net soot and NO_x emissions.

The work was carried out at fully-warm steady-state conditions at engine speeds of 1500 rpm and 1800 rpm, predominantly using a single injection strategy. With a single injection the Start of Injection (SOI), fuel rail pressure, and rate of EGR have been examined with a view to realising PCCI combustion. Timing ranges of -20° to +3°ATDC, rail pressures of 500-1200 bar, and EGR rates of 0-60% have been investigated. The responses looked at have been engine-out soot, NO_x, HC, and CO emissions, fuel consumption, and combustion noise. It is shown that variation of the parameters has allowed PCCI combustion to be achieved in a restricted operating region, offering improvement in the NO_x-soot trade-off. This region is limited on the available test engine by oxygen availability due to the specifications of the turbocharger and EGR systems. Engine speeds up to 2000 rpm (at 2.5 bar BMEP), and loads of 4.4 bar gross IMEP (at 1500 rpm) have been found to be the limits, beyond which soot and CO emissions rise excessively.

It is shown that enhancing the mixing time and intensity are both desirable in achieving PCCI combustion. The net soot reduction mechanism exploited with PCCI combustion strategies is reducing soot formation to outweigh the reduction in oxidation. Enhancing the mixing intensity by increasing injection pressure is highly effective at reducing soot output, but at the expense of brake specific fuel consumption. Increasing the mixing time can also be effective in reducing soot output, but careful parameter selection is required to avoid excessive soot output. Retarded or highly advanced injection timings are shown to

reduce net soot output, but both have associated trade-offs and penalties. Retarding combustion is effective at lowering soot and NO_x emissions with low associated noise, but a fuel economy penalty is paid. Advanced combustion phasing can result in large peak rates of increase of pressure, which have been shown to correlate well with combustion noise. Overall soot reductions of up to 97% were achieved, but with associated penalties. One of the most acceptable reductions of ~90% came at the cost of a 6% increase in fuel consumption, highlighting that improvements in emissions are achievable with PCCI strategies with acceptable trade-offs.

ACKNOWLEDGEMENTS

I do not believe the experiences of working within the Engines Research Group at Nottingham University can be equalled. I feel honoured to have been part of such a wonderful and lively group and thank all who have contributed to my time here, both professionally and personally.

I am indebted to, and wish to express my gratitude towards, Professor Paul Shayler for providing both the opportunity and the support to carry out this PhD. I would not be in the position I am without his help and encouragement.

One of the reasons this research group has been so successful is the fantastic technical staff. I would like to thank all those who have assisted me for their patience, and hard work. Special thanks go to Geoff Fryer, John McGhee, and John Clark. Each is a character unto their own, and as well as the expertise they have offered, they made the experience of completing this PhD so much more enjoyable. I would also like to thank all of my research colleagues, both past and present for their support and humour. You have all made it a great place to work. Special thanks go to Dave and Nino, although everyone has contributed in their own unique way.

I wish to thank my family and friends for their love, support, and understanding during this journey. In particular I thank my parents, my grandparents, and John and Denise. Their unquestioning support has been magnificent. Finally, I would like to thank my dearest Becky for her love and support during this time. I know at times I have not been the easiest to deal with, but I thank her for being there. Without her, this work would never have come to fruition.

CONTENTS

NOMENCLATURE	III
ABBREVIATIONS.....	VI
CHAPTER 1 INTRODUCTION.....	1
1.1 OVERVIEW	1
1.2 EMISSIONS LEGISLATION	2
1.3 DIESEL COMBUSTION SYSTEMS	3
1.4 THESIS OBJECTIVES	6
1.5 LAYOUT OF THESIS	7
CHAPTER 2 LITERATURE REVIEW.....	9
2.1 INTRODUCTION	9
2.2 PCCI COMBUSTION	9
2.3 CONCEPTUAL COMBUSTION MODELS.....	12
2.4 FORMATION OF EMISSIONS.....	13
2.5 COMBUSTION NOISE	17
2.6 ENGINE OPERATING PARAMETERS WITH CURRENT GENERATION HARDWARE	18
2.7 CONCLUDING REMARKS	22
CHAPTER 3 INTERPRETATION OF PCCI PROCESSES AND DESCRIPTION OF TEST FACILITIES	23
3.1 INTRODUCTION	23
3.2 INTERPRETATION OF PCCI PROCESSES AND DEFINITION OF STUDY	23
3.3 ENGINE TEST FACILITIES	26
3.4 ENGINE INSTRUMENTATION	28
3.5 DATA ACQUISITION SYSTEMS	30
3.6 CONCLUDING REMARKS	31
CHAPTER 4 DATA PROCESSING	32
4.1 INTRODUCTION	32
4.2 EXHAUST GAS WET AND DRY ANALYSIS.....	32
4.3 CALCULATION OF AFR	33
4.4 VOLUMETRIC AND GRAVIMETRIC ANALYSES.....	34
4.5 EMISSIONS UNITS AND CONVERSION.....	35
4.6 EXHAUST GAS RECIRCULATION.....	36
4.7 EQUIVALENCE RATIOS	37
4.8 COMBUSTION EFFICIENCY.....	37
4.9 IN-CYLINDER ANALYSES	37
4.10 HEAT RELEASE ANALYSIS	42
4.11 CONCLUDING REMARKS	45
CHAPTER 5 STUDIES OF NOISE, IGNITION DELAY, AND COMBUSTION PHASING TO SUPPORT ASSESSMENT OF PCCI COMBUSTION	46
5.1 INTRODUCTION	46
5.2 COMBUSTION NOISE	46
5.3 IGNITION DELAY AND THE START OF COMBUSTION	52
5.4 EFFECT OF COMBUSTION PHASING ON CO, HC, AND FUEL CONSUMPTION	56
5.5 CONCLUDING REMARKS	60

CHAPTER 6 ENGINE BASELINE PERFORMANCE AND PROTECTION OF PRESSURE TRANSDUCERS AGAINST SOOT	61
6.1 INTRODUCTION	61
6.2 ENGINE BASELINE PERFORMANCE	61
6.3 STANDARD TEST POINT	63
6.4 TRANSDUCER ADAPTORS	64
6.5 CONCLUDING REMARKS	67
CHAPTER 7 EXHAUST GAS RECIRCULATION.....	68
7.1 INTRODUCTION	68
7.2 TEMPERATURE	68
7.3 EQUIVALENCE RATIO.....	70
7.4 EFFECT ON EMISSIONS	71
7.5 EFFECT OF EGR ON THE ENGINE AND MAINTENANCE.....	74
7.6 CONCLUDING REMARKS	74
CHAPTER 8 FUEL INJECTION PARAMETERS.....	76
8.1 INTRODUCTION	76
8.2 INJECTION TIMING AT BASELINE FUEL RAIL PRESSURE	76
8.3 POST INJECTIONS.....	79
8.4 EFFECT OF RAISING FUEL RAIL PRESSURE	80
8.5 CONCLUDING REMARKS	89
CHAPTER 9 OPERATING LIMITS OF PCCI COMBUSTION.....	91
9.1 INTRODUCTION	91
9.2 LOAD LIMITS OF PCCI COMBUSTION.....	92
9.3 SPEED LIMITS OF PCCI COMBUSTION	99
9.4 CONCLUDING REMARKS	103
CHAPTER 10 DISCUSSION AND CONCLUSIONS	105
10.1 DISCUSSION	105
10.2 FURTHER WORK	114
10.3 CONCLUSIONS.....	115
REFERENCES	117
TABLES	127
FIGURES	136
APPENDICES.....	209

NOMENCLATURE

ASOI	°CA	After Start of Injection
ATDC	°CA	After Top Dead Centre
b	-	Constant
B	m	Bore
β	-	Premixed Fraction (Proportionality Factor)
BMEP	bar	Brake Mean Effective Pressure
BS _x	kg/kWh	Brake Specific Emissions of Substance <i>x</i>
bsfc	kg/kWh	Brake Specific Fuel Consumption
c	m/s, -	Speed of Sound, constant
d	m	Diameter
c_p	kJ/kg K	Specific, Molar Heat Capacity at Constant Pressure
\tilde{c}_p	kJ/kmolK	Molar Heat Capacity at Constant Pressure
c_v	kJ/kg K,	Specific, Molar Heat Capacity at Constant Volume
\tilde{c}_v	kJ/kmolK	Molar Heat Capacity at Constant Volume
CA	°	Crank Angle
CO	%, kg/kg exh	Carbon Monoxide
CO ₂	%, kg/kg exh	Carbon Dioxide
E _A	kJ/kmol	Apparent Activation Energy
EGR	%, -	Exhaust Gas Recirculation
EI _x	g/kg fuel	Emissions Index of Substance <i>x</i>
EOI	°CA	End of Injection
FMEP	bar	Friction Mean Effective Pressure
H	kJ	Enthalpy
Δh°_f	kJ/kmol	Molar Enthalpy of Formation
HC	ppm, kg/kg exh	Unburned Hydrocarbons
H ₂ O	%, kg/kg	Water
ID	°CA, ms	Ignition Delay Period
IMEP	bar	Indicated Mean Effective Pressure
LHV	MJ/kg	Lower Heating Value
MAF	kg/hr	Mass Air Flow-rate
MAP	Pa, bar	Manifold Absolute Pressure
<i>m</i>	kg	Mass
\dot{m}	kg/s	Mass Flow Rate

\tilde{m}	kg/kmol	Molar Mass
n	kmol	Number of Moles, polytropic index
N	rpm	Crankshaft (Engine) Rotational Speed
NO	ppm, kg/kg	Nitric Oxide
NO_x	ppm, kg/kg exh	Oxides of Nitrogen
n_r	-	Crank Revolutions per Engine Cycle
O_2	%, kg/kg exh	Oxygen
OH	-	Hydroxyl Radical
p	bar	Pressure
P	kW	Power
$PMEP$	bar	Pumping Mean Effective Pressure
Q	J	Heat
R	kJ/kg K	Specific Gas Constant
\tilde{R}	kJ/kmol K	Universal Gas Constant
R^2	-	Coefficient of Determination
$ROHR$	J/° (J/deg)	Rate of Heat Release
S	m	Spray Tip Penetration
t	ms	Spray Duration
T	K, Nm	Temperature, Torque
V	m ³	Volume
W	J	Work done
x_x^*	kg/kg exh	Dry Mass Fraction of Substance x
\tilde{x}_x^*	%, ppm	Dry Mole Fraction of Substance x
x_x	kg/kg exh	Wet Mass Fraction of Substance x
\tilde{x}_x	%, ppm	Wet Mole Fraction of Substance x
λ	-	Excess Air Ratio
γ (Gamma)	-	Ratio of Specific Heat Capacities (c_p/c_v)
ψ	-	Molar N/O ratio
ϕ	-	Air-Fuel Equivalence Ratio
ϕ_{O_2}	-	Oxygen-Fuel Equivalence Ratio
η	%	Efficiency
ρ	kg/m ³	Density
τ_{id}	°, ms	Ignition Delay

Subscripts

b	Brake
bg	Burned Gas
c	Cylinder, Cycle
comb	Combustion
d	Displaced
exh	Exhaust
f	Frequency
fc	Fresh Charge
g	Gross
ht	Heat transfer
i	Indicated, intake
n	Net
p	Passage
rail	Fuel Rail
tot	Total
vol	Volumetric

ABBREVIATIONS

AFR	Air to Fuel Ratio
AFR _s	Stoichiometric Air to Fuel Ratio
BDC	Bottom Dead Centre
BGT	Bulk Gas Temperature
CAN	Control Area Network
CFD	Computational Fluid Dynamics
CI	Compression Ignition
CLD	Chemiluminescent Detector
CN	Cetane Number
CNL	Combustion Noise Level
CoV	Coefficient of Variation
Cyl	Cylinder
DI	Direct Injection
DOC	Diesel Oxidation Catalyst
DOE	Design of Experiments
DPF	Diesel Particulate Filter
ECU	Electronic Control Unit
EGR	Exhaust Gas Recirculation
EOC	End of Combustion
EVO	Exhaust Valve Opening
FCV	Fuel Cell Vehicle
FFT	Fast Fourier Transform
FGT	Fixed Geometry Turbine
FID	Flame Ionisation Device
FIE	Fuel Injection Equipment
FSN	Filter Smoke Number
FSO	Full Scale Output
GFC	Gas Filter Correlation
HCCI	Homogeneous Charge Compression Ignition
HD	Heavy Duty
HP	High Pressure
HPCR	High Pressure Common Rail
IC	Internal Combustion
INCA	Integrated Calibration and Acquisition System
ISFC	Indicated Specific Fuel Consumption

IVC	Inlet Valve Closing
LNT	Lean NO _x Trap
LTC	Low Temperature Combustion
MCC	Mixing-Controlled Temperature Combustion
MFB	Mass Fraction Burned
MK	Modulated Kinetics
NEDC	New European Drive Cycle
NVH	Noise, Vibration, and Harshness
OEM	Original Equipment Manufacturer
OFR	Oxygen Fuel Ratio
PAH	Polycyclic Aromatic Hydrocarbon
PARA	Paramagnetic (Oxygen Sensor)
PCCI	Partially-premixed Charge Compression Ignition
PM	Particulate Matter
PWM	Pulse Width Modulation
SOC	Start of Combustion
SOF	Soluble Organic Fraction
SOI	Start of Injection
Stk	Stroke
TDC	Top Dead Centre
TLA	Thermodynamic Loss Angle
UNIBUS	UNIform BULky combustion System
VGT	Variable Geometry Turbine

CHAPTER 1

INTRODUCTION

1.1 Overview

The subject of this thesis is Partially-premixed Charge Compression Ignition (PCCI) combustion strategies for compression ignition engines, and in particular what constrains the implementation of these strategies on diesel engines. PCCI differs from conventional diesel combustion in that it further promotes fuel-air mixing to limit high temperature combustion. The mixing that occurs in a conventional diffusion flame is relatively slow, and premixing fuel and air towards a more homogeneous state before the onset of hot gas reactions (start of combustion) clearly distinguishes PCCI from conventional diesel combustion. However, techniques used to improve responses such as lowering soot frequently result in a deterioration of other responses. As will be discussed, the lower combustion temperatures and enhanced mixing exploited with PCCI combustion has the potential to significantly reduce oxides of nitrogen (NO_x) and particulate emissions simultaneously. Exhaust emissions, fuel consumption, and combustion noise responses are investigated when attempting to employ a PCCI strategy on a multi-cylinder Direct Injection (DI) diesel engine of current generation hardware.

Interest in PCCI is the result of concerns over climate change and the role of emissions from the transport sector in this. The accumulation of evidence [1] that climate change is occurring and that carbon dioxide (CO_2) emissions from burning fossil fuels is responsible has focused attention on the problem and in particular the contribution from automotive vehicles. There is currently no restriction on CO_2 emissions but there are vehicle taxation incentives to use low emissions vehicles and European targets for average CO_2 emissions per kilometre for manufacturers [2]. In recent years ever more stringent legislation has been imposed on vehicle emissions with an aim to reduce their polluting effect. In Europe legislation has been through the Euro Stage system, the most recent of which was Euro Stage IV in 2005, but with Euro V coming into force in 2009 [3]. In order to meet future limits on emissions, automotive manufacturers are seeking improvements to aftertreatment systems such as Lean NO_x Traps (LNT), catalytic converters, and particulate filters. Naturally manufacturers aim to minimise the costs of these aftertreatment systems so are developing existing technologies as well as new approaches to comply with legislation. Reduction of engine-out emissions is vital to achieving this.

Within this chapter the emissions legislation that is driving the industry to reduce pollutants is summarised, and a short history of diesel combustion systems presented. Conventional and premixed charge combustion systems are introduced, before some of the alternatives to diesel engines and future industry technology are reviewed. The chapter concludes with the objectives of this thesis, and finally a description of the overall thesis layout.

1.2 Emissions Legislation

PCCI strategies offer simultaneous reductions in NO_x and soot emissions which are being heavily targeted by legislation. Research into effective strategies to reduce these species is required to meet future targets. Since 1992 new cars and light vehicles have been required to meet emission standards known as “Euro” standards. Each successive Euro standard (starting at Euro Stage I in 1992 to Stage IV in 2005) has become stricter and limited the polluting species from vehicle tailpipes more aggressively. Particulates and NO_x are considered to pose the most serious environmental and health problems and Euro V due to come into force later in 2009 would see an 80% reduction in particulate matter and a 28% reduction in oxides of nitrogen relative to Euro IV limits. To comply with Euro V and VI, diesel engine cars would have to be fitted with particulate filters, a potentially expensive aftertreatment system. Table 1.1 summarises the evolution of the Euro emission standards for diesel engine cars [3]. The data for PM and NO_x emissions are illustrated in Figure 1.1 as these are currently the species being targeted most heavily and those of greatest importance to this research work.

In 1997 the Kyoto Protocol to the United Nations Framework Convention on Climate Change was adopted with the aim of reducing the emission of Greenhouse gases deemed responsible for climate change. Between 2008 and 2012 industrialized nations have committed to reduce greenhouse gas emissions by an average of 5% compared to 1990 levels [4]. Included within the targeted gases is CO_2 , one of the main products of combustion of hydrocarbon fuels. To encourage consumers to reduce CO_2 emissions, or their so called “carbon footprint”, since 2001 Vehicle Excise Duty for new cars in the UK has been determined by their CO_2 output and fuel type [5]. Together with the substantial level of tax on automotive fuels imposed by the government, diesel powered vehicles are becoming ever more attractive due to their excellent fuel economy and improved drivability. Diesel engine vehicles offer lower fuel consumption and thus reduced CO_2 output compared to gasoline vehicles for a number of important reasons. The relative contributions are highly dependent upon the operating conditions (duty cycle), but are here listed in approximate order of their relative contribution at low power part load (urban driving):

- Diesel engines conventionally operate without throttling the intake air, reducing pumping losses.
- Although the calorific value of diesel is actually slightly lower than that of gasoline it has a greater density, resulting in a higher volumetric energy density. Fuel is sold per litre and fuel consumption is commonly stated in mpg or l/km, both favouring diesel over gasoline.
- Diesel engines generally have higher compression ratios, increasing the ideal thermal efficiency [6].
- Diesel engines operate with higher gearing and lower engine speed. Although friction tends to be higher than for gasoline engines, for a given power output, less power is dissipated as parasitic losses due to the lower engine speed.

1.3 Diesel Combustion Systems

1.3.1 Introduction to Diesel Engines

The history of diesel engines can be traced back to the late 19th century when Rudolf Diesel embarked on the development of an internal combustion engine that ignited the fuel through compression. Since then there have been many major developments in diesel engine technology, with notable improvements in fuel injection over the past 15 years. The first Common-Rail (CR) injection system was introduced in 1997 paving the way for future improvements. The opportunities made available by the introduction of High Pressure Common Rail (HPCR) electronic controlled fuel injection systems has allowed much greater flexibility in injection strategy and engine operation due to fuel pressure generation and injection being separate events. The high injection pressures and capability of multiple injections made possible with the use of the HPCR has brought about improvements in engine emissions and noise, whilst maintaining the excellent fuel consumption and energy efficiencies of the compression ignition engine [6].

Fiscal incentives and changing public opinion of diesel engines as the source of power for their vehicles has led to a dramatic increase in the market share of diesel car sales in Western Europe. Back in 1999 diesel cars accounted for 28.4% of all new cars sold, however, by 2006 diesel engine cars had outsold those fuelled by gasoline for the first time. As Figure 1.2 illustrates, the growing current market share of diesel engine cars continues to increase and was 52.2% in the first half of 2007 [7]. By the end of 2007 this figure had reached 53.3% [8].

1.3.2 Conventional Compression Ignition Combustion

Current “conventional” diesel combustion strategies typically involve a pre-injection (pilot) and a main injection, although some strategies employ more than one pilot injection and split-main injections. Modest intake boost pressures and EGR rates are employed, with typical operating ranges of modern diesel engines with conventional strategies approximately 600-4500 rpm and up to 20 bar Brake Mean Effective Pressure (BMEP) load output. The phases that characterise diesel combustion are shown in Figure 1.3 and discussed below.

Following the injection and combustion of the pilot, the main fuel quantity is injected at point “A”. The time between injection and Start of Combustion (SOC) is the Ignition Delay (ID) period (*A-B*) where fuel and air mixes before the premixed combustion phase (*B-C*). The fuel that has mixed with air to within flammability limits during the ignition delay period burns in this phase. Combustion within this phase typically has high rates of heat release with short duration combustion. The mixing-controlled combustion (MCC) or diffusion burning phase (*C-D*) follows once the fuel burned during the premixed phase has been consumed. Mixing of fuel and air determines the rate of combustion and as such a lower rate of heat release over a longer crank angle period is detected. Late combustion completes the combustion process with low rates of heat release (*D-*) [9]. As will be discussed, the length of the ignition delay period and the ratio of premixed-to-mixing controlled combustion have great influence on emissions formation and output.

The use of a pilot injection promotes the ignition of the main injection event by increasing in-cylinder temperatures and pressures. The shortened ignition delay of the main injection increases the ratio of diffusion-to-premixed burning, reducing rates of heat release and combustion noise. As will be discussed in the Literature Review that follows this Introduction, increased diffusion burning results in higher soot output and as such new approaches must be developed to reduce these engine-out emissions.

1.3.3 Partially-premixed Charge Compression Ignition and Low Temperature Combustion Systems

In 1988 Kamimoto and Bae [10] presented an equivalence ratio-temperature (Φ -T) plot which has been the basis for many studies on premixed and low temperature combustion. The authors demonstrated that soot and NO_x are formed within confined regions in the Φ -T plane (here referring to local conditions). Fuel-air equivalence ratio is discussed in Chapter 4, but describes how lean or rich a mixture is. High values of Φ relate to rich mixtures, and $\Phi=1$ corresponds to a stoichiometric mixture. Figure 1.4 and other Φ -T maps presented within this thesis include contours based on documented findings of

Kitamura et al. [11], who examined the effect of fuel composition on soot yield. The contours indicate the relative concentrations of the two emission formations. A soot formation peninsula is evident at $\Phi > 2$ and between temperatures of 1600-2500 K, whilst NO_x formation occurs at temperatures greater than 2200 K and $\Phi < 2$. Avoiding these formation regions is thus fundamental to reducing soot and NO_x production. A version of Φ -T diagram reproduced from Akihama et al. [12] is shown in Figure 1.4, highlighting previously proposed regions to exploit to reduce soot and NO_x formation.

Over recent years low temperature diesel combustion systems have become the focus of attention for many researchers aiming to exploit the potential benefits of limiting combustion temperatures so as to avoid the production of NO_x and soot. Improved premixing reduces the amount of slow MCC which is responsible for the majority of soot production that occurs at the high-temperature, fuel-rich spray core. More details on MCC and the associated soot and NO active regions are presented in Chapter 2.

A distinction can be made between these low temperature systems, differentiated by whether or not control over combustion phasing is coupled to the fuel injection event [13]. In the case of Homogeneous Charge Compression Ignition (HCCI) combustion, combustion phasing is dominated by chemical reaction kinetics and decoupled from injection timing [13] and as such there is a lack of control over combustion. Highly advanced injection timings are used to create a homogenous mixture of fuel and air prior to ignition. The premixed combustion that occurs avoids the high temperature diffusion burning and thus limits combustion temperatures which are required for NO_x formation, whilst maintaining low local equivalence ratios ($\Phi < 2$) avoids the soot formation peninsula. Unfortunately HCCI combustion systems are subject to several problems that limit their practical application. The low volatility of diesel makes vaporisation of the fuel more difficult when injected early in the cycle into lower cylinder pressure and temperature [14]. HCCI systems also suffer from wall wetting and over-leaning problems, a consequence of the early injection, giving rise to high unburned hydrocarbon (HC) emissions. Moreover, the rapid rates of heat releases that occur with the almost instantaneous combustion result in high rates of cylinder pressure rise and excessive peak pressures.

In the case of Partially-premixed Charge Compression Ignition (PCCI) control over combustion with injection strategy is retained and a greater percentage of the total charge is premixed prior to ignition relative to conventional diesel combustion. Various injection strategies are available for PCCI combustion, but commonly advanced injection timings are used in conjunction with high rates of EGR to reduce NO_x and increase mixing time. As with HCCI combustion the mixing of fuel and air and ignition with PCCI are

independent processes, but there is insufficient time available to allow complete premixing of the fuel-air mixture before the start of combustion and as such many regions rich of stoichiometric exist (partial stratification). The combustion process takes place at generally higher premixed-to-diffusion burning ratios (but not homogeneous) and lower temperature than a conventional diesel combustion process [15] as indicated in Figure 1.5. However, a significant proportion of the heat can be released in a mixing-controlled process, resulting in high peak combustion temperatures [13]. Although both charge mixing systems have the advantage of lower soot and NO_x emissions, HCCI combustion has the major disadvantage of being harder to control. Some proposed PCCI strategies have been found to be particularly effective and show great promise for future developments. A short review of three such works is provided in the Literature Review.

1.3.4 Alternatives to Diesel Engines and Future Research Focus

As well as developing diesel engine technology and strategies such as PCCI and HCCI, the automotive industry is also exploring many alternatives. Table 1.2 offers a short review of four significant research interests, including the advantages offered, how they are achieved, and current obstacles to their implementation. However, despite the potential offered by these research fields, diesel powered vehicles are still increasing in market share and warrant further research into new approaches to reduce emissions.

1.4 Thesis Objectives

The next generation of emissions targets require considerable reductions in NO_x and soot output. The advantages offered by Compression Ignition (CI) systems and HPCR fuel injection equipment (FIE) will have to be further exploited in conjunction with EGR systems to minimise engine-out emissions. Current combustion strategies involve pilot and main injection events with the use of cooled EGR. However, to reduce soot output new approaches must be taken to ensure legislative targets are met. The main challenge can be summarised as simultaneously reducing soot and NO_x emissions without creating excessive levels of combustion noise, whilst maintaining the excellent engine efficiency and fuel consumption that are currently offered by modern diesel engines.

Unfortunately measures often taken to reduce one emission species typically result in an increase of another. A classic example is the use of EGR to reduce NO_x emissions leading to increases in HC and soot output. The reduction in oxygen availability and combustion temperature together with an increase in equivalence ratio results in trade-offs requiring careful parameter optimisation. However, potential combustion regimes have been proposed that can achieve reductions in soot and NO_x simultaneously, but these frequently suffer from a number of issues that restrict their practical applicability. One such approach

that has attracted much attention is that of low temperature combustion (LTC) with higher levels of premixed charge. By reducing local equivalence ratios and limiting combustion temperatures it is possible to greatly reduce the formation of soot and NO_x as described above, but problems arise concerning control of the combustion, excessive combustion noise, and reduced combustion and fuel efficiencies [16]. Future challenges for the next generation of diesel engines include minimising emission responses without incurring too high a fuel consumption or other penalty.

A limited number of proposed partial solutions have been documented in the literature. The approaches taken by many researchers are currently limited to laboratory environments and may be impractical for real world applications in vehicles. The purpose of the work contained within this thesis is to develop the understanding of what approaches are successful and the constraints encountered in adapting a modern DI diesel engine to operate a PCCI strategy whilst, importantly, maintaining control over combustion through injection strategy. Ultimately the main aim is to simultaneously reduce soot and NO_x emissions without incurring excessive penalties. Specifically, the output of soot, NO_x , HC and CO emissions, fuel consumption and combustion noise level will be considered. In the available literature the effect on combustion noise level is rarely considered in detail, with qualitative statements about the likelihood of excessive noise being a potential issue more common, if mentioned at all. An exception is a paper co-authored by the author of this thesis [17]. Due to the nature of increased premixed combustion, rapid rates of heat release can result in high combustion noise levels, potentially limiting its application. Within this thesis, implications as to any required engine maintenance and instrumentation are also presented. The author's work also lends itself to being further developed to meet specific targets through optimised calibration, which is a potential future project.

1.5 Layout of Thesis

Following this introduction a review of pertinent literature regarding PCCI and low temperature combustion, emission formation, together with current generation hardware are given in Chapter 2. An interpretation of the processes involved with PCCI combustion and a review of the test facilities and sensors is given in Chapter 3, which details the engine rig setup and the data acquisition systems. The experimental facilities allowed the desired measurements to be taken and recorded before being processed as explained in Chapter 4. Included are the calculation of AFR, emissions calculations and the units used within this thesis, calculation of temperatures, and heat release analysis, the latter of which is invaluable in understanding the combustion characteristics. The experimental

conditions presented are representative of those encountered during NEDC operation. The data presented are concentrated at 1500 rpm and 1800 rpm.

The factors and strategies relating to combustion noise are investigated in Chapter 5 together with the influence and determination of start of combustion and the ignition delay. Collection and assessment of data to analyse the engine baseline performance are evaluated in Chapter 6. This was carried out to establish the overall behaviour of the engine under ECU control to establish any limitations that may be encountered. Whilst carrying out this investigation a problem with one of the sensors was encountered and a new pressure transducer adaptor designed. This is discussed in detail, together with analysis of a standard test point, used to monitor repeatability and identify errors.

Chapters 7 and 8 respectively deal with the effect of EGR and injection strategies on emissions, the determinants of their production and output, the trade-offs that exist, and what can be achieved using different strategies. The findings are then exploited in Chapter 9 to investigate the speed and load limits of PCCI combustion, which clearly highlights the challenges of reducing soot and NO_x without incurring significant penalties. Finally in Chapter 10 the final discussions and conclusions are presented together with proposed further work.

CHAPTER 2

LITERATURE REVIEW

2.1 Introduction

This review is separated into seven sections and begins with an introduction into PCCI combustion, how it differs from conventional combustion, and an overview of practical applications. Mixing-controlled combustion plays a highly important role in emission formation and a well accepted conceptual model is reviewed with an emphasis placed on the development of the fuel jet, local mixture conditions, and their consequences. The chapter then moves on to review the formation of emissions with particular attention paid to NO_x and soot as the simultaneous reduction of these is one of the main aims of the research. Combustion noise is reviewed before current generation hardware and the potential they offer in engine development are covered. Finally, conclusions drawn from the available literature are given.

2.2 PCCI Combustion

2.2.1 Introduction to PCCI Combustion

Various combustion strategies have been proposed to avoid the soot and NO_x formation regions as shown in Figures 1.4 and 1.5. As was introduced in Chapter 1, PCCI combustion is defined by increased amounts of premixed charge relative to conventional combustion, whilst importantly retaining control over combustion through injection strategy. Several different acronyms have been used in the literature when investigating PCCI combustion, but this is the notation that will be used explicitly throughout this thesis. Figure 1.5 adapted from [18] expands upon Figure 1.4 to demonstrate the regions encompassed during conventional and PCCI combustion. The figure demonstrates the effect of increasing the rate of EGR and improving mixing as the larger conventional combustion area shifts and shrinks to the PCCI combustion area. Overall local equivalence ratios are more uniform and temperatures lower than with conventional combustion.

The summary of operating regions depicted in Figure 1.5 provides a useful overview of the challenge faced. However, computational works have been published that further develop the understanding of combustion progression within the Φ -T plane. Figure 2.1 illustrates example time histories of two combustion events, one resulting in high soot output, the

other low soot. The time period included ranges from 20% to 80% Mass Fraction Burned (MFB) and summarises the Computational Fluid Dynamics (CFD) findings documented in [12]. The shaded areas represent regions that encompass the majority of gas cells from the 3D-CFD calculation, but do not give density information. Instead they are drawn here to describe the combustion progression for the two cases. Although initially starting with similar profiles, as the combustion event progresses two key differences are seen to be the maximum temperatures reached and the distribution of equivalence ratios. By 60% MFB (third diagrams from top) the high smoke condition significantly encroaches the soot formation peninsula, whereas the smokeless case merely approaches it. As more fuel is burned (bottom diagrams) some of the gas cells of the smokeless case do indeed impinge the soot formation region, but the lower temperatures help minimise the formation. In contrast a much greater proportion of the high smoke condition gas cells fall in the soot formation region, with higher peak temperatures. The overall result is clearly greater overall formation of soot in the high smoke case, but the diagrams do not give any indication as to the relative oxidation processes. Nevertheless, net soot output is likely to be significantly higher for the high soot formation case, which highlights the need to reduce formation. This is exploited in PCCI strategies.

Despite the charge not being completely premixed (homogeneous), the same principles are applied to obtain low emissions as with HCCI [19]. The factors used to manipulate combustion conditions towards the PCCI mode of operation are primarily the injection strategy and level of EGR. The effect of increasing EGR is to lower combustion temperatures and reduce oxygen availability. The decrease in oxygen concentration and combustion temperatures reduces the rate of oxidation of species including soot, HC and CO [20]. Injection timings with PCCI are not as advanced as in HCCI, and in some cases are in fact retarded after TDC [21, 22]. When injection is advanced, long ignition delays enhance premixing and lower flame temperatures due to the formation of overall lean mixtures, as described with HCCI operation [23], whilst retarded timings look to exploit the lower temperatures in the expansion stroke. The level of EGR used is higher than in conventional operation, but must be selected in conjunction with injection timing to maintain desired combustion phasing. Unfortunately advancing injection timing to compensate for the increase in ignition delay with EGR to allow nearer optimum combustion phasing is likely to result in increased soot output as demonstrated by work published by the author in Ref. [17].

2.2.2 Practical Implementations of PCCI

Although many studies have been carried out on premixed charge combustion, only a limited number of practical operation modes have been demonstrated in real engines [24].

Three proposed strategies are discussed below together with their limitations and engine demands.

The Modulated Kinetics (MK) concept developed by Kimura et al. [21, 22, 25] is a promising combustion mode that utilises increased EGR rates, increased injection pressure, high swirl rates, and retarded injection (close to or after TDC) to lower combustion temperatures and limit the formation of NO_x and soot. In-cylinder gas temperatures are relatively low for retarded combustion phasings, and as such thermal decomposition of the diesel fuel is inhibited, which reduces soot production. A key feature of the MK concept is that the ignition delay must be longer than the injection duration so that all of the fuel is injected prior to ignition, allowing better premixing. This places an upper limit on the quantity of fuel deliverable at realistically achievable fuel rail pressures, thus limiting load output. Nevertheless, the second generation MK systems expanded the operating range and can now meet the criteria set by the Japanese 10-15 mode urban drive cycle for light-duty vehicles [24]. Unfortunately not all production engines are capable of generating the swirl ratios required, and the available test engine used in this thesis was not equipped with working port deactivation to generate swirl. The degree to which the temperature of EGR gases and intake charge has to be reduced is also a major consideration in the application of MK, and an appropriate compression ratio must be used to avoid early ignition.

The UNiform BUIky combustion System (UNIBUS) proposed by Toyota involves the combination of an early injection (for example -36 to -54°ATDC) followed by a later trigger injection (for example $+5^\circ\text{ATDC}$) into the produced cold flame. NO_x emissions below 70 ppm with simultaneous near zero smoke have been reported [26]. Injecting the main fuel quantity into a cool flame promotes the evaporation of the fuel, but the temperatures experienced are not high enough for thermal cracking of the hydrocarbon fuel which would result in increased soot output [24]. The UNIBUS mode of operation has been used to cover half the speed and load map [26], but is ineffective for high intake temperatures and inappropriate compression ratios since combustion must be avoided during injection to avoid MCC [27]. Precise control over injection timing is required to prevent the fuel spray impinging on the cylinder walls, and boost pressure must be sufficiently high to limit rates of pressure rise [26].

Akihama et al. [12] demonstrated that smokeless combustion is not limited to lean equivalence ratios when they presented a comprehensive Φ -T map based on 3D-CFD analysis, detailing the soot and NO_x production regions. As illustrated by Figure 1.4, HCCI represents only a small region of the operating map, with the possibility of running

with very high local equivalence ratios achievable if temperatures are kept below the 1600 K required for soot formation. In their work large amounts of cooled EGR (up to 60%) were used to restrict temperatures inside the fuel jet to below the soot formation threshold. However, the high EGR requirement limits power output. The PCCI combustion regime is therefore not limited to extremely lean mixtures and control over combustion phasing and rate can be maintained, both clear practical benefits over current HCCI operation. However, load output is a major hindrance to this combustion strategy due to the levels of dilution required to limit temperatures [12], and combustion noise can also be excessive for inappropriately phased combustion.

2.3 Conceptual Combustion Models

The conceptual model of mixing-controlled combustion proposed by Dec [28] and added to by Flynn et al. [29] has been widely referred to as a description of the early stages of mixing-controlled combustion which identifies the regions of initial soot formation, fuel-rich premixed burn, thermal NO production and soot oxidation. Figure 2.2 illustrates an idealised sequence of schematics for the conceptual model prior to the end of injection. The cold fuel jet is seen to initially penetrate the combustion chamber as liquid fuel (1.0°-2.0°ASOI). Downstream of the injector air is entrained into the fuel jet which begins to vaporise and from 2.0°ASOI onwards a vapour region begins to develop. By 3.0°ASOI the liquid fuel has reached its maximum penetration with hot air vaporizing all fuel beyond this location.

The vapour phase continues to propagate downstream of the liquid jet, with a head vortex emerging at approximately 4.5°ASOI. By 5.0°ASOI temperatures in the plume reach ~750 K and fuel breakdown begins, leading to the formation of large Polycyclic Aromatic Hydrocarbons (PAH) across the leading portion of the jet. Temperatures increase to ~825 K as these reactions continue and more hot air is entrained, increasing the rates of oxidation reactions with temperatures in the range 1600-1700 K reached. The penetrating jet causes these products of rich combustion to be pushed aside before being re-entrained into the jet. Importantly these re-entrained species mostly comprise carbon monoxide (CO) and hydrocarbons derived from the fuel that act as the building blocks of particulates.

By 6.0°ASOI small soot particles are seen to form over a large region of the jet cross section that arise from the first part of the fuel-rich premixed burn. From 6.5°ASOI Figure 2.2 shows the presence of a thin diffusion flame on the jet periphery between the fuel-rich premixed burn products and the surrounding fresh air where temperatures of ~2700 K are reached [28, 29]. The last part of the premixed burn is represented by the schematic at

8.0°ASOI. The jet continues to grow and soot concentration increases, most significantly in the leading edge of the head vortex, whilst the diffusion flame continues as a thin reaction zone on the boundary between the jet and surrounding air. By 9.0°ASOI the remainder of the premixed air is consumed and combustion evolves to purely MCC.

The final schematic in part (a) of Figure 2.2 indicates the head vortex has become well formed contains a much larger soot concentration (which by this point are also of larger size). Soot particle size remains small in the central part of the jet except in the head vortex, whilst the soot formed originating from the diffusion flame continue to be present along the jet periphery. Beyond the 10.0°ASOI timeframe, a MCC quasi-steady reacting fuel jet occurs as illustrated by Figure 2.2 part (b) which continues to the end of injection. The overall shape and soot distribution do not change significantly, except that particle size within the head vortex increase. Labelled are the production zones of various species, together with associated temperatures.

Although mixing-controlled combustion remains important in PCCI combustion, the combustion that occurs in PCCI regimes is not conventional and as such the conceptual model above has been updated to include features of early-injection low temperature combustion [16], as shown by Figure 2.3. Fuel penetrates further into the cylinder than in the conventional conceptual model (note the different scales), a potential source for increased HC emissions should wall wetting occur. The first stage fuel ignition contributes to the vaporisation of the liquid fuel, whilst the enhanced mixing results in significantly lower soot formation in the second-stage combustion. The fuel-rich regions in the head of the jet are the location of soot formation [16]. This updated conceptual model is for early-injection low-temperature diesel combustion (LTC), but other LTC injection strategies exist whose features may differ to those noted above.

2.4 Formation of Emissions

2.4.1 Soot

Particulate Matter (PM) is an umbrella term that can be sub-divided. Eastwood [30] separates particulate matter (PM) into three categories; Insoluble Fraction, Soluble Organic Fraction (SOF), and Sulphates. Soot is generally accepted to be the insoluble fraction of particulate matter, whilst the latter two categories are described as volatiles since their physical state is strongly dependent on temperature. A more detailed summary of these can be found in [31]. Soot forms early in the combustion process when local fuel rich areas exist, whereas soot oxidation occurs later when more air is entrained into the fuel spray [32]. The main path of carbon molecules in diesel combustion is to react with

oxygen to form carbon monoxide and, later, carbon dioxide. Thus the molecular carbon/oxygen ratio in the reactants is the determinant in the formation of solid carbon, the critical ratio being unity [9]. When the ratio is greater than one, some of the carbon molecules will fail to bond with oxygen, forming solid carbon. It is therefore crucial to keep local fuel-air equivalence ratios low to avoid this formation. Soot is known to form instantly as very small condensation nuclei. Surface growth and the coalescence of nuclei lead to the formation of primary particles called spherules, which have a consistent diameter of approximately 30 nm. The spherules can undergo one of two processes; agglomeration into larger particles, or oxidation, effectively a surface burning process which provides gas phase products [32]. Heywood [9] summarises the processes leading to the production of soot particles as; Nucleation, surface growth, agglomeration, and finally adsorption and condensation.

In experimental work, soot output in the exhaust is considered as the net result of two competing processes; soot formation and soot oxidation [33, 34]. Mixing-controlled combustion discussed in the previous section is deemed responsible for the majority of the soot formation where fuel pyrolysis takes place in poor oxygen availability (high local Φ). Combustion propagation in the MCC phase is dependent on fuel-air mixing, with the lack of oxygen and slower burning providing suitable conditions for soot formation. The review above in section 2.3 also details formation locations of soot and the corresponding soot distribution pattern within the spray, shown schematically in Figure 2.2. A reduction in the relative proportion of fuel burned in the MCC phase and subsequent increase in proportion of premixed burning forms the basis of PCCI strategies to reduce soot formation.

2.4.2 Oxides of Nitrogen

Emissions of NO_x are being strongly targeted by legislation as they contribute to the formation of acid rain and photochemical smog [6]. Almost all production of NO occurs during mixing-controlled combustion. Both diesel and gasoline engines produce high levels of NO_x , but in gasoline engines these can be removed with the use of 3-way catalysts which are unfortunately unsuitable for diesel applications due to the excess air [19].

The most widely accepted mechanism for the thermal formation of nitric oxide (NO) is that of Zeldovich [35], described by the equations below [9]. High combustion temperatures cause oxygen molecules to dissociate to atomic oxygen, which initiates nitric oxide formation chain reactions. The availability of oxygen and the in-cylinder temperatures are key variables in the formation of nitric oxide.



Although NO dominates the composition of NO_x, up to 10-30% of the total oxides of nitrogen can be composed of nitrogen dioxide (NO₂), generated by the conversion mechanism [9]:



Heywood [9] explains that the critical time period for the formation of oxides of nitrogen in compression ignition engines is between the start of combustion and the occurrence of peak cylinder pressure when the burned gas temperatures are highest. As temperatures cool due to volume expansion and mixing of hot gases with cooler burned gas, the equilibrium reactions are quenched and the decomposition of NO stopped. The mixing with cooler burned gases does not occur with gasoline engines which are assumed to have essentially uniform mixture. As such the freezing process occurs more rapidly in diesel combustion and much less NO decomposition occurs [9].

The conceptual model of diesel combustion described previously and depicted in Figure 2.2 indicates the location of NO formation on the flame periphery. High temperatures result from combustion within the diffusion flame since conditions are near stoichiometric. These conditions are ideal for NO production by the thermal mechanism, with formation occurring on the lean side of the jet periphery (where oxygen is present) [28]. However, the flame front covers a small area and this thermal mechanism is relatively slow. A major proportion of total NO formation may therefore occur during the later stages of the diffusion burning or in hot-gas reactions after combustion terminates. Compression of previously burned mixture to higher temperatures increases the NO formation rate. Despite lower peak temperatures during this time, residence time for NO formation is appreciably longer and the amount of gas involved can be much greater [28]. The intensity of the premixed burn is significant in MCC since air temperature increases with premixed intensity, raising the temperature in the diffusion flame, resulting in higher NO production [17, 36]. As will be discussed, exhaust gas recirculation (EGR) is a technique frequently used to reduce oxides of nitrogen.

2.4.3 Unburned Hydrocarbons and Carbon Monoxide

Unburned hydrocarbon (HC) emissions are compounds derived from the fuel. HC emissions contribute to the formation of smog and may include photochemically reactive species as well as carcinogens [37]. Their output is highly dependent on oxygen availability and as such emissions of unburned hydrocarbons are generally lower in

concentration than gasoline engines because diesel engines operate with excess air (lean) [9]. Potential sources of HC emissions include [38]:

- Fuel impingement on combustion cylinder walls with insufficient air motion to evaporate it before the end of combustion
- Fuel that becomes trapped in crevices surrounded by cool metal surfaces
- Fuel injected and mixed beyond the limit of flammability (over-lean)
- Fuel that is injected late in the cycle, such as with post injections
- Evaporation or entrainment of lubrication oil from cylinder walls
- Quenching of combustion flame on cylinder walls
- Evaporation of fuel trapped in the injector sac nozzle [39]
- Fuel that is insufficiently mixed with air to combust (over-rich) [40]

Near complete oxidation of HCs has been found to require temperatures of at least ~1200 K [41]. This temperature has been reported to be independent of original fuel type, which is intuitive since the final reaction chemistry is unaffected by the original fuel structure [42].

Carbon Monoxide (CO) is a product of incomplete combustion, formed when hydrocarbon species are not completely oxidised to carbon dioxide. It is a colourless and odourless gas highly toxic to human beings and other life forms. As with unburned hydrocarbons there are several potential sources of CO emissions which include over lean mixture regions that burn slowly and over rich regions that have insufficient oxygen availability for complete combustion [43]. High CO have been found to occur in lean regions in the temperature range $800 < T < 1400$ K as well as in rich mixtures at all temperatures high enough to oxidise the source fuel [41]. In hydrocarbon flames the dominant reactions for oxidation of carbon monoxide are [42]:



Of particular importance in the oxidation of CO is the amount of OH present. Sjöberg and Dec [42] demonstrated OH radical concentration increases exponentially with peak charge temperature. They explain that oxidation of CO is dominated by the reaction described in Equation 2.5, and as such the oxidation process is highly sensitive to temperature. A minimum temperature of ~1500 K was found to be necessary for near complete CO oxidation, a figure consistent with [41]. A weak dependence on engine speed has also previously been reported, although the required minimum temperature remained $1500 \text{ K} \pm 50 \text{ K}$ in the range 600-2400 rpm [44]. The speed affects the dwell time at peak temperature, but the process is dominated by the sensitivity of OH radical production to

temperature. As with HCs, the original fuel compound does not affect the final oxidation process and was deemed independent of fuel type and autoignition characteristics [42], but the required local equivalence ratio varies in accordance with fuel in order to attain the required threshold temperature. Complete oxidation of HCs occurs at lower temperature than that of CO [41], allowing CO to remain in an unoxidised state, leading to higher CO than HC emissions.

Improvements in engine-out emissions combined with the use of highly effective aftertreatment systems such as Diesel Oxidation Catalysts (DOC) have significantly reduced tailpipe emissions of HC and CO. However, future emissions legislative targets require significant reductions in NO_x and soot emissions. The use of higher levels of EGR and increased equivalence ratios together with other in-cylinder measures to reduce the formation of these species could have an adverse affect on HC and CO output, especially as oxidation catalysts require a minimum “light-off” temperature in the region of 190-200°C for effective catalytic conversion [45].

2.5 Combustion Noise

Noise emitted by a vehicle has been subject to mandatory standards for nearly 40 years [46]. As Figure 2.4 illustrates, noise limits have been reduced from 82 dB(A) in 1976 to the current level of 74 dB(A) [46], but there is currently no specific legislation relating to the noise attributed to combustion from a motor vehicle. However, it is unlikely that Combustion Noise Levels (CNL) greater than 85 dB(A) will be acceptable to engine manufacturers [17] since extra noise dampening will be required for passenger comfort, incurring increased cost, weight, and taking up further space within the engine bay. The contributions to overall engine noise are summarised in the flow chart in Figure 2.5.

Combustion noise is the noise radiated in response to the compression and combustion pressure development. It is highly dependent upon the rate of increase of cylinder pressure following ignition, the peak cylinder pressure, and the compression ratio [38]. As shown in Figure 2.5, it can be separated into direct and indirect sources [47] and flow noise. Direct combustion noise is attributed to gas forces acting on the structure assuming that the piston velocity in the axial and transverse directions is zero. This noise is transmitted through the cylinder head, upper part of the engine block, and via the crank train, main bearings and crankcase. Indirect combustion noise is the result of gas forces causing components to move through their clearances, causing impacts. An example is that of piston slap where the cold piston is forced into the cylinder wall [47].

High rates of change of in-cylinder pressure have been shown to have a major influence in the combustion noise generated [17]. Rapid rates of heat release are a possible side effect of PCCI combustion since a greater proportion of the heat is released in a shorter period of time compared with conventional combustion. Higher levels of combustion noise are therefore a potential issue. Combustion noise can be reduced by retarding combustion relative to TDC, incurring a thermal efficiency penalty. The fuel consumption penalty becomes significant. Employing a pilot injection can be effective at decreasing the ignition delay of the main injection and thus reducing the rate of heat release and consequently in-cylinder pressure rise. This is a highly effective method for containing combustion noise, but as will be discussed in later sections, comes at the expense of soot output. Moreover, increasing boost pressure has also been reported as being effective in decreasing the rate of change of pressure due to increasing heat capacity [26, 48].

2.6 Engine Operating Parameters with Current Generation Hardware

2.6.1 Intake Charge Conditions

Boosting the intake air is beneficial in achieving higher load outputs and maintaining equivalence ratios sufficiently low to avoid increasing soot output and deteriorating combustion efficiency [27]. Increasing intake pressure, either with the use of a turbocharger driven off the exhaust system or a supercharger driven from the crankshaft enables a greater mass of air and EGR into the cylinder, increasing the output capability of the engine [49]. Increasing boost pressure can shorten ignition delay, but can allow higher levels of EGR and more retarded injection timings [50], both of which can be exploited for PCCI combustion. The greater flow of air into the engine can also increase the overall heat capacity of the charge, which has been shown to be beneficial in reducing rates of pressure rise in the cylinder [26, 48].

Variable Geometry Turbine (VGT) turbochargers are widely employed to improve the efficiency of the exhaust gas turbocharging process. The energy transfer from exhaust gas to turbine impeller can be regulated by moveable nozzle guide vanes, which change the gas flow area and angle of incidence onto the turbine [51]. Figure 2.6 illustrates a schematic of a VGT turbocharger with two settings, one for high turbocharger pressure, and the other for low. At low-speed low-load conditions when exhaust gas energy is low, little work is transferred to the turbocharger. However, although varying the turbocharger vanes will have limited effect on boost pressure, it can strongly influence exhaust manifold pressure, the driving force of EGR flow. Thus, by moving the VGT vanes as well as the EGR valves, better control over EGR flow rate is possible. Hawley et al. [52] reported a

reduction in NO_x levels of up to 45% using VGT combined with EGR, compared to Fixed Geometry Turbine (FGT) levels, without compromising fuel consumption or smoke. Exploiting the highly coupled nature of the VGT turbocharger and external EGR systems is vital to reach performance targets. With FGTs there is limited useable boost below engine speeds of around 2000 rpm, and at higher speeds the pressure ratio would be too great so has to be limited with a wastegate to maintain constant pressure. VGT turbochargers are more flexible in operation than conventional wastegated turbochargers and as well as boosting the power density of the engine, VGT turbocharging can potentially improve brake specific fuel consumption (bsfc) by reducing pumping losses. By optimising boost pressure, especially at part load where pumping losses play an important role on fuel economy, significant bsfc improvements are possible [53].

Exhaust Gas Recirculation (EGR) is a technique commonly used to control NO_x formation and emission in both diesel and gasoline engines. For a pipe of fixed dimensions, external EGR flow is determined by the driving force between the exhaust and inlet manifolds ($p_{exh} - p_i$). This pressure difference is governed by the EGR valve and VGT vane positions (where appropriate), but a limit exists as to the level of EGR that can be achieved without the addition of a system that maintains a pressure difference between the two manifolds. This is generally achieved by throttling the intake air, which reduces the fresh air inlet manifold pressure allowing more EGR flow due to the higher exhaust-side pressure due to the effects of the turbocharger [52].

EGR is essential to achieve simultaneous low soot and NO_x output in PCCI combustion without prohibitively high fuel consumption penalties due to poor combustion phasing. However, lower temperatures can cause deterioration in combustion efficiency (especially at low load). Recycled exhaust gas acts as a diluent. Increasing the level of EGR reduces the oxygen concentration (dilution effect) and increases thermal capacity of the charge as oxygen-containing fresh air is displaced by burned gas products (thermal effect) [54-56]. In particular carbon dioxide (CO_2) and water (H_2O) have high heat capacities and act to lower in-cylinder temperatures and slow the rate of heat release [13]. The reduction in peak temperature is beneficial in reducing NO_x [57] and soot formation since the EGR rate influences the path in the Φ -T plane through changes in the flame temperature and ignition [13]. However, Aceves and Flowers [58] found that in low temperature diesel combustion soot precursors are low at low EGR, but increase rapidly as EGR is raised. After reaching a maximum they decreased rapidly to near zero as the charge mixture approached stoichiometric. It was also found that reducing the rate of mixing and increasing temperature tend to increase the equivalence ratio at ignition, considerably increasing soot precursor production. Several studies including [12, 59, 60] have demonstrated a

reduction in soot output once the EGR rate exceeds a threshold. At this point departure from conventional EGR-soot and NO_x -soot trade-offs is realised, allowing the simultaneous reduction of both emissions.

Although EGR gases are cooled prior to reaching the inlet manifold, intake temperature rises with EGR fraction as cooler fresh air is displaced. Reducing intake temperatures has been shown to be beneficial in reducing NO_x and soot emissions. When developing the MK regime, Kimura et al. [22] reported a decrease in intake gas temperature from 117°C to 67°C resulted in a reduction in the order of 90% in soot emission, and around 30% for NO_x . Ishikawa et al. [61] investigated the effect of heat exchanger efficiency of an EGR cooler on combustion by improving cooler heat rejection from 2.8kW to 7.3kW. The temperature in the intake manifold decreased from 110°C to 36°C , increasing in the charge density and oxygen concentration. This resulted in a reduction of soot emissions due to minimising the high equivalence ratio zone, $\Phi > 2$, but at the expense of HC emissions. Limiting flame temperatures with high rates of EGR contained NO_x output. Overall, faster reaction rates due to increased oxygen availability were deemed to be offset by slower reaction rates due to cooler temperatures and increased thermal capacity, leading to no overall change in heat release or NO_x .

2.6.2 Fuel Injection Equipment and Operating Parameters

A schematic of a typical High Pressure Common Rail (HPCR) system is shown in Figure 2.7. In a HPCR fuel injection system pressure generation and fuel injection are separate events, allowing highly flexible injection strategies at much higher pressures [6]. Fuel is pressurised by a High Pressure (HP) pump before being delivered to a common-rail accumulator, which helps reduce the variation in the high pressure of the fuel [62]. The fuel is then delivered to the individual injectors via short rigid pipes, with the injection event controlled by the ECU. Modern HPCR systems can achieve injection pressures of up to 2000 bar and up to 6 injections per cycle per cylinder, allowing significant reductions in engine-out emissions, noise and fuel consumption [63].

The latest generation common-rail Fuel Injection Equipment (FIE) incorporates piezo-electric controlled injectors that are capable of extremely rapid switching and as such the possibility of shorter injection durations, very small injection quantities, and multiple injections per cycle [6]. Piezo injectors exploit the piezoelectric properties of crystals to deform when a voltage is applied. This change in structure is transmitted hydraulically to the rapidly switching nozzle needle, acting much faster than conventional solenoid injectors. However, the HPCR system is subject to certain limitations. The major disadvantage from a technical point of view is that of rail interactions. When an injector

nozzle opens to inject fuel into the cylinder, a pressure wave travels upstream of the injector into the common-rail, resulting in pressure oscillations [62]. The subsequent injection may then be affected by this pressure wave, resulting in an incorrect fuel delivery in that injection event [64]. These injection-to-injection variations are most severe following a main injection since a large fuel quantity is usually delivered. The pressure wave from a pilot or other low quantity injection is normally small in amplitude and as such does not cause the same problem [62].

The Start of Injection (SOI) influences the temperature during the ignition delay period, the peak flame temperature reached, as well as the cooling of the in-cylinder charge during the latter part of the combustion process as volume expansion takes place [13]. Retarding injection timing is effective at lowering combustion temperatures, which reduces thermal decomposition and thus soot formation [20, 24]. Retarding injection timing from -7° to $+5^\circ$ ATDC is a key modification in the MK mode of operation, resulting in reduced NO_x but increased HC emissions [25]. Retarding timing is also effective at prolonging ignition delay, allowing more mixing time. Another approach for reducing soot output is advancing SOI for a single injection, which can be effective in increasing the ignition delay and providing more time for premixing. However, combustion must be phased so as to avoid increased NO_x , HC and CO emissions and increased fuel consumption, but soot output is highly dependent upon injection timing [17]. With a two injection strategy, Kook and Bae [14] found advancing the main injection provided sufficient time for homogeneous premixing, but that if the main injection was too advanced the vaporization of the diesel fuel was reduced due to the lower initial air temperature, increasing wall wetting. The second (smaller) injection timing was optimised to promote ignition for the given air temperature, resulting in lower emissions.

As well as investigating injection timings, injection pressure is also the focus of attention. For a fixed fuel injection quantity, increasing the injection pressure shortens the injection duration. Increasing injection pressure is associated with reduced soot emissions [23, 57] due to better atomisation and enhanced air entrainment, reducing formation. The higher associated jet velocities are advantageous in achieving a premixed state between fuel and air [14]. Increasing injection pressure has been found to promote early soot formation near to the injector, but to reduce soot concentration more rapidly later in the cycle, reducing residence time for soot formation [34]. The improvement has been attributed to improved oxidation of formed soot since higher OH radicals have been predicted with higher pressures [23], the concentration of which is known to have a significant influence in the oxidation process of soot [9].

However, the ignition delay can be reduced and combustion is commonly advanced with increased injection pressure. This increases rates of heat release (faster burning) with shorter associated combustion duration and high peak pressures, which can lead to increased NO_x emissions [59]. In one study NO_x emissions increased considerably, especially at part load and low speed [65]. It is also worthwhile to note here that within the available literature the effect on combustion noise has mainly been hypothesised but not investigated directly. Fuel consumption has also been reported to decrease with increased injection pressure in some studies [15, 57] as combustion phasing is advanced and combustion duration shortened. The fuel's energy is therefore released at a more efficient combustion phasing and overcomes the higher parasitic losses associated with the generation of higher pressures [59], although this was reported in a heavy duty engine.

Another concern is that of over-penetration of the spray leading to increased HC and soot emissions. Spray penetration, S , has been correlated to the following expression [66]:

$$S = A \cdot \left(\frac{P_{fuel} - P_{cylinder}}{P_{cylinder}} \right)^b \cdot (d \cdot t)^c \quad (2.8)$$

Where d is the nozzle hole diameter, A , b and c are constants, and t is the spray duration. Higher fuel pressure can therefore result in greater spray penetration, potentially resulting in increased HC and soot emissions should wall wetting occur.

2.7 Concluding Remarks

Within this chapter the concept of PCCI combustion has been reviewed together with important emissions formation mechanisms and current generation engine hardware. PCCI combustion potentially offers a solution to simultaneously reducing NO_x and soot emissions by reducing formation of both species. The operating regions that are exploited to achieve this have been introduced and a description given to where PCCI combustion falls relative to other operating strategies. Some of the most successful PCCI strategies have been reviewed, but problems exist with each of the proposals, meaning their implementation on all diesel engines may not be possible. The determination of engine-out emissions is highly complex, and reviews into mechanisms and conceptual models to explain the formation and oxidation of important species have been given. The operation of current generation hardware, including VGT turbochargers, EGR systems and HPCR FIE were included since control over intake conditions, mixture preparation, and injection capabilities are fundamental to PCCI strategies. Chapter 3 will expand upon the PCCI processes and give details on the test equipment used during the experimental investigations.

CHAPTER 3

INTERPRETATION OF PCCI PROCESSES AND DESCRIPTION OF TEST FACILITIES

3.1 Introduction

The purpose of this chapter is to examine the available combustion strategies to achieve the goal of simultaneously reducing soot and NO_x emissions, and summarise the experimental facilities available. The first part of the chapter presents interpretations of conventional and PCCI processes with the use of Φ -T maps, which help to define the study. The requirements for the engine test facility thus required control over the injection strategy and EGR rate in order to assess the relative benefits and hindrances to adapting the combustion strategy from its baseline calibration.

The second part of the chapter describes the test engine and experimental facilities used within this thesis. Instrumentation was required to monitor various pressures, temperatures, speeds, as well as exhaust emissions. The engine had previously been used for a former project and had been installed on the test bed and instrumented with many of the required sensors, which included thermocouples, pressure transducers, speed sensors, and exhaust analysers. In particular, in-cylinder pressure data and the composition of exhaust species were required to a high degree of accuracy and repeatability. Additional instrumentation installed included the smoke and combustion noise meters which will be discussed within this chapter. Short reviews of the specifications of the dynamometer, cooling, EGR and fuel systems are presented before an overview of the engine sensors and emissions measurement equipment are given. The data acquisition equipment and control of the ECU and engine parameters are detailed before concluding remarks are offered.

3.2 Interpretation of PCCI Processes and Definition of Study

Reducing soot formation is a key mechanism to reducing net soot output with PCCI strategies. Avoidance of the soot formation peninsula in the Φ -T plane is required to achieve this, but a number of combustion paths are available. The use of EGR to reduce temperatures is vital to PCCI combustion strategies. Figure 3.1 illustrates the maximum temperatures that could be obtained at a given equivalence ratio for complete combustion. The contours on the left diagram, reproduced from Refs [13, 67], represent the maximum

temperatures that can be achieved for fuel mixed with ambient air initially at 1000 K for varying levels of ambient oxygen concentration. The effect of increasing dilution on the combustion paths is clear. As the ambient oxygen concentration decreases, the maximum temperature obtainable at a specified equivalence ratio decreases. This is a key mechanism in the adaptation to PCCI combustion. However, the paths illustrated in Figure 3.1 are for equilibrium mixture temperatures, and in reality a distribution of fuel-air mixtures and temperatures will be present. Therefore ensuring the overall ambient oxygen concentration is below 15% does not guarantee that the soot and NO_x formation regions will be avoided. However, the degree to which the overall oxygen availability is reduced does place a limit on load output for complete combustion. The right diagram, adapted from [60], represents the maximum achievable temperatures of fuel packets in the jet core with an ambient oxygen concentration of 10% for different initial ambient temperatures. Increasing ambient gas temperature clearly raises the core temperature at a given equivalence ratio, implying that control over ambient temperature can be used to aid the avoidance of the soot and NO_x formation regions.

Developing upon this, four proposed combustion paths are described below together with the factors used to achieve them. Paths taken by typical fuel parcels through the Φ -T plane under conventional, PCCI, and HCCI combustion are illustrated in Figure 3.2, adapted from [13]. A distribution of equivalence ratios will actually be present along the paths and therefore even though the arrows may not pass through either formation region, some formation of that species may occur depending on the spread of the distribution. The conceptual diagrams help to explain the mechanisms to achieve reduced soot and NO_x emissions and should be viewed whilst reading the following strategy summaries, which are based on the proposed findings of Kook et al. [13]. Conventional combustion will be discussed first, before a short summary given to HCCI. More detail is given to two different PCCI strategies, comparing and contrasting how they achieve the emission reductions. The proposed paths offer insight into the causes for soot and NO_x formation, but say nothing about other responses such as fuel consumption, combustion noise, or combustion efficiency. These will be investigated within this thesis.

Conventional combustion is characterised by adiabatic mixing processes followed by rapid premixed combustion. During the premixed burn, rates of heat release are high and little additional mixing takes place. The charge is insufficiently mixed prior to the onset of premixed combustion to avoid the soot formation peninsula. Once the premixed fuel has been consumed, the speed of combustion is limited by the rate of mixing between fuel and air. This mixing-controlled combustion significantly increases the peak temperatures encountered, which follow the peak combustion temperature curve referred to in Figure

3.1. The increase in temperature and reduction in local equivalence ratio as mixing continues causes the fuel packets to enter the NO_x formation region, before cooling as the cylinder volume increases. Both soot and NO_x emissions are therefore generated from conventional combustion [13].

With the proposed pathway for HCCI combustion mixing of the fuel and air is essentially complete prior to the onset of combustion. The fuel is burned within the premixed phase with no MCC to consider and both formation regions are avoided. Two PCCI strategies are summarised below with reference to the path taken. Both strategies use increased levels of dilution to limit temperatures and exploit high levels of premixing to avoid soot formation.

The first proposed paths for PCCI combustion is for retarded injection timing (around TDC) and moderate-high levels of EGR (~15% O_2 concentration). Start of combustion occurs in the expansion stroke and as such in-cylinder temperatures during the ignition delay period are lower than for conventional combustion. This provides more time for mixing and helps generate lower local equivalence ratios at SOC compared with conventional combustion. The late phasing and expanding volume cools the charge and combined with the diluent molecules limits the peak temperatures encountered. Soot formation is expected to be greatest at the end of premixed burning as this is when the path is closest to the soot peninsula. Mixing-controlled combustion follows the premixed phase, which increases the temperature and reduces local equivalence ratios. Dilution and the retarded phasing and slower mixing rates during MCC allow combustion temperatures to be limited and are highly effective at avoiding the NO_x formation region. Modulated Kinetics introduced in section 2.2 is an example combustion strategy that exploits this path [13].

The second proposed PCCI combustion path is for advanced injection timing (around -20°ATDC) and high levels of EGR (~10% O_2 concentration). The higher level of dilution compared with the retarded strategy described above could be expected to result in a higher local equivalence ratio at SOC. However, the extended ignition delay allows more time for mixing and the two cases have similar local equivalence ratios at ignition, although the advanced strategy remains higher. Should the temperature increase sufficiently the path would still pass through the soot formation peninsula. The premixed phase finishes close to TDC and temperatures increase, following the peak flame temperature curve until volume expansion cools the charge. Large amounts of air must be mixed with the partially-burned fuel to achieve low equivalence ratios due to the low oxygen availability. It can therefore be difficult to complete the mixing processes before

in-cylinder temperatures decrease below the ~ 1500 K threshold required for complete rapid oxidation of CO [41, 42], resulting in reduced combustion efficiency. It is worthwhile to note that the equivalence ratio at which the mixture temperature reaches that required for the start of significant heat release increases with the level of dilution due to the extra heat capacity of diluent molecules [13]. This effect can be seen in Figure 3.2 whereby the equivalence ratio at the end of mixing for the advanced (more dilute) case is higher than that of the retarded (less dilute) path. This has repercussions when attempting to avoid the soot formation region.

The above discussion underlines the aims of PCCI combustion strategies to avoid the formation regions of both soot and NO_x . However, it is apparent that there is not one single solution to the problem and many variables must be considered. The factors manipulated to adapt towards a PCCI operating strategy within this thesis are the injection strategy and the rate of EGR. A review of the available test facilities used within these investigations is detailed below and will conclude this chapter.

3.3 Engine Test Facilities

The experimental studies were carried out on a batch 2 (pre-production) Lion V6 2.7l DI diesel engine, the production version of which is present in the S-Type, XF and XJ Series Jaguar cars. Table 3.1 summarises the engine specification. The engine was installed on a test bed with instrumentation, together with data acquisition systems and an integrated rig control system. The engine was equipped with twin-VGT turbochargers which adjust the exhaust-gas pressure acting on the turbine in response to the required turbocharger pressure, an intercooler, and had an external EGR system. This enabled the engine to provide a specified maximum power of 206 bhp (152 kW) at 4000 rpm, and maximum torque of 435 Nm at 1900 rpm. Intercooling reduced the temperature of the compressed intake air, thus increasing its density and oxygen availability for combustion, resulting in improved efficiency of the cylinder charge process. The engine had a high HPCR direct injection fuel system including ‘multiple-point’ injection. The fuel quantity provided by each of the six Siemens VDO Automotive piezo actuated injectors allowed highly accurate fuel metering of up to six injections per cycle per cylinder at up to 1650 bar fuel rail pressure. The orifice diameters of 140 microns provided an extremely fine spray of diesel fuel to help create a uniform fuel-air mixture.

A manual gearbox supplied by Jaguar was run in top gear corresponding to a ratio of 1:1, connecting the engine to the dynamometer, which in turn simulated the load conditions. The Froude AG250 eddy current engine dynamometer had a maximum power of 250kW, a speed limit of 6000 rpm, and maximum torque of 1200 Nm. The casing housed twin

magnetizing coils that produce a retarding controllable magnetic field that resisted the applied torque. A precision strain gauge load cell provided a measurement of total input torque to an accuracy of $\pm 0.25\%$ of full rated torque of dynamometer. The dynamometer had low inertia and could measure speed to an accuracy of ± 1 rpm [68]. Calibration was carried out using weights loaded at a known distance from the centre of rotation.

Two independent cooling systems were used to dissipate heat generated by the test rig. The first, illustrated in Figure 3.3, was used to dissipate the heat generated by the dynamometer, engine cooling system, and the EGR coolers. The engine radiator was replaced with a heat exchanger to reduce the engine coolant temperature. The cooling lines were connected to a Carter air blast cooler with heat load of 530kW, consisting of a fin coil (tube bundle) with the hot coolant flowing inside the tubes and the cooling (ambient) air perpendicular over the tubes. The second cooling system was used for the intake intercooler and fuel coolers, and used cold water from the mains supply. The high rail pressure caused the temperature of the fuel to increase and had to be reduced in the injector overflow return line. An electronically controlled valve was used to regulate the water flow through the intercooler. The valve opening controlled the water flow to achieve a post-compressor air inlet temperature of 35°C.

Exhaust gas was diverted from the exhaust system via an external circuit incorporating EGR valves actuated by stepper motors with positional feedback (one per bank) and returned to the intake side of the engine. Prior to re-entry into the intake manifold the recycled exhaust gases passed through production shell-and-tube heat exchangers. The engine induced air flow was measured by hot-wire anemometer Mass Air Flow (MAF) sensors, monitored by the engine and data acquisition systems. Due to known deviation of MAF sensor readings air flow to the engine was calculated using an oxygen balance, an explanation of which is detailed in Chapter 4. The exhaust system was modified to enable safe extraction of the exhaust gases from the laboratory and the Diesel Particulate Filter (DPF) removed to prevent it clogging with particulates and requiring regeneration.

An AVL 733S Fuel Balance was used to measure the fuel flow over a 120s period to allow an accurate value to be recorded. It operated on a gravimetric measuring principle and allowed for a direct measurement of the fuel mass consumed. Its 1800g capacity was sufficient for a continuous measurement and allowed consumptions of 0-150 kg/h to be measured to an accuracy of 0.1%. Figure 3.4 illustrates the setup of the fuel circuit, including the integration of the AVL Fuel Balance.

3.4 Engine Instrumentation

The positions of pressure, temperature, and speed sensors are shown on the schematic in Figure 3.5. In-cylinder pressure could be measured in five of the six cylinders using three Optrand D322 fibre optic (two in bank A and one in bank B), and two Kistler 6055B (one per bank) pressure transducers. A dummy glow-plug was installed in the remaining sixth cylinder. Each Kistler transducer was connected to a Kistler 5011 charge amplifier, consisting of a high-gain inverting voltage amplifier with a MOSFET as its input to achieve high insulation resistance [69]. The transducers were installed in the glow plug ports and replaced the glow plugs which were surplus to requirement since cold starts were not carried out below laboratory ambient temperatures. As will be discussed in following chapters, high levels of soot were encountered during engine testing, both under conventional combustion strategy and when exploring the field of PCCI combustion. This gave rise to clogging of the adaptors in which the pressure transducers were mounted. The impact on the pressure measurements and subsequent post processing of the data such as IMEP was significant. An investigation was carried out to evaluate four designs of adaptor to provide protection against thermal shock and fouling. This investigation is discussed in detail in Chapter 6.

All other engine pressures were measured using Kulite PT 2054 (2000 Series) pressure transducers. These low power transducers had an accuracy of 0.01% and resolution of 0.001% [70]. Pressure measurements were taken at various positions throughout the intake, exhaust, aftertreatment, and EGR sections of the engine. K-Type thermocouples calibrated in a thermostatic oil bath were located throughout the intake, exhaust, aftertreatment, and EGR sections of the engine. Temperatures of oil and coolant at various stages were also measured with these thermocouples. The turbochargers on each bank of the engine were fitted with Micro-Epsilon turboSPEED 135 sensors, with a speed range of 500-400000 rpm and an output 0-10 V with resolution of 0.1% FSO [71]. These speeds were monitored to check the operation of the turbochargers.

Combustion Noise Level (CNL) was measured using an AVL 450 combustion noise meter. The device enabled outputs representative of the overall noise level to be given in dB or an A-weighted sound pressure level in dB(A) by changing the position of an electrical jumper. The use of such a weighting has previously been found to correlate well with subjective assessment of loudness or noisiness for different types of sound [72]. Computation of an overall noise level involves analysis of multiple frequencies that are weighted prior to output of the best approximation of the noise loudness. Noise levels are given in decibels, a logarithmic scale whereby an increase in 10 dB signifies a doubling in loudness [73]. Within this thesis CNL will be given in dB(A).

To monitor the crankshaft position, a Hohner W4D91R (W-series) incremental optical encoder was connected to the crankshaft via a mounting disk. It was suitable for speeds up to 6000 rpm and had two outputs; one pulse every half degree of crankshaft rotation to trigger the data acquisition system, and one pulse every complete revolution (every 360°). The encoder TDC marker was set to match TDC in cylinder 1 on bank A using an AVL 428 TDC capacitance probe. Using this sensor the metallic piston acted as a capacitance plate such that the voltage output was inversely proportional to the distance between the probe and the piston. Therefore TDC is known to be the location of the stationary point from the probe voltage output. Any difference (error) between the shaft encoder position and true TDC was then accounted for in the online dSPACE model.

A MaxSys 900 Series Model 964D Emission System was used to analyse the engine emissions by taking a continuous sample of exhaust gas. It comprised a main rack containing the analysers, cooler/dryer, distribution oven and internal heating line controllers. A smaller rack containing the Model 352 Dual Stream Heated Pre-filter/pump unit and external heated line controllers and associated equipment was also incorporated into the system. The CO₂ analyser for measuring levels in the intake manifold was contained in an additional smaller rack. Figure 3.6 illustrates the setup of the emissions analysers. Sample exhaust gas was drawn from downstream of the turbocharger through a heated sample line maintained at 190°C to prevent water condensation. The sample passed to the Model 352 unit where it was passed through a disposable filter before passing into the Model 340 Distribution Oven. The sample was then split into two streams, one hot and the other cold. One stream was heated and fed to the HC and NO_x analysers. The second stream passed to the Model 203SM cooler/dryer to remove the water vapour before the CO, CO₂, and O₂ analysers. The specifications of the five analysers are given in Table 3.2, which includes the specification of the regulated span gases required for calibration of each of the analysers. The analysers were calibrated for both zero and span gases before every testing session and the engine would be run periodically at a standard test condition to ensure consistency of the data and check for errors before the required testing was carried out. Analysis of the standard test condition is given in Chapter 6.

An AVL 415S Variable Sampling Smoke Meter was used for measurement of the soot content of the exhaust gas. The variable sampling volume allowed even very low soot concentrations in the exhaust to be measured. The smoke meter measured the exhaust gas volume that passed through the filter paper in a measuring pipe and calculated the effective length. It determined the paper blackening with an optical reflectometer head, and subsequently determined the soot content in the gas. The Filter Smoke Number (FSN) as

defined in ISO 10054, soot concentration (mg/m^3), and pollution level (%) could be output.

3.5 Data Acquisition Systems

A dSPACE modular hardware system was used for data acquisition from the engine sensors and for engine control. It consisted of a single processor, three A/D boards, and a Control Area Network (CAN) board. A schematic showing the individual inputs and outputs of the individual boards, together with how they were integrated into the test rig are shown in Figure 3.7. Table 3.3 details the specifications of the A/D boards.

The DS1005 PPC board featured a Motorola PowerPC 750 processor running at 480MHz and provided the real-time calculation power to the system and the interface to the I/O boards and to the host PC. The peripheral high speed bus interface to the dSPACE I/O boards allowed for transfer rates up to 20 Mbytes/s. Two DS2003 A/D boards specifically designed for the implementation of high-speed multivariable digital controllers were used for the analogue sensors. They incorporated two separate 16-bit A/D converters with 32 channels per board and were programmable over the range 4-16bit. The input voltage range for the channels was $\pm 5\text{V}$ or $\pm 10\text{V}$. Figure 3.7 denotes the inputs and outputs of the two boards. A DS2001 high-speed A/D board was used for the in-cylinder pressure transducers. The data acquisition system was triggered every half-degree of crankshaft rotation by the optical shaft encoder. This board had five parallel A/D channels, programmable resolution (4, 8, 12, or 16-bit resolution).

The DS4302 CAN Interface board featured four CAN channels and connected the modular dSPACE system to the BUS. It allowed the dSPACE system to participate in CAN-bus traffic without the need for additional interface electronics. The ECU monitored the measurements of the engine sensors and controlled the required actuators. Monitored values included temperatures, crankshaft and camshaft angular positions, pressures, and feedback from engine actuators. With the use of look-up tables and stored maps the ECU output the required signal to the engine actuators. For example, if the EGR rate required is deemed to be 30% at a particular condition, the ECU sends signals to the VGT vane actuators and EGR valves to facilitate this result. The position of the EGR valves is monitored with positional feedback, allowing the parameters to be continuously updated as required. ECU measurement signals were monitored and recorded using the PC based software package INCA (Integrated Calibration and Acquisition System), connected to the PC via CAN link. Engine sensor measurements such as fuel rail pressure, injection duration, MAF, intake temperature and pressure, and coolant temperature could be recorded. INCA also allowed certain calibration variables to be overridden, including; the

injection timing (SOI) and quantities of up to six injections per cylinder per cycle together with their respective injection quantities, EGR valve positions, VGT vane positions, fuel rail pressure, and the ability to disable fuel injection events individually. A screenshot of the INCA user-interface with selected features labelled is given in Figure 3.8.

3.6 Concluding Remarks

This chapter has introduced the processes that are characteristic of conventional and PCCI combustion strategies, and has reviewed the test facilities used within this thesis. The use of Φ -T maps is invaluable in understanding the combustion paths taken. The use of EGR to dilute the intake charge will be discussed in detail later in the thesis, but its effect on potential combustion paths through its influence on oxygen concentration and ambient gas temperatures is highly important in PCCI combustion strategies. The test facilities were required to provide control over injection strategy and EGR rate to assess the adaptation from baseline calibration. The hardware and equipment used to measure and record the desired responses is the same for both strategies has been reviewed. The processing of the acquired data will be discussed in the following chapter.

CHAPTER 4

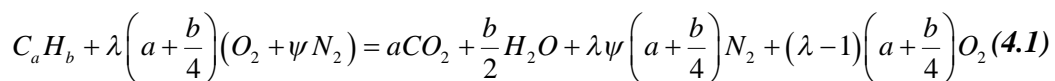
DATA PROCESSING

4.1 Introduction

In this chapter the processing of the data recorded from the engine is documented. Firstly the water content removed from the exhaust has to be accounted for when processing the emissions data. The details of the procedure employed are given before the air-to-fuel ratio (AFR) calculation is presented, after which volumetric and gravimetric analyses of the emissions data are detailed. A section is provided on the conversion between different emissions units and why they may be used. The definitions and calculations of EGR rate and equivalence ratios are presented together with the calculation of combustion efficiency. The definition of mean effective pressures used to analyse engine load behaviour are given, before moving onto the determination of bulk-gas temperature from in-cylinder pressure measurements. The assumptions and procedure for calculating a constant pressure adiabatic temperature based on an equilibrium combustion program from the literature are presented, before concluding the chapter with the evaluation of the ratio of specific heats and net heat release analysis.

4.2 Exhaust Gas Wet and Dry Analysis

Complete combustion of the hydrocarbon diesel fuel results in water and carbon dioxide according the simplified combustion equation [9]:



Where ψ is the molar N/O ratio =3.773 for air, and a/b is the H/C ratio =1.9 for the test fuel. The masses of the products can be calculated for different values of the excess air ratio, λ , (note diesel CI engines run lean so $\lambda > 1$). The total mass of the exhaust is calculated and divided by the total number of moles of exhaust to give the molecular weight of the exhaust.

The exhaust gas is chilled to 5°C to condense the majority of the water vapour out. The amount of water removed can be found from a psychrometric chart for air at atmospheric pressure. This shows that the saturation limit for air at 5°C is 0.55% by mass. Since the amount of water in the exhaust gas prior to entering the dryer is known from the simplified combustion equation above, the water lost in the dryer, and hence the amount of water still

present in the exhaust gas can be calculated. The ‘wetting’ process detailed in Appendix 1 is based on the method in [74], adapted for diesel combustion using the molecular composition of the test fuel. The dry percentage of the constituents in the exhaust from the emissions analysers can thus be converted to actual (wet) percentage of the constituents in the exhaust using equation 4.2:

$$\tilde{x}_i = \frac{\tilde{x}_i^* \cdot \left(\frac{m_{exhaust}}{\tilde{m}_{exhaust}} - \frac{m_{H_2O}(lost)}{\tilde{m}_{H_2O}} \right)}{\left(\frac{m_{exhaust}}{\tilde{m}_{exhaust}} \right)} \quad (4.2)$$

At lower AFR the difference between the amount of oxygen in the exhaust assuming complete combustion for a wet, dry and part wet (0.55% wet) becomes more significant [74] and thus must be accounted for in subsequent calculations. The percentage difference between the wet values and the 0.55% wet values are plotted against λ in Figure 4.1 for $1 < \lambda < 5$. The equation of the power curve fit for the difference between wet and 0.55% wet gives the basis for the conversion from the analysers to wet values. The samples measured by the CO₂, O₂, and CO analysers are ‘dry’ samples and as such the water removed from the exhaust must be accounted for. The wet molar fractions (%) of the measured emissions are calculated using:

$$\tilde{x}_i = \left(\frac{\tilde{x}_i^*}{0.141 \cdot \lambda^{-1.02} + 1} \right) \quad (4.3)$$

Where “*” denotes dry fractions

Since the analysers do not measure nitrogen, hydrogen, or water concentrations, the following expressions are used to determine their values [9]:

$$\tilde{x}_{H_2O} = 0.5y \frac{\tilde{x}_{CO_2} + \tilde{x}_{CO}}{\tilde{x}_{CO} / [K \cdot \tilde{x}_{CO_2}] + 1} \quad (4.4)$$

$$\tilde{x}_{H_2} = \frac{\tilde{x}_{H_2O} \cdot \tilde{x}_{CO}}{K \cdot \tilde{x}_{CO_2}} \quad (4.5)$$

Where y=1.9 and K=3.5.

The nitrogen content is determined by considering that mole fractions add up to 1:

$$\tilde{x}_{CO_2} + \tilde{x}_{CO} + \tilde{x}_{O_2} + \tilde{x}_{N_2} + \tilde{x}_{H_2O} + \tilde{x}_{HC} + \tilde{x}_{NOx} + \tilde{x}_{H_2} = 1 \quad (4.6)$$

4.3 Calculation of AFR

The test engine is equipped with MAF sensors that are monitored by the ECU. However, the accuracy of these sensors is known to vary according to running conditions [31]. For

this reason the AFR has been calculated using exhaust gas constituents through a molar oxygen balance. The molar oxygen balance is performed by comparing the theoretical oxygen content with the measured oxygen content:

$$\tilde{x}_{O_2} = \left(\frac{\tilde{x}_{O_2}^*}{0.141 \cdot \lambda^{-1.02} + 1} \right) = \left(\frac{(\lambda - 1) \left(a + \frac{b}{4} \right)}{a + \frac{b}{2} + 3.773\lambda \left(a + \frac{b}{4} \right) + (\lambda - 1) \left(a + \frac{b}{4} \right)} \right) \quad (4.7)$$

The difference between the two wet oxygen balances is calculated and an iterative goal-seek macro function employed to reduce the error to zero by changing λ . The AFR is then determined using the known composition of the diesel fuel:

$$AFR = \lambda \cdot AFR_s \quad (4.8)$$

This allows the mass flow of air to be calculated:

$$\dot{m}_{air} = AFR \cdot \dot{m}_{fuel} \quad (4.9)$$

The above method has been used by several authors, including [31]. However, when conditions approach stoichiometric, incomplete combustion can cause a deviation in the calculated AFR. Once a close approximation of the wet molar fractions of the measured exhaust gases had been determined using λ obtained from the above approach, the actual AFR is then calculated using the following expression using “wet” molar constituents as appropriate [9]:

$$AFR = 4.773 \cdot \left(\frac{M_{air}}{M_f} \right) \cdot \left[\frac{\tilde{x}_{CO_2} + (\tilde{x}_{CO} / 2) + (\tilde{x}_{H_2O} / 2) + \tilde{x}_{O_2}}{\tilde{x}_{HC} + \tilde{x}_{CO} + \tilde{x}_{CO_2}} \right] \quad (4.10)$$

Here $M_{air} = 28.96$ and $M_f = 13.93$ for an H/C ratio of 1.9. The difference between the two oxygen balances is illustrated in Figure 4.2. Note the divergence of the values of AFR as stoichiometric conditions are approached. The difference in the AFR values obtained using the MAF sensor readings and the calculated AFR are depicted in Figure 4.3. From this point onwards the AFR and mass flow of air discussed relate to those quantities calculated from the oxygen balance based on exhaust composition in Equation 4.10 and not from the MAF sensors.

4.4 Volumetric and Gravimetric Analyses

The emissions analysers record volumetric (molar) concentrations of species in the exhaust in ppm or %. However, it is useful to display emissions in other terms such as mass fractions and flow rates. The conversion from volumetric to gravimetric analysis is given below. Starting from the mass fraction of each gas:

$$x_i = \frac{m_i}{\sum m_i} = \frac{n_i \cdot \tilde{m}_i}{\sum n_i \cdot \tilde{m}_i} \quad (4.11)$$

The wet mass fractions (kg/kg-exhaust) of the measured emissions to be calculated:

$$x_i = \tilde{x}_i \cdot \left(\frac{\tilde{m}_i}{\tilde{m}_{exhaust}} \right) \quad (4.12)$$

The (wet) emission flow rates (kg/s) are calculated:

$$\dot{m}_{exhaust} = \dot{m}_{fuel} + \dot{m}_{air} \quad (4.13)$$

$$\dot{m}_i = x_i \cdot \dot{m}_{exhaust} \quad (4.14)$$

The emission flow rates can be normalised by the fuel flow rate, resulting in the calculation of the Emission Index (EI):

$$EI_i = \frac{\dot{m}_i}{\dot{m}_{fuel}} \quad (4.15)$$

When analysing trade-offs between various emissions, brake specific terms have also been calculated to allow comparison of emissions at different test points and load outputs:

$$bs_i = \frac{x_i \cdot \dot{m}_{exhaust}}{P_b} \quad (4.16)$$

4.5 Emissions Units and Conversion

Units commonly used in the research field and associated published works include molar fractions in ppm and %, the gravimetric fraction of kg/kg-exhaust, mass flow rate of emissions (kg/s), brake specific emissions (g/kWh), and emission indices (kg/kg-fuel). Mass flow rates of emissions can be considered particularly useful when performing drive-cycle testing and analyses, but trade-offs at different engine operating conditions such as speeds and loads are not so easily compared. Instead the emissions results are commonly normalised by fuel quantity or power output to allow easier comparison of data at different conditions. Emissions indices are normalised by the mass flow of fuel as described by equation 4.15. This allows data from different test conditions to be better compared since in general load is dependent on and scales with fuel delivery.

Brake specific units normalise the mass flow rate of the species by the brake power output (equation 4.16). This is again useful when comparing emissions at different conditions, but can mask the response of the emissions if dominated by the brake power. For example, Figure 4.4 illustrates NO_x emissions displayed in brake specific units and as an emissions index. The general trend for both units is NO_x decreasing with retarding SOI until around -2.5°ATDC. The emissions index at TDC increases slightly, possibly due to the low concentrations being measured in this example. However, brake load output deteriorates rapidly retarding from -2.5°ATDC to TDC as combustion is phased much later in the expansion stroke, causing a significant increase in the brake specific NO_x emission. The effect of brake output on a running condition can be analysed by examining the bsfc,

allowing a clearer understanding of brake load output and exhaust emissions. Since the majority of the testing within this work has been carried out at near fixed fuel flow rates, and brake load output has not been maximised for each test point, the majority of the data will be presented as emissions indices. Table 4.1 details the procedures to convert between the units discussed. To provide an example, at a typical operating condition of 1800 rpm 9.7 mg, 43% EGR ($\Phi=0.6$), 600 bar fuel rail pressure, single injection SOI - 2.5°ATDC the HC and CO values listed in Table 4.2 were obtained using the conversions.

The AVL 415S Smoke Meter displays the output of soot content in the exhaust as a Filter Smoke Number (FSN), defined according to the standard ISO 10054 as the loss of reflectivity of filter paper after sampling an exhaust gas column of 405 mm length. The correlation between FSN and soot concentration (mg/m^3) used has been that of Christian et al. [75], given by Equation 4.17 for FSN values less than 8 and illustrated in Figure 4.5 for $0 \leq \text{FSN} \leq 4$.

$$\rho_{\text{soot}} = \left(\frac{1}{0.405} \right) \cdot \alpha \cdot \text{FSN} \cdot e^{(\beta \cdot \text{FSN})} \quad (4.17)$$

Where $\alpha = 5.32$ and $\beta = 0.31$ for smoke meter with heated line.

The mass flow rate of soot is calculated from the soot concentration as described by [76]:

$$\text{Soot} (g/hr) = \left[\frac{\text{Soot} (g/m^3) \cdot \dot{m}_{\text{exhaust}} (g/hr)}{\rho_{\text{sample}} (g/m^3)} \right] \quad (4.18)$$

Where ρ_{sample} is the sample gas density at the measurement location.

4.6 Exhaust Gas Recirculation

The definition of rate of Exhaust Gas Recirculation (EGR) used within this thesis is:

$$\text{EGR} = \left(\frac{m_{\text{EGR}}}{m_i} \right) = \left(\frac{m_{\text{EGR}}}{m_{\text{air}} + m_{\text{EGR}}} \right) \quad (4.19)$$

It defines the mass of recycled exhaust gas as a fraction of the total inlet gas. The EGR rate is calculated by comparing the CO_2 in the exhaust and CO_2 in the intake manifold as described by the equation below, the derivation of which can be found in Appendix 2:

$$\text{EGR} = \frac{\text{CO}_{2\text{ intake}} - \text{CO}_{2\text{ atmospheric}}}{\text{CO}_{2\text{ exhaust}} - \text{CO}_{2\text{ atmospheric}}} \quad (4.20)$$

The above equation contains wet constituents. Since there is more water in the exhaust than in the intake and/or in the atmosphere, it is important to perform the EGR calculation with the wet molar fractions.

4.7 Equivalence Ratios

The fuel-air equivalence ratio (Φ) is the ratio between the actual AFR and the stoichiometric AFR, defined by:

$$\phi = \frac{AFR_s}{AFR_{actual}} \quad (4.21)$$

Since diesel engines generally run lean of stoichiometric (in contrast to gasoline engines), this parameter is used instead of the excess air ratio (λ). The fuel-air equivalence ratio above is based on the fuel delivered and the fresh air induced into the engine. It therefore does not account for the oxygen contribution to the charge from EGR. Instead the oxygen-to-fuel ratio (OFR) defined in equation 4.22 below is a more reliable measure since oxygen contributions from the fresh air and EGR are accounted for:

$$OFR = \frac{\dot{m}_{O_2}}{\dot{m}_f} = \frac{\dot{m}_a}{\dot{m}_f} \left[0.233 + x_{O_2,exh} \left(\frac{EGR}{1 - EGR} \right) \right] \quad (4.22)$$

The fuel-oxygen equivalence ratio (ϕ_{O_2}) is obtained from this OFR which relates the actual OFR to that dictated by the combustion stoichiometry. It is used to give an indication of how lean/rich the mixture is since the composition of the combustion products is greatly affected by this parameter:

$$\phi_{O_2} = \frac{OFR_s}{OFR} = \frac{0.233 \cdot AFR_s}{OFR} \quad (4.23)$$

4.8 Combustion Efficiency

Combustion efficiency is defined as the fraction of the fuel energy released by the combustion process given the energy supplied:

$$\eta_c = \frac{Q_f}{m_f \cdot Q_{LHV}} \quad (4.24)$$

It has been calculated from the combustion inefficiency ($1 - \eta_c$), as described by [9]:

$$\eta_c = 1 - \frac{\sum_i x_i \cdot Q_{LHV_i}}{[\dot{m}_f / (\dot{m}_a + \dot{m}_f)] \cdot Q_{LHV_f}} \quad (4.25)$$

Where x_i are the mass fractions of combustible products in the exhaust (CO, HCs, soot, and H₂) and Q_{LHV} are the lower heating values for each species.

4.9 In-Cylinder Analyses

4.9.1 Processing of in-cylinder pressure data

In order to reduce the impact of noise on the pressure signals 100 consecutive cycles of data were recorded and noise spikes from electromagnetic interference removed by

filtering the recorded signals with a user-designed Matlab script. In order to not remove useful and correct data, careful selection of the filter was required. Passing the data through a Butterworth filter was found to be extremely effective removing the noise spikes, but was also found to remove true values. This becomes especially apparent when analysing the rate of heat release data and this filter was therefore not used. Instead a maximum allowable peak pressure and rate of change of pressure were set based on the operating conditions with safety margins so as not to interfere with the true pressure signal readings. For example, for an operating condition of 1000 rpm 2.5 bar BMEP (54 Nm) the peak pressures did not exceed 50 bar. The filter limits were set at 75 bar and 30 bar/°CA (note data will be presented in later chapters that shows peak rates of pressure encountered did not exceed 21 bar/°CA). Any data point that exceeded the prescribed limits was removed and replaced with “Not-a-Number” (NaN). Once the noise spikes had been removed, the 100 cycles were ensemble-averaged (with NaN entries being ignored from the calculation) to obtain one average pressure trace per operating condition. Figure 4.6 illustrates an example of 100 consecutive cycles plotted after filtered (red crosses), and the subsequent ensemble-averaged pressure trace (black line). This ensemble-averaged data was then processed to calculate mean effective pressures, peak rates of change of pressure, heat release, and subsequent ignition delay.

Mean Effective Pressures (MEP) are relative performance measurements that scale the work output by the engine displacement. This is a more useful quantity than torque when comparing outputs from different engines since values are relative. For example, 200 Nm might be near maximum torque output for a 1.5l diesel engine at a given engine speed, whereas 200 Nm on a 3.0l test engine could be approaching half peak torque. However, the BMEP would be normalised such that the BMEP of the smaller displacement engine was twice that of the larger displacement engine. Details of the calculation of brake, indicated, pumping, and friction mean effective pressures are given below.

Brake power delivered to the dynamometer by the engine is given by:

$$P_b = 2\pi \cdot N \cdot T \quad (4.26)$$

BMEP is a measure of the work output of an engine available at the dynamometer.

$$BMEP = \frac{P_b \cdot n_r}{V_d \cdot N} = \frac{2\pi \cdot n_r \cdot T}{V_d} \quad (4.27)$$

Indicated performance parameters use in-cylinder pressure data to calculate the work delivered to the piston by the gas. They give insight into combustion performance and aid in the understanding of combustion characteristics. The Net Indicated Mean Effective Pressure (IMEP_n) is defined as the work delivered to the piston over the entire 4 strokes of the cycle, per unit displaced volume [9]:

$$IMEP_n = \frac{W_{c,in}}{V_d} = \frac{\int_0^{720} p \cdot dV}{V_d} \quad (4.28)$$

The Gross IMEP is the work delivered to the piston over the compression and expansion strokes only, per unit displaced volume [9]:

$$IMEP_g = \frac{W_{c,ig}}{V_d} = \frac{\int_{-180}^{+180} p \cdot dV}{V_d} \quad (4.29)$$

Both IMEPs are calculated from a numerical integration using the recorded pressure data. For the data presented in this thesis the interval is constant at 0.5°CA, which corresponds to the highest resolution output from the shaft encoder. The accuracy of the calculated IMEPs is highly dependent on correct phasing of pressure and volume data and even small phase changes can result in large percentage errors being introduced, highlighting the requirement to set the shaft encoder TDC marker output as close as possible to TDC of the engine (described in section 3.4). The difference between the two definitions is the pumping work, which represents the work done on the in-cylinder gases by the piston over the inlet and exhaust:

$$PMEP = IMEP_g - IMEP_n \quad (4.30)$$

The level of friction is estimated using:

$$FMEP = IMEP_n - BMEP \quad (4.31)$$

Note that here FMEP includes the contribution from auxiliary work (amep).

4.9.2 Estimation Bulk Gas Temperature

An estimate of the mass-averaged in-cylinder bulk-gas temperature through the closed part of the cycle is necessary for determining the ratio of specific heats (γ) which is a function of temperature and composition, as well as for estimation of the initial enthalpy of the reactants (fuel and air) prior to the start of combustion. The in-cylinder bulk-gas temperature was estimated from the in-cylinder pressure and volume, with the calculation divided into three regions as summarised by Table 4.3; compression (1-2), combustion (2-3), and expansion (3-4), demonstrated by the idealised indicator diagram shown in Figure 4.7. The polytropic exponent, n , was determined for each test case from a log p-log v plot. Two values were calculated, one for compression stroke and one for the expansion stroke. The temperature at each interval between BDC of intake (1) to SOC (2) was calculated assuming a polytropic process using equation 4.32:

$$T_i = T_{\text{intake}} \cdot \left(\frac{p_i}{p_{\text{intake}}} \right)^{(1-1/n)} \quad (4.32)$$

The temperature rise due to combustion is approximated using the method described by Brunt et al. [77]. During the combustion process (2-3) it is assumed that the combustion

can be idealised by dividing into a number of constant volume combustion processes, illustrated by the small step changes on the p-v schematic shown in Figure 4.7, and that the pressure change due change in volume and heat transfer to the walls can be modelled as a series of polytropic processes. The incremental pressure rise due to combustion can be expressed as:

$$\Delta p_{comb} = p_{i+1} - p_i \cdot \left(\frac{V_i}{V_{i+1}} \right)^n \quad (4.33)$$

Assuming perfect gas relationships and that the combustion takes place at fixed volume, the temperature rise due to combustion at each interval can be approximated by the equation [77]:

$$\Delta T_{comb} = \frac{\Delta p_{comb} \cdot V_{i+1}}{m \cdot R} \quad (4.34)$$

Where $m = m_{air} + m_{fuel} + m_{egr} + m_{residuals}$

Therefore the temperature at each interval during combustion is calculated as the combination of the temperature rise due to combustion and the polytropic temperature changes:

$$T_{i+1} = T_i \cdot \left(\frac{V_i}{V_{i+1}} \right)^{(n-1)} + \Delta T_{comb} \quad (4.35)$$

The residual fraction is unknown, but a value of 5% of total trapped mass has been used throughout this thesis. For a diesel engine 17.3:1 compression ratio the value could be expected to range from 3-10%, but the value used is consistent with other published work [9, 77]. If the actual residual fraction were greater, 10% for example, an error in the mass of trapped charge would result that would lead to an error in the calculated mass and temperature. However, the extra mass of residuals as a fraction of the total trapped charge is small. In this example an error in mass estimation of ~5.5% would occur. This effect has been investigated by other researchers [77, 78] who concluded that an error in mass estimation (or temperature) of under 5% is acceptable for heat release analysis for combustion diagnosis purposes. Brunt et al. [77] documented a charge temperature error of 10% typically leads to a 3% error in calculated heat release. Overall in the calculation of the temperatures and the ratio of specific heats presented, the contribution of the residuals is small compared with other variables such as inlet temperature, pressure, and fraction of external EGR, nevertheless its contribution has been considered.

Once combustion has terminated the pressure and temperature rises due to combustion are zero. The decrease in temperature from EOC-EVO (3-4) is estimated using a polytropic expansion with temperature and pressure at EOC as a reference point:

$$T_i = T_{\text{EOC}} \cdot \left(\frac{P_i}{P_{\text{EOC}}} \right)^{(1-1/n)} \quad (4.36)$$

An example case is demonstrated in Figure 4.8 which shows estimated bulk-gas temperature against crank angle location. In this example SOC is +0.5°ATDC, EOC is +32°ATDC:

4.9.3 Adiabatic Flame Temperature

Two adiabatic flame temperatures are defined, one for constant pressure and one for constant volume. Conventional DI diesel combustion and PCCI combustion typically span many crank angle degrees in combustion duration. The constant volume definition gives the temperature that occurs without any work delivered to the piston, and with no heat transfer or change in kinetic or potential energy (constant internal energy assumption). The constant pressure definition gives the temperature resulting from combustion without any heat transfer or change in kinetic or potential energy (constant enthalpy assumption). This definition using constant pressure is the one that will be used explicitly for the following adiabatic flame temperature calculations. For a constant pressure process the change in enthalpy is zero. From the First Law of Thermodynamics [79];

$$H_{\text{Reactants}} - H_{\text{Products}} = 0 \quad (4.37)$$

The enthalpy of the reactants is calculated by:

$$H_{\text{Reactants}} = \sum n_i \left[\Delta \tilde{h}_{f,i}^{\circ} + \tilde{c}_{p,i} (T_{\text{initial}} - 298.15) \right] \quad (4.38)$$

Since molar enthalpies are temperature dependent, data were taken from Rogers and Mayhew [80] to enable more accurate values to be used within the enthalpy calculations. Polynomial functions were applied to the data of each species to yield equations that could be used to calculate the heat capacity of the species at any desired temperature. Figure 4.9 illustrates the data graphically. The enthalpy of formation of the fuel $\Delta \tilde{h}_{f,\text{fuel}}^{\circ}$ was calculated from the definition that the molar enthalpy at the reference temperature (298.15 K) is zero, i.e. $\tilde{h}^{\circ}(T_{\text{ref}}) = 0 \text{ kJ/kmol}$. Turns [79] tabulates coefficients for polynomials for the calculation of fuel enthalpy and specific heat for reference state of zero enthalpy of the elements at 298.15 K and 1 atm;

$$\tilde{h}_f^{\circ} (\text{kJ/kmol}) = 4184 \left(a_1 \theta + a_2 \frac{\theta^2}{2} + a_3 \frac{\theta^3}{3} + a_4 \frac{\theta^4}{4} - a_5 \theta \frac{\theta^{-1}}{5} + a_6 \right) \quad (4.39)$$

$$\tilde{c}_p (\text{kJ/kmol} \cdot \text{K}) = 4.184 (a_1 + a_2 \theta + a_3 \theta^2 + a_4 \theta^3 + a_5 \theta^{-2}) \quad (4.40)$$

Where $\theta = T(K)/1000$

The coefficients used are summarised in Table 4.4. The enthalpy of formation of the fuel is estimated from data available for a general diesel fuel of molecular formula

$C_{10.8}H_{18.7}$ and molecular weight 148.6 kg/kmol, which is a smaller chain hydrocarbon with lower molecular weight than the fuel experimental fuel. In the absence of any data on a more similar compound this will be used to estimate the enthalpy of the diesel. Substituting in the coefficients and assuming that the molar enthalpy at 298.15 K is zero the result $\tilde{h}_{f, fuel}^{\circ} = -180 \text{ MJ / kmol}$ was obtained.

A chemical equilibrium code based on the work of Olikara and Borman [81] and obtained from Turns [79] was used to calculate the constant pressure adiabatic flame temperature by solving the First Law problem described in Equation 4.37. The program calculates the adiabatic flame temperature for adiabatic constant-pressure combustion with specified fuel composition, reactant enthalpy, fuel-air equivalence ratio, and pressure. The effects on composition and intake temperature of EGR are included in the calculation through the calculation of the molar fractions of the species and inlet temperature. It is assumed that the oxidiser is air with a simplified composition of 79% N_2 , and 21% O_2 , and eleven species are considered in the products of combustion: H, O, N, H_2 , OH, CO, NO, O_2 , H_2O , CO_2 , and N_2 . The calculation was performed based on inputs of the stoichiometric fuel-air equivalence ratio ($\Phi=1$). Using the overall fuel-air equivalence ratio would assume mixture homogeneity, but these conditions will not be achieved in practice. The use of the stoichiometric fuel-air equivalence ratio was expected to be more reliable when considering a standard diesel diffusion flame which would be present. As stated above the analysis assumed constant pressure, whereas in reality this does not strictly occur as fuel is burned over a finite number of crank angle degrees and thus pressures and volumes. However, either the constant pressure or constant volume constraint must be applied. The purpose of the calculation was to investigate the relationship between soot and NO_x output and temperature for different running conditions. As will be demonstrated in the thesis, the calculation proved sufficient in providing insight into the combustion behaviour.

4.10 Heat Release Analysis

Heat release analysis has been performed to gain insight into combustion characteristics. The apparent net heat release (Q_n) represents the work done on the piston and the increase in sensible energy of the trapped mass, but does not consider heat transfer or blowby losses. Apparent gross heat release (Q_g) corresponds to the total amount of chemical energy released from the fuel during combustion such that:

$$\frac{dQ_g}{d\theta} = \frac{dQ_n}{d\theta} + \left(\frac{dQ_{ht}}{d\theta} + \frac{dQ_{blowby}}{d\theta} \right) \quad (4.41)$$

Although analysis of gross heat release would be preferable in an ideal world, the aims of the research were in understanding constraints imposed on injection and EGR strategies

with a view to reducing emissions. Heat rejection has therefore not been calculated. Instead the heat release data presented within this thesis are net quantities. Net heat release analysis is well documented and enables good insight into combustion characteristics and differences between running conditions without the need to calculate heat transfer which is both a potential source of error and more complicated. The apparent net rate of heat release ($ROHR_n$), $dQ_n/d\theta$, was calculated from the single-zone First Law of thermodynamics [9]:

$$\frac{dQ_n}{d\theta} = \frac{\bar{\gamma}}{\bar{\gamma}-1} p \frac{dV}{d\theta} + \frac{1}{\bar{\gamma}-1} V \frac{dp}{d\theta} \quad (4.42)$$

A Matlab script was used to calculate the heat release. During the first iteration, the ratio of specific heats was kept constant ($\bar{\gamma} = 1.35$). Once the net rate of heat release was calculated, the cumulative net heat release was evaluated by an integration process of interval 0.5°CA .

The computed apparent rate of heat release is highly sensitive to the calculation of $\bar{\gamma}$, the value of which is known to be a function of both temperature and composition and therefore varies during the cycle. Ideally a multi-zone model would be used to calculate $\bar{\gamma}$ accounting for fuel specification, AFR, EGR, charge pressure and temperature, and development through the cycle, but commonly $\bar{\gamma}$ is determined as a function of temperature only [82]. However, due to the varied levels of dilution and composition used during the investigations within this thesis, to improve the accuracy of the computed value a second iteration of the analysis was performed, this time accounting for charge composition and temperature. Values of γ were calculated for fresh charge (pre-combustion) and for burned gases (post-combustion) based on the known AFR, rate of EGR, and composition of the exhaust gas products.

Here fresh charge (fc) consists of injected fuel and induced fresh air. c_p for the injected fuel (diesel) in the vapour phase is calculated using Equation 4.40 and the molecular weight of the fuel. c_p values for air at different temperatures were obtained from tables of thermodynamic properties in Rogers and Mayhew [80] and plotted to yield a polynomial expression as a function of temperature. c_p of the mass averaged mixture of fuel and fresh air was obtained using:

$$c_{p,fc} \left(\text{kJ} / \text{kg} \cdot \text{K} \right) = \frac{c_{p,fuel} + (AFR \cdot c_{p,Air})}{1 + AFR} \quad (4.43)$$

The ratio of specific heats was calculated using:

$$\gamma = \frac{c_p}{c_p - R} \quad (4.44)$$

Where R is assumed to be that of fresh air.

The final composition in the exhaust (burned gas) was known from the emissions analysis, but intermediate products and reactions were not accounted for. Assuming the burned mixture was in equilibrium, for each species i in its standard state at temperature T , the specific heat $c_{p,i}$ was approximated by [9]:

$$c_{p,i} = \frac{(a_{i1} + a_{i2}T^4 + a_{i3}T^2 + a_{i4}T^3 + a_{i5}T^4) \cdot \tilde{R}}{\tilde{m}_i} \quad (4.45)$$

The coefficients for CO_2 , H_2O , CO , O_2 , and N_2 were obtained from a NASA equilibrium program which uses JANAF tables of thermodynamic data. The heat capacity of the burned gas was calculated as a function of temperature based on the mass-averaged exhaust gas composition:

$$c_{p,bg} = \sum (x_{\text{CO}_2} \cdot c_{p,\text{CO}_2}) + (x_{\text{H}_2\text{O}} \cdot c_{p,\text{H}_2\text{O}}) + (x_{\text{CO}} \cdot c_{p,\text{CO}}) + (x_{\text{O}_2} \cdot c_{p,\text{O}_2}) + (x_{\text{N}_2} \cdot c_{p,\text{N}_2}) \quad (4.46)$$

γ was calculated at each time interval (every 0.5°CA) using equations 4.46 and 4.44 as a function of temperature for the exhaust gas composition of the data set. This process was performed for each data set to account for the differences in AFR and burned gas composition for each condition. Figure 4.10 illustrates an example of the variation of the ratio of specific heats for fresh charge and burned gas with temperature for an AFR of 21.8.

The computed values of γ_{fc} and γ_{bg} were then used to calculate a more accurate mass-averaged value, $\bar{\gamma}$, calculated in three separate zones. Before SOC the charge consists of fresh air, EGR, residuals, and fuel once injected, and can be expected to be fairly well mixed. $\bar{\gamma}$ for the first region (SOI-SOC) is thus given by:

$$\bar{\gamma}_{\text{SOI-SOC}} = \frac{\gamma_{fc} \cdot m_{fc} + \gamma_{bg} \cdot (m_{\text{EGR}} + m_{\text{residuals}})}{m_{\text{total}}} \quad (4.47)$$

Where $m_{fc} = m_{\text{fuel}} + m_{\text{air}}$ and $m_{\text{total}} = m_{fc} + m_{\text{EGR}} + m_{\text{residuals}}$

From the start to the end of combustion (SOC-EOC) the composition of the cylinder contents changes continuously as fresh air oxidises the fuel to form burned gas products. Although the pressure throughout the cylinder is constant, heterogeneous combustion conditions result in temperature distributions, with fresh charge and burned gas species at different temperatures. This would influence the value of $\bar{\gamma}$. Since the pressure was used to estimate the in-cylinder bulk-gas temperature only a single average temperature was

obtained which does not allow the temperature differences to be dealt with individually. However, to achieve a reasonable approximation of the average value of $\bar{\gamma}$ a weighting has been applied during the combustion development to account for changes in composition and subsequent values of $\bar{\gamma}$. A simple linear Mass-Fraction Burned (MFB) profile was established over the interval SOC to EOC using the cumulative heat release calculated during the first iteration (where $\bar{\gamma} = 1.35$). The true MFB profile more resembles an 'S' shape, but for the purpose of calculating $\bar{\gamma}$, the simpler approximation was deemed sufficient. The gradient of the straight line was normalised by the maximum cumulative heat release (Q_n) to give the MFB, ranging from 0 at SOC to 1 at EOC. This was then used in the second iteration of heat release calculations, this time using different γ values for fresh charge and burned gas that vary with temperature and mixture composition according to equation 4.48:

$$\bar{\gamma}_{SOC-EOC} = \frac{\gamma_{fc} \cdot (1 - MFB) \cdot m_{fc} + \gamma_{bg} \cdot MFB \cdot m_{fc} + \gamma_{bg} \cdot (m_{EGR} + m_{residuals})}{m_{total}} \quad (4.48)$$

Weighting the value of $\bar{\gamma}$ using the masses of fresh charge and burned gas in conjunction with the MFB profile was deemed to be the best practical approach. Although the necessary assumption of homogeneous charge and temperature distribution will incorporate a source of error in the determination of $\bar{\gamma}$, the above approach gives a good estimation. Finally, once combustion has terminated (EOC-EVO) the in-cylinder composition is assumed to be homogeneous and consisting of burned gas such that:

$$\bar{\gamma}_{EOC-EVO} = \gamma_{bg} \quad (4.49)$$

The variation of the ratio of specific heats with crank angle location is illustrated in Figure 4.11 for fresh charge using the calculated AFR, burned gas using the exhaust gas composition, and the mixture composition using equations 4.46-4.48.

4.11 Concluding Remarks

This chapter has detailed the calculations performed on the acquired test data used to assess the relative performance of the engine and combustion strategies presented within this thesis. The calculated quantities provide insight into the behaviour of the system and aid the understanding of the mechanisms responsible for the combustion behaviour. This allows the benefits and penalties of PCCI and conventional strategies to be analysed. Particular attention has been paid to the calculation of AFR, in-cylinder bulk-gas temperature, constant pressure adiabatic flame temperature, and the calculation of heat release. As will be discussed, these parameters are invaluable in understanding the responses presented.

CHAPTER 5

STUDIES OF NOISE, IGNITION DELAY, AND COMBUSTION PHASING TO SUPPORT ASSESSMENT OF PCCI COMBUSTION

5.1 Introduction

This chapter is divided into three sections which individually examine the determinants and relative importance of noise, ignition delay, and combustion phasing. Increasing the level of premix is potentially liable to increase combustion noise, which must be considered when developing a combustion strategy. An investigation into the factors that determine the ignition delay is then presented, before the effect of combustion phasing on emissions and fuel consumption is analysed. A summary of pertinent findings completes the chapter.

5.2 Combustion Noise

5.2.1 Introduction

Although there is no direct regulation of combustion noise, levels are restricted by OEMs for quality reasons to meet customer expectations of low NVH (Noise, Vibration, and Harshness). The premixing of the charge which is exploited with PCCI strategies to limit soot and NO_x formation tends also to increase noise, which is a serious disadvantage of this strategy. Combustion noise is a source of potential annoyance for both passengers and people outside of the vehicle. Values above 85 dB(A) are unlikely to be acceptable [17], although a development target of 90 dB(A) opens up the range of strategies available. The focus of the first section of this chapter is to investigate the factors responsible for the generation of combustion noise and potential solutions to limit its level. In this chapter, the contribution of combustion noise to total engine noise and to exterior pass-by noise is introduced. The measurement of online combustion noise is discussed and compared to interior (cabin) noise obtained from the recorded pressure history using proprietary software. Analysis of pertinent literature revealed that peak pressures and peak rates of pressure of rise strongly affect combustion noise level [83]. Consequently the importance of the rate of change of in-cylinder pressure (first derivative of pressure with respect to crank angle) is analysed and correlations at three different engine speeds presented, before

the ratio of ignition delay to peak rate of net heat release is considered as a potential strategy development tool. Spectral analysis of in-cylinder pressure data are presented to investigate the distribution of the energy contained in pressure traces and to attempt to identify differences between conventional and PCCI combustion.

5.2.2 Contributions to Overall Pass-By Noise

There are many noise sources from vehicles, including noise derived from rotating components (for example the crankshaft, camshaft, tyres, alternator, and water pump), torsional vibrations, structural distortion (from combustion and stress waves within the engine structure), inlet and exhaust noise, cooling fans, brake noise, road noise, and wind noise. The sources of noise that contribute to the overall pass-by noise of two passenger vehicles travelling in accordance with ISO 362 [84] are presented in Figure 5.1 [85]. Five general categories have been used to describe the contributors for a DI diesel and a gasoline powered vehicle at 74(+1) dB(A) and 74 dB(A) respectively. Engine noise from the diesel powered vehicle is seen to contribute significantly more to the overall pass-by noise than the corresponding gasoline vehicle, highlighting the importance of this contribution. The data presented in Figure 5.1 are representative of noise contributions at approximately 50 km/h. The relative contributions of each source will vary according to many factors, primarily vehicle speed. For example, at speeds of 15 km/h and less, propulsion noise (noise from engine, transmission, intake and exhaust systems) becomes most dominant [86]. Engine noise can be further separated into sub-divisions as previously illustrated by Figure 2.5. Within this thesis only combustion noise is considered in detail.

5.2.3 Interior (cabin) Noise

Passenger comfort within the vehicle cabin has become an important factor in the selection and purchase of a vehicle. The overall interior noise can be considered the combination of airborne and structure borne noise sources. The crank-based pressure data that were supplied online to the AVL 450 Combustion Noise meter were also processed using proprietary software to generate a representative noise in the interior (cabin) of a passenger vehicle similar to the ones the test engine is installed. The main function of the software is to weight the noise spectra into frequency bands to give an audible noise representation of the effect of pressure changes within the cylinder. Figure 5.2 illustrates there is a clear relationship between combustion noise (as measured by the AVL 450 Combustion Noise meter) and vehicle interior noise, with interior noise increasing with combustion noise. If a limit on interior noise is imposed, for example 65 dB(A), combustion noise has to be contained in this example below 80 dB(A) for the broad frequency band (a larger frequency range) and below 85 dB(A) for the frequency band associated with combustion

noise. To put this in context, 60 dB(A) is approximately the noise level that would be experienced in a restaurant or department store, and 70 dB(A) that from a loud radio [72].

5.2.4 Rate of Change of Pressure

As was discussed in Chapter 1, combustion noise is deemed to be strongly dependent on the peak pressure, the peak rate of change of pressure (the first derivative of pressure), and the engine speed. With this in mind the relationship between the peak rate of change of pressure measured in pressure per unit time, here presented as MPa/°CA was investigated. Figure 5.3 illustrates the clear dependence of combustion noise on peak rate of change of in-cylinder pressure at engine speeds of 1200 rpm, 1500 rpm and 1800 rpm. At low Combustion Noise Levels (CNL) the peak rate of pressure change is low, around 0.15 MPa/°CA for 72 dB(A). Here the maximum rate of pressure change is that of the motored compression of the charge. From 68-80 dB(A) Figure 5.3 shows that very small changes in peak rate of pressure increase can result in large variations in noise output for the data at 1500 rpm and 1800 rpm, but the values encountered are nevertheless low and should not pose a problem or limitation to any such calibration. In slight contrast the 1200 rpm data can be seen to diverge more progressively. As degree of constant-volume combustion increases and the combustion becomes more rapid, the rate of change of pressure increases resulting in higher CNL. As the peak rate of pressure rise increases from approximately 0.20 MPa/°CA the 1500 rpm and 1800 rpm responses begin to separate. Beyond this point CNL values recorded are higher for the faster engine speed for a given rate of pressure change, attributable to changes in frequency, dominated by engine speed.

Converting the derivative of the pressure rise from the crank domain to the time domain compensates for differences in the crank-angle duration since at higher engine speed one degree of rotation takes place in a shorter time period measured in milliseconds. Figure 5.4 illustrates the same CNL data as Figure 5.3 but in this case combustion noise is plotted against the first derivative of pressure with respect to time (i.e. MPa/ms). Smaller differences between the three data sets are noticed compared to when plotted in the crank domain. Noticeably, beyond approximately 85 dB(A) the data at 1500 rpm and 1200 rpm appear to have a very similar dependence on the rate of change of pressure, whereas the data at 1800 rpm continues to be at higher noise levels. This could potentially be attributed to the relative weightings of frequency components and peak pressures calculated using the AVL combustion noise meter algorithm. However, since only a single digital output was recorded for each data point, additional investigation would be required to further develop the understanding. Nevertheless Figure 5.3 and Figure 5.4 clearly demonstrate the importance of limiting rates of pressure rise to control combustion noise levels, and provide insight into the limiting values.

A CNL of 85 dB(A) is seen to be exceeded beyond 0.3 MPa/°CA at 1800 rpm, 0.45 MPa/°CA at 1500 rpm, whilst 0.70 MPa/°CA must be reached at 1200 rpm before achieving the same noise output. Rates of change greater than these values result in unacceptably high levels of noise generated, but the CNL at slower speeds continues to be lower, with peak values less than 92 dB(A) in contrast to the 96.5 dB(A) encountered at 1800 rpm despite equal, if not greater rates of change of pressure. The limitation of combustion noise can thus be deemed a function of engine speed, potentially allowing further exploitation of the PCCI combustion strategy at lower engine speeds. Relatively simple rational functions have been fitted to the three data sets as shown in Figure 5.3. Correlations such as these could be used by the ECU in conjunction with an installed in-cylinder pressure transducer to monitor CNL online, but more mapping at different engine speeds would be required to create a detailed and implementable data set.

Figure 5.5 highlights the importance of combustion phasing on rate of pressure rise. Retarding the start of combustion is clearly an effective approach to control the pressure rise and thus combustion noise, but phasing combustion too retarded of TDC is thermodynamically inefficient and comes at the expense of other responses such as combustion efficiency and fuel consumption. These will be discussed later in this chapter. Figure 5.5 also demonstrates that for a given speed and fuelling, different peak rates of pressure rise can occur at the same start of combustion location. This is to be expected since the combustion profile is highly dependent on injection timing and ignition delay, as well as rate of EGR. For example, at 1500 rpm with a total fuel injection quantity per cylinder of 6.8 mg, rates of pressure rise vary by up to 0.4 MPa/°CA at a given SOC location. The lower rates are clearly beneficial to suppressing combustion noise, but soot, CO, HC, and/or fuel consumption are liable to increase.

5.2.5 Ratio of Ignition Delay to Peak Rate of Net Heat Release

Increased ignition delay periods are desirable to allow time for fuel-air premixing, but can result in high rates of heat release following ignition. EGR is effective at decreasing the rate of heat release which tends to limit or reduce CNL. EGR also increases the ignition delay, suggesting that maximising the ratio of ignition delay to peak rate of heat release might be a successful development strategy. Figure 5.6 illustrates a near asymptotic relationship between the maximum rate of pressure rise and ratio of ignition delay to peak rate of net heat release, approximated by the non-linear regression model labelled.

Results for the ratio are shown plotted against combustion noise in Figure 5.7, previously presented in [17], for total fuel quantities of 9.7 mg/stk/cyl at 1800 rpm. For the single injection cases, SOI has been varied at 43% EGR, and EGR has been varied for an injection timing of -5°ATDC. The 43% EGR rate was selected to allow direct comparison

with other data at similar operating conditions not presented here, whilst the -5°ATDC injection timing was selected to allow desirable combustion phasing with respect to fuel consumption. Data from a pilot-plus-main case are also considered with a 0.8 mg pilot injection SOI -25°ATDC and main injection SOI $+1^{\circ}\text{ATDC}$. A low level of combustion noise is associated with high values of this ratio, indicating that large ignition delays allowing a high degree of premixing do not necessarily lead to high combustion noise. However, increased dilution requires a greater mass of air to be mixed with the fuel to achieve the same local equivalence ratio, requiring more time for mixing [87]. This can lead to increased soot output, which will be discussed in Chapter 7.

When the corresponding bsfc values are plotted against the same ratio (Figure 5.8) it is clear that the reduction in noise can be commonly associated with poor phasing or low combustion efficiency which incurs a high fuel economy penalty. The range bounded by unacceptable fuel economy penalty or unacceptable noise is narrow [17]. If a soot penalty is accepted, a conventional pilot injection can be used to reduce ignition delay and limit noise. In Figure 5.9 there is a clear separation of with- and without-pilot injection trends and for a given ignition delay, noise is much lower when the pilot injection is used. The data points within the dashed oval have pilot injection and a common main SOI of $+1^{\circ}\text{ATDC}$. Additionally, the results show that increasing EGR reduces rates of heat release and CNL.

Long ignition delays with low associated rate of pressure rise can be achieved using a single injection by retarding the combustion, but the poor phasing and deterioration in combustion gives rise to a high fuel economy penalty. At timings giving better phased combustion, increasing EGR to very high levels limits peak heat release rates and combustion noise but work output again deteriorates and intake throttling or other means are required to achieve the necessary gas recycling rate [17].

5.2.6 Spectral Analysis of In-Cylinder Pressure Data

The distribution of the sound energy is important in determining the perceived annoyance to the individual and is evaluated in the algorithm embedded in the AVL combustion noise meter. With this in mind a Fast Fourier Transform (FFT) has been performed on in-cylinder pressure data to investigate the noise characteristics. FFT analysis is a procedure used to analyse the frequency components of a signal. A two-sided power spectrum displays half the energy at the positive frequency and half at the negative frequency. Although there are both positive and negative frequency components, the negative components are commonly omitted when displaying the power spectrum by converting to a single-sided power spectrum, which is what is presented within this thesis.

Figure 5.10 illustrates the resultant power spectrum for the total frequency range analysed at an engine speed of 1800 rpm, equating to a frequency of 30 Hz. Four injection timings of -20, -10, -1, and 0°ATDC are included, with corresponding combustion noise levels of 96.5, 94.0, 86.1, and 81.1 dB(A) respectively. Low frequencies are seen to dominate the power spectrum. Figure 5.11 presents the same data as Figure 5.10, but against a linear frequency axis and logarithmic amplitude axis. Since there are two revolutions per cycle (4-stroke engine cycle) half engine frequency harmonics also appear. In Figure 5.10 the fundamental frequency (f) together with selected harmonics are labelled. These frequencies are all dependent on engine speed and common to all data series presented. The power spectrum increases with advancing injection timing in line with advancing combustion phasing, peak rates of change of pressure, and consequently combustion noise. However, combustion noise is normally associated with higher frequencies [88], which can be more clearly seen through inspection of Figure 5.11. The level decreases with increasing frequency for all data series, but the most advanced injection timing (corresponding to the highest combustion noise level) is consistently highest, especially at the lower frequencies included (around 300 Hz). In the interval 4.5-6.5 kHz an increase in amplitude is apparent for all data series. The peak level in this range is highest for the most advanced injection timing (-20°ATDC) and gradually decreases as the timing is retarded. This is associated with a wave travelling across the cylinder chamber (knock), the fundamental frequency of which is dictated according to:

$$f = \frac{\sqrt{\gamma \cdot R \cdot T}}{\lambda} \quad (5.1)$$

Where $\lambda = 2 \cdot l$ for the first harmonic and l is the piston bowl diameter.

The frequency of this pressure wave is highlighted in Figure 5.11 by a dashed oval. As injection timing is retarded, mixture temperatures decrease. This slows down the speed of the wave ($c = \sqrt{\gamma \cdot R \cdot T}$) and reduces its frequency. Overall noise output is calculated from the sum of the frequency contents within a given range. The higher spectral levels of the more advanced timings across a large frequency range are therefore consistent with combustion noise increasing with advancing combustion.

5.2.7 Comparison between Conventional and PCCI combustion

The results obtained when applying the FFT to three different pressure histories at 1800 rpm are illustrated in Figure 5.12 and serve to investigate the differences in spectra for the different strategies. In contrast to the data presented above, the data in Figure 5.12 are at constant brake load output (2.5 bar BMEP), but vary in SOI and EGR. As the legend describes, two of the data sets are for advanced single injections, and one for a conventional pilot-plus-main strategy. The data are ordered from highest to lowest combustion noise level. The same characteristics as identified in Figure 5.10 and Figure

5.11 are present, although the crest in the amplitude in the frequency range attributed to knock appears more constant at 5.5 kHz than found with the injection timing sweep in the previous section. Interestingly, there also appears to be two spikes in amplitude around this region for the pilot-plus-main case. This is potentially attributable to the two distinct combustion events that occur in cylinder, and appear to act to spread the spectral density over a wider frequency range. For a given load output, slightly different characteristics are therefore apparent depending on the combustion strategy employed. Reducing the spectral density at a given frequency is potentially beneficial in reducing perceived noise since noise concentrated in a narrow bandwidth is considered noisier than if the same energy were spread over a wider band. However, high-frequency noise (for example above 1.5 kHz) is judged to be noisier than a lower frequency noise which is equally loud [89]. This concludes the discussion on noise. In the section that follows, the determination of the ignition delay will be investigated.

5.3 Ignition Delay and the Start of Combustion

5.3.1 Introduction

Ignition Delay (ID) is a key parameter in achieving low soot and NO_x emissions, since increasing its duration provides more time for fuel-air mixing, potentially allowing higher fractions of pre-mixed charge. In this chapter, correlations for ignition delay are examined and the effect of ignition delay on fuel consumption and emission responses is discussed. The definition and determination of the start of combustion are detailed before the forms of previous ignition delay correlations are covered. From here, evaluation of a suitable ignition delay correlation for the author's data is presented with the aim of understanding the factors and mechanisms that determine the length of this period.

5.3.2 Determination of the Start of Combustion

The ignition delay period is defined as the time between the start of injection (SOI) and the start of combustion (SOC). The SOC and the preceding ID period are important in mixture preparation. As explained in Chapter 1, the ignition delay is the time where the fuel mixes with the air in the cylinder prior to the onset of combustion. The length of this period significantly affects the development of combustion and heat release. As well as chemical factors many physical factors are known to affect the ignition delay, including; intake air temperature and pressure, injection timing, load, fuel droplet size, injection velocity and rate, engine speed, oxygen concentration, and swirl rate [9].

Cool flame reactions are a phenomena associated with premixed combustion where low temperature combustion occurs before the start of the main ignition. The cool flame energy that is released causes in-cylinder pressure to increase, modifying the

thermodynamic state of the mixture. This has a significant effect over hot gas reactions since the main ignition occurs at a higher pressure than it would have in the absence of cool flame reactions [90]. Within this thesis the SOC for a main injection is defined as the crank angle location at which 10% of the cumulative heat release occurs, consistent with the definition used in [13, 17]. This criterion has been chosen so as to associate the SOC with that of the start of rapid high-temperature reactions and be distinguished from the cool flame reactions when two-stage ignition is evident. An example determination of SOC is given in Figure 5.13.

5.3.3 Ignition Delay Correlations

The length of the ignition delay is influenced by both physical and chemical factors and is known to be a function of mixture temperature, pressure, equivalence ratio, and fuel properties [9]. Many correlations have been proposed to predict ignition delay, the most common of which use a semi-empirical expression as proposed by Wolfer [91] which is based on the Arrhenius Equation;

$$\tau_{id} = A \cdot p^{-n} \cdot e^{\left(\frac{E_A}{\tilde{R} \cdot T}\right)} \quad (5.2)$$

Where E_A / \tilde{R} is an apparent activation energy for the fuel autoignition process, and A and n are empirical constants dependent upon the fuel and airflow characteristics [13]. Table 5.1 summarises the empirical constants employed in widely-used correlations with diesel fuel that take the form of Equation 5.2. As can be seen from the data in the table, the values of apparent activation energy and adjustable constants vary considerably between studies, which were carried out using a diesel engine, a constant-volume combustion bomb, or a steady flow reactor. Many factors are responsible for the differences in the values of empirical constants reported, but disparities in the equipment employed and the method of mixture preparation are likely to be the most significant [9]. Moreover, as well as adopting the above expression, the studies of both Assanis et al. [92] and Kook et al. [13] include terms to take account of oxygen availability through global equivalence ratio and oxygen concentration terms respectively. When considering PCCI combustion strategies this is significant, since high rates of dilution play an important role in determining the ignition delay.

A correlation for ignition delay has been developed from the experimental data collected following the approach taken in [13] accounting for oxygen availability. Including this term yields Equation 5.3, re-arranged to give Equation 5.4:

$$\tau_{id} \cdot \bar{p}^n \cdot \tilde{x}_{O_2, cyl}^f = A \cdot e^{\left(\frac{E_A}{R\bar{T}}\right)} \quad (5.3)$$

$$\ln\left(\tau_{id} \cdot \bar{p}^n \cdot \tilde{x}_{O_2, cyl}^f\right) = \left(\frac{E_A}{R}\right) \cdot \left(\frac{1}{\bar{T}}\right) + \ln(A) \quad (5.4)$$

For simplicity, the constants n and f were initially set to 1. A value of $n=1\pm0.02$ was used by the many of the works summarised in Table 5.1. The apparent activation energy and the constant A were determined by fitting experimental data to Equation 5.4. Data for single injections are shown in Figure 5.14 over a wide range of injection timings, fuel injection quantities, and rates of EGR. For injection timings within the data set around TDC, SOC commonly occurs further into the expansion stroke. For a single injection the temperature and pressure at SOC are therefore frequently lower than at the SOI conditions. The temperature and pressure data have been weighted in favour of SOC conditions in order to improve the fit and reduce scatter within the data. Increasing the weighting towards SOC conditions from 50% to 80% improved the coefficient of determination (R^2) from 0.29 to 0.80 as well as changing the profile of the line. In accordance with Equation 5.4, the gradient of the line yields the apparent activation energy and the offset enables the calculation of A . Equation 5.5 gives the expression for ignition delay obtained from the experimental data:

$$\tau_{id} = 115 \cdot \bar{p}^{-1} \cdot X_{O_2}^{-1} \cdot e^{(1692/\bar{T})} \text{ (ms)} \quad (5.5)$$

A regression analysis was performed to improve the selection of constants by minimising the least-square error between measured and predicted values. Table 5.2 summarises three of the results, along with the data from the method described above. As can be seen there are many combinations of constants that yield very similar coefficients of determination. Applying sensible constraints to the ranges that these constants can take is thus important. The best fit of the data is shown to be obtained with a high value for the empirical constant A and relatively low value for the apparent activation energy. This indicates that the expression is more sensitive to the average temperature than those listed in Table 5.1. This is attributed to the determination of SOC and average temperature between studies, noting that the data in this thesis were weighted in favour of SOC conditions. Nevertheless, despite the detailed regression analysis, the fit was not significantly improved from the initial method which was much more time efficient. The final equation for predicting ignition delay is given by:

$$\tau_{id} = 484 \cdot \bar{p}^{-1.10} \cdot \tilde{x}_{O_2, cyl}^{-0.85} \cdot e^{(1400/\bar{T})} \text{ (ms)} \quad (5.6)$$

Figure 5.15 demonstrates the effectiveness of the expression to predict the ignition delay. In the order of 220 different data points (~80% at 1800 rpm, ~20% at 1500 rpm) at various SOIs ranging from -20° to $+3^\circ$ and EGR rates in the range 0%-61% were used for the determination of the expression. However, extrapolation of the correlation outside of the original range of operating conditions could result in inaccurate prediction [9]. The data presented relate to single injections and the correlation is thus not valid for the main injection following one or more pilot injections. The use of multiple injection strategies may require extra attention to calibrate for changes in mixture preparation and thermodynamic state. For example, the correlation has been found to over-predict main ignition delay when a single pilot is also employed. The majority of this data predicted values within +30% of the unity gradient line ($x=y$), but improved calibration would be required should this be developed further and is beyond the scope of this investigation.

The high coefficient of determination value for use with single injections indicates the effectiveness of the relationship with all of the data within the $\pm 20\%$ error bands. Heywood [9] explains that a lower value of E_A / \tilde{R} indicates the importance of physical processes and that they are relevant to chemical processes. Overall the relationship clearly demonstrates that fuel introduced into increased pressures and temperatures reduces the ignition delay. High oxygen concentrations are also seen to reduce the delay since there is increased chance of fuel and air mixing to within flammability limits and promoting conditions suitable for ignition. Dilution slows down chemical reactions and limits the temperature rise from early low-temperature reactions due to the high heat capacity of recycled gases [13], thus allowing more time for mixing. However, the reduced oxygen availability in-cylinder necessitates a greater mass of air to be mixed with the fuel to achieve a given fuel-air equivalence ratio, which requires more mixing time and thus may offset the benefits of increased ignition delay [13, 87]. This trade-off will be discussed further later in the thesis.

It is clear that both mixing and reaction kinetics play an important role in determining the length of the ignition delay period. For a given oxygen concentration, increased fuel-air mixing through higher swirl ratios or increased mixing intensity due to higher injection pressures should reduce the ignition delay as flammability limits for combustion are reached earlier (mixing mechanism). Temperature and pressure are also key variables in determining the rate of reaction through reaction kinetics. Knowledge of the thermodynamic conditions in-cylinder is thus vital when predicting the location of start of combustion and the length of the ignition delay period. A model developed by Watson [83] indicates the relative importance of the ignition delay on diesel combustion. In this

model the total fuel burned in the premixed stage is defined as a fraction of the total fuel injected, expressed as a proportionality factor, β .

$$\beta = \frac{m_{premix}}{m_{total}} \quad (5.7)$$

Where the proportionality factor is given by:

$$\beta = 1 - \frac{a \cdot \phi^b}{\tau_{id}^c} \quad (5.8)$$

An increase in the ignition delay therefore favours a higher value of proportionality factor, β , and thus relative amount of premixed burning, but a strong dependence on equivalence ratio can also be seen. The parameters manipulated to increase the ignition delay are thus important when attempting to increase the amount of premixed burning. The subsequent section continues to develop the understanding by examining the effect of combustion phasing, which logically follows on from analysis of ignition delay and the start of combustion.

5.4 Effect of Combustion Phasing on CO, HC, and Fuel Consumption

5.4.1 Introduction

The final section of this chapter pertains to the effect of combustion phasing (primarily through SOC). Here in-cylinder pressure data are analysed and implications for load output and combustion efficiency discussed together with the effect of dilution and charge mixing.

5.4.2 In-Cylinder Analysis

When considering the performance of a combustion system, gross indicated performance quantities are commonly used since they are representative of the useful work available at the shaft and are not affected by ancillary loading, frictional losses, and the gas exchange processes [93]. The work delivered to the piston over the compression and expansion strokes is shown in Figure 5.16 to be a function of the location of start of combustion. Maximum work output is obtained for starts of combustion around TDC. Combustion that begins too advanced of TDC in the compression stroke results in reduced work output. Figure 5.17 details the in-cylinder analysis of an example SOI timing sweep at a fixed rate of EGR. Depicted within the figure are in-cylinder pressure prior to TDC and part way down the expansion stroke (*a*), P.dV which is used to calculate the IMEP and helps identify where work is gained and lost (*b*), the net rate of heat release (*c*), and finally the cumulative net heat release (*d*). Notably for advanced combustion phasings, and improving progressively as timing is retarded, ringing of the pressure traces is evident in

Figure 5.17. Ringing is a phenomenon associated with rapid changes of pressure which trigger acoustic modes in the combustion chamber [94]. Commonly encountered with premixed combustion, ringing manifests itself through oscillations on the pressure trace, and is more clearly identifiable on the rate of heat release graphs (c).

Advanced combustion from the earliest injection timings (-20 and -15°ATDC) are seen to occur extremely rapidly with short combustion duration and high rates of heat release. Although combustion efficiencies for these points are very high ($\sim 99\%$) the cumulative net heat releases are lower relative to more retarded combustion phasing, attributed to a greater amount of heat transfer and blowby losses [17]. Graph *a* also indicates pressures well above compression pressures before TDC. Analysis of graph *b* reveals that some negative work is introduced. Although the value of $P\cdot dV$ increases to a more positive value compared with later injection timings, recovering some of the work, the lower associated pressures down the expansion stroke result in the overall sum over the compression and expansion strokes (IMEP_g) being lower, indicating lower work output. This will naturally impact on bsfc.

For advanced injection timings that result in the shortest ignition delay period ($\sim \text{SOI}-7.5^{\circ}\text{ATDC}$) less time is available for fuel-air premixing. Since the EGR rate remains constant and mixing intensity should not be significantly varied (swirl ratio should be relatively constant and injection pressure remains unchanged), no noteworthy increase in the rate of mixing should occur. This leads to the formation of fuel rich regions which can result in increased emissions [41]. Figure 5.16 also shows that combustion that is excessively retarded of TDC also results in a decrease in work output, which deteriorates significantly the further into the expansion stroke combustion begins. Figure 5.17 reveals that as injection timing is retarded, combustion phasing retards and combustion duration increases. The reduction in peak rates of heat release and spreading out of the combustion do not cause the total net heat released to decrease until the latest start of combustion ($\text{SOI} + 1.5^{\circ}\text{ATDC}$). However, work output clearly decreases as SOC is retarded. Figure 5.18 elucidates to deteriorating combustion efficiency, corroborated by Figure 5.17 which demonstrates the spreading out and retarding of the combustion reduces the maximum $P\cdot dV$ values reached. Examination of Figure 5.18 also reveals advancing combustion phasing (SOC) to be desirable in maximising combustion efficiency. Naturally the same combustion efficiency can occur for different starts of combustion.

The use of a pilot injection of conventional timing ($\sim -20^{\circ}\text{ATDC}$) reduces the ignition delay of the main injection, advancing its combustion relative to single injection cases even for very high equivalence ratios (as labelled on Figure 5.18). However, these low air-to-fuel

ratios in combination with the injection timings employed evidently led to rapid deterioration in combustion efficiency. High rates of EGR retard the pilot combustion phasing, which for fixed main injection timing can result in the main fuel quantity being delivered into or very soon after the pilot combustion event. The higher associated pressures and temperatures act to shorten the ignition delay, giving the main fuel injection less time to mix with air. However, the high overall equivalence ratios require more time for mixing due to the low oxygen availability. This leads to a greater proportion of MCC of the main fuel injection. High levels of dilution combined with the downward motion of the piston in the expansion stroke results in longer combustion duration and reduced temperatures, which hinders the complete oxidation of CO and HCs which have been found to require temperatures of at least 1500 K and 1200 K respectively for complete oxidation [41, 42, 44]. It is clear therefore, that deterioration in combustion efficiency is strongly but not uniquely dependent on the location of start of combustion. Consequently calibration parameters such as rate of EGR and injection strategy must be carefully matched so as to avoid such deteriorations as revealed in Figure 5.18.

Specific fuel consumption exhibits an inverse relationship with work output. The top graph of Figure 5.19 illustrates that gross indicated specific fuel consumption ($isfc_g$) is a function of combustion phasing, where $isfc_g$ is given by [9]:

$$isfc_g = \frac{\dot{m}_f}{\dot{W}_{i,g}} \quad (5.9)$$

Gross $isfc$ can be seen to be dependent on the SOC location, but multiple values for the same SOC location are evident. This is related to both the combustion efficiency (Figure 5.18) and duration (defined as the period between SOC and EOC). In general terms when combustion occurs in the expansion stroke shorter combustion durations result in lower $isfc$ since a greater proportion of the fuel's chemical energy is released closer to TDC. Conversely when combustion is advanced and phased in the compression stroke longer combustion durations are beneficial in reducing $isfc$ since less negative work is introduced. This is a simplified evaluation of the trend since heat transfer and blowby effects have not been investigated which also influence work output [95], significantly so under certain conditions such as cold start where heat transfer is high and the net heat released (for a given quantity of fuel burned) is reduced.

The lower speed-load condition (1500 rpm 6.8 mg fuelling) illustrated in Figure 5.19 has higher gross indicated specific fuel consumption. This may be attributed to the net result of decreased mechanical efficiency and increase in indicated fuel conversion efficiency as the load is reduced, and a decrease in indicated efficiency (due to increasing importance of frictional and heat losses) and increased mechanical efficiency as the speed decreases [9].

5.4.3 Effect of EGR

The reduction in oxygen availability with increased EGR slows down the chemical reactions and extends combustion duration as well as increasing the time required for mixing. For highly advanced injection timings (such as -20°ATDC) this is beneficial since the dilution extends the ignition delay, thus better combustion phasing and reducing fuel consumption result. Conversely for more retarded injection timings that result in load outputs lower than maximum potential output, the reduced oxygen availability with dilution is detrimental to fuel consumption since SOC and the subsequent combustion occurs later in the expansion stroke. The severity of deterioration in fuel economy is dependent on other calibration factors such as fuel rail pressure and quantity delivered, but in general increasing the EGR rate worsens fuel consumption for these injection timings and accelerates the fuel consumption penalty. This offers the opportunity to retard injection timings and lower the rate of EGR for constant fuel consumption if a constraint were to be imposed on a particular response, such as CO or HC emissions for a given running condition. However, the consequent effects on combustion noise and other emission responses would have to be determined, with NO_x and combustion noise likely increasing (soot is more difficult to predict given the complexity of the formation and oxidation and resultant engine-out emission).

5.4.4 Temperature and Mixing

Low emissions of both CO and HC are encountered when combustion is advanced, especially before TDC. Figure 5.19 reveals CO continues to decrease (albeit slightly) with advancing SOC from TDC, however HC (shown in the bottom graph) increases slightly from its minimum value just prior to TDC. This can be attributed to a small degree of over-leaning of the fuel-air mixture as injection timings are advanced where a small proportion of the fuel mixes lean of the flammability limit, or to wall wetting. Nevertheless the most advanced injection timings within the data sets displayed are not constrained by CO and HC emissions. This is mirrored by Figure 5.18 which indicated very high levels of combustion efficiency for SOC around and before TDC.

Long ignition delays are known to be a source of HC formation due to over-mixing. Work carried out by Musculus et al. [96] has led to the understanding that a large proportion of the lean mixtures are formed at the end of injection where jet velocities are slowing down. Advancing injection timings to increase the ignition delay can thus cause increases in the formation of HC and CO emissions, but for suitably phased combustion, oxidation processes can be sufficiently completed on engine time scales to minimise engine-out emissions. This is not necessarily the case for retarded phasings. As combustion is retarded past TDC, CO and HC begin to increase. The fuel is burned in a cooler

environment further away from the thermodynamically efficient location of TDC, leading to less complete combustion and increased CO and HC emissions in the exhaust.

Analysis of Figure 5.19 highlights the severity of the increase in incomplete combustion with retarding SOC. For the data points where a pilot injection is used the injection timings of the pilot and main injections are fixed at -25° and $+1.0^\circ$ ATDC respectively, with varying level of dilution dictating the main SOC. The deterioration in combustion is seen to occur more rapidly than the data points without a pilot injection, highlighting the sensitivity to EGR-SOI combination. The pilot injection reduces the main ignition delay of the main injection which tends to advance the combustion, but the combustion duration increases as the ratio of diffusion-to-premixed burning increases. A greater proportion of the fuel is therefore burned further into the cooler expansion stroke, leading to less complete combustion. The data with pilot at 1800 rpm 9.7 mg indicate a threshold is reached, after which extremely high CO penalties are encountered.

Figure 5.19 also indicates that higher load conditions generally result in lower CO and HC emissions. Higher temperatures favour complete oxidation of formed combustible species including CO and HC, which have been reported to require at least ~ 1500 K and ~ 1200 K respectively [41, 42, 44]. The improved oxidation of the species allows more retarded combustion phasing with higher loads before deterioration in combustion efficiency. Also, as noted by [42], at lower fuelling quantities the production of the majority of CO and HC is dominated by incomplete bulk-gas reactions. The net result is an increase in engine-out emissions as shown.

5.5 Concluding Remarks

Increasing the ignition delay allows more time for fuel-air premixing, but this can be achieved in a number of ways. Conditions at the time of injection play an important role in its determination and can be exploited through injection timing. The reduction of oxygen availability with increased EGR increases ignition delay, but will be shown to have important consequences in the soot output. The start of combustion (phasing) must be considered when analysing the relative performance of combustion strategies. In general, the highest combustion efficiencies are obtained for advanced phasings, whilst minimum indicated specific fuel consumption is obtained when SOC is marginally retarded of TDC. Combustion phasing affects the heat release of the fuel and greatly influences combustion noise output, which correlates well with the peak rate of pressure rise. This tends to increase with advancing phasing and rates of heat release and combustion phasing must therefore be considered when employing potential strategies.

CHAPTER 6

ENGINE BASELINE PERFORMANCE

AND PROTECTION OF PRESSURE

TRANSDUCERS AGAINST SOOT

6.1 Introduction

The performance of the test engine operating with a calibration designed for conventional combustion is investigated within this chapter. This calibration was installed as a development aid for test bed operation and as such was not of product release quality. At the conditions examined, the calibration makes use of settings which are representative of those of the final product. Amongst other factors the strategy makes use of pilot(s) and main injections, EGR, VGT vane control, and fuel rail pressure variation.

The chapter begins with the findings from a test matrix completed to evaluate the responses obtained when operating under the pre-production calibration. In particular the trends of emissions and fuel consumption are presented, together with anomalies encountered with the testing. Following this, the evaluation of a standard operating point run periodically to assess the repeatability and consistency of results obtained is discussed. One problem encountered was fouling of in-cylinder pressure transducers and their adaptors. The design and performance of four different transducer adaptors are scrutinised, before the final discussion and conclusions relating to the chapter are given.

6.2 Engine Baseline Performance

In order to understand the engine calibration and ascertain what limits the use of a conventional DI Diesel strategy, a reference set of data was obtained to provide a useful baseline from which the performance characteristics of the PCCI combustion could be compared. The relative benefits and penalties of employing a PCCI strategy can then be better understood, as well as providing insight into potential limitations of the test engine.

The test engine used was an early development version of the production engine with components and features which were revised in later versions. The deficiencies of the early design were responsible for isolated problems at particular speeds. A prime example was of a pressure wave travelling through the intake system at certain test conditions

around 2000 rpm due to the lack of a tuned intake system with the test bed installation. This wave caused an oscillation in turbo speeds with the compressor surging then slowing. The condition 2000 rpm 200 Nm was an example case of this phenomenon, hence the slightly lower engine speed used for mapping the engine performance.

During the baseline performance experiments the dynamometer was used to fix the engine speed, whilst the load was controlled by the position of the pedal which supplied the ECU with a torque demand input. The standard settings in the ECU were used for all other variables and recorded as described per Chapter 3. Once the emissions analysers had reached the required operating temperature and had been successfully calibrated, the engine was warmed up at 1500 rpm 50 Nm with the EGR valves closed. Once the engine was fully warm and the coolant and oil temperatures had become stable, the engine speed and load of the first test point were selected. Table 6.1 illustrates the test matrix completed by taking emission measurements from both engine banks for the baseline mapping of the engine. The test matrix was completed three times over a two week period to allow an average set of data to be obtained, and any anomalies identified. The averaged emissions indices for each test point are illustrated in Figure 6.1 together with the average EGR rates and bsfc figures, the latter of which are seen to reduce with load for a given engine speed.

Graph 5 of Figure 6.1 clearly highlights the scale of the problem faced with regard to soot output from running a conventional DI diesel strategy. Smoke values in excess of 1.0 FSN are evident for the majority of the test points covered, highlighting the need to investigate strategies to reduce soot output. PCCI strategies potentially offer a solution, but any change in calibration must not incur excessive penalties from other responses such as emissions and fuel consumption. It should be noted that the pre-production strategy calibration was set up for low NO_x emissions and as such higher soot output could be expected since this would be oxidised by the DPF prior to tailpipe emission. Graph 1 (Figure 6.1) confirms the calibration has been realised, except for the 1000 rpm 150 Nm condition, where EGR was very low (graph 4), a possible anomaly in the prototype calibration. Noticeably soot emissions are very low at this point, true to the conventional NO_x-soot trade-off.

A general trend of CO and HC emissions decreasing with increasing load is evident. As loads increase a greater amount of energy can be recovered by the turbocharger and higher boost pressure can be generated, increasing the availability of oxygen in the cylinder for oxidation of the fuel and combustible species. The higher in-cylinder temperatures encountered due to the release of increased amounts of chemical energy from higher fuel

quantities is also beneficial to the oxidation processes. Again at a condition of 1500 rpm 200 Nm soot and CO emissions have not yet been optimised.

6.3 Standard Test Point

During the course of the experiments a standard test point was carried out periodically to ensure the engine and analysers were working correctly, and so consistency of results could be evaluated. In total 37 in-cylinder pressure data readings were taken, whilst 30 sets of data were recorded for all other data (such as emissions) over a period of 20 months which encompassed the major timeframe of data acquisition. The number of samples (30 or 37) is listed in Table 6.2, the difference coming from the fact that the emissions analysers were not used for every testing session. The operating conditions for the standard test point were 1500 rpm, 0.8 mg pilot injection SOI -20.5° (demand), 7.0 mg main injection SOI +1.8°ATDC (demand), EGR valves Pulse Width Modulation (PWM) 52%, VGT vanes PWM 7%, and the intake throttle wide open.

Day-to-day variations in ambient conditions such as laboratory temperature inevitably occur, but it is important that the engine and analysers behave in a consistent and repeatable manner. Performing a standard condition allows these differences to be quantified and any potential errors in the equipment rectified before testing continued. It was found that the CO₂ analyser for the intake measurement, together with the NO_x and HC analysers required the most careful attention since these were the analysers with which errors had been detected on numerous occasions. The standard test point also allowed conclusions to be drawn as to the accuracy and validity of the experimental data and the sensitivity of specific parameter measurements. Table 6.2 details the responses obtained over the 20 month period. The greatest variations were found in CO, HC, NO_x, and smoke emissions. Larger relative variations in CO and NO_x emissions can be attributed to the low values being measured. In the case of CO, the lowest measurement range that the emission analyser could be set to was 0-5%, whilst the average value of 0.12% was obtained from the standard test. Small variations in the value obtained on a particular test therefore result in high percentage and Coefficient of Variation (CoV) differences. Similarly, NO_x readings were low, again resulting in large percentage differences. Due to the complexity involved in soot formation and oxidation, and ultimately net output, variation in smoke emissions is inevitable. As will be discussed later in the thesis, small changes in temperature, airflow through the engine, rate of EGR, or other variables can significantly affect soot emissions.

Air temperature was found to vary significantly over the course of the experimental work. Over the standard condition testing, air temperature (in the laboratory) varied from 15°C to

26°C depending on the time of year, weather conditions, and the number of other engines operating in the laboratory at the same time. This affects several parameters, notably the AFR, and is believed to affect the in-cylinder behaviour of the induced gases. Engine speed, load output (brake and indicated), fuel rail pressure, and fuel consumed by the engine were all within 2% CoV, signifying the engine operating conditions were well controlled and repeatable. Overall analysis of the standard test point shows that a good degree of repeatability and accuracy was obtained, whilst the responses that showed greater variation could be explained logically, and in real world applications variations will naturally occur.

6.4 Transducer Adaptors

6.4.1 Introduction

Accurate measurement of in-cylinder pressure is essential when examining combustion characteristics and responses to applied inputs. Within the context of a fixed test-bed research environment it is not unreasonable to expect to have to perform regular maintenance on equipment including sensors. During this investigation the majority of the pressure data have been post-processed, but the use of such data in monitoring online applications (for example in closed-loop control of fuel injection strategy) are becoming evermore common [97]. In-cylinder pressure measured online could potentially be used by the engine ECU to balance cylinders, improving engine vibration and smooth running of the engine, as well as monitoring combustion noise and improving the use of commonly used look-up tables. A more detailed review of such applications can be found in [31].

Two Kistler 6055B transducers used to measure cylinder pressure were installed in place of the glow plugs. This requires the use of an adaptor to simulate the dimensions of a glow plug as well as being robust and non-sensitive to both thermal shock and fouling. Since a significant part of the experimental work carried out was at conditions producing extreme soot levels not produced on a working strategy, there existed a possibility of fouling of particular screens. In total four different pressure transducer adaptors were tested in the engine, all installed in the glow-plug holes. Problems with original designs clogging with soot had been encountered hence the experimentation with the following designs. The designs tested are illustrated in Figure 6.2, where the letters correspond to the following description;

- a) Multi-hole on flats (15x Φ 1mm)
- b) Multi-hole on chamfer (4x Φ 1mm)
- c) Open (no shielding)
- d) Slot (Φ 2.5 mm, slot 1mm x 22mm)

6.4.2 Multi-hole Design Adaptors

Adaptors (*a*) and (*b*) are dimensionally most similar to the glow-plugs they replaced. The 1mm diameter drilled holes allow the pressure to be transferred through to the transducer diaphragm for measurement. Both designs offer good shielding of the transducer, ensuring the combustion flame is quenched and unable to reach the diaphragm. Standing waves and Helmholtz resonance are not an issue since there are no open passages to consider. With adaptor (*a*) three flats were machined onto the main shaft and 5 holes drilled along each with equal spacing. In adaptor (*b*) four holes were drilled into the chamfer between the main shaft and transducer housing. Adaptor (*b*) was initially installed in both cylinders containing the reference Kistler 6055B transducers. However, during preliminary testing IMEP measurements were found to deteriorate with time. When the adaptors were removed, it became apparent that the drilled holes had become clogged with soot, potentially hindering accurate pressure measurement.

It was found that adaptor (*a*) could be left in the sooty environment of the engine longer than adaptor (*b*), but the holes still eventually became packed with soot, requiring cleaning. The effect of this clogging will be discussed in section 6.4.5. Figure 6.3 provides photographs of adaptors (*a*) and (*d*) when clean and after an extended period within the engine (dirty). Although organic deposits are found around and within the slot adaptor (*d*), it is evident that significantly less obstruction to pressure measurement is introduced compared to the more fouled multi-hole adaptor (*a*).

6.4.3 Open Design Adaptor

Removing the tip of the adaptor was considered (*c*), but this leaves the transducer exposed with insufficient shielding. The problem of clogging is therefore potentially exchanged for one related to thermal shock which can occur since there is no flame shield to quench the high-temperature combustion flame. Thermal shock results in temporary deformation of the transducer diaphragm, causing an incorrect pressure to be recorded. Although a minor consideration, a slightly larger change of approximately 1.5% in compression ratio is also encountered. For these reasons the open design was not used to collect the data presented within this work.

6.4.4 Slot Design Adaptor

With adaptor (*d*) a 22mm long 1mm slot was machined to allow soot to exit the adaptor. The open channel allowed effective pressure measurement, whilst the slot helped to solve the clogging issue and prevent resonant frequencies interfering with the measurement. The slot adaptor was designed to maintain the clearance volume as close as possible to that of the original setup with standard glow plugs installed. The reduction in compression

ratio was calculated to be 0.17, or 1%, an acceptable concession given the benefits provided during testing with high soot.

The final design negated the need for holes by having a hollow tip with sufficient material to ensure the required strength and structural rigidity. A slot machined down the side of the tip allows gas and soot to escape the cylindrical body, thus solving the problem of sooting. Keeping the slot at a width of 1mm also ensured that the combustion flame was quenched before reaching the transducer diaphragm, thus protecting against thermal shock. As noted above, photographs of clean and dirty slot adaptors are shown in Figure 6.3.

6.4.5 Adaptor Performance over Time

Due to the nature of the testing involved during the investigation, high values of soot emissions were experienced. As mentioned above, this resulted in the adaptors housing the in-cylinder pressure transducers to become clogged. The IMEP data that are included in Table 6.2 are an average of two cylinders on opposing engine banks, separated by 360° in the firing order (cylinders 3 and 4). The slot transducer adaptor (*d*) was installed in cylinder 3, whilst cylinder 4 contained adaptor (*a*) with holes drilled on flats. Figure 6.4 illustrates the variation in IMEP for the two cylinders, whilst Figure 6.5 shows the average IMEP of the two cylinders together with the engine BMEP at the standard test condition over time. Cylinder 3 is known to be more powerful than 4, and as such a difference in IMEP between the two is expected. However, after test point 12 both net and gross IMEP values from cylinder 4 deteriorate to lower values, attributed (at least in part) to the clogging of the transducer adaptor. The drop in IMEP occurred during the closed part of the cycle since gross IMEP values decreased (compression and expansion strokes only), whilst the pumping work remained relatively constant, resulting in the net IMEP continuing to be a fixed amount lower than that of the gross. The drop in IMEP was in the region of 0.25 bar and as such it was not possible to detect any anomalies in P.dV data (used in IMEP calculations). After the transducers and adaptors were removed and cleaned (Micro solution followed by ultrasonic bath) and the engine conditioned for an extra period, the IMEP values can be seen to increase closer to previous values (point 16 onwards). Variations can be expected in the absolute values over the year due to ambient conditions such as changes in temperature, humidity, and pressure, especially over the periods of time included within the data (~20 months). Once cleaned, IMEP values are seen to be consistently higher than when the adaptor was clogged. It is worthwhile to note that combustion noise levels recorded were not adversely affected, despite using the same pressure signal that was recorded by the data acquisition system. This implies combustion noise measurement is less sensitive than IMEP.

Figure 6.4 also displays the IMEP data from cylinder 3. Both gross and net IMEP values for this cylinder are seen to be much more stable across the data range with much lower variability. Although the transducer adaptor in this cylinder did become tarnished with soot (see Figure 6.3), and some soot was found on the transducer diaphragm, it was not subject to clogging and no pronounced dip in IMEP is noticed.

6.5 Concluding Remarks

This chapter has described the analysis of the pre-production engine under its baseline calibration and highlighted the requirement to resolve an important issue regarding in-cylinder pressure measurement. By acquiring steady state data over a matrix of speed and load conditions the behaviour of the engine under a conventional combustion strategy was assessed. High net soot output was encountered at the majority of conditions tested, which resulted in fouling of the in-cylinder pressure transducer adaptor. The designed transducer adaptor reduced maintenance intervals. In terms of practical application this offers a clear advantage should online pressure monitoring be required by the ECU, for cylinder balancing or monitoring combustion noise. However, some of the test conditions generated extreme soot outputs that would not be experienced in a production engine. The use of a standard test point has been invaluable in ensuring the correct operation and repeatability of the engine and sensors.

EXHAUST GAS RECIRCULATION

7.1 Introduction

This chapter addresses the use of EGR and examines the benefits and consequences of employing high fractions of recycled gas with an aim to reduce NO_x and soot emissions, CNL, and help control combustion phasing. As was explained in Chapter 2, EGR has been used extremely effectively to lower combustion temperatures and limit NO_x formation. However, increasing the level of EGR frequently results in increases in soot output due to lower oxygen concentration and lower combustion temperatures. When adapting to operate a PCCI strategy, trade-offs encountered and any negative effects must be identified and the limits understood, which are the main aims of the chapter. Particular attention is paid to the effects of temperature and equivalence ratio to understanding the emissions responses. Notably, temperature and oxygen availability will be shown to play key roles in the determination of net soot output, consistent with the formation regions shown in Figure 1.4. After discussing the effects on soot output when using varying levels of EGR, NO_x , CO and HC emissions are studied. Finally the potential detrimental effects to the engine and extra required maintenance are discussed.

7.2 Temperature

Charge temperature at the time of fuel injection affects the development of combustion and the formation of emissions. Although the Φ -T diagrams point to the significance of temperatures between 1600K and 2500K in the formation of soot in fuel rich zones, local Φ -T maps require detailed CFD simulations. An adiabatic flame temperature based on the stoichiometric fuel-air equivalence ratio is relatively easy to calculate with software available in the literature and provides a simple indicator of temperatures associated with high net soot emissions. This is likely to be a more reliable measure of temperature in a standard diesel diffusion flame than using the overall equivalence ratio, but only a fraction of the mixture will be at this equivalence ratio. Here, the adiabatic flame temperature has been calculated using the experimentally measured exhaust gas composition, the AFR, and the in-cylinder bulk-gas temperature to estimate the initial enthalpy of the reactants. Experimental data for NO_x emissions and net soot concentration in the exhaust gases are plotted against adiabatic flame temperature in Figure 7.1. Note that net soot reflects the difference between the two competing processes of formation and oxidation. Although the

partially-premixed diesel combustion is not homogeneous, high levels of net soot output nevertheless fall within a relatively narrow range of values of local stoichiometric adiabatic flame temperatures (bottom graph). Figure 7.1 illustrates that the highest levels of soot output occur in a critical range of temperatures 1600-2700K, similar to the soot formation temperatures indicated on the Φ -T diagrams [17]. The top graph illustrates the relationship between the stoichiometric adiabatic flame temperature and NO_x emissions. Low values are associated with temperatures below approximately 2300 K, after which they increase exponentially. This value compares well with the NO formation regions illustrated on the Φ -T maps which indicate the importance of temperatures over 2200 K (with $\Phi < 2$). Maintaining the peak flame temperature below this value is therefore necessary to minimise NO_x output. The knowledge gained from these relationships is extremely useful in understanding the mechanisms involved, but these temperatures are adiabatic estimates that represent the maximum values expected since heat transfer, incomplete combustion, or molecular dissociation would act to lower these values. Factors other than temperature are also important in determining the level of emissions, including oxygen availability and the degree of fuel-air mixing.

Despite passing through heat exchangers, the EGR gases are still much hotter than the fresh air that is displaced. This causes an increase in the intake temperature, illustrated by Figure 7.2 for three different speed-fuelling combinations. This increases the initial temperature of the reactants prior to ignition. The maximum achievable flame temperature also increases with ambient gas temperature as previously illustrated in Figure 3.1. Control over intake temperatures therefore has important ramifications in influencing local temperatures. Pickett et al. [60] demonstrated that the rate of soot precursor formation and the peak precursor yield increased with ambient temperature, but that the increased temperature was also beneficial to their oxidation. Similarly, the benefits of reducing intake temperature by improving the cooling of the EGR gas have been demonstrated in [61]. Increased oxygen concentration due to higher intake density was found to limit the amount of mixture with $\Phi > 2$ (locally), allowing the soot formation peninsula to be avoided to a greater extent. Nevertheless, the effect of the dilution with EGR is to lower the adiabatic flame temperatures as demonstrated in Figure 7.3. This influences the path taken in the Φ -T plane and can move local conditions into (or out of) the soot formation peninsula and is one of the mechanisms producing potentially large swings in soot emissions [17]. Although soot formation occurs on the local scale, global parameters clearly affect local conditions and the subsequent reactions.

7.3 Equivalence Ratio

The overall fuel-air equivalence ratio is dictated by the relative amount of air flow since control over the fuel injected is always maintained. The increase in temperature associated with the recirculation of exhaust gases causes a thermal throttling effect, resulting in an increase in equivalence ratio if the injected fuel quantity is kept constant.

The relationship between EGR and overall equivalence ratio is important. Typically the deterioration in soot or combustion efficiency places an upper limit in its value. Assuming EGR is not limited by other factors, such as pressure gradient between the exhaust and intake manifolds, it will be constrained by the relationship between stoichiometric air-to-fuel ratio (AFR_s), mass flow rate of fuel, and the total mass flow rate in the cylinder. Basing the overall equivalence on air and fuel induced in the fresh charge, then [17]:

$$\phi = \left(\frac{C}{1 - EGR} \right) \quad (7.1)$$

Where

$$C = \frac{AFR_s \cdot \dot{m}_f}{\rho_i \cdot \eta_{vol} \cdot nV_d \cdot \frac{N}{2}} \quad (7.2)$$

The derivation of the above equation can be found in Appendix 3. The intake air density is taken as the air density in the inlet manifold (mixture of fresh air and EGR). The relationship between ϕ calculated using the above Equations and Equation 4.21 is linear since they yield the same equivalence ratio. The expressions presented here allow the contributing factors to the determination of equivalence ratio to be separated and highlight the dependence of ϕ on EGR. Figure 7.4 demonstrates three fixed fuelling rates with $AFR_s = 14.6$ (that of the test fuel). As EGR displaces air in the intake flow, overall equivalence ratio increases and eventually exceeds an indicative upper limit, an example of which is shown in the Figure. As fuelling is increased, the upper limit on EGR drops from ~65% to ~45% then to ~25% for the three cases presented. Since the EGR will contribute to the oxygen content of the trapped charge, in effect lowering the equivalence ratio, these will be conservative limits on EGR [17].

To lower the equivalence ratio the air flow has to be increased or the fuelling rate decreased. A trade-off between available boost and EGR is encountered due to the highly coupled nature of the turbocharger-EGR systems. For the test engine there was limited boost pressure available at the lower fuelling quantities (9.7 mg and 6.8 mg) at mid-high rates of EGR. Although more boost is available at higher fuelling rates, which can be helpful in lowering Φ , for a given rate of EGR the overall equivalence ratio will be higher

than with a lower fuelling rate (as indicated by Figure 7.4). As previously mentioned reducing the intake temperature to increase its density is potentially an effective way to increase the air flow through the engine and consequently reduce the overall equivalence ratio.

7.4 Effect on Emissions

7.4.1 Soot

For a given rate of EGR the fuel-air equivalence ratio depends on the fuel quantity delivered. Therefore the data presented in the graphs in this Chapter are plotted against equivalence ratio. The fuel-oxygen equivalence ratio is important when considering soot output as it affects both the formation and oxidation processes. As the overall fuel-oxygen equivalence ratio increases, the oxygen concentration in the cylinder decreases. The higher level of dilution extends the ignition delay to allow more time for mixing [23, 27], but the mass of air that must be mixed with the fuel to achieve the same equivalence ratio increases [13]. Although the soot formation rate decreases with increasing EGR as combustion temperatures are lowered, the time required for mixing increases as the oxygen entrainment rate is low, effectively increasing the stoichiometric AFR (by mass) [87]. This increases the residence time at conditions suitable for soot formation. The soot formation rate is also highly dependent upon charge temperature. Higher charge temperatures significantly increase this rate, leading to the conclusion that intake cooling is a necessity for limiting soot production. This requires that EGR gases be sufficiently cooled prior to intake and highlights the requirement for EGR coolers of appropriate efficiency.

Lower oxygen concentration in the cylinder with increased EGR also reduces oxidation of the formed soot. The retarding of combustion phasing results in less time available for soot oxidation processes. If temperatures decrease significantly with the expanding volume, complete oxidation may not be possible. The combination of increased formation and reduced oxidation can therefore lead to increased net soot output as illustrated by Figure 7.5. Akihama et al. [12] showed that low values of soot can still be achieved at high equivalence ratios if temperatures are kept low enough and/or mixing is enhanced sufficiently to avoid (or limit) the residence time in the soot formation peninsula in the Φ -T plane (Figure 1.4). However, achieving this at higher loads is extremely challenging.

The effectiveness of increasing EGR to lower soot and NO_x is in agreement with the work of other researchers. Figure 7.6 demonstrates the effect of increasing the level of EGR on soot emissions. Taking the data at 1800 rpm 9.7 mg shown in the bottom graph as an

example, for an injection timing of -5°ATDC increasing EGR from 30% to 50% shows a significant increase in soot output. Although combustion temperatures will be lowered by the additional dilution, the reduction in temperature is not sufficient to prevent fuel pyrolysis and as such soot formation still occurred. The increase in equivalence ratio requires more mixing time and prolongs the time for soot precursor formation [13, 87]. As EGR is further increased to 52% and then 54% soot output decreased, attributed to temperatures reducing below that required for fuel pyrolysis. When this occurred the soot formation rate decreased faster than soot oxidation rate, resulting in reduced net soot output, consistent with the findings of [20]. The resultant combustion is seen in Figure 7.7 to be much more retarded and peak rates of heat release much lower as EGR increased and temperatures lowered. This trend of soot initially increasing then decreasing when an EGR threshold is reached is consistent with other contemporary works including [12, 20, 23]. However, as Figure 7.6 indicates, this trend is not always seen to occur. Here soot output for several data series are seen to exhibit the conventional EGR-soot trade-off, indicating PCCI combustion is not achieved. Low soot output is still obtainable at high equivalence ratios with retarded injection timing and combustion phasing, but this results in deteriorating combustion efficiency and increased fuel consumption. For example, for the rich point circled on the top graph of Figure 7.6 the molar content of CO is 1.7% (EI_{CO} 0.23 kg/kg-fuel). Reducing soot formation is crucial to PCCI strategies since oxidation processes are negatively affected by reductions in oxygen availability and lower temperatures. Avoiding the formation regions as shown in Figure 3.2 is essential.

7.4.2 NO_x

The Φ -T maps indicate that the formation of oxides of nitrogen occurs above 2200 K at local equivalence ratios less than 2. Emissions of NO_x are primarily controlled with EGR, although injection timing and mixture preparation also affect their production. Diluting the intake mixture with EGR lowers combustion temperatures as the diluent molecules absorb heat. In particular the burned gas products of H_2O and CO_2 have high heat capacities. The reduction in temperature and oxygen availability is detrimental to soot oxidation, but is advantageous in suppressing NO_x . The reduction of NO_x with increasing equivalence ratio is illustrated in Figure 7.8. Clearly the higher the EGR rate (and consequently equivalence ratio), the lower the NO_x emitted. However, the figure suggests that once a certain equivalence ratio is reached, the extra increase in EGR required to further reduce NO_x emissions requires a much larger relative increase in Φ which is likely to impose constraints on other responses such as soot, combustion efficiency, and fuel consumption. Beyond this condition dependent threshold further increase of EGR may result in a case of diminishing returns of benefit-cost when considering all responses collectively.

7.4.3 NO_x-Soot Trade-off

With conventional combustion a well documented trade-off between soot and NO_x emissions exists. Increasing the rate of EGR has been shown to reduce NO_x emissions, but can result in increased soot. However, extending the time for mixing and reducing combustion temperatures can be effective in reducing both emissions. Figure 7.9 demonstrates the effect of varying EGR fraction on the trade-off at fixed injection timings. For the higher fuelling case (top graph) low soot is shown to be achievable for retarded injection timings where combustion occurs later in the cooler conditions of the expansion stroke. Slightly more advanced injection timings are seen to be prone to higher outputs of soot, exhibiting the traditional trade-off with NO_x. This highlights the importance of correctly matching EGR and injection timing. Departure from the traditional NO_x-soot trade-off is also evident, which ultimately is the goal of employing low-temperature PCCI combustion. Starting from low EGR and increasing the recycled fraction, soot is seen to increase. After reaching its peak it then begins to fall, at which point both soot and NO_x decrease with increasing EGR, demonstrating simultaneous low soot and NO_x values can be achieved through equivalence ratio control with appropriate injection timing.

7.4.4 CO, HC, bsfc, and the NO_x-HC trade-off

The sources of CO and HC emissions differ. CO is a product of incomplete combustion, and the many sources of HC emissions have been discussed in Chapter 2. Nevertheless, oxidation of both species is dependent on oxygen availability and temperature and thus highly sensitive to the rate of EGR. Figure 7.10 illustrates the effect on CO and HC emissions for the same data sets presented above for soot and NO_x. A dependence on SOI can be seen where a more retarded injection timing, with corresponding more retarded combustion phasing, generally results in higher CO and HC emissions. The deterioration in HC can also be seen to occur at lower equivalence ratios for more retarded injection timings. Spatially, increasing EGR slows down the rate of oxidation throughout the cylinder, significantly so in the squish volume, resulting in increased CO and HC emissions from this region [41]. The greater mass of air that must be mixed with the fuel with increased dilution is also detrimental to the oxidation processes of CO and HC. Higher fuelling quantities generate higher load output and higher in-cylinder bulk-gas temperatures due to the extra chemical energy released compared with lower fuelling rates. The extra temperature is beneficial to the oxidation processes and as such combustion phasing can be more retarded before combustion efficiency deteriorates rapidly. The effect of dilution on specific fuel consumption is also significant. The bottom graph of Figure 7.10 demonstrates that bsfc tends to increase with increasing equivalence ratio, but that the severity of the increase is also a function of injection timing. Raising EGR fraction retards combustion phasing and the causes the heat release to spread out.

Combined with the deterioration in combustion efficiency (shown by the increase in CO and HC emissions), the result is reduced load output and a consequential increase in bsfc.

NO_x and HC emissions have shown a traditional trade-off relationship. Whereas the NO_x-SOOT trade-off can be improved by shifting combustion away from the formation regions in the Φ -T plane, NO_x and HC behave in opposite ways with EGR and temperature. As the equivalence ratio is increased (by increasing the rate of EGR), NO_x emissions reduce but at the expense of HC emissions, illustrated in Figure 7.11. Retarding combustion can be effective at reducing NO_x, but again HC emissions increase due to the lower temperatures affecting their oxidation.

7.5 Effect of EGR on the Engine and Maintenance

The use of increased levels of EGR has been shown to potentially result in significant increases in soot emissions. The effect on the reliability of the engine must also be considered for a practical application. Certain vulnerabilities have been noted that have required extra maintenance to be carried out to uphold smooth running of the engine. Components and systems affected include:

- In-cylinder pressure transducer adaptors clogging (design dependent)
- EGR valves sticking due to clogging effect or contamination (results in turbo speed imbalance between the two banks)
- Internal surfaces of EGR coolers becoming fouled due to soot deposition. This can affect the thermal performance of the cooler [98] and restrict the gas pathway.

Although the maintenance on these parts is relatively straightforward in a test bed environment, reduced service intervals on vehicles would not necessarily be tolerated by consumers and access to the affected components is less readily available when installed in a vehicle. Also, it is interesting to note that the next generation V6 diesel engine which is due to replace the 2.7l version will be equipped with different EGR and turbocharger systems. In the new 3.0l setup the EGR valves will be located on the exhaust manifold side of the EGR cooler (hot-side) in contrast to the inlet side (cold-side) on the current generation engines [99]. This change has been implemented to prevent condensation of combustion deposits which can affect the efficiency of the EGR system, which will hopefully improve the problem of sticking valves noted above.

7.6 Concluding Remarks

The use of EGR is necessary to limit combustion temperatures and avoid excessive NO_x formation, but soot output is liable to increase. To avoid increases in net soot output formation must be reduced to a greater extent than oxidation. Increasing EGR raises the overall fuel-air equivalence ratio proportional to $1/(1 - EGR)$. Despite increasing ignition

delay, a greater mass of ambient air must be mixed with the fuel to attain a given local equivalence ratio, which consequently affects the combustion path in the Φ -T plane. Although a highly complex process, high levels of net soot fall within a relatively narrow range of adiabatic flame temperatures (1600-2700K) based on the stoichiometric equivalence ratio. Similarly, NO_x output is relatively low until a threshold flame temperature of 2300K after which it increases exponentially. The effect of global parameters on local conditions is therefore highly important, and EGR rates must be carefully selected with injection timing to avoid excessive emissions and appropriate combustion phasing.

CHAPTER 8

FUEL INJECTION PARAMETERS

8.1 Introduction

Injection timings have a significant effect on formation and oxidation of emission species, combustion noise levels, and fuel consumption. Within this chapter these responses are investigated when subjected to injection timing (SOI) sweeps, ranging from retarded of TDC, to highly advanced in the compression stroke up to -20°ATDC . Work published by the author in [17] documented the effect on emissions at baseline fuel rail pressure, with particular interest paid to soot emissions. The benefits and penalties of various injection timings are assessed to provide an understanding of the trade-offs encountered when exploiting potential strategies to simultaneously reduce soot and NO_x emissions. When a pilot injection of conventional timing is employed ($\sim -20^{\circ}\text{ATDC}$) its combustion increases the in-cylinder pressure and temperature and reduces the ignition delay of the main injection as explained in Chapter 5. Consequently, less time is available for premixing of the main injection. Results previously presented have highlighted the effect this has on soot emissions. The use of a conventional pilot injection strategy is thus limited by soot output due to reduced levels of premixed charge and increased levels of MCC. The effect of a pilot will be discussed in Chapter 10, but in the following chapter in order to provide a clearer understanding of the influence of injection timing on the responses the results presented concentrate on single injection strategies at fixed rate of EGR. Two speed-fuelling rates comparable to NEDC conditions are presented and scrutinised, before the possibility of adding a post-main injection to reduce soot output is discussed. The second part of the chapter addresses the effect of raising rail pressure on the responses investigated.

8.2 Injection Timing at Baseline Fuel Rail Pressure

8.2.1 Soot and NO_x output

As with increasing the level of dilution, injection timing greatly affects the level of soot output, as illustrated in Figure 8.1 graph *a*. The earliest injection timings presented allow long ignition delays to premix the charge. With reference to Figure 3.2 this allows the soot formation region to be avoided to a greater extent. Combustion occurs before TDC with rapid rates of heat release and short associated combustion durations (Figure 5.17 on

page 164). Plenty of time for oxidation of formed soot is available as the combustion process is complete soon after TDC, but this is dependent on oxygen availability and temperature. For advanced injection timings such as -15° to -10° ATDC, ignition delays shorten (Figure 8.1 graph *b*) as the in-cylinder pressure and temperature increase approaching TDC. The reduced mixing time allows for less premixing, with the combustion path more akin to that of conventional combustion (Figure 3.2 top graph) with increased diffusion burning and higher soot output. Further retarding injection timing can be seen to result in lower soot output. This is attributed to lower temperatures as combustion occurs further into the expansion stroke, whilst further extending the ignition delay, providing more time for mixing. Combustion commences at a lower local equivalence ratio than for the advanced SOI PCCI strategy due to the SOI-EGR combination, which helps to avoid the soot formation region. Examination of the in-cylinder pressure data reveals that combustion spreads out and lower rates of heat release are generated. The effect of EGR rate on soot output is also shown in Figure 8.1 graph *a* for two speed-fuelling conditions. Although the same rise and fall in soot is found with injection timing for all four data sets, higher rates of EGR clearly result in more violent swings in soot output. Despite increasing the ignition delay (Figure 8.1 graph *b*), the increased time for soot formation with increased dilution combined with lower soot oxidation rates results in higher net peak soot outputs as the soot formation peninsula in the Φ -T plane is not avoided. Peak soot output was found to correspond to when the start of combustion is a few degrees retarded of TDC (note, SOC is not shown here, but can be determined from Figure 8.1 graph *b*), which corresponds to optimal fuel economy.

As noted in [100], injection timing has a major effect on NO_x emissions, with the emissions increasing with timing advance. This is illustrated in Figure 8.1 graph *c* where NO_x emissions increase with advancing injection timing at fixed EGR. Since NO_x formation is kinetically governed, and its production occurs predominantly within the diffusion flame and in the burned gases following the end of combustion, there must still be partial heterogeneity even at the most advanced injection timings. Peak in-cylinder pressures increase in line with advancing SOI as combustion is advanced (Figure 5.17 graph *a* on page 164). The increase in NO_x emissions correlates with the peak in-cylinder pressure as injection timing is advanced as shown by Figure 8.2. The higher pressures lead to higher combustion temperatures and residence (dwell) time at conditions suitable for NO formation as previously burned gases are compressed to higher pressures and temperatures. This trend was also found experimentally using the same test engine by Catanese [31], who proposed a generic function for the prediction of NO_x emissions which correlated well with a function of peak in-cylinder pressure. It should be noted that combustion efficiencies deteriorate for the more retarded combustion phasings and as such

less of the fuel energy is released. Consequently there is less opportunity for NO_x formation. However, the differences in combustion efficiencies between advanced (for example -10°ATDC) and highly advanced (-20°ATDC) injection timings is negligible for the data presented ($< \sim 1\%$), but NO_x emissions are seen to be consistently higher for the more advanced timings. This highlights a minor drawback when displaying data in the form of emission indices.

The NO_x -soot trade-off for different injection timings is illustrated in Figure 8.3 with a single injection. Two rates of EGR are given for each speed-fuel quantity condition presented. At the lower rates of EGR for each of the conditions (35% and 50%) the NO_x range within the trade-offs is seen to be larger, but the soot range smaller. In both cases higher peak soot outputs were found at the higher EGR rates. The optimum points are generally seen to be at the most retarded injection timings, where NO_x is minimised and soot is close to the minimum. However, this results in poor combustion efficiency and high fuel consumption as combustion phasing is retarded excessively far away from TDC. Highly advanced injection timings that resulted in extremely low levels of soot (Figure 8.1 graph *a*) can be seen in Figure 8.1 graph *c* to be at the expense of higher NO_x emissions. If such advanced injection timings were to be used a high rate of EGR is shown to help reduce the NO_x penalty, but combustion noise levels are still excessively high ($\sim 96 \text{ dB(A)}$ for this case).

8.2.2 Fuel consumption, CO, and HC

Low emissions of both CO and HC were encountered when combustion was advanced, especially before TDC. Graph *a* of Figure 8.4 illustrates that CO continued to decrease with advancing SOI from TDC, however HC (shown in graph *b*) increased slightly from its minimum value corresponding to an SOI of -12.5°ATDC where combustion was phased just prior to TDC. This could be attributed to a degree of over-leaning of the fuel-air mixture where a small proportion of the fuel mixes lean of the flammability limit. Wall wetting by the fuel spray due to over-penetration in the lower ambient density environment is also possible. Nevertheless even the most advanced injection timings within the data sets displayed exhibit low CO and HC emissions and do not constrain the choice of advanced timing strategies. As combustion is retarded past TDC, CO and HC begin to increase. As was discussed in Chapter 5, the fuel is burned in a cooler environment further away from the thermodynamically efficient location of TDC. The residence times above the temperatures required for rapid near complete oxidation (1500 K and 1200 K for CO and HC respectively [41]) are reduced, leading to less complete combustion. The effect of EGR on the emission responses is also visible in the figures. Increased dilution is seen to result in higher CO and HC emissions, a consequence of reduced oxidation rates.

For advanced injections the major source of CO and HC production likely stems from excessive fuel penetration in the squish volume with lower ambient density, leading to over-rich mixture formation. With more retarded injections less fuel is delivered to the squish region and more to the piston bowl. Over-lean mixtures can form that lead to slower combustion and therefore delayed oxidation in cooler environments. This leads to an increase in emissions, the severity of which accelerates with retardation [41]. Inspection of Figure 8.4 graph *c* illustrates an optimum SOI exists for each speed-fuel quantity condition. The lowest specific fuel consumption values are obtained when SOC occurs slightly retarded of TDC. Here no negative work is introduced in the compression stroke that later would have to be recovered. Therefore adjusting the SOI to compensate for the increase in ignition delay with higher levels of EGR allows fuel consumption to be minimised. However, comparison with Figure 8.1 reveals that these timings occur within the higher regions of soot output, as more of the fuel is burned under conventional combustion conditions, potentially prohibiting the use of these timings.

Load conditions also affect the emission indices for CO and HC and bsfc, with responses increasing as the fuel quantity was reduced. Taking the cases of 1800 rpm 9.7 mg 43% EGR and 1500 rpm 6.8 mg 60% EGR as examples, both have very similar overall fuel-air equivalence ratios (0.62) but the lower speed-load case has consistently higher CO and HC emissions across the timing range. Sjöberg and Dec [42] explain that the formation of these species is dominated by incomplete bulk-gas reactions as fuelling is decreased. Over-lean mixtures with associated low combustion temperatures hinder complete oxidation of CO in the time periods available.

8.3 Post injections

The effectiveness of adding a post-main injection has been examined. The chief difficulty observed with the main-only and pilot-plus-main injection strategies is limiting soot levels at combinations of EGR and injection timings which offer acceptable noise, NO_x and bsfc outputs. A post-main injection has been used to increase soot oxidation previously formed by the main fuel combustion. Yun and Reitz [101] and others [102-104] suggest that a small post-main injection raises temperature and generates turbulence promoting mixing both of which help the oxidation of soot formed earlier. The results plotted in Figure 8.5 are for a post-main injection of 0.8 mg/stk/cyl (injector demand) with the main quantity adjusted to maintain the total injected constant at 9.7 mg/stk/cyl. The data cover a range of timings of the post-main injection for two rates of EGR; 35% and 45%. Minimum soot output can be seen to occur when the post-main is injected in the range 20-30°ATDC. At this timing, the post-main reduced soot by 1/4-1/3, whilst NO_x and combustion noise remain

unchanged and the penalty in HC emissions is negligible at earliest timing in the range (shown in Figure 8.5) [17]. This level of soot reduction is consistent with other published works [102-104], and the use of a post-main injection therefore allows an improvement in the NO_x -soot trade-off. As illustrated by Figure 8.5 the disadvantage of the post-main injection is a fuel consumption penalty is incurred because the post-main fuel has been taken from the main event and contributes relatively little to the work output. If the post-main is injected too early, such as in the region shaded in Figure 8.5, the fuel is injected into the main combustion event resulting in increased pyrolysis of the fuel and higher soot output. Retarding the post-main past the optimum stated can still reduce soot output, but at the expense of fuel economy and HC emissions.

Maintaining the desired fuel injection quantities was also a significant problem with the current test engine setup. Following the main injection event a pressure wave can travel through the common-rail accumulator, leading to instability in the system and fuel rail interactions where an incorrect post injection is delivered (in quantity and injection pressure). Damping of these pressure oscillations may be required should subsequent injection strategies be pursued further. Overall although post injections can reduce soot, this has not been found to be a particularly effective route to limit soot emissions with the available test engine and the benefit must be weighed against penalties to fuel consumption and HC emissions [17]. Reducing the amount of soot formed was deemed a higher priority, and will be pursued further in the subsequent sections of the thesis. The use of multiple injections to reduce soot emissions can be found in other pertinent works, including Eastwood [105] and Brooks [76].

8.4 Effect of Raising Fuel Rail Pressure

8.4.1 Overview

The effect of fuel rail pressure has been investigated with the aim of reducing soot and NO_x emissions by improving mixture preparation. Pickett and Siebers [67] explain that increasing the distance between the injector and the farthest upstream location of high temperature combustion (the lift-off length) allows greater entrainment of air into the fuel jet. Figure 8.6 illustrates the proposed effect on the combustion path through the Φ -T plane for a generic PCCI strategy. The effects of raising rail pressure on the responses examined earlier in the chapter have been explored, with particular attention paid to soot. The degree to which the rail pressure has to be increased to obtain the desired reductions in soot output is also investigated. The changes in combustion characteristics are discussed and related to the effects on emission, fuel consumption, and combustion noise responses. Two different operating conditions are presented throughout, culminating in a

discussion of implications when considering potential combustion strategies. The findings of this chapter are incorporated into the investigations in Chapter 9 to determine a broader operating region of PCCI combustion.

The injection pressure was increased by raising the pressure in the fuel rail. Figure 8.7 illustrates the reduction in injection duration with increasing fuel rail pressure. Although the engine could theoretically deliver up to 1650 bar rail pressure, this level was not approached for safety reasons since the engine was a pre-production model. The highest rail pressure demanded was 1200 bar, leaving a generous safety margin, but allowing the trends to be examined. In the data presented, injection timing sweeps were carried out at fixed EGR rates at two different speed-load conditions; Case *A* at 1500 rpm 6.8 mg, and case *B* at 1800 rpm 9.7 mg. EGR rates of 60% and 48% (average Φ of 0.6 and 0.8) were used for the two cases respectively to facilitate low NO_x emissions and help limit combustion noise from excessive rates of heat release. Results from experiments at baseline rail pressures have been included in the results to act as a benchmark against which the responses at higher rail pressure can be compared.

Before the findings are discussed, it is worthwhile to note here that a discrepancy is noticed in the responses for the injection timing of -5°ATDC for case *B*, highlighted by dotted circles where appropriate on Figure 8.12 through to Figure 8.16. For this data, despite the injection timing, fuel quantity, and fuel rail pressure being fixed in the engine management, the combustion phasing was retarded by several degrees. This caused reductions in combustion noise and soot, and increased CO and HC emissions as well as bsfc. The exact cause of the retarded heat release is unknown, but this isolated condition highlights the importance of control over FIE.

8.4.2 Combustion characteristics

The in-cylinder pressure data and derived heat release analysis for three example injection timings of -17.5° , -12.5° , and -2.5° are shown in Figure 8.8, Figure 8.9, and Figure 8.10 respectively. These timings are representative of highly advanced, advanced, and relatively retarded injection timings and will act as examples for results discussed in the following sections. Comparison of the three Figures reveals that rates of change of pressure and the peak pressures encountered decrease as injection timing is retarded, reducing the combustion noise level (shown later in Figure 8.18). It is also interesting to note that the total net heat released increases as injection timing and consequently combustion phasing is retarded. This is in spite of the fact that combustion efficiency deteriorates as combustion is more retarded in phasing, attributable to reduced heat transfer and blowby losses [17].

For the most advanced SOI, rates of heat release tend to increase from 600 bar to 1200 bar rail pressure, but the differences in peak rates for the highest pressures are marginal. Very similar heat release profiles are noted for rail pressures of 800 and 1000 bar, although differences in emission and fuel consumption responses are found. For an advanced SOI (-12.5°ATDC), rate of heat release increases with rail pressure and combustion can be seen to be slightly more advanced for the highest two rail pressures (Figure 8.9). In all cases combustion is phased such that the majority of the fuel energy is released after TDC, which helps to improve indicated fuel conversion efficiency relative to the most advanced injection timings.

The effects of increasing rail pressure with injections close to TDC, such as -2.5°ATDC , is to advance the combustion phasing leading to a reduction in ignition delay (Figure 8.11). The peak rate of heat release and cumulative total for the 1200 bar case are lower than the other rail pressure cases. This can be partly explained by a deterioration in combustion efficiency as indicated by Figure 8.12 (bottom graphs), but does not offer a complete explanation. During the testing the fuel quantity demand was adjusted to maintain total fuel consumption to a target mass flow rate. With the experimental setup it was not possible to measure the actual fuel delivered to individual cylinders and as such variations in the distribution of fuel between the cylinders could theoretically vary slightly depending on the rail pressure and injection timing. The effect of cylinder balancing was previously investigated on the test engine by a previous researcher [31], but this was not implemented into the engine strategy. Variations in fuel delivered and thus potential heat released could therefore have occurred. The emissions results are presented in terms of emissions indices and therefore account for variations in fuelling, but the calculated Mean Effective Pressures and heat release analysis are not normalised by fuel quantity.

Conditions suitable for auto-ignition must be reached before the onset of combustion reactions. For the current test engine the earliest SOC obtained has been in the region -10°ATDC . Combustion does not initiate until at least this location, where temperature and pressures are suitable providing the charge has mixed within flammability limits. As illustrated by Figure 8.11 the ignition delay for the most advanced injections is therefore not greatly affected by the increase in injection pressure. However, increased mixing intensity and enhanced air entrainment are achieved. For advanced injection timings, such as -7.5°ATDC (corresponding to near peak soot output), the fuel is injected into a hotter and higher pressure environment compared with the advanced injection timing cases. Thermodynamic conditions are favourable for ignition once the charge has mixed sufficiently. The increased injection pressures enhance the mixing and as such reduce the

time required to mix within flammability limits. This can advance the combustion and hence shorten the ignition delay, as shown in Figure 8.11 for SOIs more retarded than -7.5°ATDC .

8.4.3 Soot and NO_x Output

The effect of fuel rail pressure on soot emissions for different injection timings is illustrated in Figure 8.13. As the legends indicate, variations in the overall equivalence ratio were obtained due to differences in airflow through the engine. Naturally variations between individual points exist but all were within 5% of the mean value of Φ . The same trend of soot output increasing, reaching a maximum in the SOI range -10° to -5°ATDC , then decreasing as injection timing was further advanced was encountered at all injection pressures, consistent with the findings presented at baseline rail pressure. As the rail pressure increases, soot output clearly decreases across the whole injection timing range. The higher speed-load condition has higher associated soot output which can be attributed to a number of causes. Firstly despite the lower EGR rate, the equivalence ratio is significantly higher. Secondly, the tolerance to EGR decreases as the fuel quantity increases and a greater amount of chemical energy is released [106]. This will be discussed further in Chapter 9 where load and speed limits are investigated.

The locations of peak soot output highlighted on Figure 8.13 vary between the two conditions with the corresponding SOI for the higher speed-load case (case *B*) being more advanced (bottom graph). In both cases, however, a reduction in soot output of 94-96% was achieved when increasing the fuel pressure from the respective baseline values to the maximum values presented (900 bar and 1200 bar). Better atomization of the fuel with increased injection pressure resulting in a greater number of droplets of smaller size, combined with improved air entrainment within the fuel spray helps to reduce local equivalence ratios. For example, by increasing injection pressure from 900 bar to 1200 bar Nishida et al. [107] reported an increase of approximately 40% more air entrained into the spray which reduced the average equivalence ratio of the spray. The increase in jet velocity also creates increased in-cylinder turbulence and improved fuel-air mixing intensity [18, 108]. The combined effects result in lower local equivalence ratios and shifts conditions away from the soot formation region [18]. Returning to the proposed combustion path in the Φ -T plane depicted in Figure 8.6, the lower local equivalence ratios that form with lower spatial fuel density in the cylinder which helps to avoid the soot formation region shown on the Φ -T maps. Soot oxidation is also likely improved as found by [23], who predicted higher concentrations of OH radicals with increased rail pressures. However, in the experimental work presented within this thesis it is not possible to separate the effects since it is net soot in the exhaust that is measured. Although reduction

in soot is obtained across the entire timing range with increased rail pressures, it is most noticeable around peak soot output timings, where ignition delay and thus mixing time are shortest. The greater proportion of diffusion burning at the lowest rail pressure (600 bar in case *B*) is possibly more identifiable from the cumulative heat release graphs (*c*) than in (*b*) for the earlier injection timings (Figure 8.8 and Figure 8.9) since it is not masked by ringing. For these timing examples, the lowest pressure has lower associated peak rates of heat release and longer combustion durations. This more progressive burning has emission response implications, leading to higher relative levels of soot.

Despite the reduced mixing time with increased injection pressure for SOIs around TDC, soot emissions are still reduced since the benefit from improved mixing intensity outweighs the penalty of less mixing time. It is evident that both improving mixing intensity (increased injection pressures) as well as longer mixing times (advanced injection providing long ignition delays) are effective at reducing soot emissions [18, 108]. However, combustion temperatures were still high enough to form NO_x , but the data presented in Figure 8.14 demonstrate the high rates of EGR (60% and 48%) were effective at suppressing its formation with peak values obtained not exceeding 1.1 g/kg fuel at either test condition. Advancing SOI from -2.5° to -20°ATDC resulted in an increase in NO_x emissions. The higher in-cylinder pressures encountered at advancing timings lead to an increase in generation of NO_x as noted previously. Examination of Figure 8.14 reveals that a stronger dependency exists with overall equivalence ratio than rail pressure in that higher equivalence ratio data sets (510 and 700 bar) exhibit lower NO_x outputs. This suggests that control over dilution dominates the effect on NO_x emissions to a greater extent than rail pressure at this condition, which does not limit the strategy of raising pressure. In contrast, when rail pressure was increased in case *B*, a minor increase in NO_x emissions was detected. Although Figure 8.11 demonstrates that large differences in ignition delay were not found, peak rates of heat release were generally greater for the higher injection pressures, especially across the timing range -15° to -7.5°ATDC where bsfc is at its minimum. Yun et al. [108] demonstrated similar findings with NO_x increasing with increasing rail pressure, but their results were obtained without EGR and found ignition delay decreased. However, the use of heavy rates of EGR in this current investigation maintained extremely low NO_x values (~ 30 ppm), in contrast to the 1200 ppm encountered in [108] which could account for some of the differences. Mixture preparation must also be considered. The more advanced phasing and higher associated temperatures with increased rail pressure would tend to increase NO_x production, but the improved mixing intensity with higher rail pressures leads to the formation of lower local equivalence ratios and reduces the amount of high temperature mixing-controlled combustion, thus partially offsetting the effect [15]. The combination of high rates of

EGR and improved mixing are thus countered by increased peak pressures as rail pressure increased, leading to only negligible variations on NO_x emissions. With reference to the Φ -T maps, the simplified combustion regions highlighted in Figure 1.5 demonstrate the effect of increasing the level of dilution and improving mixture preparation as combustion progresses from conventional to PCCI.

Despite the EGR rate being regulated to maintain the target value, the equivalence ratio became slightly leaner as injection timing is retarded. The more retarded combustion that ensued resulted in higher pressures at EVO, and consequently those pre-turbine, allowing more work to be recovered by the turbochargers. Boost pressure increased (albeit slightly), but AFR increased by 8% between the most advanced SOI to the most retarded. The increased air flow and intake pressure resulted in more oxygen in the cylinder which could enhance NO_x formation, but temperatures were likely lower due to the phasing, more than counteracting the oxygen availability in formation terms.

8.4.4 Fuel Consumption

Although increasing the injection pressure is highly effective at reducing soot emissions, a fuel consumption penalty is incurred. The severity of the increase in bsfc when raising fuel pressure from the baseline values is illustrated in Figure 8.15. To minimise the penalty, injection timing can be phased so as to maximise brake load output, but this corresponds to the range of peak soot output. Circled on the graphs are the lowest bsfc points for baseline and highest pressure cases. Increases in bsfc of 32% and 16% are incurred for cases A and B respectively whilst the corresponding soot emissions fall 94% and 97%. However, Figure 8.13 reveals that significant reductions in soot can still be obtained without raising the fuel pressure TO the maximum values. This is promising when considering the soot-bsfc trade-off illustrated in Figure 8.16. For example, in case B increasing fuel pressure to 800 bar yields an 88% reduction in soot at the cost of only 6% bsfc increase relative to the baseline fuel pressure. In practical terms this might well be a more realistic strategy, corroborated by the proposals in [65]. As the top graph on Figure 8.13 demonstrates, the reduction in soot with increasing fuel pressure is more progressive than the higher speed-load condition, but the overall soot emissions indices are lower. Although increasing fuel pressure in this case from 510 bar to 700 bar lowers soot by 73% at minimum bsfc timings, a significant expense of a 22% increase in fuel consumption is still incurred.

One of the main contributing factors to the increase in bsfc is the extra power consumed by the High Pressure (HP) fuel injection pump that increases in proportion to the rail pressure [6]. This is identified in the increase in Friction Mean Effective Pressure (FMEP)

shown in Figure 8.17, which includes contributions from friction and auxiliary loading as explained in Chapter 4. Since the timing sweeps were carried out at as close to fixed fuel quantity as possible, the reduction in brake load output naturally results in an increase in bsfc. A threshold SOI of around -7.5°ATDC exists, after which bsfc increased rapidly in line with deteriorating BMEP. Case A (lower load condition) fares worse than case B in terms of fuel consumption penalty due to the lower work output. The increase in consumed power is thus a more significant proportion of the available energy than with case B, resulting in a much worse increase in bsfc. As discussed above, for injection timings around TDC raising the rail pressure advances the combustion phasing. Although this reduces the mixing time available, soot emissions are not adversely affected since the improvement in soot formation outweighs the penalty of reduced mixing time. It would also be expected that the advancement in phasing would be beneficial to fuel consumption, but any improvement cannot be separated from the negative impact of increased friction and auxiliary work and thus higher bsfc. Nevertheless, examination of Figure 8.15 reveals that more advanced injection timings and thus combustion phasing reduces fuel consumption at a given rail pressure for timings retarded of minimum bsfc.

8.4.5 CO and HC Emissions

An increase in HC emissions might be expected with increased rail pressure due to over-penetration of the spray resulting in fuel impingement on cylinder walls. However, this was not found. The top graphs of Figure 8.12 illustrate the response of HC emissions to increasing injection pressure for the timing sweeps. For injection timings between -20° and -10°ATDC HC emissions are at their minimum. With the minor exception of the 510 bar rail pressure data (case A) very little difference in HC emissions is noticed until timings are more retarded than -5°ATDC . Beyond this point HC emissions begin to increase rapidly as combustion is phased later into the expansion stroke and combustion durations are further extended. The cooler combustion that arises hinders the complete oxidation of the combustible species as volume increases with downward piston movement. CO emissions increase monotonically with retarding injection timing. Interestingly the responses of 800 bar and 1000 bar for case B show remarkably similar values. From -20°ATDC to -5°ATDC the higher fuel pressures generally result in the lowest CO outputs. Helmantel [18] also noted a decrease in indicated specific CO emissions with increasing rail pressure, but attributed the findings to differences in the overall equivalence ratio between the tests. There does not seem to be an easily identifiable trend with overall equivalence ratio, but the improved air entrainment and mixing with the higher rail pressures generates locally leaner equivalence ratios, resulting in more complete combustion and thus reduced CO emissions. Further work with CFD simulation would be useful to ascertain the causes. For case B beyond this threshold

timing of -5°ATDC CO generally increases with rail pressure, whilst for case *A* no discernable dependence on rail pressure is identified, except that the lowest pressure (510 bar) is consistently lower until injection timings of -2.5°ATDC and more retarded.

As rail pressure increases there is little change in combustion efficiency, shown in the bottom graphs of Figure 8.12. An increase in incomplete combustion is therefore not a contributing factor to the increase in bsfc with raised fuel pressure in the injection timing range -20° to -7.5°ATDC as the same amount of fuel is burning to completion. However, combustion efficiency is seen to deteriorate thereafter, contributing to the increase in bsfc as less chemical energy is released. In general, HC and CO emissions are lower for the higher speed-load condition (case *B*) despite the higher equivalence ratio, attributed to higher bulk-gas temperatures encountered due to the extra energy released by a larger fuel quantity.

8.4.6 Combustion Noise

The rates of change of pressure, which were shown in Chapter 5 to correlate well with combustion noise levels, show similar trends across the SOI range for the different injection pressures. High rates of EGR help to control combustion noise by reducing the peak rates of heat release and spreading out the combustion. However, CNL has been shown to be potentially problematic when selecting appropriate injection-EGR strategies. As rail pressure increases, higher rates of heat release are generated for early injection timings, illustrated by Figure 8.8 and Figure 8.9. However, Figure 8.18 demonstrates significant increases in CNL were not encountered with increased rail pressure, with peak changes falling within 1.5 dB(A) for case *B* despite shorter combustion durations. Overall at this condition the lowest rail pressure (600 bar) consistently yielded the lowest combustion noise. Larger changes in noise were found with case *A*, but greater variations in equivalence ratio were encountered compared with case *B*. Overall excessive combustion noise penalties were not encountered at this condition, indicating that raising injection pressure does not impose a limitation when considering combustion noise output for these conditions.

More noticeable effects on combustion noise occur with retarded injection timing. With increased injection pressures the advancement in combustion phasing leads to higher noise levels as demonstrated by Figure 8.18. For both cases *A* and *B*, CNL tends to increase with rail pressure around TDC. This is perhaps more clearly identifiable in the top graph (case *A*) where a change in order of the data lines is visible for timings more retarded than -5°ATDC . After this point the data series fall into order of highest noise with increasing rail pressure, consistent with the more advanced combustion that occurs. However, the

rates of change of pressure associated with these points are in the region 0.13-0.25 MPa/°CA where small changes can result in relatively large swings in noise as demonstrated previously in Figure 5.3. Nevertheless the absolute values are all low.

Overall, noise levels for case *B* are significantly higher than those of case *A*. Combustion noise levels over 90 dB(A) are unlikely to be acceptable for a working strategy, but injection timing must be retarded to after -7.5°ATDC before sub-85 dB(A) values are obtained. In contrast, even injection timings as advanced as -20°ATDC were nearly possible for the highest fuel pressures in case *A*. The relative weighting factor given to combustion noise when designing a combustion strategy will thus depend on the running conditions, with more emphasis paid to it at higher speed conditions. In strategic terms retarding injection timing as much as possible is most effective at reducing combustion noise, but is likely to incur penalties in combustion efficiency and fuel consumption.

8.4.7 Strategy Options and Summary Table

The main factors investigated have been injection timing, fuel rail pressure, and the rate of EGR. To realise PCCI combustion several strategies have been found to be successful with respect to achieving very low engine-out soot and NO_x emissions. Each strategy, however, has been found to come at the expense of other responses, in some case with severe penalties. High levels of EGR have been shown to be effective in limiting NO_x production and to some extent controlling combustion noise, but can result in higher soot outputs. The effect of advancing the injection timing to compensate for the increased ignition delay and better phase the combustion in order to minimise fuel consumption resulted in an increase in soot emissions and combustion noise, whilst raising the fuel rail pressure had an opposing effect, but at the expense of bsfc. Table 8.1 summarises the effects of raising rail pressure relative to baseline values at optimal bsfc. The increase in bsfc with raising rail pressure is more striking at lower load, but soot output is generally easier to control at these conditions and thus warrants less of an increase in rail pressure. Figure 8.19 illustrates a 3D representation of soot output for different injection timings and rail pressures. The relationship between fuel pressure and injection timing is clearly non-linear, highlighting the importance of matching EGR, SOI, and rail pressure. It also implies that it is not necessarily essential to increase to the maximum fuel pressure to achieve acceptable benefits in soot emissions, which can help limit any bsfc penalty. For example, raising rail pressure from 600 bar to 800 bar in case *B* allowed ~90% decrease in soot with a respectable 6% bsfc penalty.

Table 8.2 and Table 8.3 summarise the strategy options investigated within this thesis. The colours and arrows represent the relative improvements and penalties relative to

baseline values. Inspection of the table reveals that NO_x is one of the easier responses to control, generally with the use of moderate-to-high rates of EGR (condition dependent). Soot emissions can be reduced in several different ways. Increasing the ignition delay allows more time for premixing, however, achieving this through increasing the rate of EGR leads to an increase in overall equivalence ratio. The reduced availability of oxygen within the cylinder requires that a greater mass of air be mixed with the fuel to attain the same local equivalence ratio. This extends the time required for mixing, affecting the path taken through the Φ -T plane and increases the residence time for soot formation. If temperatures are not kept low enough this is prone to increasing the net soot output since soot oxidation processes are hindered by the reduced oxygen availability and lower temperatures due to the dilution of charge. A wide range of injection timings for single injection events have been investigated, ranging from -20°ATDC to retarded of TDC. Increasing ignition delay by advancing injection timing has been found to be a more effective strategy for reducing soot, but comes at the expense of combustion noise. Fuel consumption is also higher than optimum, and NO_x emissions can be excessive for lower rates of EGR and require a trade-off with CO and HC emissions which are dependent on the level of dilution (EGR). Advanced timings offer the best phasing with respect to fuel economy, but result in conventional combustion and the highest soot outputs, but NO_x , CO, HC and noise can be acceptable. Retarded timings offer a combination of increased ignition delay and a cooler environment for combustion, both of which help to simultaneously reduce soot and NO_x emissions. These findings are consistent with the proposed paths taken through the Φ -T plane introduced in Figure 3.1. Although combustion noise is also low, combustion efficiency and fuel consumption are sacrificed.

Some responses have been found to be more important than others for specific strategies. Combustion noise imposes less of a constraint at lower speed-fuelling conditions, allowing better combustion phasing to be selected for reduced fuel consumption. In contrast, higher fuel rail pressures can be employed to reduce soot at higher loads with less of a fuel consumption penalty. Post injections can be effective at reducing soot, but come at the expense of increased fuel consumption and potentially HC emissions. However, careful mapping of fuel rail interactions is required for use of this strategy.

8.5 Concluding Remarks

Advancing injection timing to increase the ignition delay or compensate for rates of EGR is practical in theory, but large swings in soot emissions have been encountered. Net soot output is highly dependent on injection timing. The time available for mixing is a key determinant, but output is also sensitive to the level of dilution. Highly advanced or retarded injection timings successfully reduce soot output due to long mixing times, and

cool combustion. Unfortunately optimum timing with regards to fuel economy corresponds to near peak soot output. Increasing mixing intensity by raising fuel rail pressure is highly effective at reducing soot emissions across all injection timings, but comes with an associated fuel consumption penalty due to the extra power consumed by the HP fuel pump. Both injection timing and rail pressure parameters affect local conditions, and the selection of each varies according to condition. For example, at lower speed-load conditions there is less scope to increase rail pressure, but soot and noise output impose less of a constraint even for optimum fuel economy. In contrast, higher speed-load conditions require more retarded phasing and higher rail pressure to achieve acceptable reductions.

CHAPTER 9

OPERATING LIMITS OF PCCI

COMBUSTION

9.1 Introduction

Thus far the majority of the data presented have been at fixed engine speeds, and at fuelling rates with associated loads in the range 0.7-4.9 bar BMEP. However, these combinations cover only a relatively small region of the operating map of the engine. Consequently the load and speed limits that dictate the practical operating region of PCCI combustion with the current test engine will be investigated in two separate studies. Building on the knowledge obtained in the previous chapters a single injection strategy was employed in both investigations with injection timings around TDC (-5° to $+3^{\circ}$ ATDC). This was chosen to exploit the lower temperatures and pressures of the expansion stroke to facilitate low soot, NO_x , and CNL responses.

Presented first is the load limit investigation, carried out at fixed engine speed. Work documented in the available literature points to oxygen deficiency and intolerance to EGR as posing limits [15, 109]. As such particular attention is paid to analysis of in-cylinder pressure data and equivalence ratio to help explain the emission responses presented. The effect on load output with increased fuelling is discussed, which highlights the importance of equivalence ratio at both ends of the load scale. The section concludes with a discussion of potential strategies to allow increased load outputs together with the operating limits and potential implications.

The second section of the chapter covers the speed limit study conducted at constant load. As with the load study the aim is to determine how much engine speed can be increased before the said penalties are encountered. Although little pertinent information was found in the available literature, it was anticipated that the reduced mixing time at higher engine speeds would be the major hindrance to PCCI combustion. An overview of the experimentation methodology is followed by the analysis of the in-cylinder pressure data and the emission responses, ultimately allowing conclusions as to the limiting mechanisms to be drawn. A discussion as to the potential strategies is included at the end of the investigation, before final conclusions concerning the whole chapter are given.

9.2 Load Limits of PCCI Combustion

The upper limit of achievable load output of PCCI combustion was investigated by increasing fuelling at a fixed engine speed of 1500 rpm and EGR rate. SOI was adjusted to maintain constant location of peak combustion pressure (here defining combustion phasing), which maintained the location of peak rate of heat release [109]. The experiments were carried out at four fuel rail pressures varying from 550 bar to 1200 bar at an engine speed of 1500 rpm. The pressures selected were consistent with the three pressures employed at 1500 rpm together with the maximum pressure used at 1800 rpm in Chapter 8. 1500 rpm was selected as a representative speed to allow comparison with the data presented in the previous chapters together with work in the available literature. The fixed rates of EGR and combustion phasings presented were chosen based on preliminary tests to enable NO_x and combustion noise to be contained without excessive fuel consumption penalties, and to provide the opportunity to have low soot outputs with combustion in the cooler expansion stroke. Two data sets are presented at 45% EGR and a combustion phasing of $+13^\circ\text{ATDC}$ (Case A), and 35% EGR with $+16^\circ\text{ATDC}$ phasing (Case B).

Within this section in-cylinder pressure data are analysed to gain an understanding of the combustion characteristics together with a discussion on the overall equivalence ratios which will be shown to play a central role in determination of the limits. Following this, the emission responses, fuel consumption implications, and noise output are scrutinised to allow potential strategy paths to be proposed and hardware implications discussed. The speed limit investigation is then presented.

9.2.1 In-cylinder pressure analysis and equivalence ratio behaviour

The in-cylinder pressure and heat release data presented in Figure 9.1 are for the lowest fuel rail pressure of 550 bar, but are representative of the combustion characteristics encountered at each rail pressure when increasing load. In graph *a* the in-cylinder peak combustion pressures are seen to increase with load. The rate of heat release curves, shown in graph *b*, indicate that the location of peak rate of heat release remains constant corresponding to the location of peak rate of change of pressure. Importantly the peak rate increases with load which has noise ramifications.

The cool flame reactions characteristic of two-stage premixed ignition remain conspicuous across the load range for case A but become less distinct at the highest load for case B. This effect is more exaggerated at lower fuel rail pressures, with the cool flame reactions more identifiable at the higher pressures (900-1200 bar) due to enhanced mixing and

improved air entrainment. The differences between cases *A* and *B* are attributed to differences in mixture preparation resulting from the combined effects of varying levels of dilution and SOI location. At increased loads the higher EGR and more advanced injection timing of case *A* potentially favours the cool flame reactions which affect the main ignition and subsequent hot gas reactions which occur at a higher pressure than without the cool flame [90]. The improved visibility of the cool flame heat release at the higher dilution case (*A*) is potentially explained by the higher equivalence ratio of the premixed fuel, leading to higher rates of low-temperature heat release since reaction rates are proportional to the fuel concentration [110]. However, as will be discussed in following sections, this does not necessarily have a positive effect on emission responses.

As fuelling and load are increased the combustion characteristics can be more clearly separated into two phases; premixed combustion and a mixing-controlled burning “bump”. This is reflected in Figure 9.1 graphs *b* and *c* whereby a greater proportion of the fuel energy is seen to be released at a slower rate (MCC) leading to longer combustion durations. This indicates a change in the combustion regime as the characteristics of PCCI combustion become less apparent [109] with a reduction in the degree of premix and a subsequent increase in the proportion of mixing-controlled combustion. Figure 9.2 demonstrates the effect on gross IMEP load output and fuel-oxygen equivalence ratio as the fuel quantity injected increased. Load output increased linearly with fuelling up to ~11.5 mg for case *A* and ~15 mg for case *B*. Beyond these fuelling rates further increase resulted in little extra load output and in fact a reduction for case *A* caused by the diminishing tolerance to EGR. The increase in equivalence ratio with fuelling is caused by the inability to increase the induction of fresh air. As load output is increased the exhaust gas temperature (shown in Figure 9.3 at the post turbine location) increased linearly which directly impacted the intake temperature (and density) due to the fixed rate of EGR. Despite a marginal increase of up to 4% in intake pressure, this increase in temperature throttled the engine of fresh oxygen-containing air. With the engine setup very little extra boost pressure was available due to limitations predominantly caused by the highly coupled nature of the turbocharger-EGR systems. The lack of control over the induced fresh air caused by the load-EGR schedules therefore introduced a limitation. For example, little boost pressure was available at low loads, whilst the use of high EGR rates also limited the energy that could be recovered by the turbocharger. This could potentially be overcome by hardware changes such as the type and or size of the aspiration system (for example use of a crank driven supercharger), or by facilitating further cooling the EGR gases and thus intake temperature to increase intake density and fresh air flow into the engine. It is also important to note here that increasing the fuel-air equivalence ratio with increasing fuelling results in different engine behaviour compared to when the

increase was caused by increasing the rate of EGR as shown in Chapter 7. Whereas increasing the level of dilution is potentially effective at reducing soot output by lowering temperatures below the threshold required to form soot, this is not the case when the EGR rate is fixed and the increase in fuel-air equivalence ratio is caused by an increase in fuelling alone. Here, globally stoichiometric conditions are approached without extra diluent molecules to absorb heat of combustion, ultimately leading to higher combustion temperatures and less available oxygen.

9.2.2 Soot

Figure 9.4 illustrates the effect of increasing engine load on net soot output for the four different fuel rail pressures. It is evident that for each rail pressure, increasing the fuel quantity to increase load output resulted in an increase in net soot output, attributable to the decreasing oxygen availability [109]. However, the severity of increase is dependent on rail pressure. At low pressure (550 bar) soot increased progressively with load, whereas at high pressure (1200 bar) a more sudden increase was encountered once a threshold load output was reached. At low fuelling rates soot output was low due to low fuel-oxygen equivalence ratios which offered an abundance of oxygen for premixing with the fuel, as well as being beneficial to soot oxidation processes. Ignition delays in the range 9-11°CA provide reasonable time for premixing, whilst combustion temperatures were limited by the combined effects of retarded phasing and dilution. Although ignition delay increased marginally with load (from 9°CA to 11°CA), the reduction in oxygen concentration (increase in equivalence ratio) with fuel quantity injected required that a greater mass of air be mixed with the fuel [13]. This leads to an increase in the residence time for soot formation [87]. The degree of premixing is therefore lower at higher fuelling for a given fuel rail pressure, supported by the appearance of increased MCC in the heat release (Figure 9.1 graphs *b* and *c*) and is consistent with Equation 5.8 [83]. The lower oxygen availability also hindered soot oxidation, the net result being the increases reported. This trend was repeated for the different fuel rail pressures, but raising rail pressure enhanced the air entrainment into the spray and provided extra kinetic energy to improve fuel-air premixing. These effects are reflected in Figure 9.4 which demonstrates that higher rail pressures result in lower soot outputs across the load range.

The combination of the two aforementioned effects offers a viable explanation as to the cause of the increased soot output that clearly limits the increase in load output for PCCI combustion. Insufficient mixing increases soot formation whilst oxidation simultaneously decreases due to low oxygen availability. This leads to a net increase in soot output, a conclusion supported by the findings in [109]. These results are also consistent with the numerical findings of Bianchi et al. [106] who concluded that the maximum rate of EGR

tolerated by the system under PCCI combustion diminishes with increasing load where a greater amount of energy is released with higher fuel quantities. This leads to the conclusion that mixture preparation is intrinsic to reducing soot output [14, 113, 115] so as to avoid the formation peninsula as indicated in the Φ -T maps or limit any associated residence time.

9.2.3 Combustion efficiency and Fuel consumption

At the lowest load conditions CO and HC emissions were particularly high, although this is not unique to PCCI combustion. At these conditions a clear trend of combustible species (CO and HC) increasing with rail pressure was identifiable. Since injection timing and air-flow did not vary significantly, no discernable differences in spray penetration would be expected, pointing to over-leaning of the mixture as the source of the increase. Combustion efficiency improved with increasing load as the higher associated temperatures aid oxidation processes. Figure 9.5 illustrates that HC emissions decreased monotonically with increasing load, whilst CO emissions followed a very similar trend until a threshold, after which they increased rapidly. Kim et al. [41] reported finding CO decreasing but HC remaining relatively unchanged as load increased. They attributed the higher CO at lower load to incomplete combustion of lean mixtures at relatively low temperatures in the squish volume. At the lowest loads presented soot yield does not impose a limitation, but inferior combustion efficiencies caused by over-lean mixtures and lower temperatures are potentially problematic. The near linear relationship between engine load and exhaust gas temperature downstream of the turbine outlet which would be immediately upstream of the oxidation catalyst is plotted in Figure 9.3. Contemporary DOCs typically require temperatures of $\sim 200^{\circ}\text{C}$ for light-off [15]. It can be seen that an engine output of approaching 3 bar IMEP_g is required to produce the required gas temperature. These low operating loads potentially impose a limitation on the operating regime and would require careful optimisation and selection of aftertreatment systems of suitable conversion efficiency for a practical application.

Figure 9.6 illustrates the effect on bsfc of raising load output. The contours reflect the differences in BMEP caused by the increase in fuel rail pressure. Although differences in mixture preparation and the subsequent combustion occur due to varying amounts of kinetic energy and disparity in spray breakup, the major difference in the values is attributed to the extra power consumed by the high pressure fuel pump [111]. However, analysis of Figure 9.1 graph *b* indicates that combustion duration is shortened with increasing rail pressure. Since combustion phasing is fixed, less of the fuel's energy is released further away from TDC which improves thermal efficiency and acts to somewhat reduce the fuel consumption penalty.

Fuel consumption decreased with increasing load output until a threshold was reached. The decrease at a given rail pressure is credited to a lower fraction of the overall work being lost in overcoming friction. Higher rates of heat transfer to cylinder walls would, however, be expected due to higher in-cylinder temperatures, but this has not been investigated and will not be discussed further in this work. The extra energy released when fuelling and load output are increased generates higher bulk-gas temperatures which are beneficial to the oxidation processes of soot, CO and HCs, but is offset by the lower oxygen availability as equivalence ratios increase. Once the threshold was reached Figure 9.6 indicates that fuel consumption begins to deteriorate in-line with the increase in CO and soot. Although bulk-gas temperatures are significantly higher than the lower load tests and exceeded the 1500 K required for complete oxidation of CO to CO₂ [41, 42, 44], the availability of oxygen was low. Therefore, despite long residence times for oxidation, CO emissions remained high. As such the mixture was too rich to sustain complete combustion and dramatic increases in CO output were recorded, consistent with the findings in [109]. The increase in MCC caused a more spread out heat release (longer combustion duration) and likely acted to further decrease combustion efficiency due to the expanding combustion volume [27]. Temporarily not taking into account the fuel consumption penalty, engine-out CO emissions of over 130 g/kg-fuel (0.8% wet volumetric fraction in this example) were encountered for case A at 4.1 bar IMEP_g. Although exhaust temperatures were well in excess of the 200°C for light-off of contemporary DOCs [15], values of this order are unrealistic for any real-world application. Combustion efficiency can therefore also be deemed a limit to the attainable load output under PCCI combustion.

9.2.4 NO_x and Combustion Noise

Retarded combustion phasings and appropriate levels of dilution contained NO_x emissions to peak values of 2.2 g/kg-fuel and 4.4 g/kg-fuel for cases A and B respectively. Increasing the fuelling and load might have been expected to increase NO_x production due to greater chemical energy being released leading to longer residence times at conditions above the 2200 K required for their formation. However, the opposite can be seen to have occurred in the NO_x-soot trade-off graphed in Figure 9.7 whereby lower NO_x emissions were obtained at higher loads, consistent with the findings of Yun and Reitz [109]. Since combustion temperatures were higher, this result was attributed to the significantly lower oxygen availability and inferior mixing, which resulted in higher local equivalence ratios that avoided the NO formation region shown in the Φ -T maps. Moreover, increasing fuel rail pressure could have been expected to increase NO_x formation due to more rapid combustion, but this is offset against improved fuel-air premixing, leading to little variation in NO_x emissions at a given load output. Figure 9.7 also illustrates for the same

load output lower NO_x emissions were obtained with a higher EGR rate despite more advanced combustion phasing (Case A). However, in both cases higher rates of EGR would be required at lower load due to the higher oxygen concentration. The appropriate rate of EGR required is a function of fuelling (load), consistent with Equation 8.2. For combustion better phased with respect to minimised fuel consumption (around TDC), excessive rates of change in pressure and subsequently high levels of combustion noise can also occur. Since the location of peak rate of heat release was maintained constant, increasing the quantity of fuel delivered provided the potential for increased rates of pressure rise. This was manifested in the increase in combustion noise illustrated by Figure 9.8 with a much larger increase found with the lower EGR case. At the lowest loads increasing rail pressure has been shown to cause deterioration in combustion efficiency due to over-leaning. Less energy is therefore released for a given fuel injection quantity which reduces the rates of heat release and peak changes in pressure. When the higher load combustion limit was reached and combustion efficiency deteriorated, noise similarly decreased since less energy was released and the rate of pressure rise decreased.

9.2.5 Potential Strategy

On the basis that NO_x emissions do not constrain the increase in load, the proposed strategy involves minimising soot yield and fuel consumption until the aforementioned combustion limits are reached. If an excessively high fuel rail pressure were to be employed, brake load output decreases. The approach is therefore to keep the rail pressure as low as possible within the development target soot limits. Should an optimisation routine be carried out the relative importance of fuel consumption and soot would have to be weighted, but within this work one generic strategy is described based on minimising soot output within a maximum bsfc penalty of up to 5% of minimum bsfc at the particular operating load. In general terms the minimum bsfc was associated with the lowest rail pressure (550 bar), which therefore mainly acted as the baseline for each load. Figure 9.9 illustrates the soot-bsfc trade-off strategy path following this criterion. Fuelling is increased at the lowest fuel rail pressure permitted to minimise bsfc. Once the soot outputs associated with the various rail pressures begin to diverge the gain in soot reduction becomes more significant, at which point the operating point moves to a higher rail pressure. With selected points labelled, Figure 9.9 shows that the appropriate rail pressure increases with load for both cases, but that an optimum point is reached beyond which soot increases rapidly. Using this method the optimum point would be chosen as 4.4 bar IMEP_g using a rail pressure of 900 bar (Case B). This limit is comparable with the findings in [109] but significantly lower soot emissions were obtained in the work presented in this thesis for similar NO_x outputs, attributed to lower rates of EGR but more retarded injection timings employed.

9.2.6 Intake pressure implications

The increase in fuel-air equivalence ratio with increased load limited the operating range. Therefore the extent to which the intake pressure would have to be increased to maintain the overall fuel-air equivalence ratio constant has been investigated. The fuel quantity required to maintain a given load output and the intake temperature expected were estimated by extrapolating data previously collected. Details of the calculation are given in Appendix 4. Combining Equations 7.1 and 7.2 and substituting the intake density using the ideal gas law it follows that:

$$p_{\text{intake}} = \frac{AFR_s \cdot \dot{m}_f \cdot R \cdot T_{\text{intake}}}{\eta_{\text{vol}} \cdot \phi \cdot n V_d \cdot \frac{N}{2} \cdot (1 - EGR)} \quad (9.1)$$

The intake pressure required for a given rate of EGR and desired fuel-air equivalence ratio can thus be estimated. For the calculation it has been assumed that the volumetric efficiency (based upon intake conditions) remains constant at a value equal to that obtained in previous experiments at lower load. Figure 9.10 demonstrates the required absolute intake pressure required to maintain an equivalence ratio of $\Phi=0.7$ at 1500 rpm as a function of engine load. Intuitively under these constraints higher intake pressure is required the higher the demanded rate of EGR. Also intake pressure increases with engine load, consistent with the findings presented within this chapter. In case *B* presented above a load output of 4.4 bar was achieved. Absolute intake pressures of 2 bar and 3 bar would be required for load outputs of 7 bar and 10 bar IMEP_g respectively, which is unachievable with the current hardware configuration.

To validate the calculations experimental data from [18] was used to estimate the required intake pressure based on given operating conditions. This gives insight into the robustness of the calculation when using data from different engines. For an intake temperature of 60°C, $\Phi=0.67$, $N=2000$ rpm, and IMEP of 13 bar, Equation 9.1 was used to estimate the required intake pressure assuming the same volumetric efficiency of 90%. The fuel flow was estimated by scaling the author's data to account for the faster engine speed. An intake pressure of 3.4 bar was obtained compared to the 2.9 bar stated in [18]. However, combustion was more advanced in [18] and as such it is reasonable to assume a lower fuel flow would be required to obtain a given load output relative to a more retarded phasing. Adjusting for this yielded a required intake pressure of 2.99 bar, within 0.1 bar of the documented value used in [18]. Due to assumptions that have to be made during the calculations the values obtained are only estimates, but imply the process is robust enough to draw conclusions as to the required intake pressures for different load outputs. Further discussion on the required intake pressures are given in the final chapter.

9.3 Speed Limits of PCCI Combustion

The second limiting factor investigated was the engine speed limit. As the engine speed increases each crank angle interval takes place in a shorter period in the time domain. It is likely, therefore that ignition delay times will shorten as engine speed increases, allowing less time for premixing. Soot would thus be expected to be a limiting factor. A similar approach to the load limit investigation was adopted whereby the rate of EGR and combustion phasing were maintained constant, but in this study the brake work output was kept constant at 2.5 bar BMEP (54 Nm) and the engine speed increased using the dynamometer. The delivered fuel quantity and injection timing were adjusted to maintain both the combustion phasing and brake torque output. A single test case is presented throughout. The presentation of the findings follows the same structure as the load study, with in-cylinder and equivalence ratio data analysed before considering soot emissions, fuel consumption and combustion efficiency, NO_x emissions and combustion noise. Final strategies are proposed before the chapter concludes with a discussion on both studies.

9.3.1 In-cylinder pressure analysis and equivalence ratio behaviour

The representative in-cylinder pressure and heat release data presented in Figure 9.11 are again at the lowest fuel rail pressure of 550 bar, and are representative of the combustion characteristics encountered at each rail pressure. Graph *a* illustrates the in-cylinder peak compression pressures increased with engine speed. As the engine speed was increased the mass flow rate of fresh air naturally increased (in kg/s), but a marginal decrease in air flow through the engine per stroke (in kg/stk) was encountered (not plotted here). The decrease in airflow of approximately 6% from 1000 rpm to 2000 rpm was, however, somewhat offset by a small increase in intake pressure (in the order of 4% increase from 1000 rpm to 2000 rpm). The higher intake pressures therefore led to higher compression pressure into which the fuel was injected. Although little change in the peak combustion pressure is noticed, graph *a* indicates that higher pressures were sustained further down the expansion stroke. This is reflected in Figure 9.12 whereby for a given fuel rail pressure IMEP_g generally increased with engine speed. Also displayed in Figure 9.12 is the fuel-oxygen equivalence ratio. The increase in equivalence ratios is attributed to the combined effects of a marginal decrease in air flow through the engine per stroke, and an increase in the required fuel delivery (depicted in Figure 9.13).

The rate of heat release and cumulative net heat release plots illustrated in graphs *b* and *c* respectively indicate a change in combustion characteristics as engine speed increased. The rate of heat release plotted in $\text{J}/^\circ\text{CA}$ decreased with increasing engine speed. However, 1°CA takes place in a shorter time in ms at higher engine speed. The net rate of heat release plotted in J/ms (or kW) is therefore greater for a higher engine speed (for a

given release in $\text{J}/^\circ\text{CA}$). Nevertheless the decrease in peak rate of heat release from 1000 rpm to 2000 rpm was approximately $20 \text{ J}/^\circ\text{CA}$, which does not represent a 50% decrease. The cool flame reactions also became less distinct and dampened as speed increased. These last two observations are indicative of a change in combustion characteristics.

Graph *c* of Figure 9.11 illustrates a more progressive combustion profile as engine speed increased. A smaller fraction of the heat was released in the premixed phase with a subsequent increase in the amount of MCC. Combustion duration increased, with a greater proportion of the fuel energy released further away from TDC. The cumulative total heat release increased with speed because a greater quantity of fuel was required to maintain the load output of 2.5 bar BMEP. As well as combustion phasing, the relative amount of heat transfer and friction are also important, although the discussion here will not go into great detail. The average heat transfer per unit time increases with engine speed as do frictional losses [9]. As was noted in Chapter 1, one of the benefits of diesel engines is that they operate at slower speeds with higher gearing which helps to reduce power lost to friction. However, the analysis here concentrates on brake output and combustion characteristics.

9.3.2 Soot

When investigating the load limits the increase in equivalence ratios caused large increases in soot and CO emissions, with an associated fuel economy penalty. Figure 9.14 illustrates the effect on soot emissions for increasing engine speeds. As found previously in Chapter 8 and the earlier part of this Chapter, higher fuel rail pressures had lower associated net soot outputs at all rail pressures, but soot output remained essentially low until an engine speed of 1500 rpm was reached. Beyond that, more significant increases in soot output were liable to be encountered, but are a function of rail pressure. Intuitively, a faster engine speed was attainable at higher rail pressure before soot output increased rapidly. The fuel quantities varied from 9.1 to 11.1 mg/stk/cyl depending on the test point, but as with the previous chapters the emissions were normalised by the fuel quantity to allow a clearer representation (displayed as emission indices).

Since data presented prior to this study have been at fixed engine speed, ignition delay has been displayed in units of crank-angle degrees ($^\circ\text{CA}$). However, it is important to consider the mixture preparation and combustion in the time domain to account for the changes in engine speed. Figure 9.15 illustrates ignition delay plotted in both the crank and time domains. As engine speed increased, in order to maintain the combustion phasing and brake load output the fuel injection had to be increased in quantity and advanced in timing. The location of the start of combustion remained relatively constant and as such the

ignition delay in crank-angle degrees increased with engine speed. However, it can be seen that the delay period in ms decreased with increasing speed. The fuel and air therefore had less time to mix prior to the onset of hot gas reactions. Comparison of Figure 9.12 and Figure 9.14 indicates a clear relationship between fuel-oxygen equivalence ratio and soot output. The increase in equivalence ratio required a greater mass of air to be mixed with the fuel and together with the reduced mixing time resulted in a lower degree of premixing and longer residence times in regions suitable for soot formation. This is in agreement with Figure 9.11 where lower rates of heat release (in J/°CA) and longer combustion durations are visible at higher engine speeds. The reduction in the degree of premixing and subsequent increase in the amount of mixing-controlled combustion is hence deemed responsible for an increase in soot formation, whilst the lower oxygen availability with increasing engine speed hinders oxidation processes. Moreover the reactions take place in a time period inversely proportional to the engine speed, and consequently time available for oxidation decreases with increasing engine speed.

9.3.3 Combustion efficiency and Fuel consumption

The CO and HC emission responses are illustrated in Figure 9.16 for the different engine speeds. As engine speed increased a minor decrease in HC emissions was recorded, whilst CO emissions remained effectively constant until a speed of 2000 rpm, after which their emission approximately doubled. The higher temperatures achieved at faster speeds helped to reduce the HC output, but CO emissions were not improved. This latter observation can be explained by recalling that complete oxidation of CO to CO₂ requires higher temperatures than the oxidation processes of HC. The increase in equivalence ratio with increasing engine speed previously discussed also meant that oxygen availability was lower, which naturally had an adverse effect on oxidation processes. As the engine speed exceeded 2000 rpm the reduced time available for oxidation together with the possibility of incomplete mixing provided potential reasons for the increase in CO emissions.

At a given engine speed the bsfc increased with fuel rail pressure. As illustrated by Figure 9.17 optimal bsfc was found around 1250 rpm for all cases tested and can be seen to increase with engine speed. Although not plotted here, combustion efficiency was not found to deteriorate until speeds in excess of 2000 rpm, indicating that combustion phasing was more likely responsible for the bsfc increase. Figure 9.13 demonstrates the fuel flow required to maintain the load output. In contrast to the units of mg/stk/cyl displayed in the load study previously, here fuel flow required to maintain load output is given on secondary vertical axis in the form of g/s to account for engine speed. As well as advancing the injection timing to maintain the combustion phasing, an increase in fuel

quantity delivered was required to maintain the brake load output. This is identified in the cumulative heat release (Figure 9.11 graph *c*) whereby a greater fraction of the energy is released closer to TDC for the slower engine speeds. As engine speeds increased there was less time available to the combustion processes which increased in duration in the crank domain. For example, at +15°ATDC the heat released was ~220 J at 1000 rpm but only ~175 J at 2000 rpm. The extra energy at higher speed was released further into the expansion stroke, which was less efficient at generating work output and required higher fuel inputs resulting in increased bsfc. A consequence of this was higher exhaust temperatures as less of the fuel energy was transferred to the coolant and more energy was passed to exhaust enthalpy. As with the load study, the engine-out emissions of CO constrain the selection of PCCI combustion as engine speed increased. The linear increase in exhaust temperature as speed was increased is shown in Figure 9.13, together with the total fuel quantity required to maintain the load. It can be seen that for the operating conditions presented, the exhaust gas temperature was only below 200°C for the 1000 rpm test case. Assuming conversion rates of any catalytic converter are high for temperatures in excess of this level (~200°C), tailpipe emissions should not be in excess of the legislative demands. However, as decreases in combustion efficiency manifested in this case through significant increases in CO emissions, careful consideration may be required for an optimal strategy.

9.3.4 NO_x and Combustion Noise

Combustion noise level was shown previously to be a function of engine speed (Figure 5.3). The data presented in Figure 9.18 illustrate that combustion noise increased with engine speed. However, the reduced fraction of premixed combustion and increased amount of MCC might have been expected to reduce combustion noise. As engine speed increased the first derivative of pressure with respect to crank angle decreased, but when viewed in the time domain the peak rate of change of pressure in MPa/ms increased slightly, although no clearly identifiable trend in the data was found. However, the frequency distribution of the noise will have changed, resulting in an overall increase in measured combustion noise. Combustion noise of 85 dB(A) or lower is desirable for passenger comfort, which was attainable until an engine speed of 1500 rpm. Further increases in noise with higher speeds were recorded, but sub-90 dB(A) levels for all operating speeds less than 2250 rpm provides a suitable operating range when considering the limitation posed by engine speed.

Similarly with NO_x emissions, no discernable trend in the data plotted in Figure 9.19 can be noticed except that in all cases NO_x output is extremely low and below 0.6 g/kg-fuel. The use of retarded combustion phasing and appropriate rates of EGR therefore allowed

engine speed to be increased without further consideration of NO_x emissions. A general trend could be a minor decrease in NO_x output as speed increases, potentially due to the more retarded combustion phasing and reduced oxygen availability, but nevertheless values within 0.1 g/kg-fuel of the mean are encountered for all data points.

9.3.5 Potential Strategy

Soot, CO, and combustion noise have been found to pose the greatest obstacles when increasing engine speed whilst operating a PCCI combustion strategy. Fuel consumption, NO_x , and HC emissions were less of an issue. The strategy proposed below is based upon the fact that soot is the main limiting response. Increasing fuel rail pressure has been shown to increase bsfc due to the extra power consumed by the high pressure fuel pump, highlighted in Figure 9.17. Using this data and the same criteria as with the load limit study, namely allowing a maximum increase of 5% from minimum bsfc at each engine speed, the minimum soot outputs were chosen to provide a strategy path. Figure 9.20 illustrates this path, starting from the lowest engine speed of 1000 rpm, and extending up to 2250 rpm. Soot output can be seen to increase with engine speed except for the increase from 1250 to 1500 rpm, caused by the increase in fuel rail pressure. Minimum bsfc is found at 1250 rpm, which is partly due to a lower rail pressure of 700 bar being selected from the 5% bsfc criteria, and partly due to the bsfc contour profile shown in Figure 9.17. Except for engine speeds of 1250 and 2250 rpm, fuel rail pressure of 900 bar was chosen. This allowed the best reduction in soot output without exceeding the fuel consumption criteria. However, a general trend of soot increasing from 1500 rpm upward is clear, the penalties of which become more severe the faster the engine speed. Unlike the load study, from this point a trade-off between soot and bsfc does not exist, rather they both increase together. From the data presented it can be concluded that 2000 rpm is a reasonable limit to the PCCI combustion, beyond which soot output increases sharply. Figure 9.14-Figure 9.19 show that up to this speed the emission responses do not pose a serious issue with the operating regime, although combustion noise levels in the region 88-89 dB(A) were encountered. It should be noted that the conclusions given here are based on the data presented, and have not been optimised. The aim has been to give the reader an understanding as to the limits encountered when attempting to increase the speed output of the engine, and not provide a final calibration. A discussion of the findings of the two studies will now be given to summarise the findings, which concludes this chapter.

9.4 Concluding Remarks

Oxygen availability limited the speed and load output of PCCI combustion. Although conditions remained globally lean, locally insufficient mixing occurred to sustain PCCI combustion. As fuel delivery was increased to increase load output, overall equivalence

ratios increased, requiring a greater mass of ambient air be mixed with the fuel. This was a hardware limit due to the trade-off between boost and EGR deliverable by the engine. For the generic PCCI strategy fuel rail pressure should be kept as low as possible within soot limits in order to minimise any bsfc penalty. As fuelling is increased, the operating point effectively moves along the NO_x -soot trade-off from high NO_x and low soot, to low NO_x and high soot. As load demands increase more retarded injection timings with higher rail pressure and lower rates of EGR (or increased boost pressures) are ideal. Overall the load and speed limits reported are similar to those documented in the available literature, including [21, 25], but the limits presented in this thesis were obtained without hardware modifications to a current generation DI diesel engine.

Maximum sustainable engine speed was similarly limited by oxygen availability and the inability to premix the fuel with air within engine timescales. Although the mass flow of induced air increased with speed, the actual fresh air induced per stroke decreased. In contrast fuel delivery had to be increased to maintain the desired load output, leading to an increase in overall equivalence ratio. Accompanied by a reduction in ignition delay, increased soot output resulted. Raising rail pressure was effective up to a threshold, but penalties in fuel consumption dominated the trade-off after a given engine speed. The speed limit is thus also hardware limited and methods for improving mixing and/or increasing the oxygen availability are required to expand the operating range. The proposed strategy to increase engine speed makes use of moderately high fuel rail pressures for the majority of engine speeds, but beyond a threshold speed, soot and bsfc increase simultaneously, despite increasing rail pressure.

Figure 9.21 illustrates the speeds and loads tested for the majority of the data presented within this chapter and the rest of the thesis. Highlighted are the speed and load limits that have been discussed above, together with the limits associated with the Modulated Kinetics (MK) combustion regime. The speed and load limits encountered within this study are comparable with those of the 1st generation MK [25]. Comparison of the limits with this study highlight allowing variable swirl ratio could help significantly in the expansion of the operating regions. Similarly, further cooling of the EGR gases was employed in the 2nd generation MK regimes with great benefit in soot and NO_x emissions. However, this would require hardware modifications which will be discussed further in the Chapter 10 that follows. Little other pertinent literature relating to the speed limits of PCCI combustion was found, but comparable limits were found with Eastwood et al. [105] although significantly lower smoke output was achieved in the work documented in this thesis.

CHAPTER 10

DISCUSSION AND CONCLUSIONS

10.1 Discussion

This chapter is divided into three sections beginning with a discussion of the objectives of the work, a review of the important mechanisms exploited to reduce NO_x and soot output, together with the feasibility and future of PCCI combustion strategies. Following this further work is proposed, that has been separated into work that originates from limitations with the available test facilities, and work that would compliment and build upon the findings of the current investigation. Conclusions of the thesis are then presented.

10.1.1 Objectives of the work

The main aim of this investigation has been to determine if and how far a modern DI diesel engine could be operated on a PCCI combustion strategy to simultaneously reduce soot and NO_x emissions without changes to engine hardware. Although the available test engine was of pre-production specification, it allowed manipulation of injection strategy and EGR rate which was exploited in the investigation. Comparison of the findings with other published work provides insight into what hardware changes maybe beneficial to increase the operating range or improve specific responses.

The concept of reducing soot and NO_x formation through control over temperature and mixing can be traced back to the original Φ -T presented by Kamimoto and Bae [10]. However, as was discussed in Chapter 2 work reported in the literature is typically limited to hardware and operating conditions much narrower than those encountered in real-world applications. Some of the most successful practical proposals were also reviewed [12, 21, 22, 25, 26], but were limited in their range of operation even with hardware modifications. In Chapter 3 idealised combustion paths were reviewed to explain the characteristic paths encountered with different combustion strategies. Engine-out emissions have been examined in this thesis at speed and load conditions typical of NEDC requirements. Fuel injection parameters and EGR rates have been studied as routes to enhance the premixing of the charge and lower combustion temperatures. A generic PCCI strategy was investigated in Chapters 7-9 to assess the constraints imposed on fuel injection and EGR strategies to achieve low soot and NO_x emissions simultaneously. Importantly, control

over combustion through injection strategy was required, which partly distinguished the combustion regime from HCCI.

10.1.2 Soot and NO_x emissions

DI diesel injection gives rise to a distribution of local equivalence ratios and temperatures in the cylinder. Soot formation occurs in the early stages of mixing-controlled combustion where inhomogeneity in the fuel-air mixture results in high local equivalence ratios in the jet core [28]. With reference to the Φ -T maps reviewed in Chapters 2 and 3, soot is known to form between temperatures of 1600 K and 2500 K at local equivalence ratios greater than 2. However, a large area under the soot formation peninsula exists that can be exploited with PCCI combustion. In contrast, a greater proportion of soot oxidation occurs later in the cycle and continues further in the expansion stroke, the rate of which is highly dependent on local oxygen availability and temperature. The measured soot content in the exhaust reflects the difference between these two competing processes and in the experimental work carried out it has not been possible to separate out the relative contributions. However, proposed combustion paths and mechanisms presented in Chapter 3 explain the expected trends in soot formation. Oxidation processes are expected to be negatively affected by the increased level of dilution employed with PCCI strategies due to reduced oxygen concentration and lower temperatures. The mechanism for reducing net soot output with PCCI combustion strategies is thus reducing the amount of soot formed to outweigh the reduction in oxidation.

NO_x is predominantly formed at temperatures greater than 2200 K at local equivalence ratios under 2 [11, 12]. Ideally both soot and NO_x formation regions would be completely avoided, but this has been found to be no trivial matter. In Chapter 7 it was shown that global parameters affect local conditions with a strong dependence on stoichiometric adiabatic flame temperature existing between soot and NO_x output. NO_x was found to increase exponentially at temperatures above 2300 K, whilst peak soot outputs were found in the range 1600-2700 K. Premixing of charge and control over temperatures is therefore crucial in obtaining simultaneously low emissions and has been the driving force behind this work.

10.1.3 Practicality of PCCI Combustion with a current generation engine

PCCI combustion is a broad term that encompasses many different operating strategies that fall between conventional diesel combustion and true HCCI combustion. The charge is not universally mixed to the same local equivalence ratios as with HCCI, and regions of inhomogeneous charge remain that result in part of the heat being released during a mixing-controlled combustion phase. The major benefit over HCCI strategies is that

control over combustion is maintained through the injection strategy. Nevertheless, the premixing of the fuel and air prior to ignition with PCCI combustion is greater than with conventional combustion.

To increase the amount of premixed charge, methods to increase both the mixing time and mixing intensity were investigated. Combustion of a conventional pilot injection advances ignition of the main event, shortening the available time for premixing and reducing oxygen available to the main injection. The result is higher local equivalence ratios at the time of ignition. Figure 10.1 illustrates proposed combustion pathways based on experimental findings at constant injection timing retarded of TDC with and without a conventional pilot injection. The higher temperature and local equivalence ratio at SOC when a pilot is employed results in the combustion path passing through both soot and NO_x formation regions. Without a pilot, longer ignition delays are possible and PCCI combustion can be achieved allowing the soot peninsula to be better avoided. The more retarded combustion phasing also helps cool the charge as the volume expands, which allows the NO_x formation region to be better avoided. Results presented in Chapters 5-8 highlight the effect of a conventional pilot on soot emissions. Consequently for the majority of the investigation the pilot injection was removed and the work concentrated on a generic single injection strategy. The single injection strategies that have been explored act as a baseline for this generic PCCI strategy. The use of multiple injections, such as multiple fuel injection events advanced of TDC in the compression stroke may be beneficial in enhancing fuel-air mixing, but this has not been investigated in this thesis.

Control over NO_x emissions has been found to be relatively simple in comparison with soot output, with moderate-to-high levels of EGR the most practical approach as presented in Chapters 7 and 8. The overall fuel-air equivalence ratio was shown to increase in proportion to $(1 - \text{EGR})^{-1}$ which limited the level of dilution with increased fuelling without penalties in HC and CO emissions. Despite increasing the ignition delay, a greater mass of ambient air must be mixed with the fuel to attain a given local equivalence ratio as EGR is increased, which can increase soot output [13, 87]. However, departure from the traditional EGR-soot trade-off was found possible once a threshold EGR level was reached, although this was not found to be possible for all injection timings. Improvement in the soot- NO_x trade-off is therefore possible when using EGR with appropriate injection timing, but was shown to come at the expense of combustion efficiency and fuel economy.

In contrast, in Chapter 8 increasing the ignition delay by modifying the injection timing was shown to be much more effective at reducing soot output. Large swings in soot output were encountered, with peak soot occurring at timing associated with optimal fuel

economy. Both highly advanced and retarded injection timings were found to be most successful at increasing ignition delay and providing increased mixing time, but with differing combustion characteristics. In Chapter 8 advanced combustion was shown to yield low soot, HC, and CO emissions, together with acceptable bsfc, but high rates of heat release which generated excessive combustion noise. NO_x emissions were also shown to increase with advancing phasing as peak in-cylinder pressures increased. In contrast, for retarded phasing low soot and NO_x emissions were found possible together with low combustion noise, but at the expense of combustion efficiency and fuel consumption. The relative benefits of the injection timings were found to be dependent on speed and load requirements.

As well as increasing the available time for fuel-air premixing, increasing the mixing intensity is also a key mechanism in achieving PCCI combustion through improved mixture preparation. Enhancing the mixing intensity of fuel and air can be achieved through air motion and fuel injection. The test engine was not able to vary swirl, but the effect of injection pressure was investigated in Chapter 8. As was reviewed in Chapter 2, increasing rail pressure improves air entrainment in the fuel spray, forming lower local equivalence ratios. This is extremely beneficial to reducing soot output since soot formation is reduced and its oxidation potentially improved. However, this was found in Chapter 8 and Chapter 9 to come with an associated fuel consumption penalty due to increased work consumed by the high-pressure fuel pump.

The load and speed limits of PCCI combustion were found to be limited by oxygen availability. The speeds and loads achieved with the generic PCCI strategy presented in Chapter 9 are consistent with those documented in the literature [25, 26, 105, 109], and are notably similar to the 1st generation MK strategy [25]. Comparison with these studies and the UNIBUS concept [26] suggests further cooling of the intake charge and promoting more premixing could further expand the operating region with PCCI combustion. Lower fuel rail pressures could also potentially be employed if cooler intake temperatures and enhanced air mixing were achievable, benefiting fuel consumption. Overall, the results are encouraging and suggest that improving mixing, together with increasing boost pressure in combination with the intake density and oxygen concentration with further intake cooling, could allow higher load and speed limits.

10.1.4 Wider Implications of PCCI Strategies

Within this thesis higher injection pressures, moderate-to-high levels of dilution, and either highly advanced or retarded injection timings with a single injection have been found to be beneficial to achieving PCCI combustion. The findings of the investigations in Chapter 9

indicated that higher boost pressure is required to limit the overall fuel-air equivalence ratio to achieve higher speed and load outputs. However, sufficient dilution must still be employed to limit combustion temperatures. In Chapter 9 a load output of 4.4 bar IMEP_g was obtained at 1500 rpm using 35% EGR and retarded combustion phasing. Consideration of Equation 9.1 and Figure 9.10 offers insight into the boost pressures required to increase load at constant fuel-air equivalence ratio. To double the load output to 9 bar IMEP_g an intake pressure of ~2.6 bar (1.6 bar boost) would be required to maintain the overall equivalence ratio at $\Phi=0.7$. If the required pressure could be generated without further cooling intake temperatures, very high in-cylinder bulk-gas temperatures would be generated. As was discussed in Chapter 3 this increases the maximum achievable temperature in the jet core. The effect on the combustion path shown in the Φ -T plane as proposed in Figure 3.1 indicates higher soot and NO formation. Therefore despite maintaining the target overall equivalence ratio PCCI combustion may not be attainable and the combustion path must still be considered. With boost pressures this high the tolerance of the engine to excessive in-cylinder pressures must also be considered. Assuming a polytropic compression process without combustion, motored pressures of ~100 bar would be experienced with the engine even in the absence of combustion. With the addition of combustion pressures care would have to be taken not to exceed peak cylinder pressure limits to avoid damage to, or in the worst case, destruction of the engine. The general industrial trend is for lowering compression ratios. This would be beneficial in reducing in-cylinder pressure and bulk-gas temperatures, as well as providing longer associated ignition delays.

With the available current generation test engine the highly coupled nature of the turbocharger-EGR systems limited the available boost pressure and thus operating range of PCCI combustion. The high temperature of the EGR increased the intake temperature with load, displacing cold fresh air and limiting the available boost pressure. Reducing the intake temperature is therefore crucial to expanding the operating region of PCCI combustion. Improved cooling of the EGR gases would increase the intake density and allow lower intake pressures for a given rate of EGR, but any increase in size of the heat exchangers would have to be weighed against increased mass, and potential transport delays must be considered should the path be made longer. The maximum achievable combustion temperatures would also be reduced, which would benefit the reduction in NO formation, whilst the lower required boost pressures would limit the motored peak in-cylinder pressures. Furthermore reducing overall equivalence ratios by increasing boost pressures would likely result in lower CO and HC emissions due to improved oxygen availability and higher ambient temperatures, both of which benefit oxidation processes. The increased heat capacity with higher intake pressures has previously been shown [26,

48] to be beneficial in reducing peak rates of pressure rise. As was documented in Chapter 5 this would help reduce combustion noise which correlates well with peak rates of pressure increase. The extra oxygen availability would require a lower mass of ambient air to be mixed with the fuel to attain a given local equivalence ratio which would reduce the time required for mixing and shorten residence times for formation of soot. Lower fuel rail pressures could then potentially be used which would reduce the power consumed by the HP fuel pump, ultimately benefiting fuel economy. However, this would have to be offset against any increase in fuel consumption due to the generation of the required boost pressure.

Engine technology and hardware have naturally advanced from that of the available test engine, but the latest available literature is consistent with the findings and proposals of this thesis. Load outputs achieved in the literature vary depending on the strategy employed, the test equipment, and development targets set (the maximum allowable response value). As was reviewed in Chapter 9 loads of up to 13 bar IMEP have been documented with PCCI combustion, but with excessive combustion noise expected [18]. However, to achieve this, boost pressure of approaching 2 bar and intake temperatures cooled to 60°C were required in conjunction with high rates of EGR (46%), fuel rail pressure (1800 bar), swirl, and extended intake valve opening. Outside of a laboratory environment or without major EGR heat exchanger modifications, intake temperatures are likely to be much greater due to the high rate of EGR. This would require even higher boost pressures to maintain the equivalence ratio of 0.67 used in this particular study. Generation of the required boost pressures and EGR rates proposed presents a considerable challenge and changes in hardware would be required to achieve these values across a large operating range. Even contemporary VGT turbochargers generate little boost below a threshold exhaust gas mass flow, pointing to supercharging or a more sophisticated turbocharging process.

Modern electronically controlled HPCR fuel injection systems are also favourable to PCCI combustion strategies. A great degree of flexibility and control will continue to be available and research is being conducted into ultra-high pressure fuel injection of ~3000 bar [112]. In conjunction with this, smaller nozzle holes are also being used to further improve atomisation of the fuel and allow smaller injection quantities to prevent limiting the injector capabilities. The combined effects are improved air entrainment, and reduced spray tip penetration and fuel film that adheres to the wall surface [112]. Due to the smaller orifice area of the nozzles more holes may be required. Even if the current FIE could provide 3000 bar rail pressures, the findings presented in Chapter 8 indicate the increase in fuel consumption is likely to be unacceptably high. Doubling rail pressure

from 600 bar to 1200 bar increased the minimum bsfc by 16% for at a particular operating condition (1800 rpm 9.7 mg/stk/cyl), with even more severe bsfc penalties for a lower load condition (1500 rpm 6.8 mg/stk/cyl). This trade-off must therefore be considered.

The work in this thesis has been carried out at steady state operating conditions, with results presented in 7-9 illustrating the sensitivity of soot output to changes in AFR. Transient conditions introduce different challenges, the most serious of which is expected to be control of AFR since a finite delay exists before the turbocharger and EGR systems stabilise following a change in demand. Re-mapping of the turbocharger to accommodate these needs could reduce the impact, but lean or rich mixtures could be generated for very short periods. This will have adverse effects on emission responses as they do with conventional strategies and is expected to cause the greatest problem.

10.1.5 Aftertreatment Considerations

The emissions considered in this thesis have been engine-out. In a vehicle the exhaust system would incorporate aftertreatment systems such as DOCs, LNTs, and/or DPFs. The exhaust temperatures encountered with the majority of the testing were generally over 200°C and should thus enable effective catalytic light-off [15] and oxidation of HC and CO. This could allow a slightly higher concentration of CO and HC species to escape the cylinder, although this may negatively impact fuel consumption.

The findings at steady state have indicated the combustion system can be very sensitive to minor changes in EGR (Chapter 7) and injection parameters (Chapter 8), whilst transients have the potential to cause AFR mismatches and varied mixture preparation. This leads to the conclusion that a DPF will be required on vehicles for the foreseeable future. Nevertheless, reducing engine-out soot is still beneficial as it reduces the frequency of DPF regeneration. For regeneration, temperatures of approximately 600°C and oxygen concentrations of ~5% are required [6], but exhaust temperatures this high are rarely encountered upstream of the DPF except at high engine speeds and loads. The use of a heavily retarded post injection is commonly used to increase the exhaust temperature, but has an associated fuel consumption penalty. This penalty is reduced when regeneration intervals are increased and the potential for downsizing of the aftertreatment is also possible, which could help reduce weight. The financial cost, however, is still likely to be relatively high, which will continue to impact the overall cost of vehicles.

10.1.6 Alternatives to PCCI Combustion

Diesel combustion strategies are continually developing to increase performance and reduce engine-out and tailpipe emissions. PCCI combustion strategies presented face stiff

competition from conventional diesel combustion, HCCI, alternative fuelled engines such as gasoline and biofuels, and non-internal combustion engines.

As indicated in Chapters 5 and 6, conventional combustion has the advantage of a wide operating range, excellent fuel economy, low HC and CO emissions, and relatively low combustion noise. A significant engine-out penalty in soot output must be accepted to operate this regime and places a greater emphasis on the DPF aftertreatment systems. NO_x formation can be reduced effectively by increasing the level of EGR by reducing peak combustion temperatures and oxygen availability. This is liable to increase soot formation and negatively affect oxidation, resulting in increased net soot output and movement along a NO_x -soot trade-off. Although lower temperature combustion, local equivalence ratios are too high to be deemed PCCI combustion.

Although the near zero emissions of soot and NO_x offered by HCCI combustion, are clearly desirable, many problems still exist. Cycle-to-cycle variations in combustion, the lack of control over combustion with injection timing, poor vaporisation of diesel fuel, high HC and CO emissions, potentially excessive combustion noise levels, and difficulties with transient conditions are currently limiting its application.

A limitation of the investigation was that it was not possible to investigate the use of close coupled injections due to fuel-rail interactions. The use of a split-main injection strategy has previously been proposed [76] that allowed reductions in NO_x and soot of approximately 20% and 40% respectively with fuel economy and CO penalties of +3% and +30% respectively, caused by the retarded phasing of the second main injection. Not all emission and fuel consumption responses could be reduced simultaneously, with trade-offs required. Nevertheless, at higher speed-load conditions, split-main injection strategies may have an advantage over PCCI strategies without hardware modifications. In future, industrial trends may change, with downsizing and turbocharging of gasoline vehicles a potential substitute. In the long term alternatives to non-renewable fossil fuels must be found. As was reviewed in 0 several alternatives to diesel powered vehicles are gaining popularity, including electric, fuel-cell, or hybrid powered vehicles. The use of alternative fuels including biofuels is also being investigated. The relative merits and current problems of each are summarised in Table 1.2. Nevertheless, research into diesel technologies remains at the forefront of engine technology and must continue to be pursued further.

10.1.7 The Future for PCCI Combustion Strategies

PCCI combustion clearly has advantages over conventional combustion in terms of soot output, but has been shown to be limited in its range of operation. In Chapters 7-9 EGR was shown to be essential to reduce combustion temperatures to limit NO_x without incurring an excessive fuel consumption penalty. Within this thesis it has been shown that without engine hardware modifications PCCI combustion is achievable on a contemporary DI diesel engine. Moreover, several injection and EGR strategies have been shown in Chapters 7-9 to be successful at achieving PCCI combustion. Strategy selection is a function of maximum allowable response outputs, engine speed, and required load output. To avoid excessive combustion noise rate of peak pressure increase must be contained, but the relative importance of combustion noise was shown in Chapter 5 to increase with engine speed. Advanced combustion phasing was shown to be potentially problematic when demanding low combustion noise, but was shown in Chapter 8 to offer very low soot emissions. Fuel consumption was found to be a function of combustion phasing and duration, deteriorating rapidly as phasing was retarded. Nevertheless, with the generic PCCI strategy pursued in this thesis a more retarded combustion phasing with increase fuel rail pressures was found to offer the best compromise when increasing load output, but ultimately oxygen availability was found to constrain the operating range. Importantly, the investigation carried out in this thesis used the same hardware for both PCCI and conventional strategies. This offers a clear advantage and a duel mode strategy is likely to be the most acceptable approach when considering the future of PCCI combustion. The results presented in Chapters 5-9 has shown that PCCI combustion can be employed at low engine speed-load conditions without hardware modifications. These conditions encompass a significant proportion of drive-cycles. The mode could then be switched to conventional combustion or a split-main strategy for higher speed-load operation.

However, the use of next generation hardware offers the possibility of expanding the operating of PCCI combustion with industrial trends described earlier in this discussion lending themselves to PCCI strategies. This could allow a greater use of PCCI combustion and reduced dependence on conventional combustion at higher operating speeds and loads. Although a DPF would continue to be required, the fuel consumption penalty associated with its regeneration could be improved. Furthermore, the baseline generic single injection strategy investigated in this thesis may well be improved with the use of multiple injections to enhance fuel-air mixing.

10.2 Further Work

- The boost characteristics of the turbocharger system limited the operating range of PCCI combustion. The use of a supercharger or remapping of the existing turbocharger would potentially provide increased flexibility.
- Increasing the mixing intensity to enhance premixing is beneficial. Port deactivation was non-operational on the test engine but was further developed and present on the later production version. Investigation into the variation of swirl ratio would also benefit the adaptation to PCCI, potentially allowing slightly lower rail pressures to be used to limit any fuel economy penalty. Although some pertinent literature is available, combustion noise must also be considered.
- Exploring the effect of compression ratio on adapting to a PCCI strategy would be interesting since the general industry trend is towards lowering values. This should increase ignition delays and thus mixing times, but could result in poorer combustion and thermal efficiencies.
- Only fully-warm steady state conditions have been investigated. Transients that would naturally occur should the strategy be implemented in a vehicle (including drive cycles) introduce new and different problems. The transient response of EGR and adequate AFR control/response pose significant challenges.
- The full potential of the HPCR FIE has not been fully exploited. Multiple injection strategies could be investigated with an aim to increasing the premixing of fuel and air with multiple shots of fuel. The effect of fuel rail interactions must be considered. In the work presented only one factor at a time has been changed. DOE could be used to investigate the effects of multiple injection strategies.
- The constraints and limits of adapting to a PCCI strategy have been investigated but not optimised. Optimisation strategies based on reducing specific target emissions could be developed, for example minimising NO_x without exceeding baseline fuel consumption. Optimisation of load and speed limits over a wider range of EGR-combustion phasing operating conditions would also be worthwhile.
- There is potential scope for investigating the effect of soot clogging under pre-determined operating conditions with two transducers installed in one cylinder (measuring the same pressure), but housed in different adaptor designs. This would allow a more direct comparison of the performance of the adaptors but would require the cylinder head to be modified to accommodate the two adaptors.

10.3 Conclusions

- PCCI combustion is defined by high levels of premixed charge whilst retaining control over combustion through injection timing. It offers the simultaneous reduction of NO_x and soot emissions.
- Using an engine of current generation hardware not originally setup for PCCI strategies, PCCI combustion has been successfully implemented up to an engine load of 4.4 bar gross IMEP (at 1500 rpm) and up to a conservative engine speed of 2000 rpm (at 2.5 bar BMEP). With the available test engine both were limited by oxygen availability:
 - Load output was limited by the boost characteristics of the turbocharger coupled with high intake temperatures.
 - Speed was limited by poor availability of oxygen and insufficient mixing.
- Increasing boost pressures is vital to expand the operating region of PCCI combustion, but hardware modifications would be necessary to achieve this. Further cooling of EGR gases to increase intake density would be of great benefit.
- A duel mode strategy is most appropriate with PCCI combustion used at lighter speed-load demands and the regime switched to a conventional strategy for the higher operating regions, both using the same hardware.
- Mixture preparation with PCCI strategies is characterised by lower and more uniform local equivalence ratios at ignition and increased dilution. The net soot reduction mechanism exploited with PCCI combustion is decreasing soot formation to outweigh the reduction in oxidation, which is hindered with increased dilution.
- NO_x emissions can be well controlled with EGR for both PCCI and conventional combustion. However, when achieving this with conventional combustion the charge is not sufficiently premixed to be deemed PCCI combustion. The result is a traditional NO_x -soot trade-off.
- Combustion noise is highly dependent on and correlates well with the peak rate of pressure rise and engine speed, but is not unique to PCCI combustion strategies. With PCCI strategies high levels of premix and advanced combustion phasing can result in rapid rates of heat release, which generate large peak rates of increase of pressure and subsequently excessive combustion noise levels.

- Using PCCI combustion strategies the emission responses of soot, NO_x , CO and HC have been examined together with fuel consumption and combustion noise level, at conditions comparable to NEDC requirements. These cannot all be reduced simultaneously
- Operating with a single main injection a number of strategies are available to simultaneously reduce soot and NO_x emissions:
 - High EGR and highly advanced injection timing provides a long ignition delay for premixing. Rapid rates of heat release can result in high combustion noise, but low CO and HC outputs are achievable. This is a potential strategy for lower speed-load running conditions where combustion noise levels are lower.
 - Moderate-to-high EGR and retarded combustion phasing reduces temperatures and increases ignition delay to allow further premixing. Combustion efficiency and increased fuel consumption penalties are paid, but lower rates of heat release result in low combustion noise. This strategy is more suited to higher load operating conditions since higher bulk-gas temperatures are generated, beneficial to CO and HC oxidation processes.
 - Increasing fuel rail pressure across all injection timings can significantly reduce soot output, but a trade-off with bsfc is required due to the power consumed by the high pressure pump. Large soot reductions of ~90% at a reasonable bsfc penalty ~+6% are achievable and could allow injection timing to be advanced to improve isfc.
- The addition of a post-main injection reduced soot emissions by up to a third, but incurred an increase in fuel consumption and HC emissions. Fuel rail interactions also pose a problem in controlling injection pressures and quantities, which can give rise to increased fuel consumption and a potential deterioration in combustion.
- isfc is primarily a function of combustion phasing and duration. Minimum isfc values were found when combustion occurs just retarded of TDC, deteriorating when phasing is advanced or significantly retarded. isfc of PCCI combustion is comparable to conventional isfc values, but bsfc potentially higher.
- Employing PCCI combustion strategies offers the advantage of increased intervals between DPF regenerations, which benefits fuel economy. Aftertreatment will still be required to meet tailpipe emission targets due to the sensitivity of combustion to charge composition and mixture preparation.

REFERENCES

- [1] Intergovernmental Panel on Climate Change (IPCC) Website. *Climate Change 2007: Synthesis Report. Summary for Policymakers*. http://www.ipcc.ch/pdf/assessment-report/ar4/syr/ar4_syr_spm.pdf. Accessed Aug. 2008
- [2] European Commission Website. *Reducing CO₂ emissions from light-duty vehicles*. http://ec.europa.eu/environment/air/transport/co2/co2_home.htm. Accessed Aug. 2008
- [3] DieselNet: Diesel Emissions Online. *Emission Standards: Europe: Cars and Light Trucks*. <http://www.dieselnets.com/standards/eu/ld.php>. Dieselnet Website, Accessed May 2007
- [4] United Nations Framework Convention on Climate Change. *Kyoto Protocol*. http://unfccc.int/kyoto_protocol/items/2830.php. Accessed Jan. 2008
- [5] Environmental Protection UK Website. *Car Pollution*. <http://www.environmental-protection.org.uk/transport/car-pollution/>. Accessed Jan. 2008
- [6] Robert Bosch GmbH. *Diesel-Engine Management Systems and Components*. John Wiley & Sons Ltd, 4th edition 2005
- [7] U.S. Department of Energy: EERE (Energy Efficiency and Renewable Energy). *Diesel Car Sales Top Gasoline Car Sales in Europe*. http://www1.eere.energy.gov/vehiclesandfuels/facts/2007_fcvt_fotw481.html. US Dept. of Energy Website, Accessed Sept. 2007
- [8] European Automobile Manufacturers' Association (ACEA) *Automobile production expanded by 5.3% in 2007: Trend toward diesel remains*. http://www.acea.be/index.php/news/news_detail/automobile_production_expanded_by_53_in_2007. Accessed Aug. 2008
- [9] J. B. Heywood. *Internal Combustion Engine Fundamentals*. McGraw-Hill Book Company, 1988
- [10] T. Kamimoto and M.-H. Bae. *High Combustion Temperature for the Reduction of Particulate in Diesel Engines*. SAE Paper 880423. Society of Automotive Engineers, 1988
- [11] T. Kitamura, T. Ito, J. Senda and H. Fujimoto. *Mechanism of Smokeless Diesel Combustion with Oxygenated Fuels Based on the Dependence of the Equivalence Ratio and Temperature on Soot Particle Formation*. International Journal of Engine Research, **3** (4). 223-248, 2002

- [12] K. Akihama, Y. Takatori, K. Inagaki, S. Sasaki and A. Dean. *Mechanism of the Smokeless Rich Diesel Combustion by Reducing Temperature*. SAE Paper 2001-01-0655. Society of Automotive Engineers, 2001
- [13] S. Kook, C. Bae, P. C. Miles, D. Choi and L. M. Pickett. *The Influence of Charge Dilution and Injection Timing on Low-Temperature Diesel Combustion and Emissions*. SAE Paper 2005-01-3837. Society of Automotive Engineers, 2005
- [14] S. Kook and C. Bae. *Combustion Control Using Two-Stage Diesel Fuel Injection in a Single-Cylinder PCCI Engine*. SAE Paper 2004-01-0938. Society of Automotive Engineers, 2004
- [15] A. Knafl, T. J. Jacobs, S. V. Bohac and D. N. Assanis. *The Load Limits of Low Temperature Premixed Compression Ignition Diesel Combustion*. ISCE 2006, The 2nd International Symposium on "Clean and High-Efficiency Combustion in Engines", Tianjin, China, 2006
- [16] M. Musculus, J. E. Dec and L. M. Pickett. *In-Cylinder Imaging of Conventional and Advanced, Low-Temperature Diesel Combustion*. Diesel Engine Emissions Reduction Conference, Chicago, 2005
- [17] B. Keeler and P. J. Shayler. *Constraints on Fuel Injection and EGR Strategies for Diesel PCCI-Type Combustion*. SAE Paper 2008-01-1327. Society of Automotive Engineers, 2008
- [18] A. Helmantel. *Reduction of NO_x Emissions from a Light Duty DI Diesel Engine in Medium Load Conditions with High EGR Rates*. SAE Paper 2008-01-0643. Society of Automotive Engineers, 2008
- [19] J. E. Dec. *Advanced compression-ignition engines--understanding the in-cylinder processes*. Proceedings of the Combustion Institute, **32** (2). 2727-2742, 2009
- [20] T. J. Jacobs, S. V. Bohac, D. N. Assanis and P. G. Szymkowicz. *Lean and Rich Premixed Compression Ignition Combustion in a Light-Duty Diesel Engine*. SAE Paper 2005-01-0166. Society of Automotive Engineers, 2005
- [21] S. Kimura, O. Aoki, Y. Kitahara and E. Aiyoshizawa. *Ultra-Clean Combustion Technology Combining a Low-Temperature and Premixed Combustion Concept for Meeting Future Emission Standards*. SAE Paper 2001-01-0200. Society of Automotive Engineers, 2001
- [22] S. Kimura, H. Ogawa, Y. Matsui and Y. Enomoto. *An Experimental Analysis of Low-Temperature and Premixed Combustion for Simultaneous Reduction of NO_x and Particulate Emissions in Direct Injection Diesel Engines*. International Journal of Engine Research, **3** (4). 249-259, 2002
- [23] F. Tao, Y. Liu, B. H. RempelEwert, D. E. Foster, R. D. Reitz, D. Choi and P. C. Miles. *Modelling the Effects of EGR and Injection Pressure on Soot*

- Formation in a High-Speed Direct-Injection (HSDI) Diesel Engine Using a Multi-Step Phenomenological Soot Model*. SAE Paper 2005-01-0121. Society of Automotive Engineers, 2005
- [24] T. Fang, R. E. Coverdill, F. Chia-fon and R. A. White. *Combustion and Soot Visualization of Low Temperature Combustion within an HSDI Diesel Engine Using Multiple Injection Strategy*. SAE Paper 2006-01-0078. Society of Automotive Engineers, 2006
- [25] S. Kimura, O. Aoki, H. Ogawa, S. Muranaka and Y. Enomoto. *New Combustion Concept for Ultra-Clean and High-Efficiency Small DI Diesel Engines*. SAE Paper 1999-01-3681. Society of Automotive Engineers, 1999
- [26] R. Hasegawa and H. Yanagihara. *HCCI Combustion in DI Diesel Engine*. SAE Paper 2003-01-0745. Society of Automotive Engineers, 2003
- [27] W. L. Hardy and R. D. Reitz. *A Study of the Effects of High EGR, High Equivalence ratio, and Mixing Time on Emissions Levels in a Heavy-Duty Diesel Engine for PCCI Combustion*. SAE Paper 2006-01-0026. Society of Automotive Engineers, 2006
- [28] J. E. Dec. *A Conceptual Model of DI Diesel Combustion Based on Laser-Sheet Imaging*. SAE Paper 970873. Society of Automotive Engineers, 1997
- [29] P. F. Flynn, R. P. Durrett, G. L. Hunter, A. O. Zur Loye, O. C. Akinyemi, J. E. Dec and C. K. Westbrook. *Diesel Combustion: An Integrated View Combining Laser Diagnostics, Chemical Kinetics, and Empirical Validation*. SAE Paper 1999-01-0509. Society of Automotive Engineers, 1999
- [30] P. Eastwood. *Critical Topics in Exhaust Gas Aftertreatment*. Research Studies press LTD, 2000
- [31] A. Catanese. *Emission Characterization and Cylinder Pressure Information for Applications in the Electronic Engine Management of Diesel Engines*. Ph.D. thesis, University of Nottingham, 2006
- [32] X. Li and J. Wallace. *A Phenomenological Model for Soot Formation and Oxidation in Direct-Injection Diesel Engines*. SAE Paper 952428. Society of Automotive Engineers, 1995
- [33] R. J. Crooks, G. Sivalingam, M. A. A. Nazha and H. Rajakaruna. *Analysis of Soot Particulate Formation in a High-Pressure Confined Spray-Flame*. SAE Paper 1999-01-3488. Society of Automotive Engineers, 1999
- [34] R. E. Morgan, M. R. Gold, O. Laguitton, C. Crua and M. R. Heikal. *Characterisation of the Soot Formation Processes in a High Pressure Combusting Diesel Fuel Spray*. SAE Paper 2003-01-3086. Society of Automotive Engineers, 2003
- [35] Y. B. Zeldovich and P. Y. Sadovnikov. *Oxidation of Nitrogen in Combustion*. Academy of Sciences, USSR. 1947

- [36] M. Badami, F. Millo and D. D. D'Amata. *Experimental Investigation on Soot and NOx Formation in a DI Common Rail Diesel Engine with Pilot Injection*. SAE Paper 2001-01-0657. Society of Automotive Engineers, 2001
- [37] H. Koren and M. S. Bisesi. *Handbook of Environmental Health; Biological, Chemical, and Physical Agents of Environmentally Related Disease*. CRC Press, 4th edition 2003
- [38] M. F. Russell. *The dependence of diesel combustion on injection*. Proceedings of the I Mech E Seminar Future Engine and System Technologies - The EURO IV Challenge, (S490/005/97). 65-82, 1997
- [39] M. Taschek, C. Fettes and A. Leipertz. *Analysis of the Combustion Process in a Heavy-Duty Transparent Diesel Engine Equipped with 4-Valve Cylinder Head and Common Rail Injection System*. SAE Paper 2001-01-3181. Society of Automotive Engineers, 2001
- [40] M. F. Russell, C. D. Young and S. W. Nicol. *Modulation of Injection Rate to Improve Direct Injection Diesel Engine Noise*. SAE Paper 900349. Society of Automotive Engineers, 1990
- [41] D. Kim, I. Ekoto, W. F. Colban and P. C. Miles. *In-cylinder CO and UHC Imaging in a Light-Duty Diesel Engine during PPCI Low-Temperature Combustion*. SAE Paper 2008-01-1602. Society of Automotive Engineers, 2008
- [42] M. Sjöberg and J. E. Dec. *An investigation into lowest acceptable combustion temperatures for hydrocarbon fuels in HCCI engines*. Proceedings of the Combustion Institute, **30** (2). 2719-2726, 2005
- [43] I. Khan, G. Greeves and C. Wang. *Factors affecting smoke and gaseous emissions from direct injection engines and a method of calculation*. SAE Transactions 730169. Society of Automotive Engineers, 1973
- [44] M. Sjöberg and J. E. Dec. *Combined Effects of Fuel-Type and Engine Speed on Intake Temperature Requirements and Completeness of Bulk-Gas Reactions for HCCI Combustion*. SAE Paper 2003-01-3173. Society of Automotive Engineers, 2003
- [45] B. Carberry, G. Grasi, S. Guerin, F. Jayat and R. Konieczny. *Pre-Turbocharger Catalyst - Fast catalyst light off evaluation*. SAE Paper 2005-01-2142. Society of Automotive Engineers, 2005
- [46] Department for Transport Website. *The environmental impacts of road vehicles in use*. <http://www.dft.gov.uk/pgr/roads/environment/cvtf/theenvironmentalimpactsofroa3793>. Accessed Jan. 2008
- [47] A. Saad and EI-Sebai. *Combustion Noise Prediction Inside Diesel Engine*. SAE Paper 1999-01-1774. Society of Automotive Engineers, 1999

- [48] R. Hasegawa, I. Sakata, T. Koyama and H. Yangagihara. *Numerical Analysis of Ignition Control in HCCI Engine*. SAE Paper 2003-01-1817. Society of Automotive Engineers, 2003
- [49] J.-O. Olsson, P. Tunestal and B. Johansson. *Boosting for High Load HCCI*. SAE Paper 2004-01-0940. Society of Automotive Engineers, 2004
- [50] T. Lee and R. D. Reitz. *The Effect of Intake Boost Pressure on MK (Modulated Kinetics) Combustion*. JSME International Journal, **46** (Series B, No 3). 2003
- [51] R. S. Wijetunge, J. G. Hawley and N. D. Vaughan. *Application of Alternative EGR and VGT Strategies to a Diesel Engine*. SAE Paper 2004-01-0899. Society of Automotive Engineers, 2004
- [52] J. G. Hawley, F. J. Wallace and A. Cox. *Reduction of Steady State NO_x Levels from an Automotive Diesel Engine Using Optimised VGT/EGR Schedules*. SAE Paper 1999-01-0835. Society of Automotive Engineers, 1999
- [53] Y. Chi, J. Cheong, C. Kim and K. Choi. *Effects of VGT and Injection Parameters on Performance of HSDI Diesel Engine with Common Rail FIE System*. SAE Paper 2002-01-0504. Society of Automotive Engineers, 2002
- [54] N. Ladommatos, S. M. Abdelhalim, H. Zhao and Z. Hu. *The Dilution, Chemical, and Thermal Effects of Exhaust Gas Recirculation on Diesel Engine Emissions - Part 1: Effect of Reducing Inlet Charge Oxygen*. SAE Paper 961165. Society of Automotive Engineers, 1996
- [55] N. Ladommatos, S. M. Abdelhalim, H. Zhao and Z. Hu. *Effects of EGR on Heat Release in Diesel Combustion*. SAE Paper 980184. Society of Automotive Engineers, 1998
- [56] N. Ladommatos, S. M. Abdelhalim, H. Zhao and Z. Hu. *The Dilution, Chemical, and Thermal Effects of Exhaust Gas Recirculation on Diesel Engine Emissions - Part 2: Effect of Carbon Dioxide*. SAE Paper 961167. Society of Automotive Engineers, 1996
- [57] F. Payri, J. Benajes, S. Molina and J. M. Riesco. *Reduction of Pollutant Emissions in a HD Diesel Engine by Adjustment of Injection Parameters, Boost Pressure and EGR*. SAE Paper 2003-01-0343. Society of Automotive Engineers, 2003
- [58] S. M. Aceves and D. L. Flowers. *A Detailed Chemical Kinetic Analysis of Low Temperature Non-Sooting Diesel Combustion*. SAE Paper 2005-01-0923. Society of Automotive Engineers, 2005
- [59] T. Rente, S. Gjirja and I. Denbratt. *Experimental Investigation of the Effect of Needle Opening (NOP) Pressure on Combustion and Emissions Formation in a Heavy Duty DI Diesel Engine*. SAE Paper 2004-01-2921. Society of Automotive Engineers, 2004

- [60] L. M. Pickett, J. A. Caton, M. P. B. Musculus and A. E. Lutz. *Evaluation of the equivalence ratio-temperature region of diesel soot precursor formation using a two-stage Langrangian model*. International Journal of Engine Research, 7. 349-370, 2006
- [61] N. Ishikawa, Y. Ohkubo and K. Kudou. *Study on the Effects of EGR Cooler Performance on Combustion Properties of the Pre-mixed Compression Ignition Combustion by Multi Cylinder DI Diesel Engine*. SAE Paper 2007-01-1881. Society of Automotive Engineers, 2007
- [62] N. A. Henein, M.-C. Lai, I. Singh, L. Zhong and J. Han. *Characteristics of a Common Rail Diesel Injection System under Pilot and Post Injection Modes*. SAE Paper 2002-01-0218. Society of Automotive Engineers, 2002
- [63] F. Mallamo, M. Badami and F. Millo. *Analysis of Multiple Injection Strategies for the Reduction of Emissions, Noise, and BSFC of a DI CR Small Displacement Non-Road Diesel Engine*. SAE Paper 2002-01-2672. Society of Automotive Engineers, 2002
- [64] M. Badami, F. Mallamo, F. Millo and E. E. Rossi. *Influence if Multiple Injection Strategies on Emissions, Combustion Noise and BSFC of a DI Common Rail Diesel Engine*. SAE Paper 2002-01-0503. Society of Automotive Engineers, 2002
- [65] D. T. Hountalas, D. A. Kouremenos, K. B. Binder, V. Schwarz and G. C. Mavropoulos. *Effect of Injection Pressure on the Performance and Exhaust Emissions of a Heavy Duty DI Diesel Engine*. SAE Paper 2003-01-0340. Society of Automotive Engineers, 2003
- [66] H. Hiroyasu and M. Arai. *Structures of Fuel Sprays in Diesel Engines*. SAE Paper 900475. Society of Automotive Engineers, 1990
- [67] L. M. Pickett and D. L. Siebers. *Non-Sooting, Low Flame Temperature Mixing-Controlled DI Diesel Combustion*. SAE Paper 2004-01-1399. Society of Automotive Engineers, 2004
- [68] Froude Hofmann Website. *Eddy Current Engine Dynamometers*. http://www.froudehofmann.com/product_family_2.htm. Accessed Sept. 2005
- [69] Kistler Website. *Continuous Pressure Monitoring Products*. http://www.kistler.com/gb_en-gb/221_ContinousMonitoring/Continuous-Pressure-Monitoring.html. Accessed Sept. 2005
- [70] Paroscientific, Inc. Website. *Precision Pressure Instrumentation*. www.paroscientific.com. Accessed Sept. 2005
- [71] Micro-Epsilon Website. *Revolution counter for turbochargers*. http://www.micro-epsilon.com/products/custom-designed-sensors/OEM-Automotive/Turbolader_rpm/index.html. Accessed Feb. 2006

- [72] H. W. Lord, W. S. Gatley and H. A. Evensen. *Noise Control for Engineers*. McGraw-Hill Book Company, 1980
- [73] C. Matthews. *IMechE Engineers' Data Book*. Professional Engineering Publishing Ltd, 2nd edition 2000
- [74] S. T. Jones. *Experimental Investigations, Modelling and Control of Direct Injection Gasoline Engines*. Ph.D. thesis, University of Nottingham, 2002
- [75] R. Christian, F. Knopf, A. Jaschek and W. Schindler. *A new method of measuring Filter Smoke Number with increased sensitivity*. MTZ 54, 1993
- [76] T. D. Brooks. *Split-Main Injection Strategies For Diesel Engines And Their Influence On Emissions And Fuel Consumption*. Ph.D. thesis, University of Nottingham, 2005
- [77] M. F. J. Brunt, H. Rai and A. L. Emtage. *The Calculation of Heat Release Energy from Engine Cylinder Pressure Data*. SAE Paper 981052. Society of Automotive Engineers, 1998
- [78] F. Payri, S. Molina, J. Martín and O. Armas. *Influence of measurement errors and estimated parameters on combustion diagnosis*. Applied Thermal Engineering, **26** (2-3). 226-236, 2006
- [79] S. R. Turns. *An Introduction to Combustion: Concepts and Applications*. McGraw-Hill Book Company, 2nd edition 2000
- [80] G. F. C. Rogers and Y. R. Mayhew. *Thermodynamic and Transport Properties of Fluids*. Blackwell Publishers Ltd, 5th edition 1995
- [81] C. Olikara and G. L. Borman. *A Computer Program for Calculating Properties of Equilibrium Combustion Products with Some Applications to I. C. Engines* SAE Paper 750468. Society of Automotive Engineers, 1975
- [82] M. F. J. Brunt and K. C. Platts. *Calculation of Heat Release in Direct Injection Diesel Engines*. SAE Paper 1999-01-0187. Society of Automotive Engineers, 1999
- [83] N. Watson, A. D. Pilley and M. Marzouk. *A Combustion Correlation for Diesel Engine Simulation*. SAE Paper 800029. Society of Automotive Engineers, 1980
- [84] *Acoustics - Measurement of noise emitted by accelerating road vehicles - Engineering method, International Organization for Standardization*. International Organization for Standardization 1998
- [85] J. Affenzeller and A. Rust. *Road Traffic Noise - a Topic for Today and the Future*. VDA - Technical Congress 2005, 2005
- [86] A. Rust. *Noise Technology Status Report: Community Noise Research Strategy Plan*. Coordination of European Research for Advanced Transport Noise Mitigation (CALM), 2003

- [87] C. A. Idicheria and L. M. Pickett. *Soot Formation in Diesel Combustion under High-EGR Conditions*. SAE Paper 2005-01-3834. Society of Automotive Engineers, 2005
- [88] A. Kettlety, Senior NVH Engineer, Ford Motor Company Ltd *Personal Communication*. 2007
- [89] J. D. Irwin and E. R. Graf. *Industrial Noise and Vibration Control*. Prentice-Hall, 1979
- [90] V. Sohm, S.-C. Kong, D. E. Foster, T. Morikawa and M. Iida. *A Computational Investigation into the Cool Flame Region in HCCI Combustion*. SAE Paper 2004-01-0552. Society of Automotive Engineers, 2004
- [91] H. H. Wolfer. *Ignition Lag in Diesel Engines*. VDI-Forschungsheft 392, Translated by Royal Aircraft Establishment, Farnborough Library No. 358, UDC 621-436.047, August 1959, 1938
- [92] D. N. Assanis, Z. S. Filipi, S. B. Fiveland and M. Syrimis. *A Predictive Ignition Delay Correlation under Steady-State and Transient Operation of a Direct Injection Diesel Engine*. ASME Journal of Engineering for Gas Turbines and Power **125** (2). 450-457, 2003
- [93] A. Ormond. *The Influence of Valve Timing and Other Features on the Combustion and Emissions Characteristics of a DISI Engine*. Ph.D. thesis, University of Nottingham, 2007
- [94] A. Vressner, A. Lundin, M. Christensen, P. Tunestal and B. Johansson. *Pressure Oscillations During Rapid HCCI Combustion*. SAE Paper 2003-01-3217. Society of Automotive Engineers, 2003
- [95] K. Y. Cheng, P. J. Shayler and M. Murphey. *The influence of blow-by on indicated work output from a diesel engine under cold start conditions*. Proceedings of the IMECH E Part D Journal of Automobile Engineering, **218** (3). 333-340, 2004
- [96] M. Musculus, T. Lachaux, L. M. Pickett and C. A. Idicheria. *End-of-Injection Over-Mixing and Unburned Hydrocarbon Emissions in Low-Temperature-Combustion Diesel Engines*. SAE Paper 2007-01-0907. Society of Automotive Engineers, 2007
- [97] Ricardo Company Website. *Press Release: Ricardo announces clean diesel technology breakthrough*. <http://www.ricardo.com/media/pressreleases/pressrelease.aspx?page=85>. Accessed Oct. 2008
- [98] Y. Bravo, Y. L. Lázaro and J. J. García-Bernard. *Study of Fouling Phenomena on EGR Coolers Due to Soot Deposits - Development of a Representative Test Method*. SAE Paper 2005-01-1143. Society of Automotive Engineers, 2005

- [99] *The New Jaguar XF Diesel* S. <http://www.jaguar.co.uk/uk/en/latest/news/current/The-new-XF-V6-Diesel-S.htm>. Jaguar UK Website, Accessed Jan. 2009
- [100] R. C. Yu and S. M. Shahed. *Effects of Injection Timing and Exhaust Gas Recirculation on Emissions from a D.I. Diesel Engine*. SAE Paper 811234. Society of Automotive Engineers, 1981
- [101] H. Yun and R. D. Reitz. *Combustion optimization in the low-temperature diesel combustion regime*. International Journal of Engine Research, **6** (513). 2005
- [102] C. Park, S. Kook and C. Bae. *Effects of Multiple Injections in a HSDI Diesel Engine Equipped With Common Rail Injection System*. SAE Paper 2004-01-0127. Society of Automotive Engineers, 2004
- [103] F. Payri, J. Benajes, J. V. Pastor and S. Molina. *Influence of the Post-Injection Pattern on Performance, Soot and NO_x Emissions in a HD Diesel Engine*. SAE Paper 2002-01-0502. Society of Automotive Engineers, 2002
- [104] S. K. Chen. *Simultaneous Reduction of NO_x and Particulate Emissions by Using Multiple Injections in a Small Diesel Engine*. SAE Paper 2000-01-3084. Society of Automotive Engineers, 2000
- [105] P. Eastwood, Y. Hardalupas, T. Morris, A. Taylor, K. Tufail and T. Winstanley. *The effect of multiple fuel-injections on emissions of NO_x and smoke with partially-premixed diesel combustion in a common-rail diesel engine*. IMechE Internal Combustion Engines: Performance, Fuel Economy and Emissions. p285-301, 2007
- [106] G. M. Bianchi, G. Cazzoli, P. Pelloni and F. E. Corcione. *Numerical Study Towards Smokeless and NO_x-less HSDI Diesel Engine Combustion*. SAE Paper 2002-01-1115. Society of Automotive Engineers, 2002
- [107] K. Nishida, J. Gao, T. Manabe and Y. Zhang. *Spray and mixture properties of evaporating fuel spray injected by hole-type direct injection diesel injector* International Journal of Engine Research, **9** (4). 347-360, 2008
- [108] H. Yun, M. Sellnau, N. Milovanovic and S. Zuelch. *Development of Premixed Low-Temperature Diesel Combustion in a HSDI Diesel Engine*. SAE Paper 2008-01-0639. Society of Automotive Engineers, 2008
- [109] H. Yun and R. D. Reitz. *An Experimental Investigation on the Effect of Post-Injection Strategies on Combustion and Emissions in the Low-Temperature Diesel Combustion Regime*. Journal of Engineering for Gas Turbines and Power, **129** (279). 2007
- [110] D. S. Kim and C. S. Lee. *Improved emission characteristics of HCCI engine by various premixed fuels and cooled EGR*. Fuel, **85** (5-6). 695-704, 2006

- [111] R. Bosch. *Diesel-Engine Management Systems and Components*. John Wiley & Sons Ltd, 4th Edition 2005
- [112] W. Zhang, K. Nishida, J. Gao and D. Miura. *An experimental study on flat-wall-impinging spray of microhole nozzles under ultra-high injection pressures* Proceedings of the IMechE Part D Journal of Automobile Engineering, **222** (9). 1731-1741, 2008
- [113] dSPACE GmbH. *High-resolution A/D boards*. http://www.dspaceinc.com/ww/en/inc/home/products/hw/modular_hardware_introduction/i_o_boards/a_d_boards.cfm. Accessed June 2008
- [114] L. J. Spadaccini and J. A. TeVelde. *Auto-Ignition Characteristics of Aircraft-Type Fuel*. Combustion and Flame, **46**. 283-300, 1982
- [115] F. Pischinger, U. Reuter and E. Scheid. *Self-Ignition of Diesel Sprays and its Dependence on Fuel Properties and Injection Parameters*. ASME Journal of Engineering for Gas Turbines and Power, **110**. 399-404, 1988
- [116] Nautica Dehumidifier Website. *Psychrometric Chart*. www.nauticadehumid.com. Accessed Aug. 2007

CHAPTER 1

Euro Stage	Date	Exhaust Emissions (g/km)				
		CO	HC	NO _x	HC+NO _x	PM
I	Jul-92	2.72	-	-	0.97	0.14
II (IDI)	Jan-96	1	-	-	0.7	0.08
II (DI)	Jan-96	1	-	-	0.9	0.1
III	Jan-00	0.64	-	0.50	0.56	0.05
IV	Jan-05	0.50	-	0.25	0.30	0.025
V	Sept-09	0.50	-	0.18	0.23	0.005
VI	Sept-14	0.50	-	0.08	0.17	0.005

Table 1.1: Euro Emission Standards for Diesel Engine Cars [3]

Research	Potential advantages	How they are achieved	Current issues/obstacles
Downsizing	Reductions in fuel consumption	<p>Turbocharging small engines to yield high specific power output at reduced weight.</p> <p>Improved efficiencies afforded by:</p> <ul style="list-style-type: none"> ▪ Lower frictional losses (smaller moving parts) ▪ Reduced pumping losses (smaller swept volume) ▪ Lower heat rejection (reduced internal surface area) 	<ul style="list-style-type: none"> ▪ Knocking ▪ Engine lifespan (higher BMEPs, cylinder wear, mechanical and thermal resistance of components) ▪ Response time of assisted aspiration
Fuel Cell Vehicles (FCV)	<ul style="list-style-type: none"> ▪ Higher efficiency (~50%) compared to internal combustion engines (~30%) [110]. ▪ CO₂ and H₂O only exhaust products 	Fuel cell stacks generate electricity from electrolytic reaction with hydrogen and oxygen to drive an electric motor which replaces I.C. engine	<ul style="list-style-type: none"> ▪ Low energy density of hydrogen ▪ Storage requirements (high pressure tanks) ▪ Lack of re-fuelling infrastructure (~20 hydrogen fuelling stations in USA [111]) ▪ Lower driving range than gasoline or diesel fuelled vehicles.
Biofuels	<ul style="list-style-type: none"> ▪ Reduced dependence on petroleum fuels is beneficial and fuels are renewable ▪ Lower overall CO₂ output compared with contemporary fossil fuels 	Biofuels can be produced from plants which absorb CO ₂ as they grow, offsetting the CO ₂ output from combustion of the fuels.	<ul style="list-style-type: none"> ▪ Formation of acids and solids at high temperature using biodiesel can compromise the working of the fuel system ▪ Wax crystal formation at low temperatures can clog fuel filters. ▪ Energy content of ethanol is lower than that of gasoline (~35% less), limiting vehicle range ▪ E85 bio-ethanol currently 10-25% more expensive than gasoline [111].
Hybrid Technology	Reductions in fuel consumption	Utilising at least two power sources, one of which is commonly a gasoline or diesel powered engine	<ul style="list-style-type: none"> ▪ Cost and weight of suitable batteries for onboard storage of electricity ▪ CO₂ saving of the vehicle needs to be offset against the source of electricity generation [111].

Table 1.2: Alternatives to Diesel Engines and Future Research Focus

CHAPTER 3

Component(s)	Specification
Engine	Twin-turbo V6 DI Diesel
Bore x Stroke	81.0 x 88.0 mm
Connecting rod length	160 mm
Displacement	2720 cc
Compression ratio	17.3:1
Piston	Cast aluminium bowl design, double wave gallery cooling
Fuel Injection Equipment	HPCR (max. 1650 bar), $\Phi 140\mu\text{m}$ x 6-hole piezoelectric injectors. Micro sac nozzle. 156° cone angle

Table 3.1: Test Engine Specification

Analyser	Type	Gas	Ranges	Accuracy	Span
3000HM	FID	THC	0-4, 10, 40, 100, 1000, 4000, 10000 ppm	$\pm 1\%$ range or ± 0.2 ppm whichever is greater	2970 ppm
4000VM	CLD	NO/NO _x	0-4, 10, 40, 100, 1000, 4000, 10000 ppm	$\pm 1\%$ range or ± 0.2 ppm whichever is greater	985 ppm
7100M	GFC	CO	0-5, 10, 20 %	$\pm 1\%$ range or ± 0.5 ppm whichever is greater	1.006%
7200M	GFC	CO ₂	0-5, 10, 20 %	$\pm 1\%$ range or ± 0.5 ppm whichever is greater	10.06%
8000M	PARA	O ₂	0-5, 10, 25 %	$\pm 0.01\%$ O ₂ repeatability	20.83%
LEGEND					
FID	Heated flame ionisation device with cylindrical collector, flame detector, igniter				
CLD	Chemiluminescent reaction of NO and O ₃ , with photomultiplier sensor				
GFC	Gas filter correlation, non dispersive infra-red with solid state detector				
PARA	Paramagnetic oxygen sensor				

Table 3.2: Specifications of the Exhaust Gas Analysers and span gas for calibration

Board	Channels	A/D converters	Resolution	Sample time (2 channels)	Sample time (all channels)
DS 2001	5 in	5	Up to 16 bit	5.0 μs (16 bit)	5.0 μs (16 bit)
DS 2003	32 in	2	Up to 16 bit	5.7 μs (16 bit)	72.5 μs (16 bit)

Table 3.3: dSPACE high resolution A/D board specifications [113]

CHAPTER 4

		Convert Emissions to				
		Molar fraction %, ppm (\tilde{x}_i)	Gravimetric fraction kg/kg-exh (x_i)	Mass flow rate kg/hr (\dot{m}_i)	Brake specific kg/kWh (BS_i)	Emissions Index kg/kg-fuel (EI_i)
Convert Emissions from	Molar fraction %, ppm (\tilde{x}_i)	1	$\times \left(\frac{\tilde{m}_i}{\tilde{m}_{exh}} \right)$	$\times \left(\frac{\tilde{m}_i \cdot \dot{m}_{exh}}{\tilde{m}_{exh}} \right)$	$\times \left(\frac{\tilde{m}_i \cdot \dot{m}_{exh}}{\tilde{m}_{exh} \cdot P_b} \right)$	$\times \left(\frac{\tilde{m}_i \cdot \dot{m}_{exh}}{\tilde{m}_{exh} \cdot \dot{m}_f} \right)$
	Gravimetric fraction kg/kg-exh (x_i)	$\times \left(\frac{\tilde{m}_{exh}}{\tilde{m}_i} \right)$	1	$\times (\dot{m}_{exh})$	$\times \left(\frac{\dot{m}_{exh}}{P_b} \right)$	$\times \left(\frac{\dot{m}_{exh}}{\dot{m}_f} \right)$
	Mass flow rate kg/hr (\dot{m}_i)	$\times \left(\frac{\tilde{m}_{exh}}{\dot{m}_{exh} \cdot \tilde{m}_i} \right)$	$\times \left(\frac{1}{\dot{m}_{exh}} \right)$	1	$\times \left(\frac{1}{P_b} \right)$	$\times \left(\frac{1}{\dot{m}_f} \right)$
	Brake specific kg/kWh (BS_i)	$\times \left(\frac{P_b \cdot \tilde{m}_{exh}}{\dot{m}_{exh} \cdot \tilde{m}_i} \right)$	$\times \left(\frac{P_b}{\dot{m}_{exh}} \right)$	$\times (P_b)$	1	$\times \left(\frac{P_b}{\dot{m}_f} \right)$
	Emission Index kg/kg-fuel (EI_i)	$\times \left(\frac{\dot{m}_f \cdot \tilde{m}_{exh}}{\dot{m}_{exh} \cdot \tilde{m}_i} \right)$	$\times \left(\frac{\dot{m}_f}{\dot{m}_{exh}} \right)$	$\times (\dot{m}_f)$	$\times \left(\frac{\dot{m}_f}{P_b} \right)$	1

Table 4.1: Conversion table for emissions species

		Unit				
		\tilde{x}_i	x_i	\dot{m}_i	bs_i	EI_i
Species, i	HC	227 ppm	329 mg/kg exh	7.2 mg/s	2.5 g/kWh	8.1 g/kg fuel
	CO	0.21%	1.5 g/kg exh	33 mg/s	11.3 g/kWh	37 g/kg fuel

Table 4.2: Example unit conversion values from a typical operating point

	Process
1-2	Polytropic compression from intake conditions
2-3	Constant volume combustion processes
3-4	Polytropic expansion from EOC conditions
4-1	Isochoric exhaust

Table 4.3: Summary of processes modelled in calculation of bulk-gas temperature

	Value
a1	-9.1063
a2	246.97
a3	-143.74
a4	32.329
a5	0.0518

Table 4.4: Coefficients for calculation of molar heat capacity of diesel fuel

CHAPTER 5

Study	Ref	Fuel	Equipment	A	n	E_A / \tilde{R}
Wolfer	[91]	CN>50	Constant-volume bomb	0.44	1.19	8360
Watson	[83]	Diesel	Diesel engine	3.45	1.02	2100
Spadaccini	[114]	No. 2 Diesel	Steady flow reactor	4.0E-10	1	20080
Pischinger	[115]	CN=50	Steady flow reactor	0.0081	1.14	7813
Assanis	[92]	No. 2D CN=40	Diesel engine	2.4	1.02	2100
Kook	[13]	CN=47.1	Diesel engine	12.254	1	3242

Table 5.1: Summary of empirical constants employed in ignition delay correlations with diesel fuels

Constant	A	n	f	E_A / \tilde{R}	Equation	R ²
n=1.00, f=1.00	115	1.00	1.00	1692	y=0.990x	0.936
E_A / \tilde{R} =2100	85	0.95	0.70	2100	y=0.996x	0.895
n=1.02	240	1.02	0.85	1450	y=1.007x	0.948
Unconstrained	484	1.10	0.85	1400	y=1.002x	0.957

Table 5.2: Results of least-squares regression on equation constants for Ignition delay correlation

CHAPTER 6

		Engine Speed (rpm)				
		700	1000	1500	2000	2500
Brake Load (Nm)	0	✓	x	x	x	x
	50	x	✓	✓	✓	✓
	100	x	✓	✓	✓	✓
	150	x	✓	✓	✓	✓
	200	x	x	✓	1800 rpm	✓

Table 6.1: Test matrix for baseline engine performance. Ticks where test condition carried out, crosses where condition not carried out

Parameter	No tests	Mean	Standard Deviation	CoV (%)	Percentage minimum	Percentage maximum
Engine speed (rpm)	37	1500.7	0.53	0.0	-0.1	+0.1
Engine BMEP (bar)	37	2.33	0.04	1.7	-0.05	+0.04
Inlet pressure (bar)	37	1.007	0.01	1.0	-2.1	+2.5
Air intake temp. (°C)	37	23.3	2.6	11.0	-35.6	+16.0
Fuel flow (kg/hr)	37	2.42	0.046	1.9	-6.1	+4.7
AFR	37	24.4	0.78	3.2	-5.2	+5.7
Fuel rail pressure (MPa)	37	54.0	0.46	0.9	-0.0	+0.0
bsfc (kg/kWh)	37	0.308	0.00	1.4	-3.3	+2.2
Oil temperature (°C)	37	98.9	1.5	1.5	-5.3	+1.5
Fuel Temperature (°C)	37	15.9	3.0	18.7	-44.5	+28.7
Exhaust port temp. (°C)	37	212.6	5.6	2.6	-5.5	+7.0
IMEP gross (bar)	37	3.73	0.08	2.0	-0.05	+0.05
IMEP net (bar)	37	3.55	0.10	2.7	-0.06	+0.05
Smoke (FSN)	30	1.43	0.23	15.8	-24.3	+54.1
NO _x (ppm)	30	33.8	5.1	15.5	-35.6	+37.1
HC (ppm C3)	30	161	16.3	10.1	-19.5	+17.4
CO (%)	30	0.12	0.02	14.9	-20.3	+41.6
EGR, wet (%)	30	44.5	2.4	5.3	-10.5	+8.3
Combustion Noise (dBA)	37	84.3	0.8	0.9	-3.5	+1.1

Table 6.2: Standard Test Point data variations

CHAPTER 8

	Fuel Pressure (bar)	Soot	NO _x	HC	CO	Noise	bsfc
Case A 1500 rpm 6.8 mg 60% EGR	550	-42%	+130%	+54%	+50%	-1.1 dB	+15%
	700	-73%	+49%	+47%	+55%	-1.6 dB	+22%
	900	-96%	+148%	+43%	+39%	+0.5 dB	+32%
Case B 1800 rpm 9.7 mg 48% EGR	800	-88%	-3%	+6%	-41%	+1.5 dB	+6%
	1000	-95%	+14%	+12%	-36%	+1.0 dB	+12%
	1200	-95%	+41%	+14%	-30%	+1.7 dB	+16%

Table 8.1: Summary of fuel rail pressure effects relative to baseline data for lowest bsfc

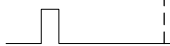





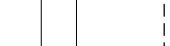

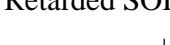
Strategy	EGR	$P_{Fuel\ Rail}$	bsfc	NO _x	Soot	CO	HC	Noise
Pilot + Main (conventional) 	Low	Base	-	↓	↑↑	-	↓↓	-
Pilot + Main (increased EGR) 	Highest	Base	↑↑	↓↓	-	↑↑	↑↑	↓↓
	High	Base	-	↓	↑↑	-	↓↓	-
Pilot + Main + Post (optimal soot reduction) 	High	Base	↑	↓↓	↑↑	↑↑	↑↑	-
	Low	Base	-	↓	↓	↑	-	-
Single Main Most Advanced SOI 	Highest	Base	-	↓↓	↑	↑	↓	↑↑
	High	Base	-	↑↑	↓↓	↓↓	↓	↑↑
	Low	Base	-	↑↑	↓↓	↓↓	↓↓	↑↑
Single Main Advanced SOI (min. bsfc) 	Highest	Base	-	↓↓	↑↑	↑↑	↓	↑↑
	High	Base	↓	-	↓	↓	↓↓	↑↑
	Low	Base	-	↑↑	↓	↓	↓↓	↑↑
Single Main Retarded SOI 	Highest	Base	↑↑	↓↓	↓↓	↑↑	↑↑	↓↓
	High	Base	↑↑	↓↓	↓↓	↑↑	↑↑	↓↓
	Low	Base	↑	↓	↓↓	↑↑	↑↑	-
Single Main Most Advanced SOI 	High	Highest	↑↑	↓↓	↓↓	↓	↓	↑↑
	High	High	↑	↓↓	↓↓	↓	↓	↑↑
Single Main Advanced SOI (min. bsfc) 	High	Highest	↑	↓↓	↓↓	↑	↓	↑↑
	High	High	↑	↓↓	↓	↑↑	↓	↑↑
Single Main Retarded SOI 	High	Highest	↑↑	↓↓	↓↓	↑↑	↑↑	↓↓
	High	High	↑↑	↓↓	↓↓	↑↑	↑↑	↓↓
LEGEND								
Response		bsfc kg/kWh	NO _x , Soot, CO, HC g/kg fuel			Noise (85) dB(A)		
↑↑	Unacceptable penalty	>+15%	>+50%			>+5		
↑	Increased penalty	+5% to +15%	+10% to +50%			+2.5 to +5		
-	Baseline	-5% to +5%	-10% to +10%			-2.5 to +2.5		
↓	Improvement	-15% to -5%	-50% to -10%			-5 to -2.5		
↓↓	Significant improvement	<-15%	<-50%			<-5		

Table 8.2: Summary of strategy responses for 1800 rpm 9.7 mg total fuel delivery. Representative injection strategy sketches shown in strategy column







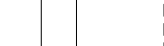

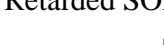
Strategy	EGR	$P_{Fuel\ Rail}$	bsfc	NO _x	Soot	CO	HC	Noise
Pilot + Main (conventional) 	Low	Base	-	↓	↑↑	↑↑	↑	↓
Pilot + Main (increased EGR) 	Highest	Base						
	High	Base						
Pilot + Main + Post (optimal soot reduction) 	High	Base						
	Low	Base						
Single Main Most Advanced SOI 	High	Base	-	↓↓	↓↓	↑	↓	↑↑
	Low	Base	↑↑	↑↑	↓↓	-	↓	↑
Single Main Advanced SOI (min. bsfc) 	High	Base	↓	↓↓	-	↑↑	↓	-
	Low	Base	-	↑	↓↓	↑	↓	↑
Single Main Retarded SOI 	High	Base	↑↑	↓↓	↓↓	↑↑	↑↑	↓↓
	Low	Base	↑↑	↓↓	↓↓	↑↑	↑↑	↓↓
Single Main Most Advanced SOI 	High	Highest	↑↑	↓↓	↓↓	↑↑	↑	-
	High	High	↑↑	↓↓	↓↓	↑↑	↑	-
Single Main Advanced SOI (min. bsfc) 	High	Highest	↑↑	↓↓	↓↓	↑↑	↑	-
	High	High	↑↑	↓↓	↓↓	↑↑	↑↑	-
Single Main Retarded SOI 	High	Highest	↑↑	↓↓	↓↓	↑↑	↑↑	↓↓
	High	High	↑↑	↓↓	↓↓	↑↑	↑↑	↓↓
LEGEND								
Response		bsfc kg/kWh	NO _x , Soot, CO, HC g/kg fuel			Noise (85) dB(A)		
↑↑	Unacceptable penalty	>+15%	>+50%			>+5		
↑	Increased penalty	+5% to +15%	+10% to +50%			+2.5 to +5		
-	Baseline	-5% to +5%	-10% to +10%			-2.5 to +2.5		
↓	Improvement	-15% to -5%	-50% to -10%			-5 to -2.5		
↓↓	Significant improvement	<-15%	<-50%			<-5		

Table 8.3: Summary of strategy responses for 1500 rpm 6.8 mg total fuel delivery. Representative injection strategy sketches shown in strategy column

CHAPTER 1

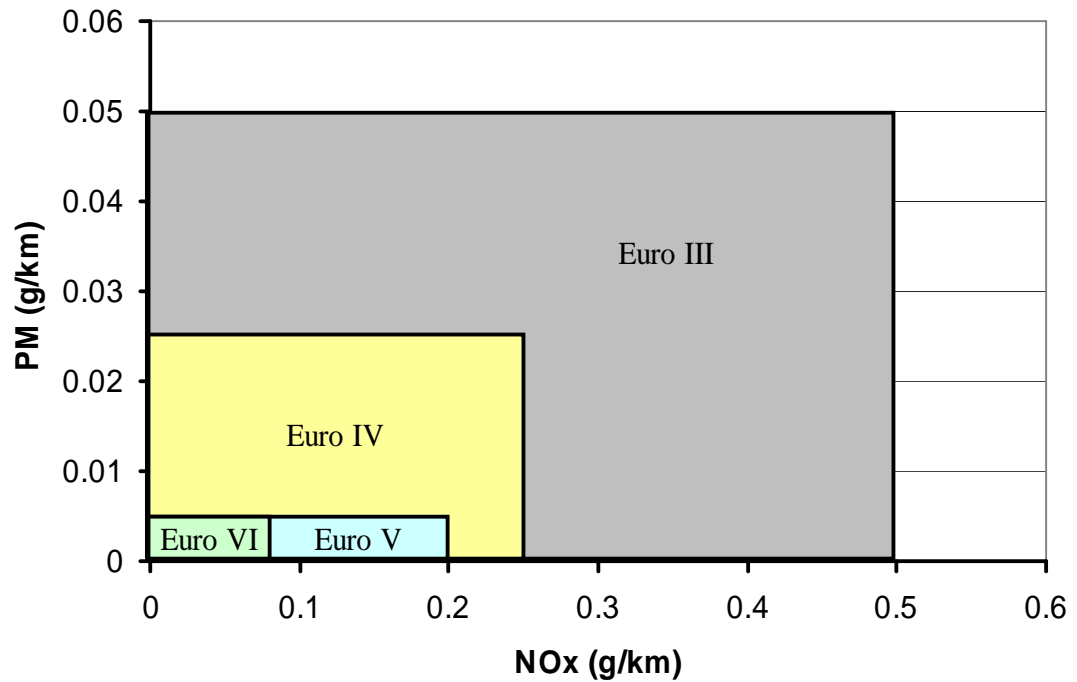


Figure 1.1: Euro Stage Limits for PM and NO_x emissions [3]

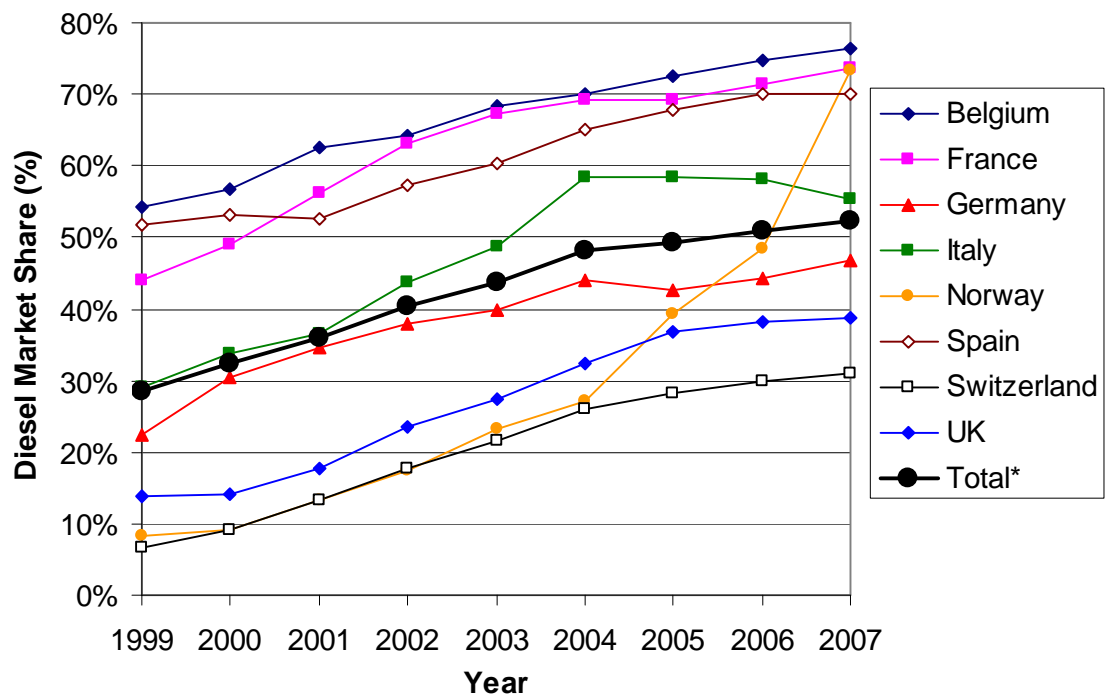


Figure 1.2: Western Europe Diesel Car Market Share, 1999-2007 [7]

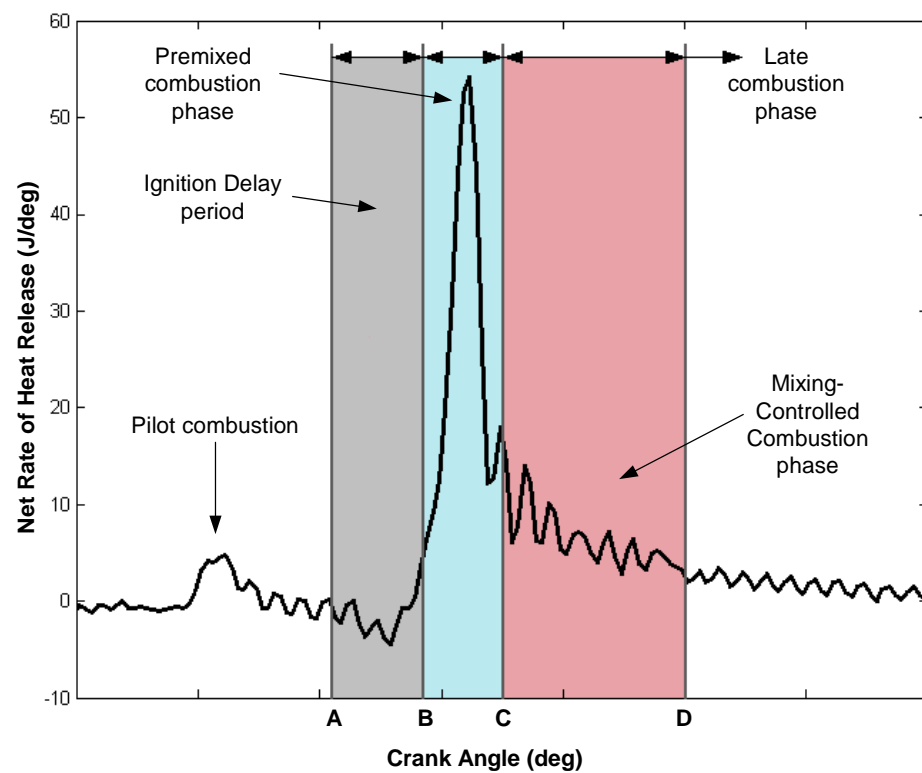


Figure 1.3: Heat Release diagram showing diesel combustion phases for a conventional pilot and main injection strategy

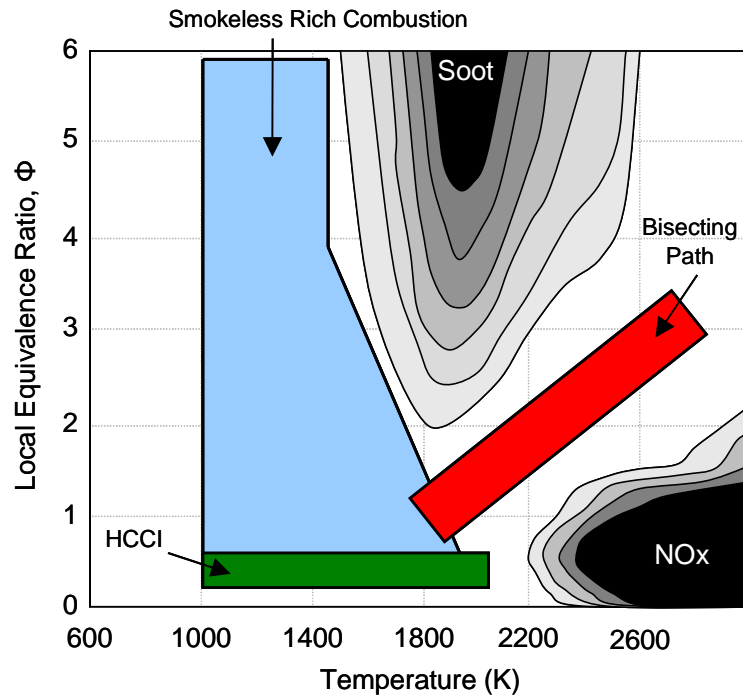


Figure 1.4: Soot and NO_x formation in the Φ -T plane with simplified regions of interest, reproduced from [12]

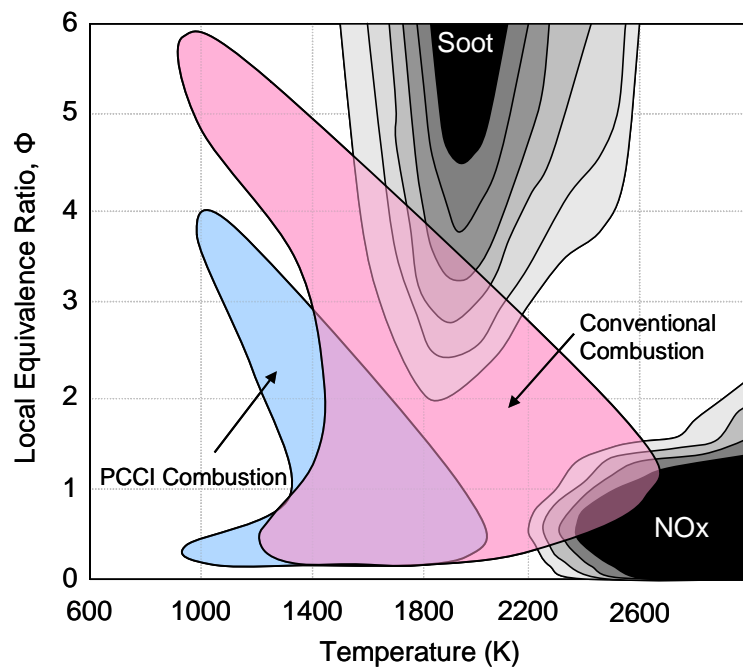


Figure 1.5: Φ -T map indicating simplified regions where conventional diesel and PCCI combustion occur, reproduced from [18]. Diagram shows the effect of increasing EGR and increasing fuel-air premixing to achieve PCCI combustion

CHAPTER 2

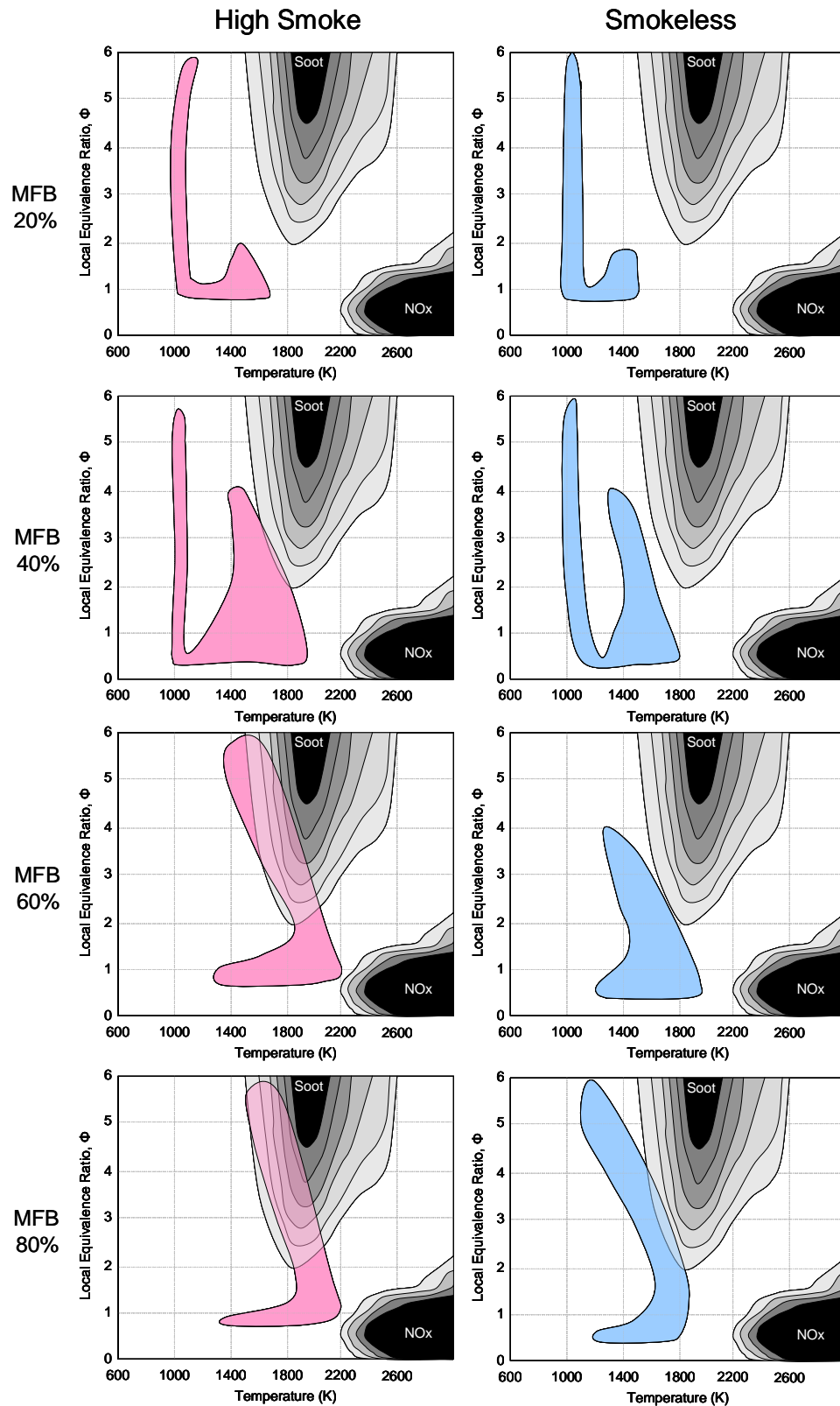


Figure 2.1: Time histories of Φ and T conditions for high and low smoke cases for Mass Fraction Burned from 20% (top) to 80% (bottom). Shaded areas represent Φ and T condition of gas cells from 3D-CFD calculation, reproduced from [12]

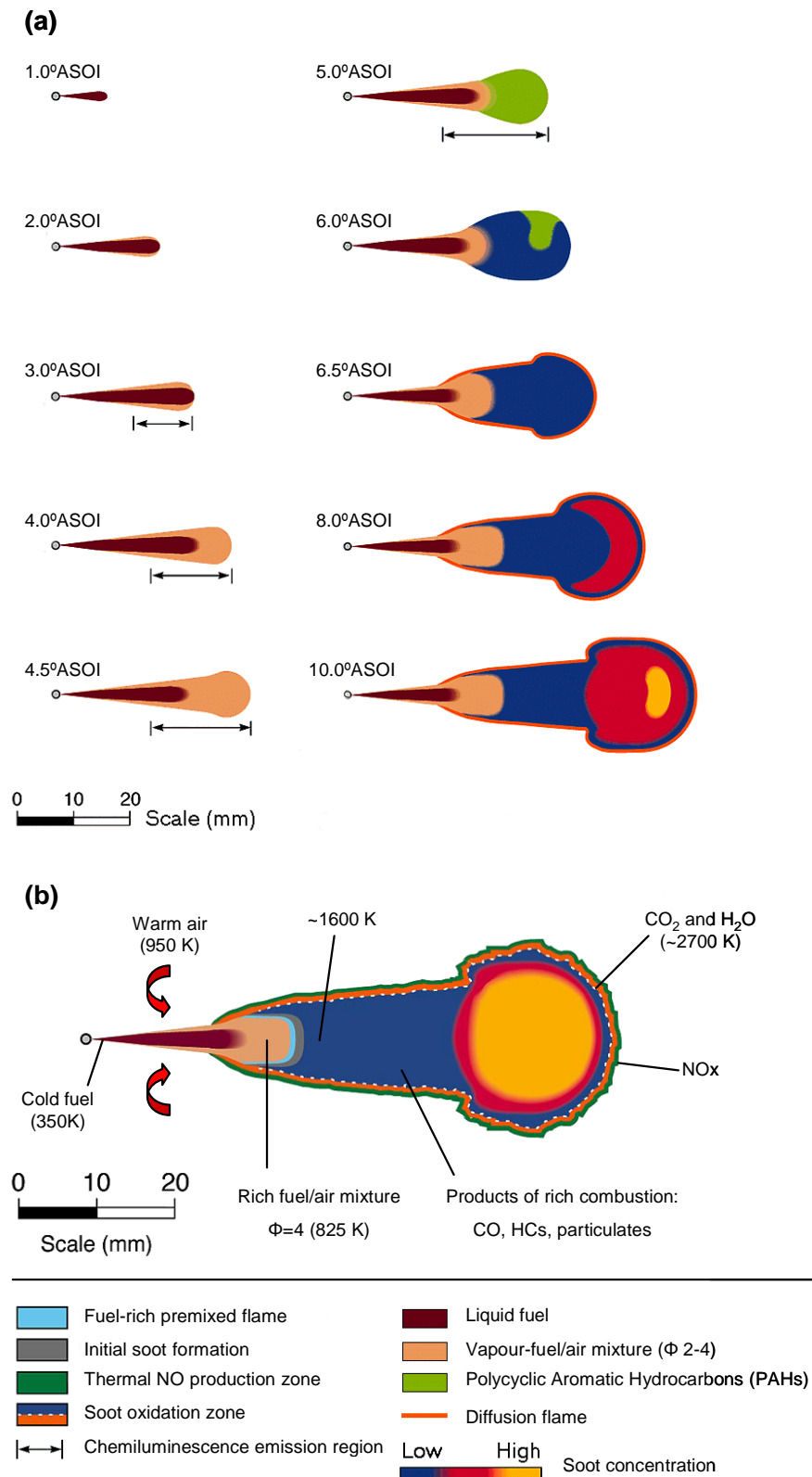


Figure 2.2: Conceptual model of DI diesel combustion during the first part of MCC [28] (figure reproduced from [29]). (a) Schematics of temporal sequence during early stages of MCC. (b) Quasi-steady burning jet representative of remainder of MCC.

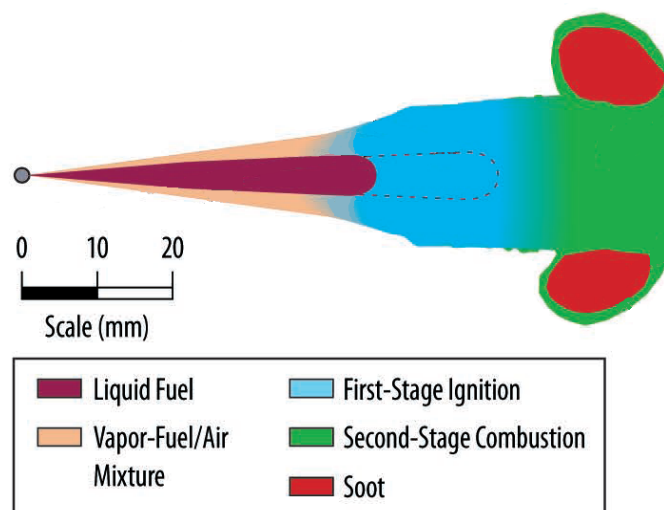


Figure 2.3: Conceptual model for early-injection Low Temperature (PCCI) Combustion [16]

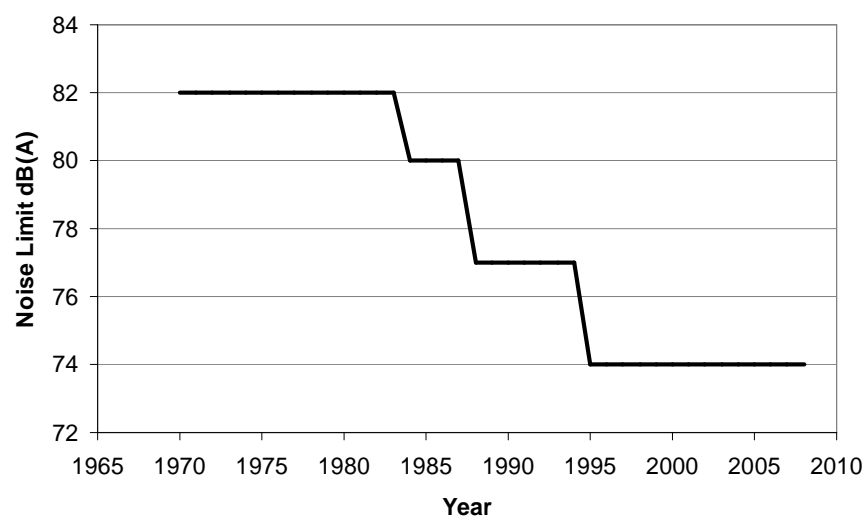


Figure 2.4: Vehicle noise limits as dictated by EU Directives through the period 1970-2008 [46]

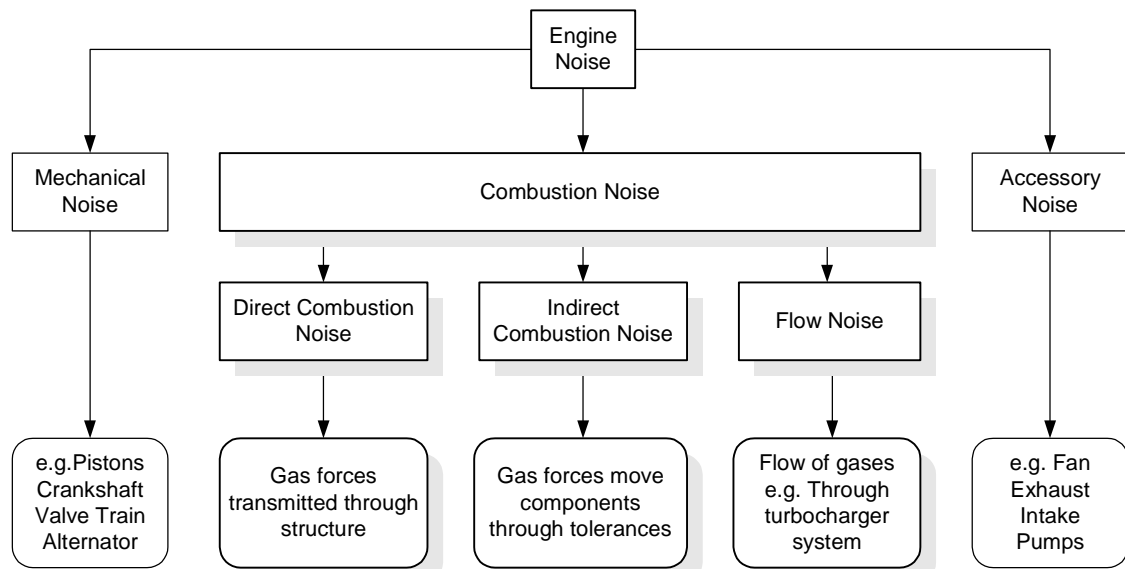


Figure 2.5: Sources of Engine Noise

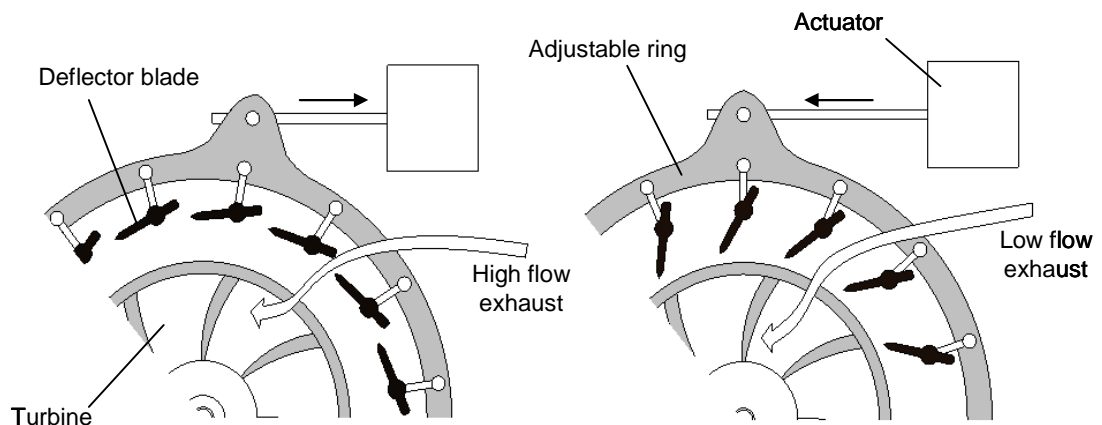


Figure 2.6: Schematic of Variable Geometry Turbine Turbocharger operation. Left: Blades set for high turbocharger pressure. Right: Blades set for low turbocharger pressure. Reproduced from [6]

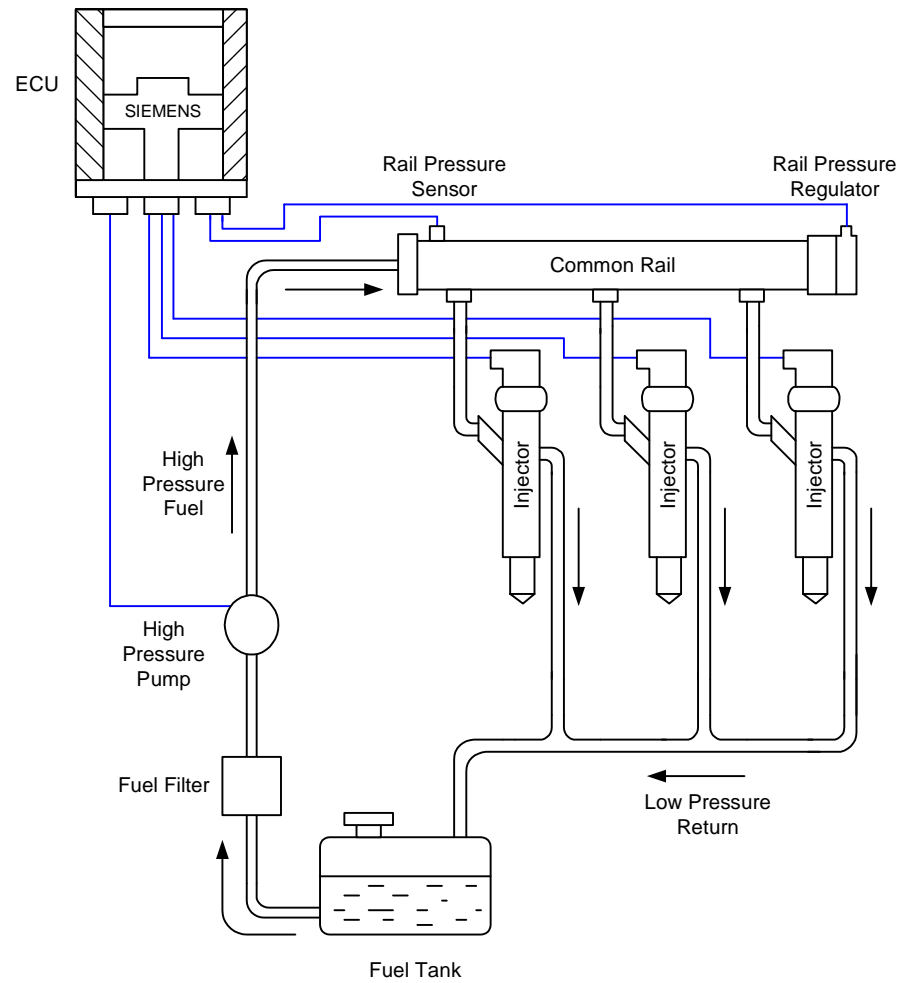


Figure 2.7: Schematic of simple HPCR Fuel Injection System

CHAPTER 3

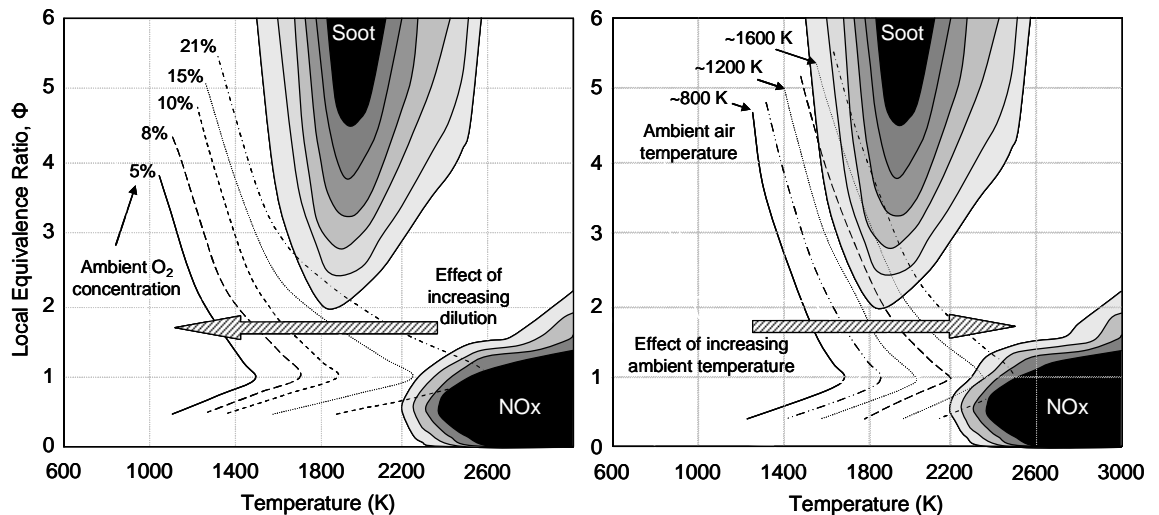


Figure 3.1: Representative Φ - T diagrams illustrating the maximum achievable temperature for complete combustion at the specified equivalence ratio. Left: For a fuel element mixed to equilibrium with the ambient air initially at 1000 K for varying ambient oxygen concentrations. Right: For jet core with 10% ambient oxygen concentration for varying initial ambient temperatures. Figure adapted from Refs [13, 67] and [60].

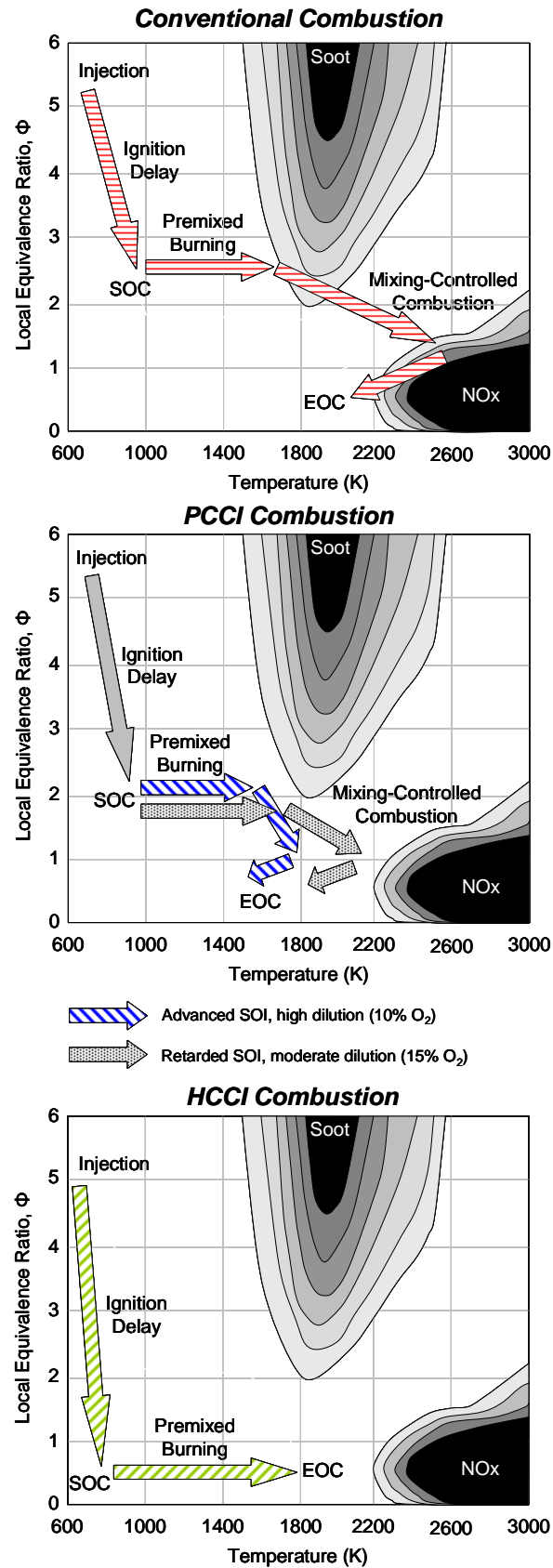


Figure 3.2: Qualitative representation of proposed paths taken by typical fuel parcels in the Φ -T plane during combustion for different combustion strategies. Diagram adapted from figure within [13].

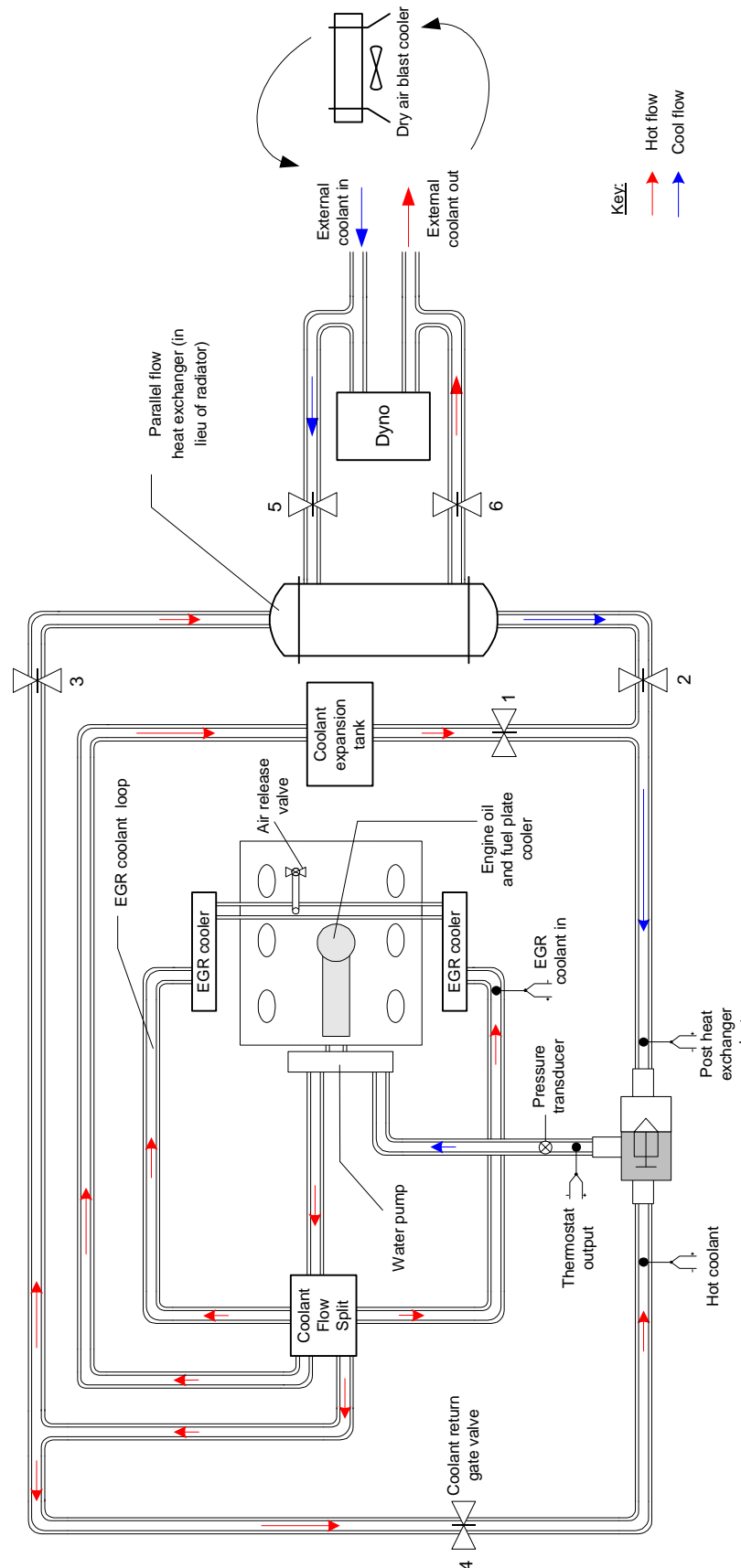


Figure 3.3: Schematic of the engine cooling system. The flow directions and relative temperatures are labelled for fully warm operation (not to scale)

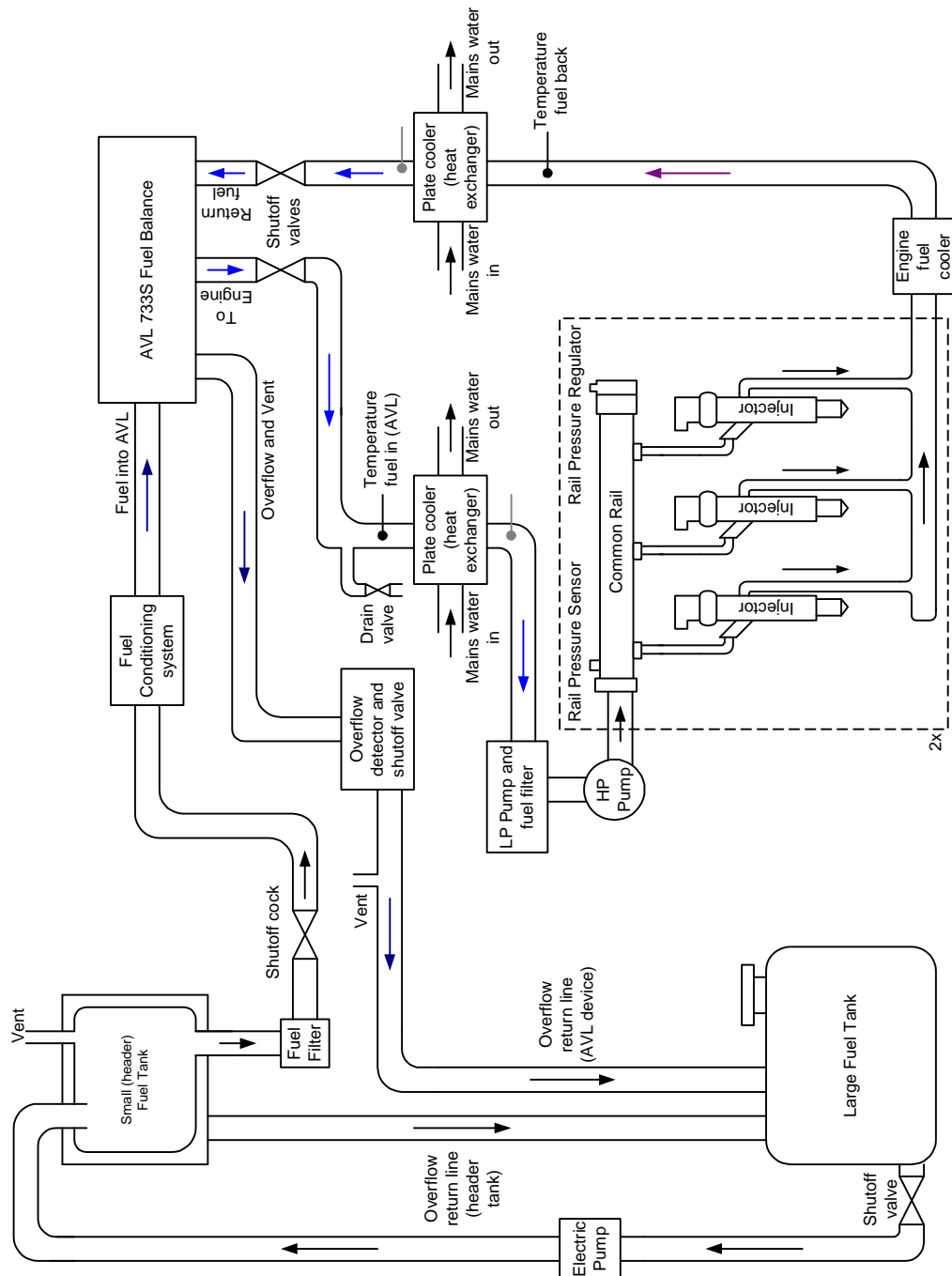


Figure 3.4: Schematic of the test rig fuel circuit (not to scale)

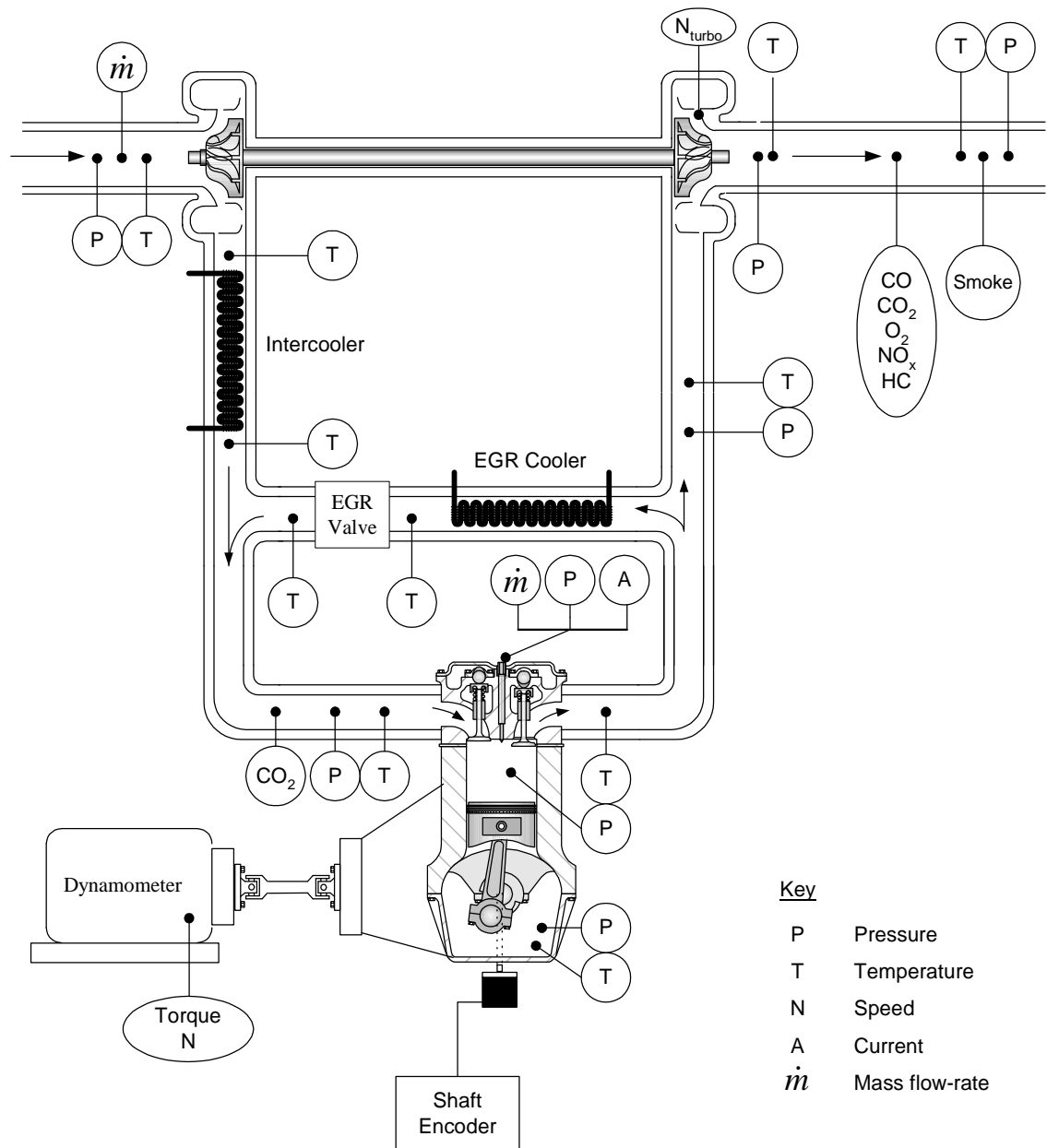


Figure 3.5: Schematic of sensor locations in the experimental setup (not to scale)

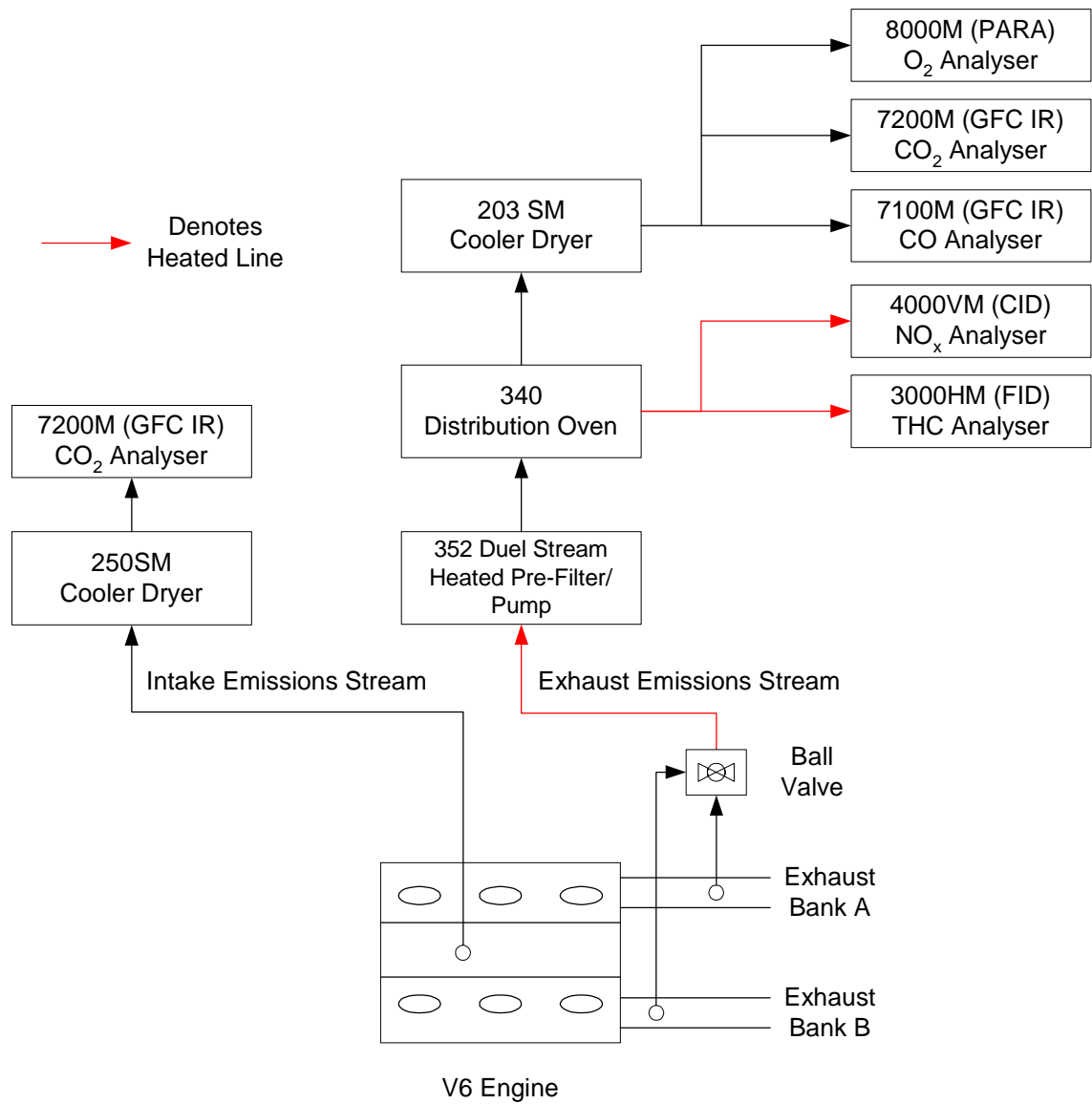


Figure 3.6: Schematic of the exhaust gas emissions analysers setup

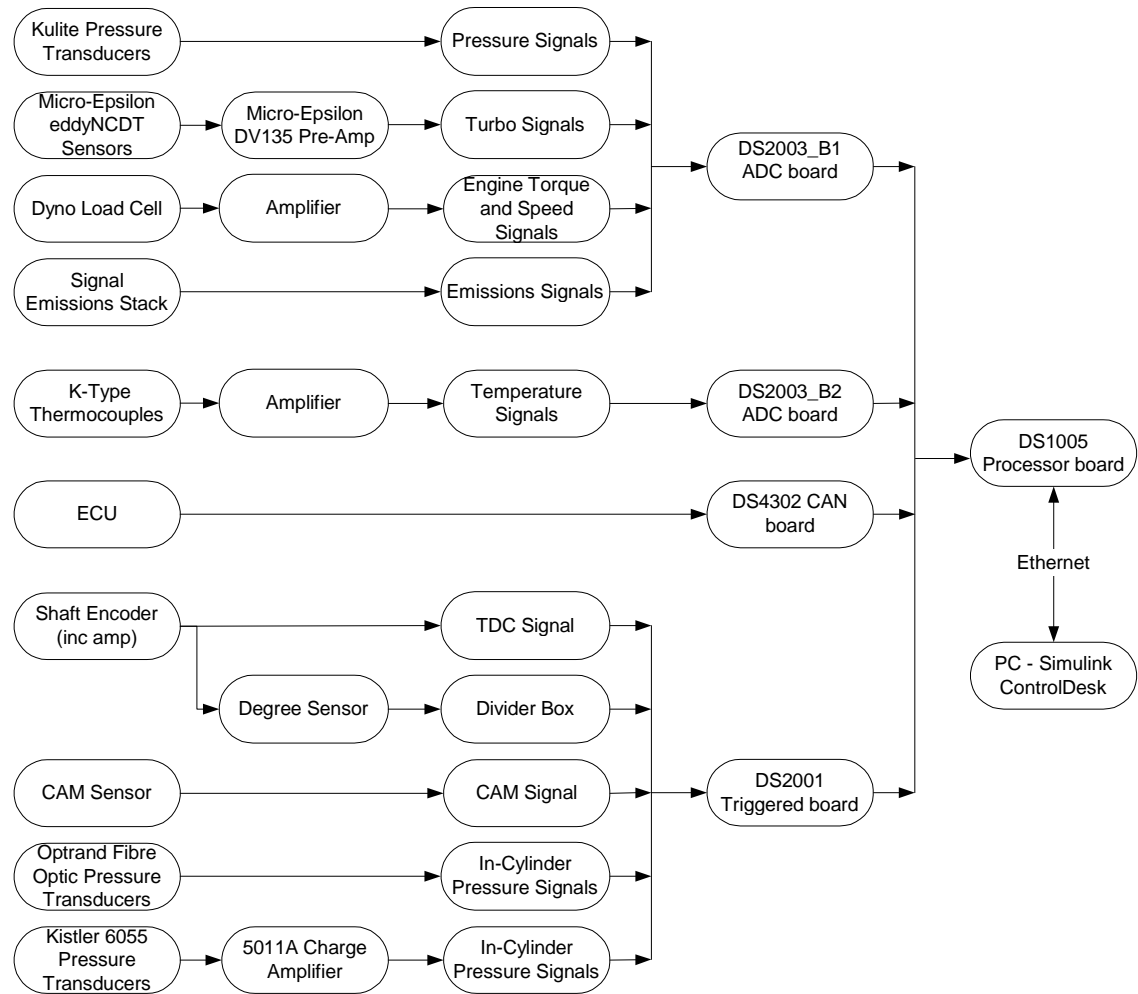


Figure 3.7: Schematic of inputs and outputs in the dSPACE data acquisition system

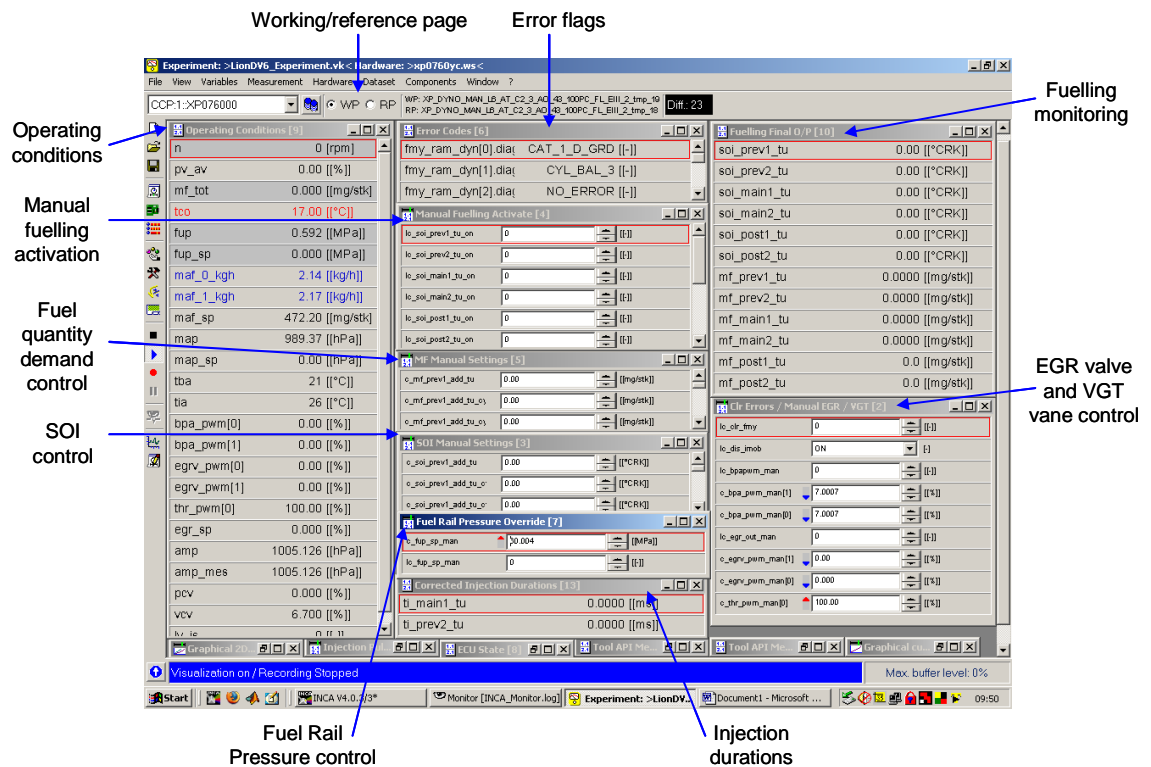


Figure 3.8: Screenshot of INCA user interface for control over ECU

CHAPTER 4

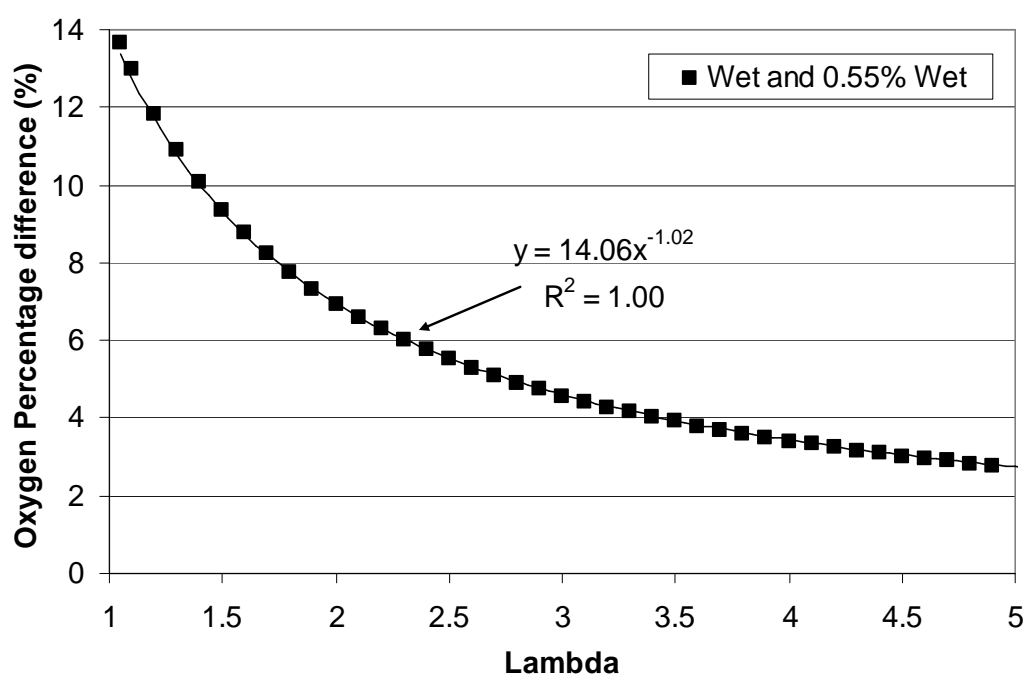


Figure 4.1: Oxygen percentage difference against excess air (λ) to convert from dry to wet measurement

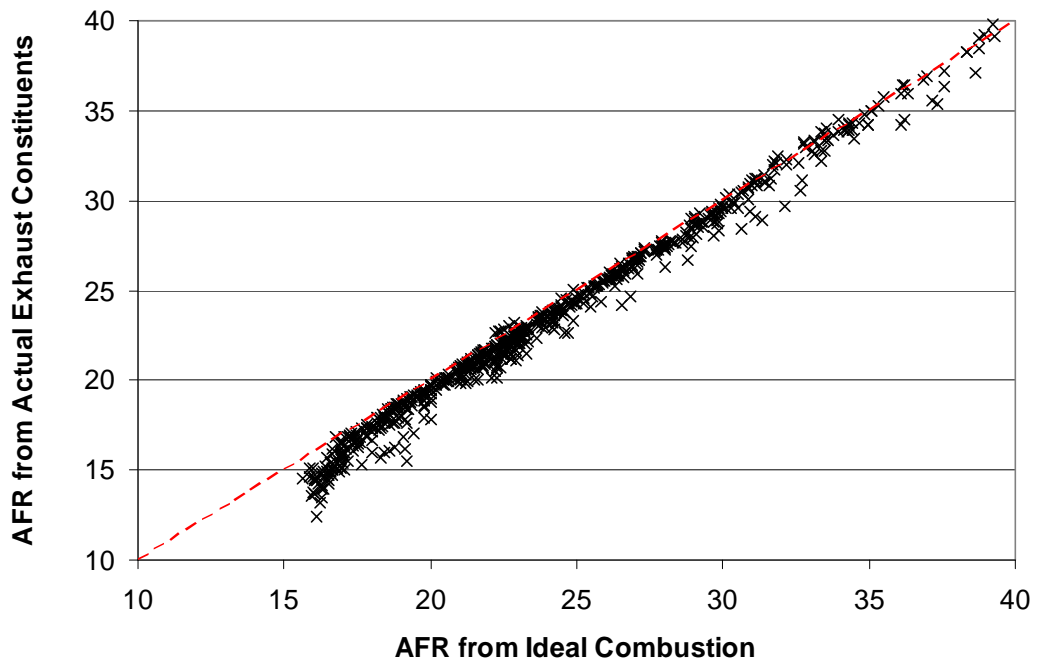


Figure 4.2: Difference in AFR determined from oxygen balances using actual exhaust constituents (Equation 4.10) and ideal constituents (Equation 4.7). Red dashed line denotes $x=y$

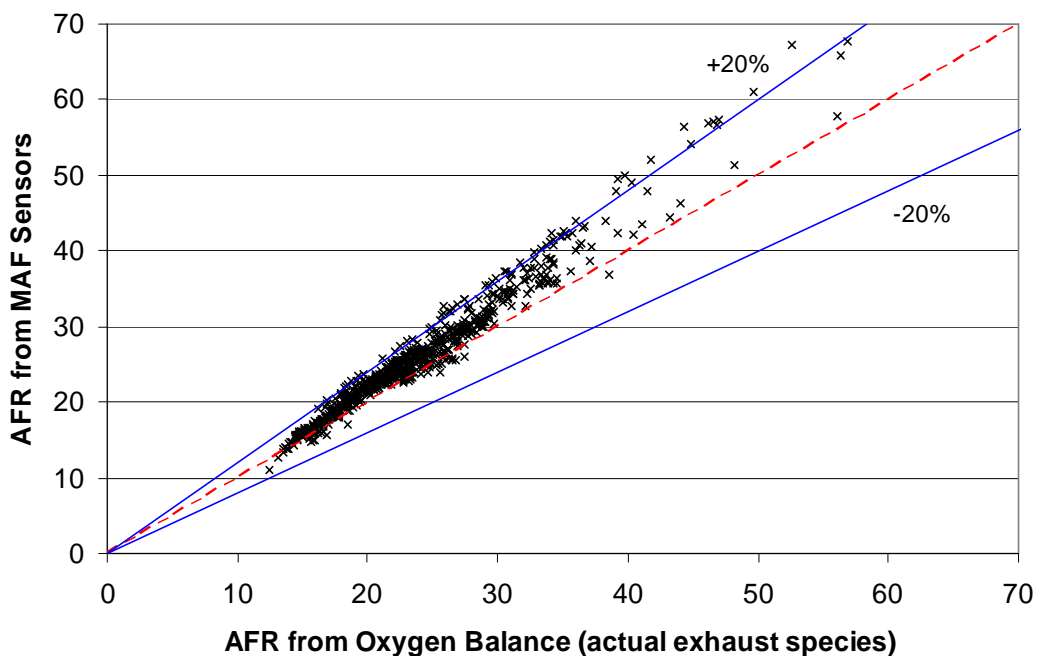


Figure 4.3: Comparison of AFR obtained from the MAF sensors and the oxygen balance calculation based on actual exhaust composition. Red dashed line denotes $x=y$, blue lines are $\pm 20\%$ variation

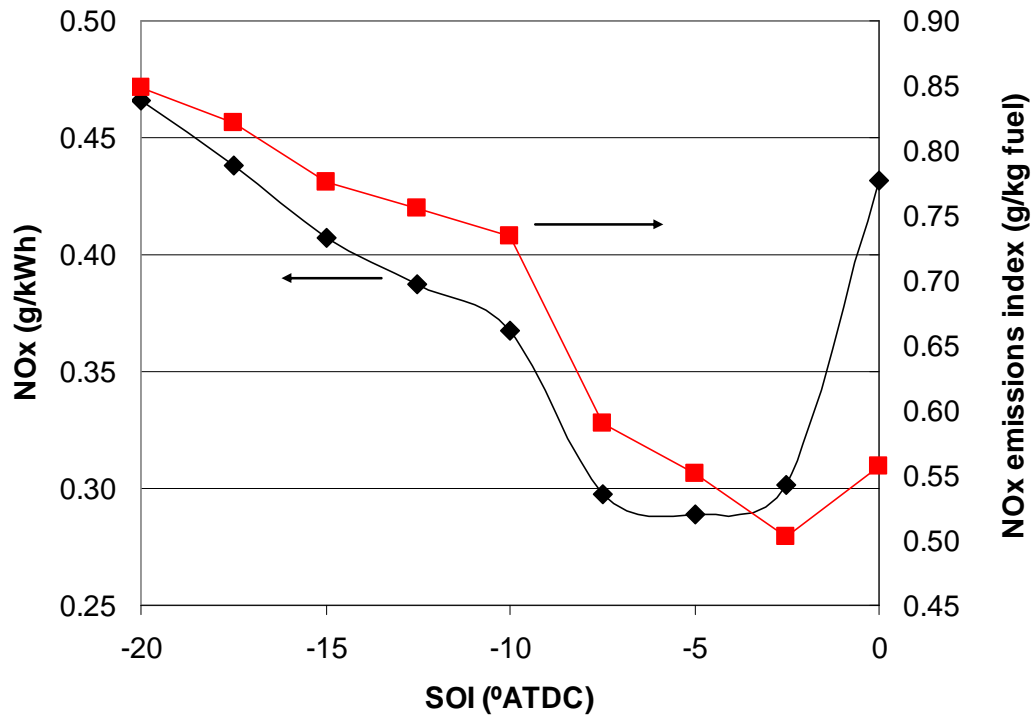


Figure 4.4: Comparison of NO_x data displayed in brake specific units and as an emissions index

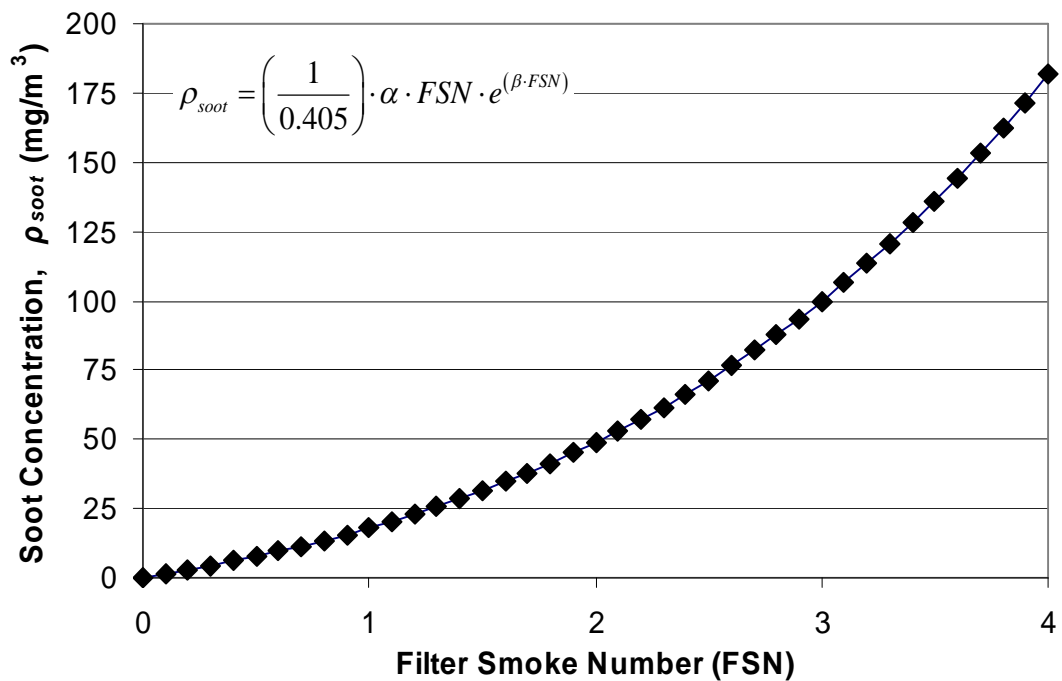


Figure 4.5: Soot concentration in the exhaust as a function of FSN as described by the embedded equation where $\alpha=5.32$ and $\beta=0.31$ [75]

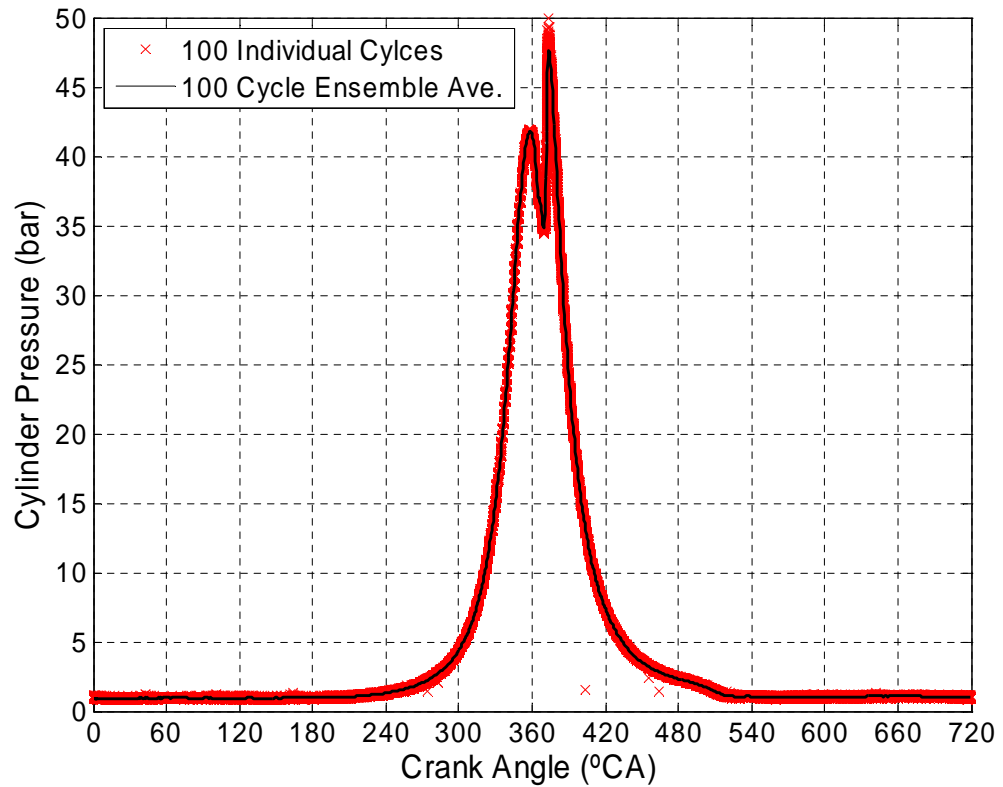


Figure 4.6: Example of 100 individual consecutive cycles (red crosses) after filtering noise spikes and corresponding ensemble-averaged data of the 100 cycles (black line). Data at 1000 rpm 10.2 mg/stk/cyl fuelling SOI -3.0°ATDC, 45% EGR, 1200 bar fuel rail pressure.

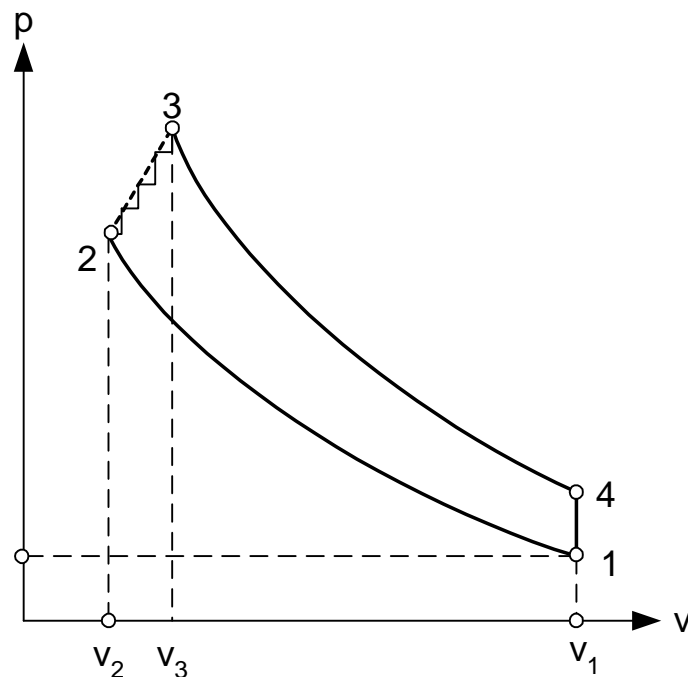


Figure 4.7: Idealised p - V indicator diagram to illustrate processes undergone during the cycle

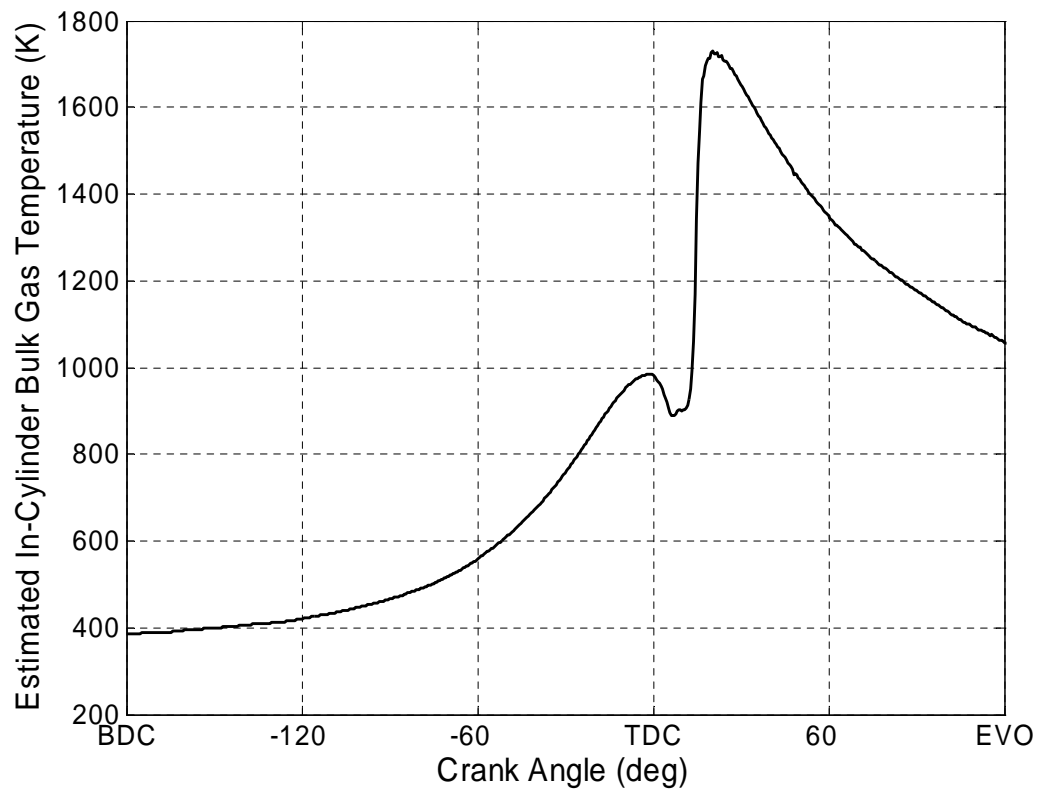


Figure 4.8: Example of variation bulk-gas temperature during the closed part of the cycle

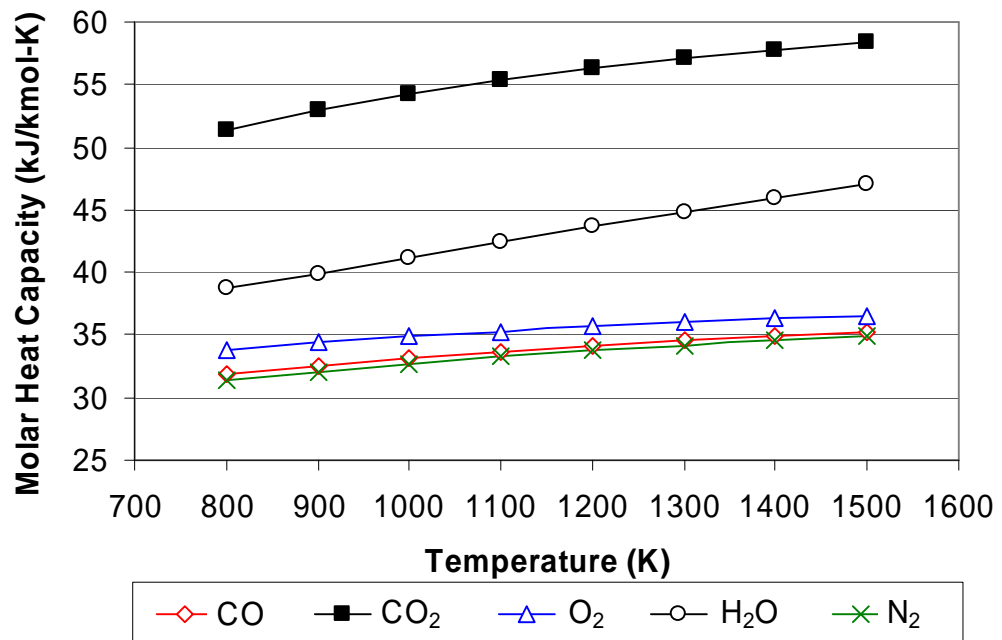


Figure 4.9: Molar heat capacities for standard reference state as a function of temperature. Data obtained from [80]

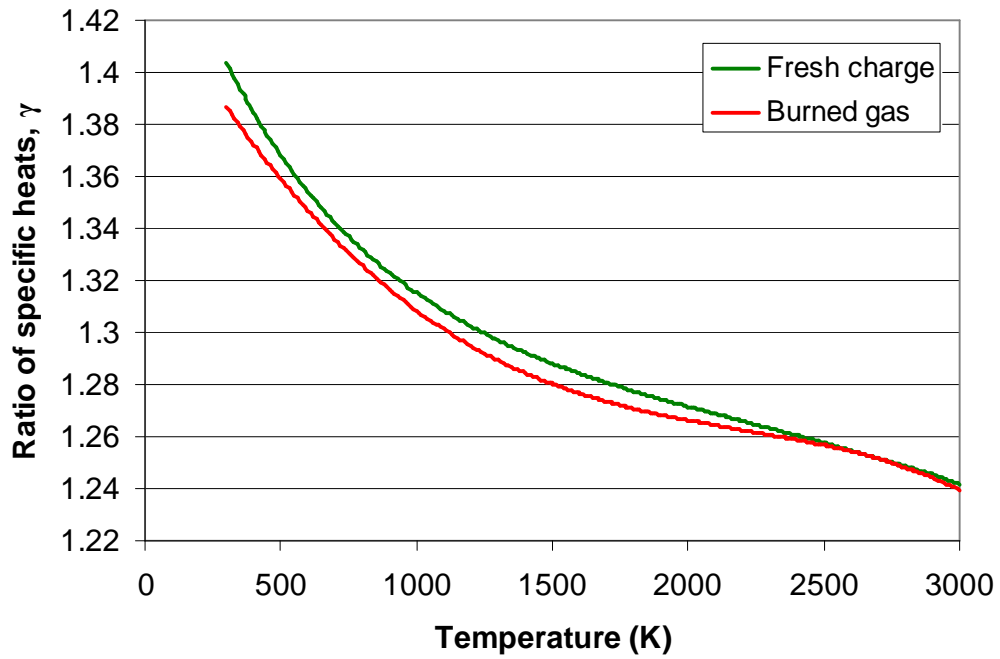


Figure 4.10: Ratio of specific heats as a function of temperature for fresh air and burned gas. Example data at 1800 rpm 10 mg, SOI -1°ATDC single injection, EGR 42%, 3 bar BMEP.

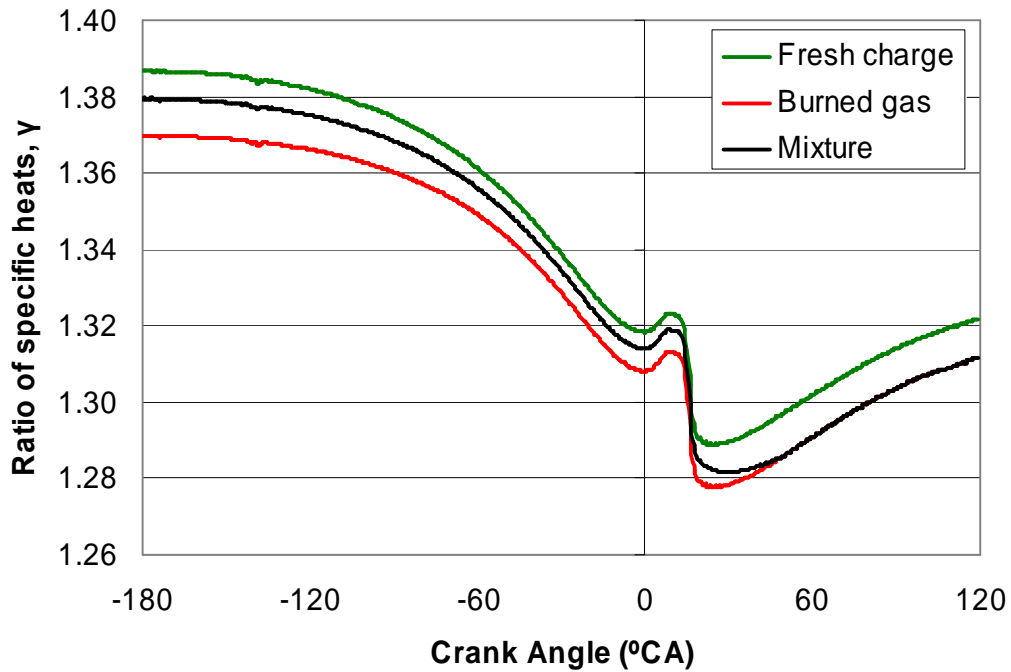


Figure 4.11: Variation of ratio of specific heats for fresh charge, burned gas, and the mixture composition against crank angle. Data at 1800 rpm 10 mg, SOI -1°ATDC single injection, EGR 42%, 3 bar BMEP

CHAPTER 5

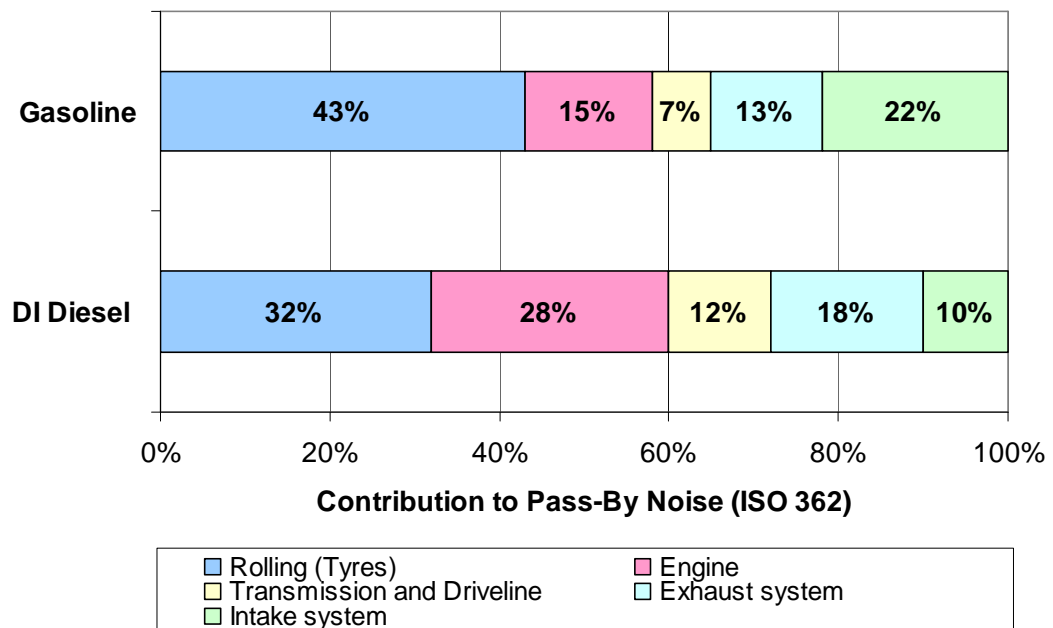


Figure 5.1: Contributions to overall pass-by noise for passenger vehicles under current legislative limits (ISO362), reproduced from [85]

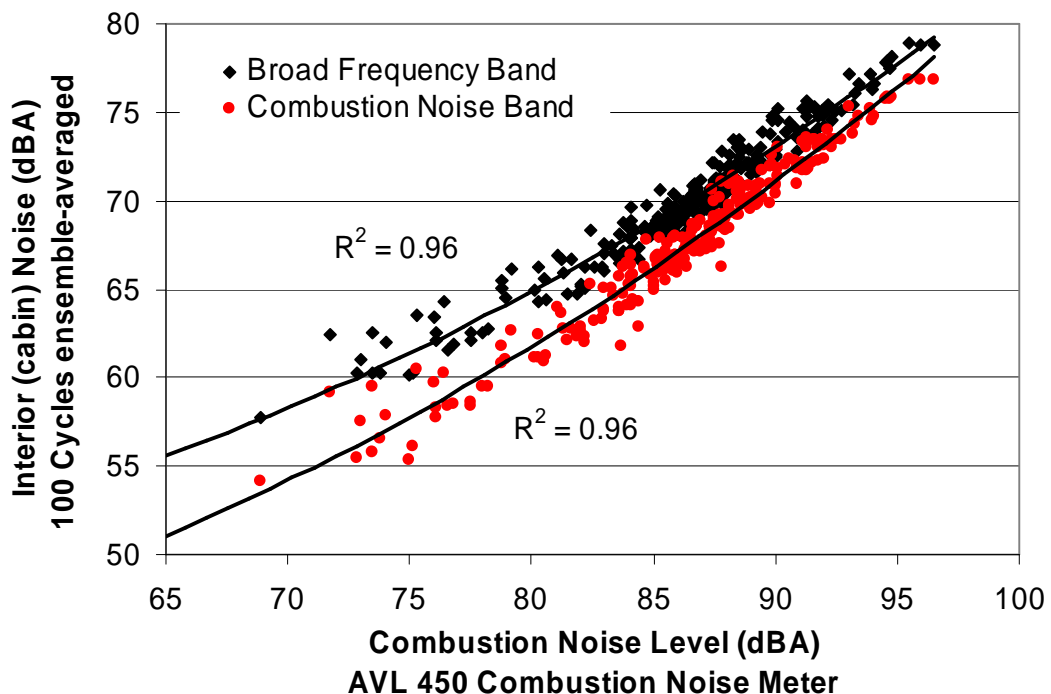


Figure 5.2: Relationship between combustion noise and vehicle interior noise (data at 1500 and 1800 rpm)

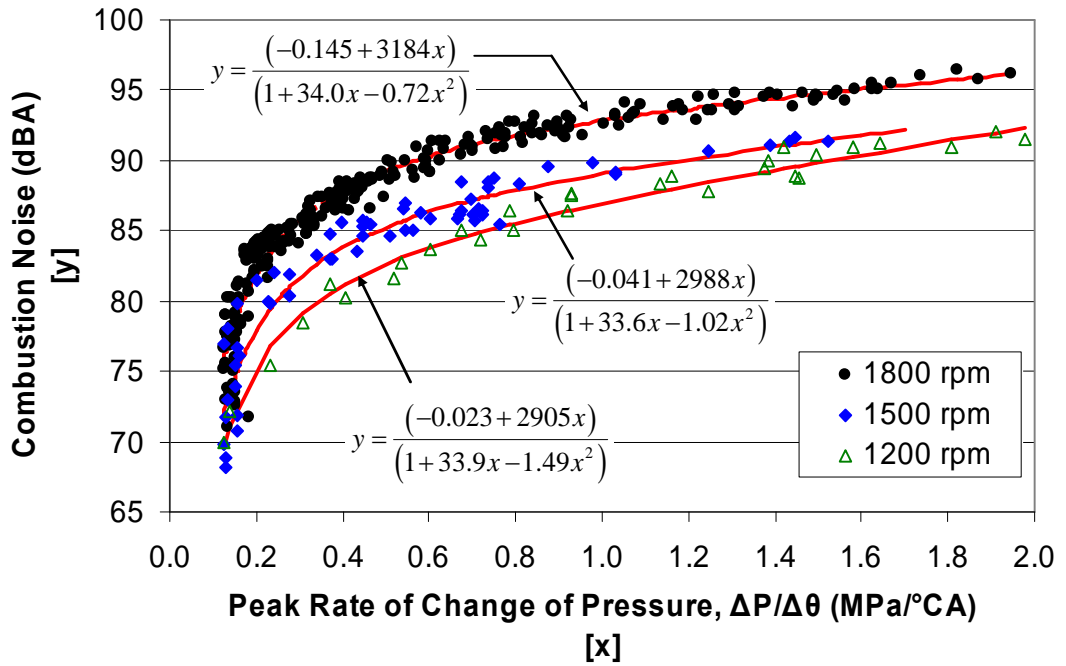


Figure 5.3: Relationship between peak rate of change of in-cylinder pressure in MPa/°CA and combustion noise at 1200 rpm, 1500 rpm, and 1800 rpm. Various fuel injection quantities, SOIs, and EGR rates.

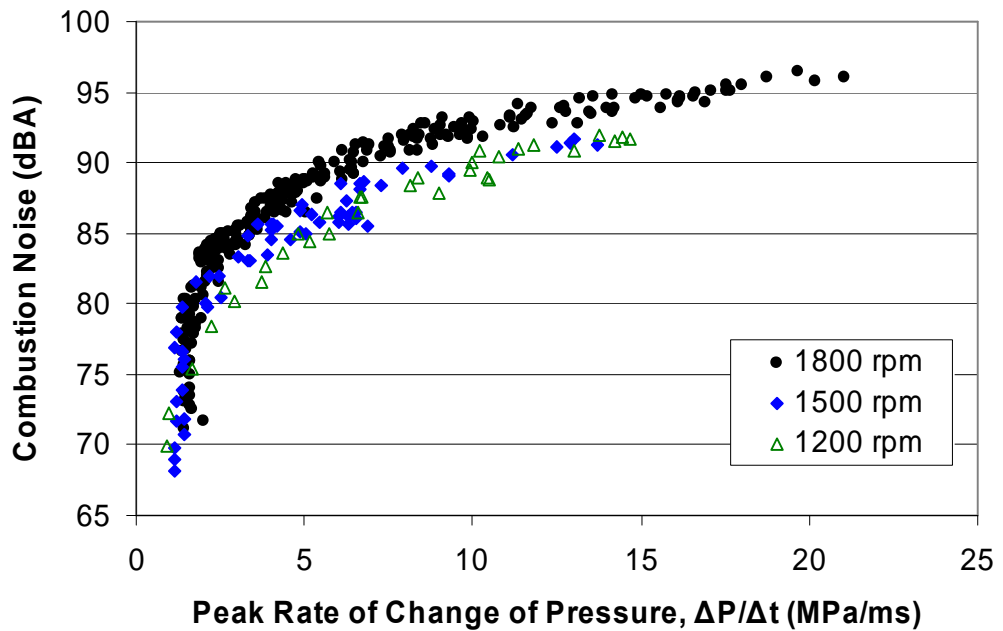


Figure 5.4: Relationship between peak rate of change of in-cylinder pressure in MPa/ms and combustion noise at 1200 rpm, 1500 rpm, and 1800 rpm. Various fuel injection quantities, SOIs, and EGR rates.

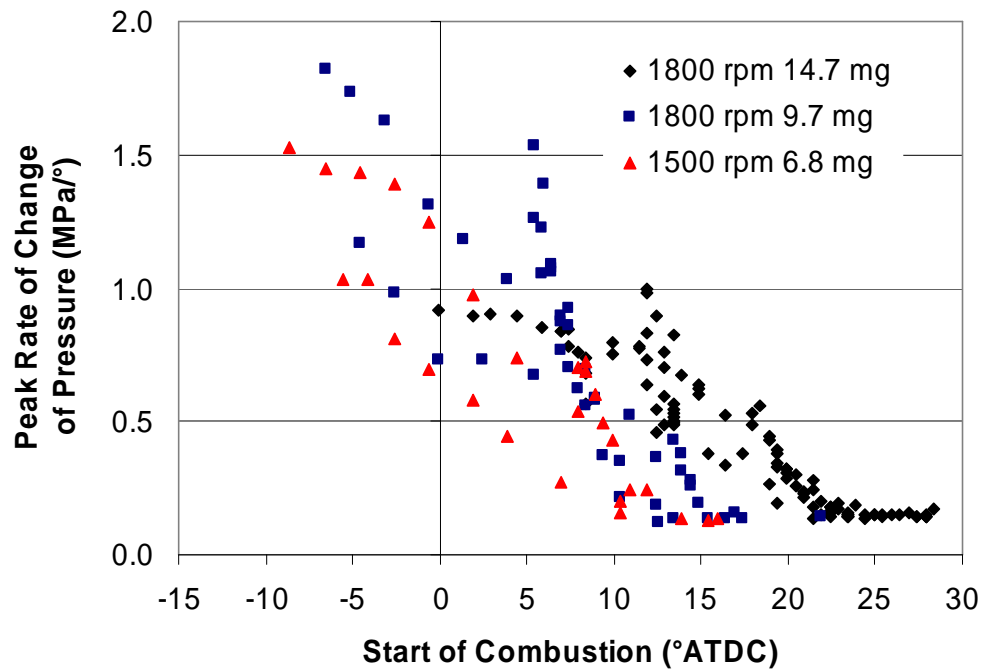


Figure 5.5: Dependence of maximum rate of change of in-cylinder pressure on start of combustion location

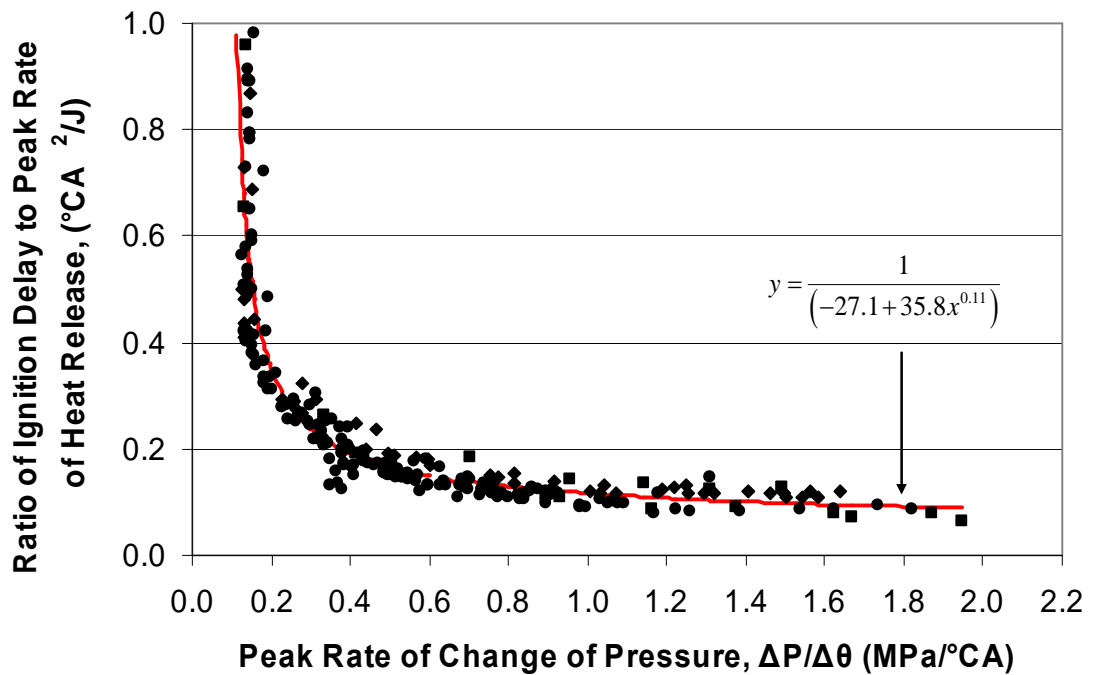


Figure 5.6: Relationship between peak rate of change of in-cylinder pressure and ratio of ignition delay to peak rate of net heat release. Labelled is the non-linear regression model fitted to the data

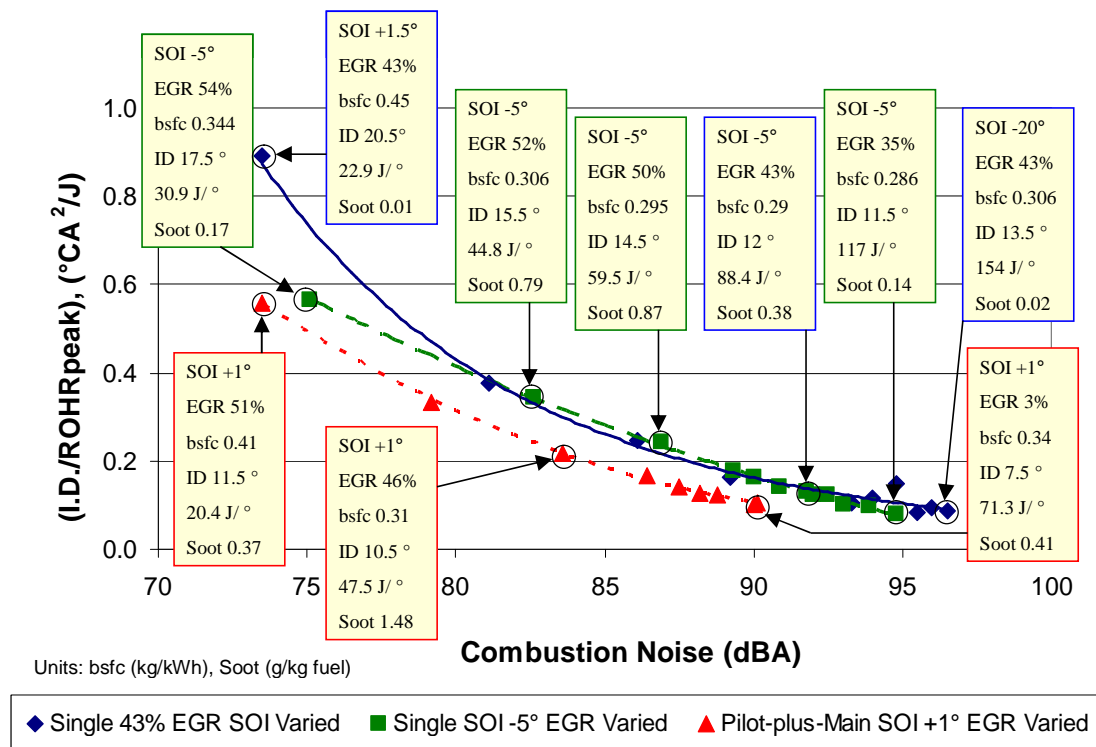


Figure 5.7: Ratio of ignition delay to peak rate of net heat release against combustion noise at 1800 rpm 9.7 mg/stk/cyl 600 bar fuel rail pressure

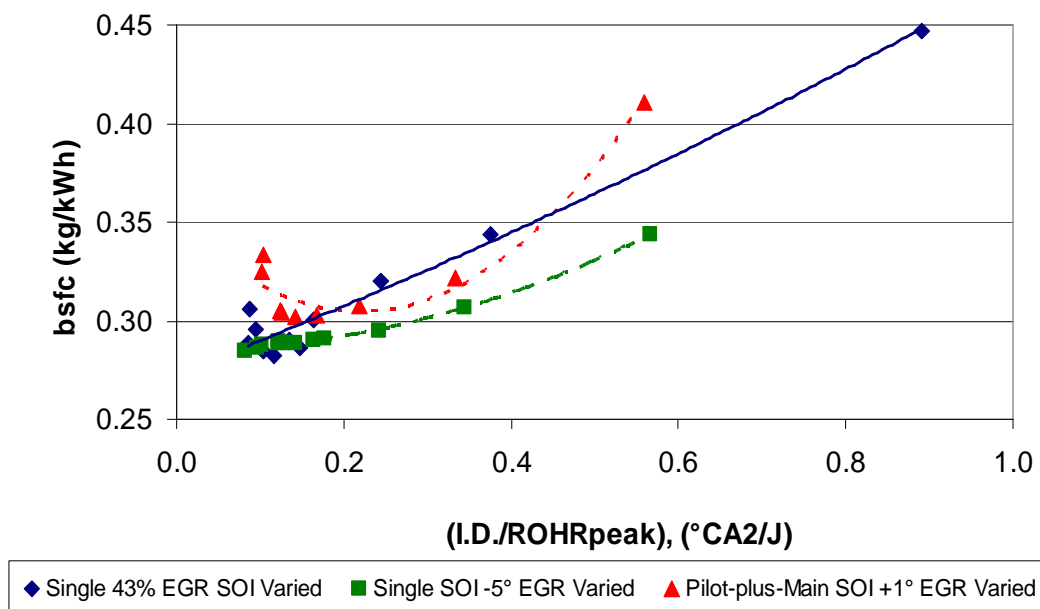


Figure 5.8: Relationship between ratio of ignition delay to peak rate of heat release and bsfc at 1800 rpm 9.7 mg/stk/cyl 600 bar fuel rail pressure

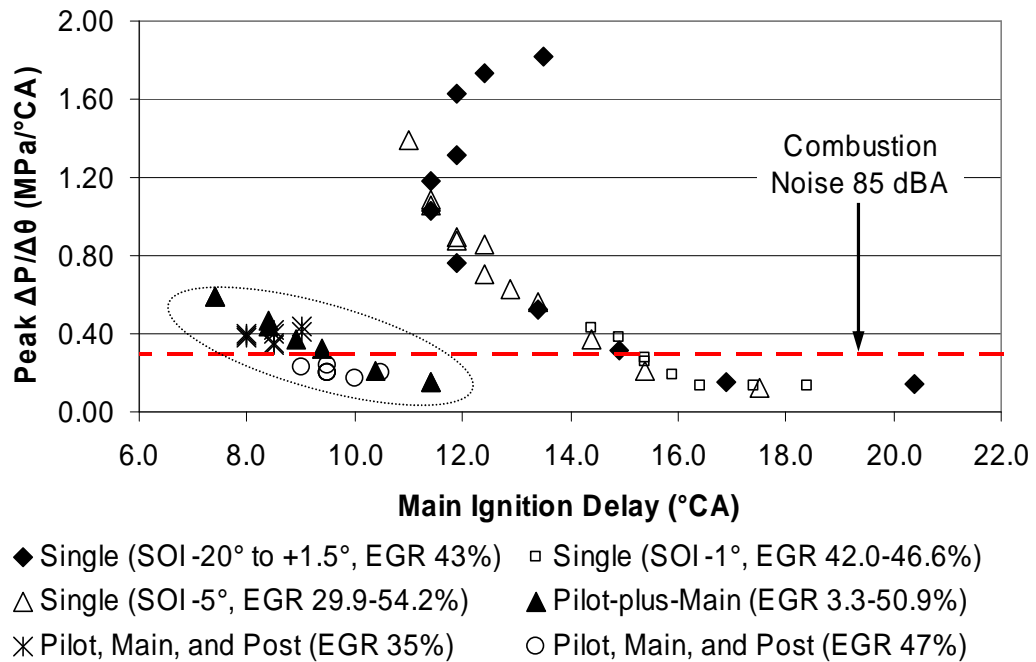


Figure 5.9: Ignition delay of main injection versus peak rate of change of in-cylinder pressure (1800 rpm 600 bar fuel rail pressure data). Data with a pilot injection highlighted by dashed oval. Red line represents 85 dB(A) at 1800 rpm.

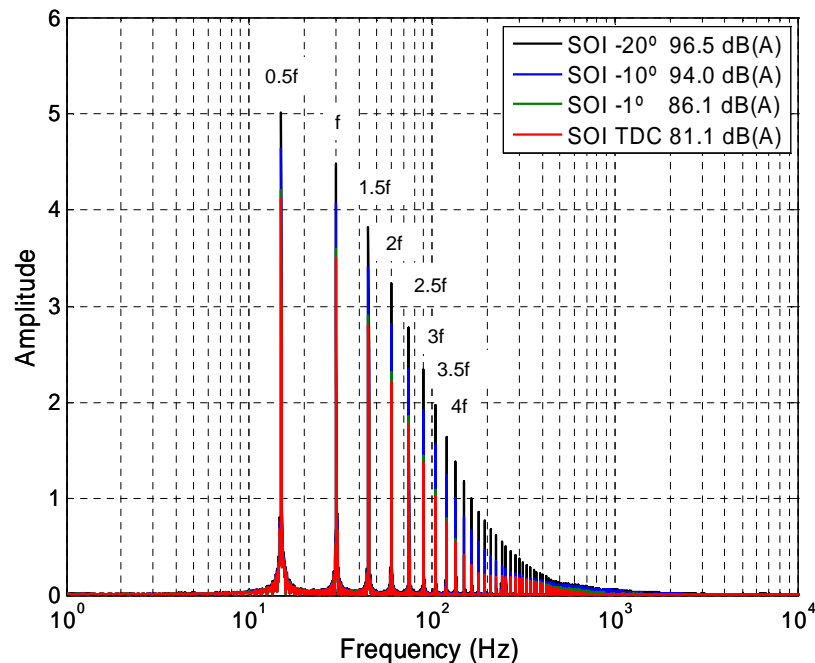


Figure 5.10: Single-sided power spectrum from FFT analysis of 100 consecutive in-cylinder pressure traces with logarithmic frequency axis. Data: 1800 rpm (30 Hz) 9.7 mg single injection EGR 43%, SOI Varied. Harmonics of engine fundamental frequency, f , are labelled. Legend entries give SOI and CNL

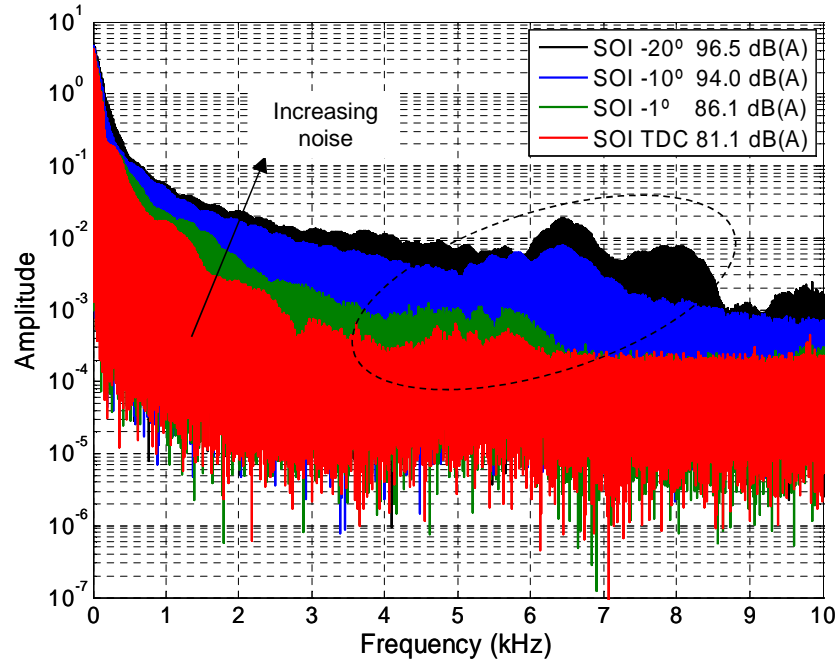


Figure 5.11: Single-sided power spectrum from FFT analysis of 100 consecutive in-cylinder pressure traces with linear frequency axis. Data: 1800 rpm 9.7 mg single injection 43% EGR, SOI Varied. Legend entries give SOI and CNL. Dashed oval highlights increased amplitudes caused by pressure wave travelling across piston bowl.

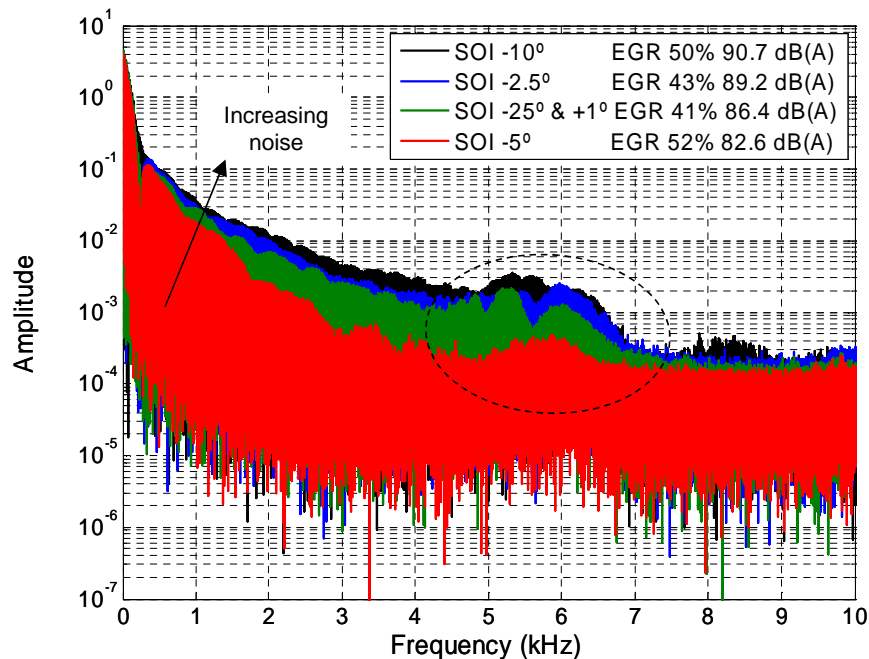


Figure 5.12: Single-sided power spectrum from FFT analysis of 100 consecutive in-cylinder pressure traces with linear frequency axis. Data: 1800 rpm 55 Nm (2.5 bar BMEP). Legend entries give SOI, EGR, and CNL. Dashed oval highlights increased amplitudes caused by pressure wave travelling across piston bowl.

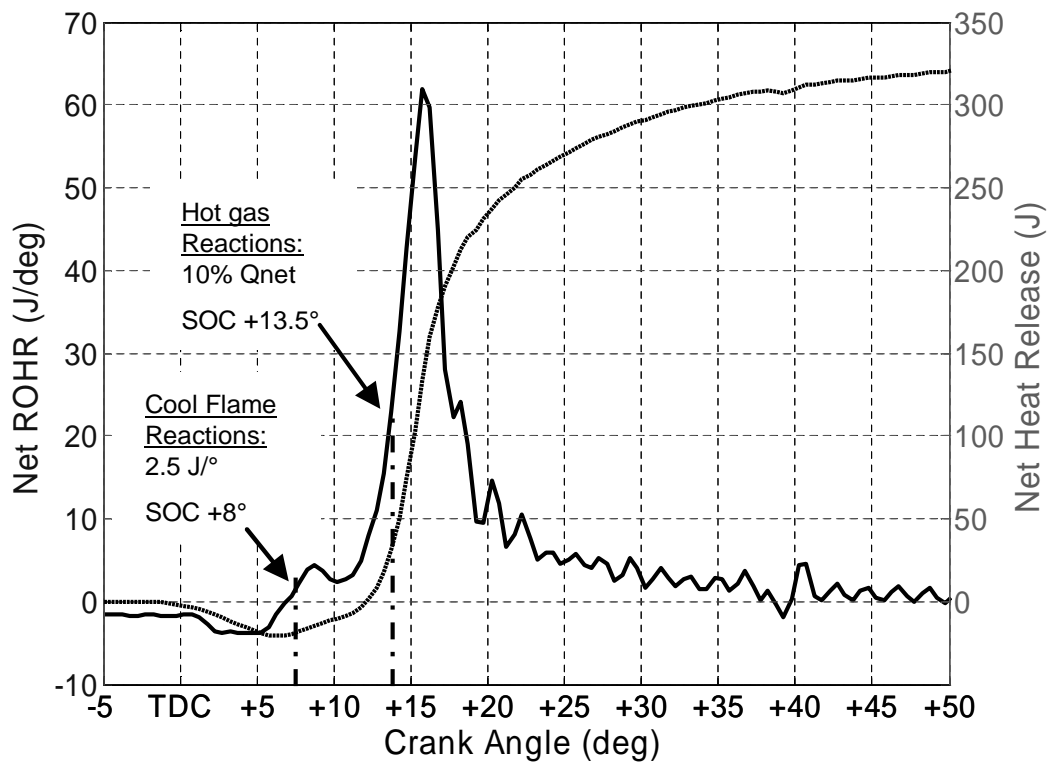


Figure 5.13: Definition of SOC illustrating low-temperature and hot gas reactions

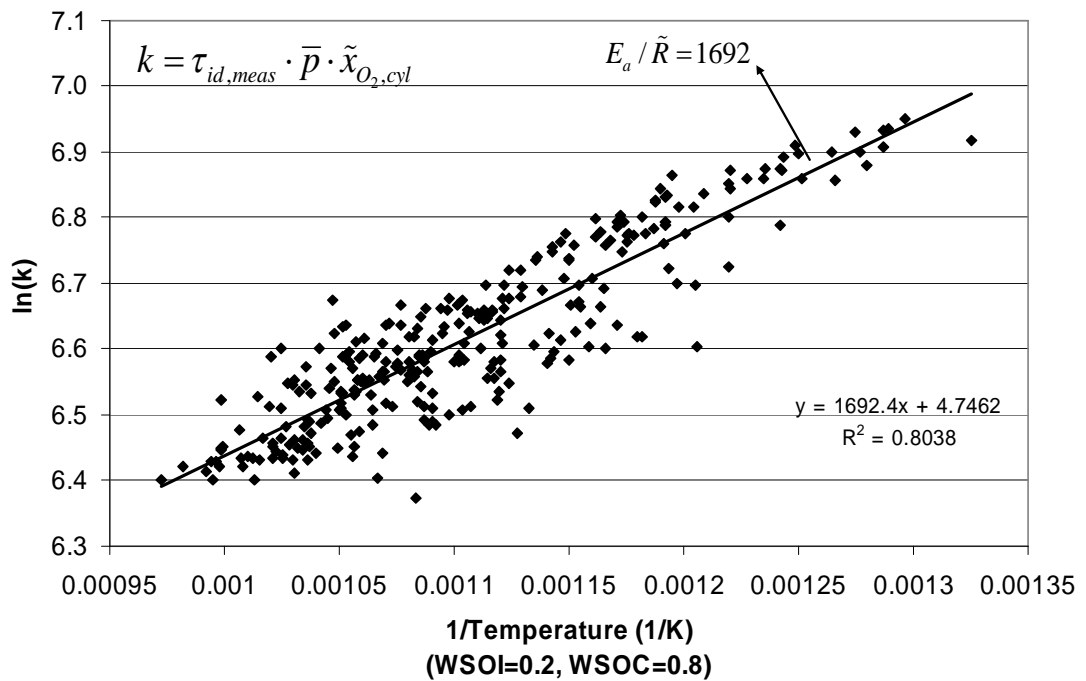


Figure 5.14: Determination of constant A and Apparent Activation Energy E_a / \tilde{R} . Single injections only. 20% Weighting (W) to SOI conditions, 80% to SOC conditions

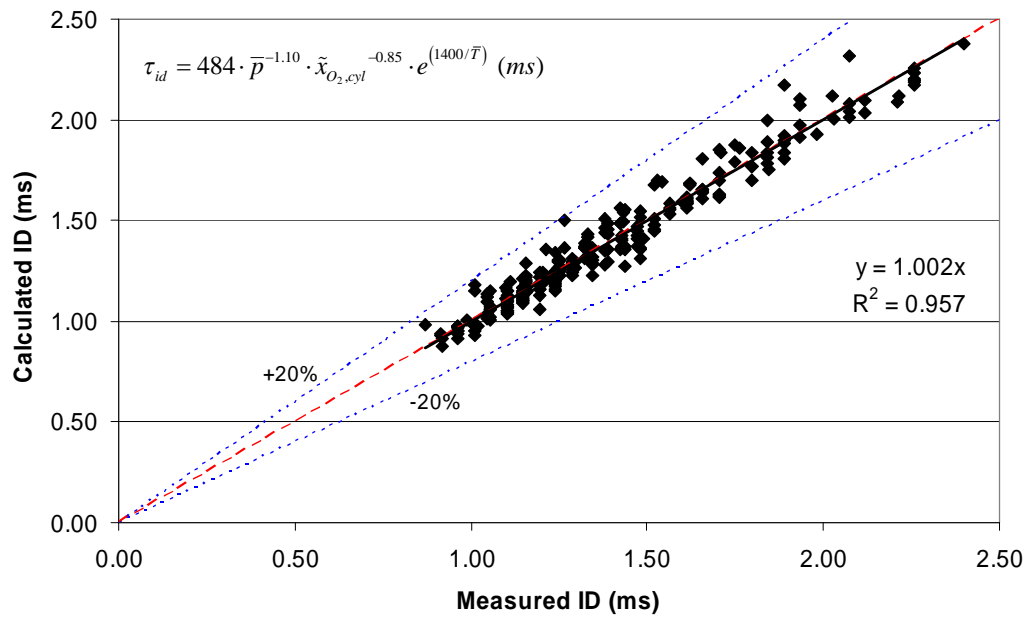


Figure 5.15: Comparison of measured vs. calculated ignition delay using the final expression. Single injection data only at 1500 rpm and 1800 rpm. Correlation used for calculated values shown in top corner. Red line denotes $x=y$, blue lines illustrate $\pm 20\%$ variation. 20% Weighting (W) to SOI conditions, 80% to SOC conditions

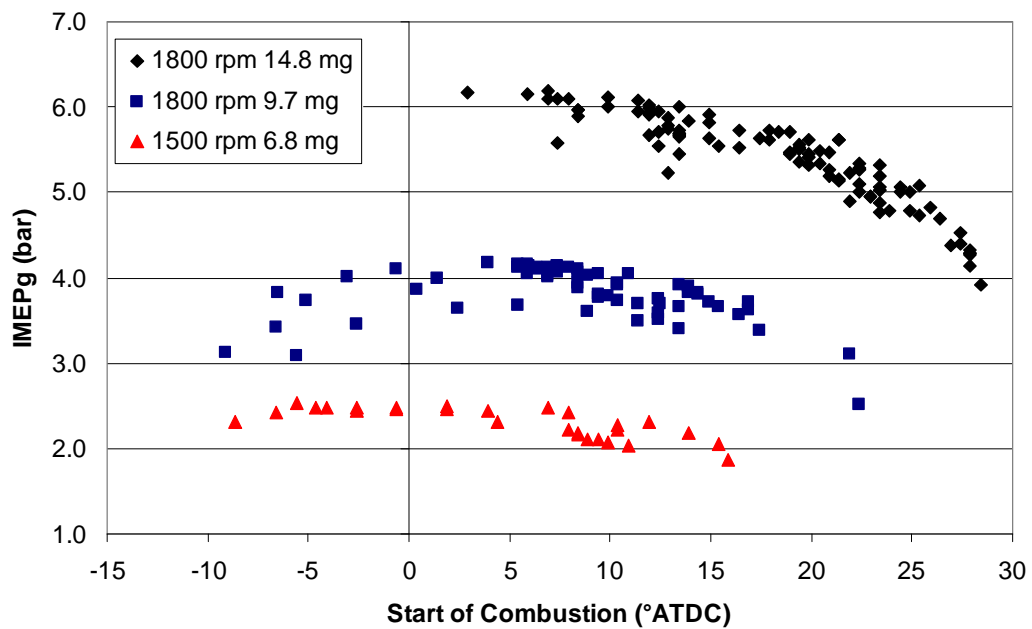


Figure 5.16: Gross IMEPg (average of cylinders 3 and 4) against location of start of combustion

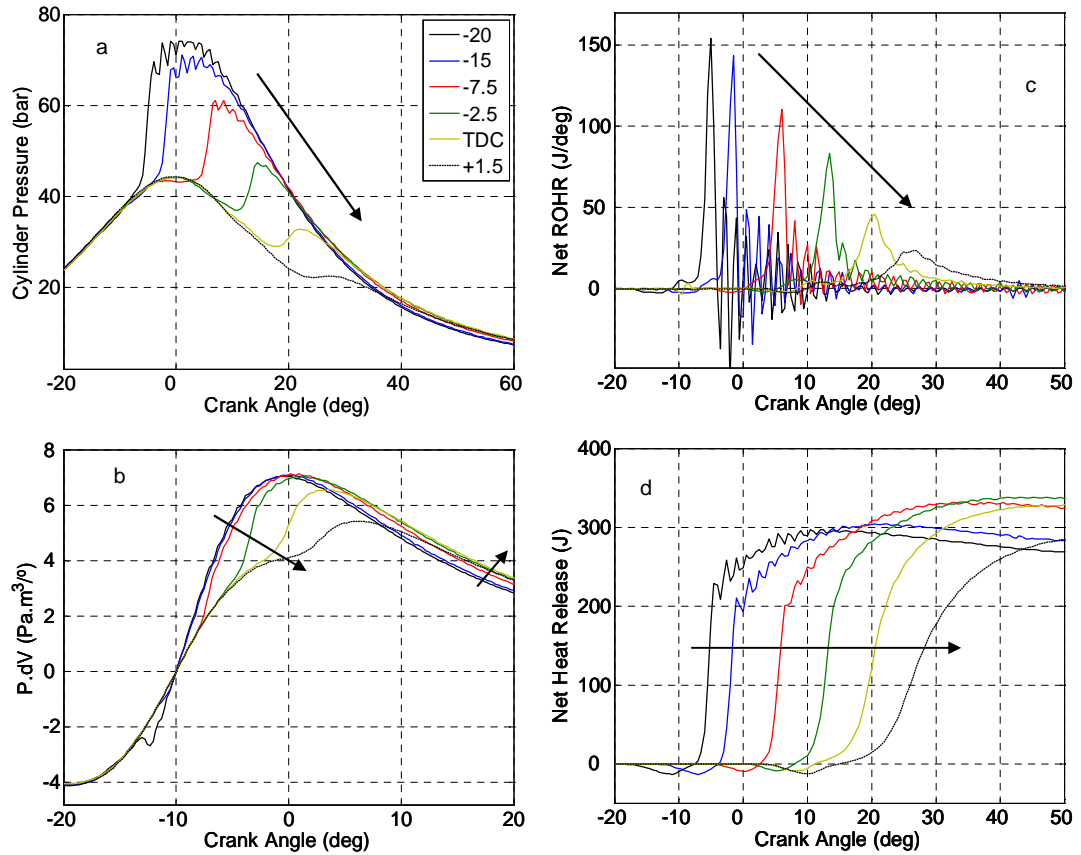


Figure 5.17: In-cylinder analysis at 1800 rpm 9.7 mg 43% EGR 600 bar rail pressure. a) Cylinder Pressure (bar), b) P.dV (Pa.m³/°), c) Net Rate of heat release (J/°), d) Cumulative net heat release (J). Legend denotes SOI, arrows indicate effect of retarding injection timing.

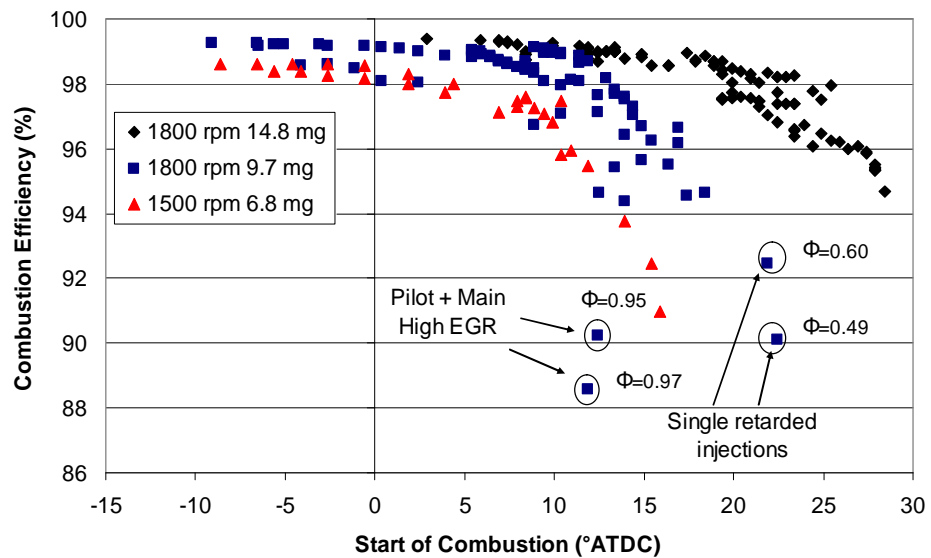


Figure 5.18: Dependence of combustion efficiency on start of combustion. Selected low efficiency data points are labelled for single and pilot-plus-main injections to highlight factors that must be considered when aiming to maintain high combustion efficiency

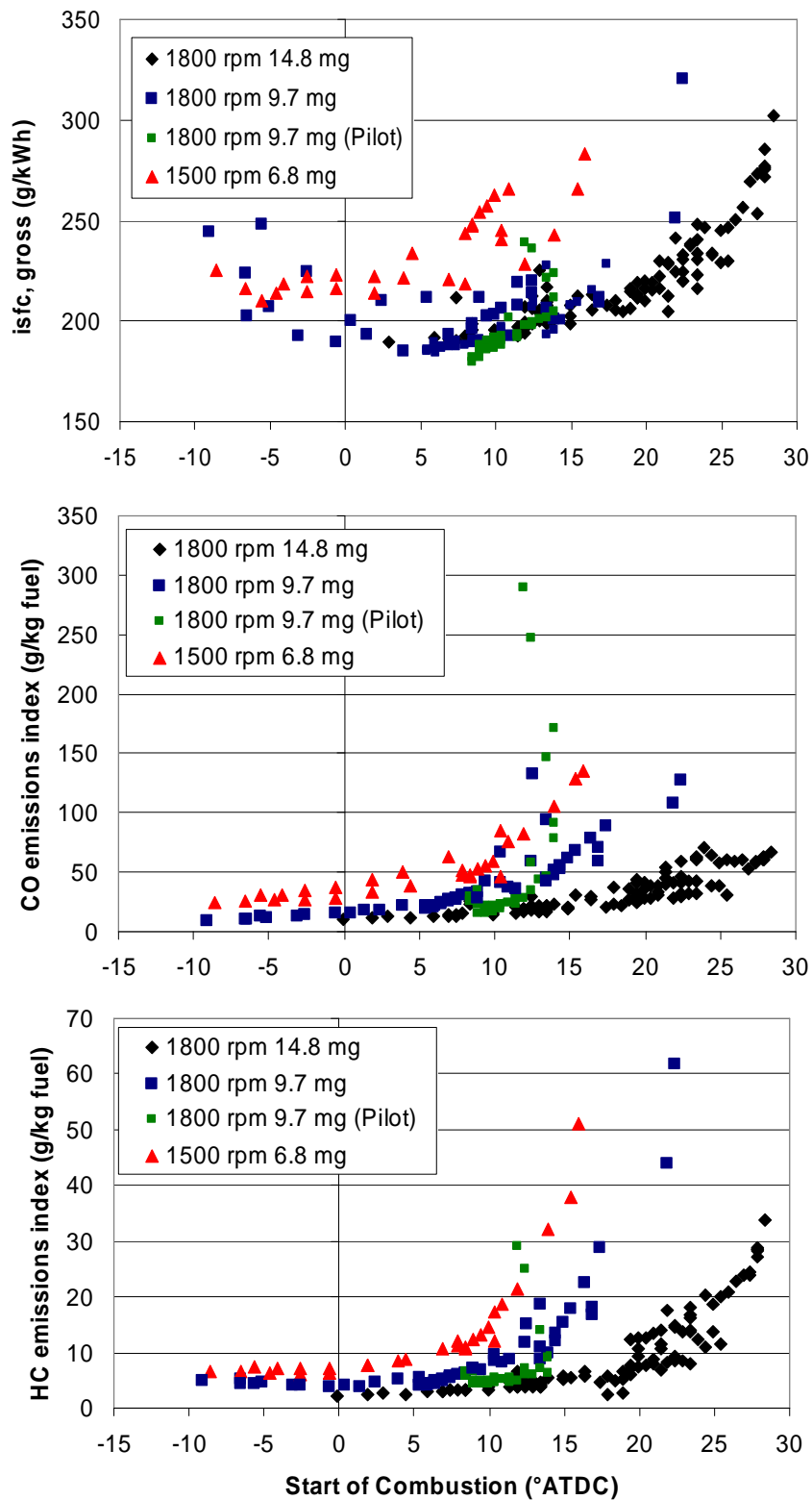


Figure 5.19: Dependence of gross indicated fuel consumption (top), CO (middle) and HC (bottom) emissions on location of SOC.

CHAPTER 6

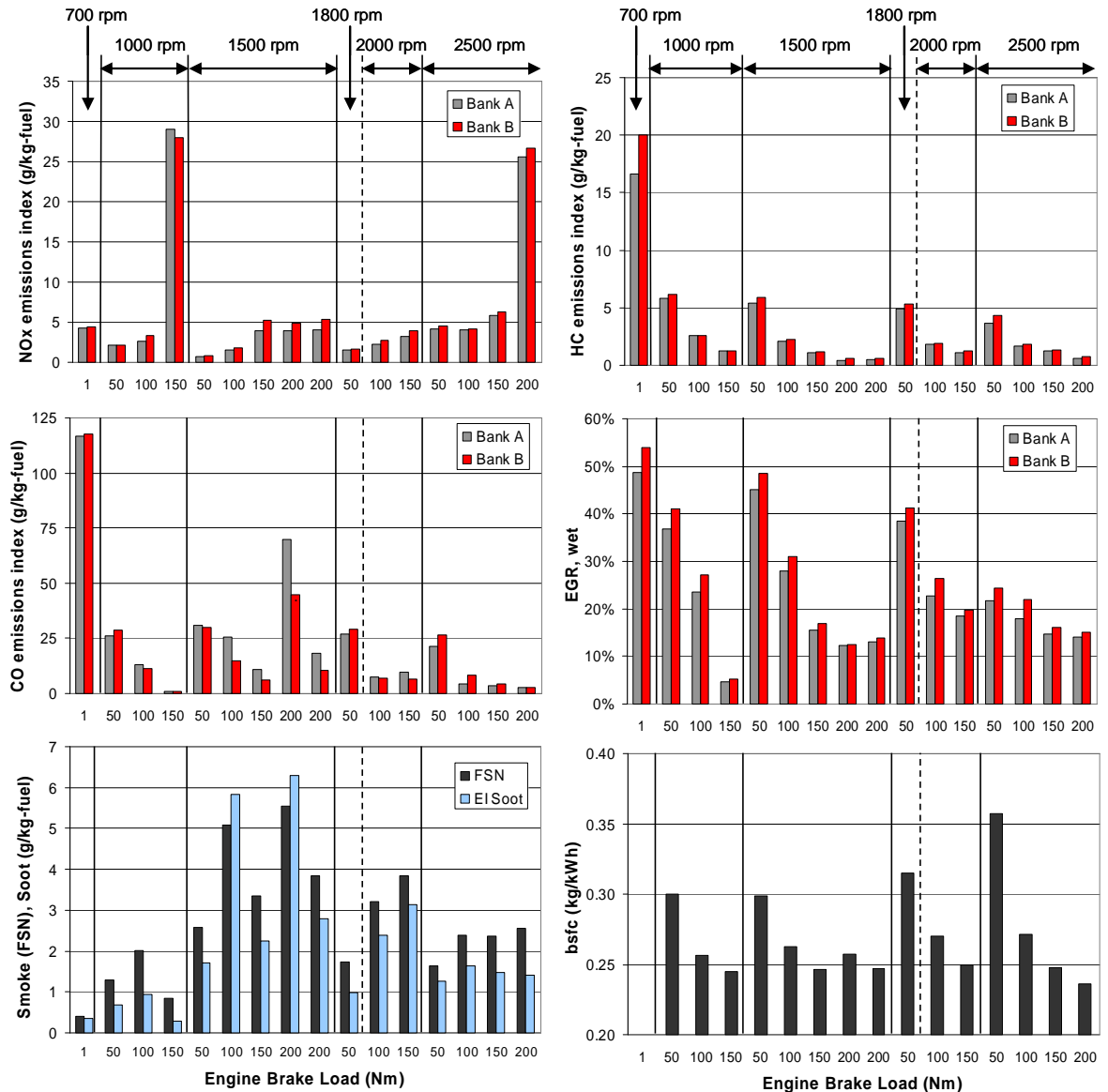


Figure 6.1: Baseline engine responses against engine brake load. Data grouped by engine speed as labelled. Graphs numbered 1-6 from left-to-right. Red and Grey bars correspond to engine banks.

Graph 1: NO_x emissions index (g/kg-fuel), data from both engine banks

Graph 2: HC emissions index (g/kg-fuel), data from both engine banks

Graph 3: CO emissions index (g/kg-fuel), data from both engine banks

Graph 4: EGR rate (%) after wetting procedure emissions index (g/kg-fuel), data from both engine banks

Graph 5: Smoke (FSN) and Soot emissions index (g/kg-fuel) from Bank B

Graph 6: bsfc for the engine (average values from measuring emissions from both banks). 700 rpm data removed to allow more appropriate scale.

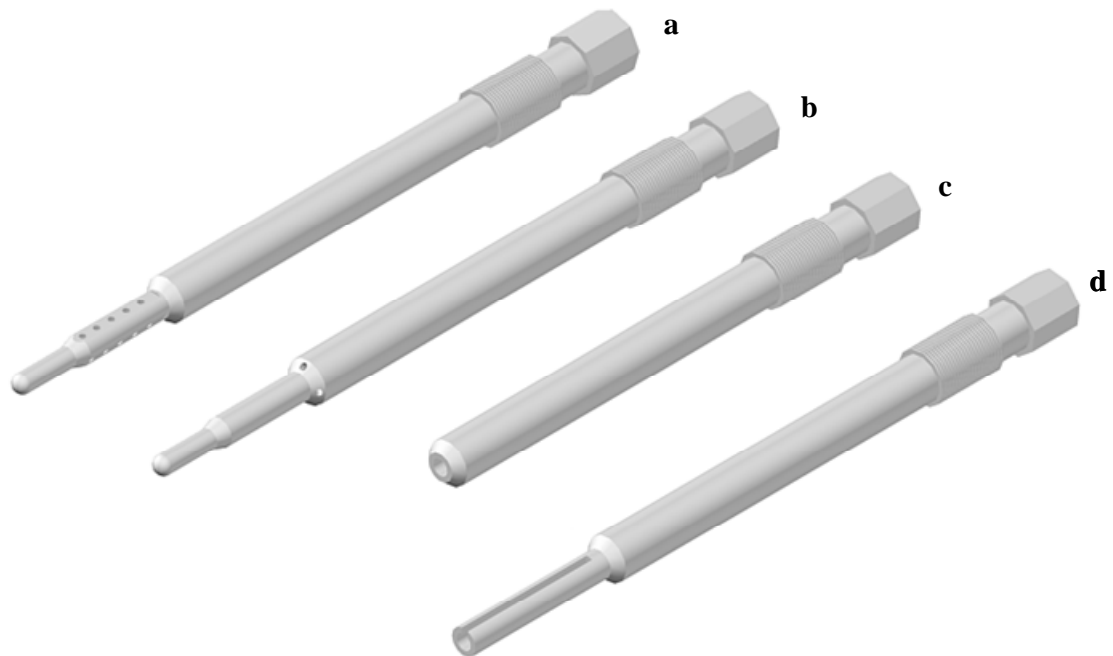


Figure 6.2: CAD drawings of transducer adaptors installed in the glow plug holes in the cylinder head. *a) Multi-hole on flats ($15 \times \Phi 1\text{mm}$). b) Multi-hole on chamfer ($4 \times \Phi 1\text{mm}$). c) Open (no shielding). d) Slot ($\Phi 2.5\text{ mm}$, slot $1\text{mm} \times 22\text{mm}$)*

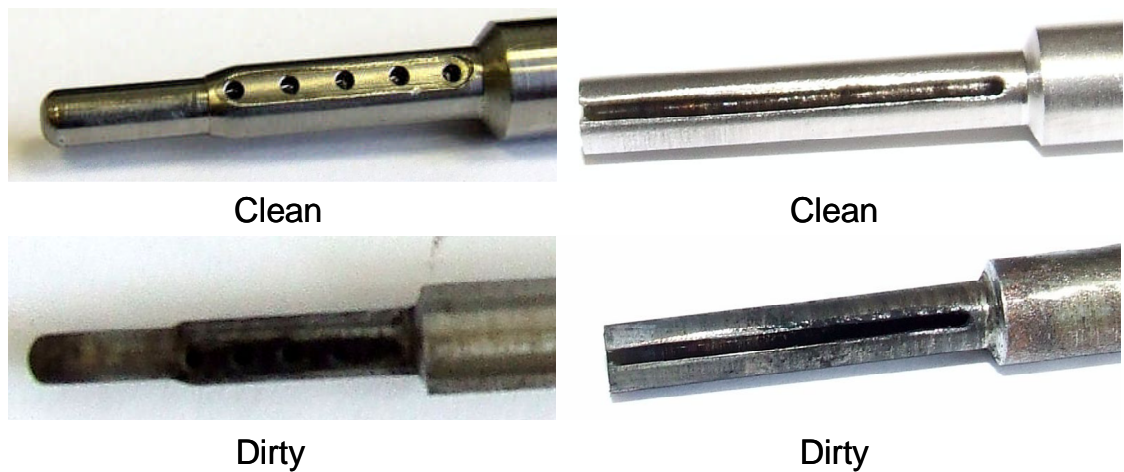


Figure 6.3: Photos of clean and dirty adaptors. *Left: Adaptor (a), Right: Adaptor (d)*

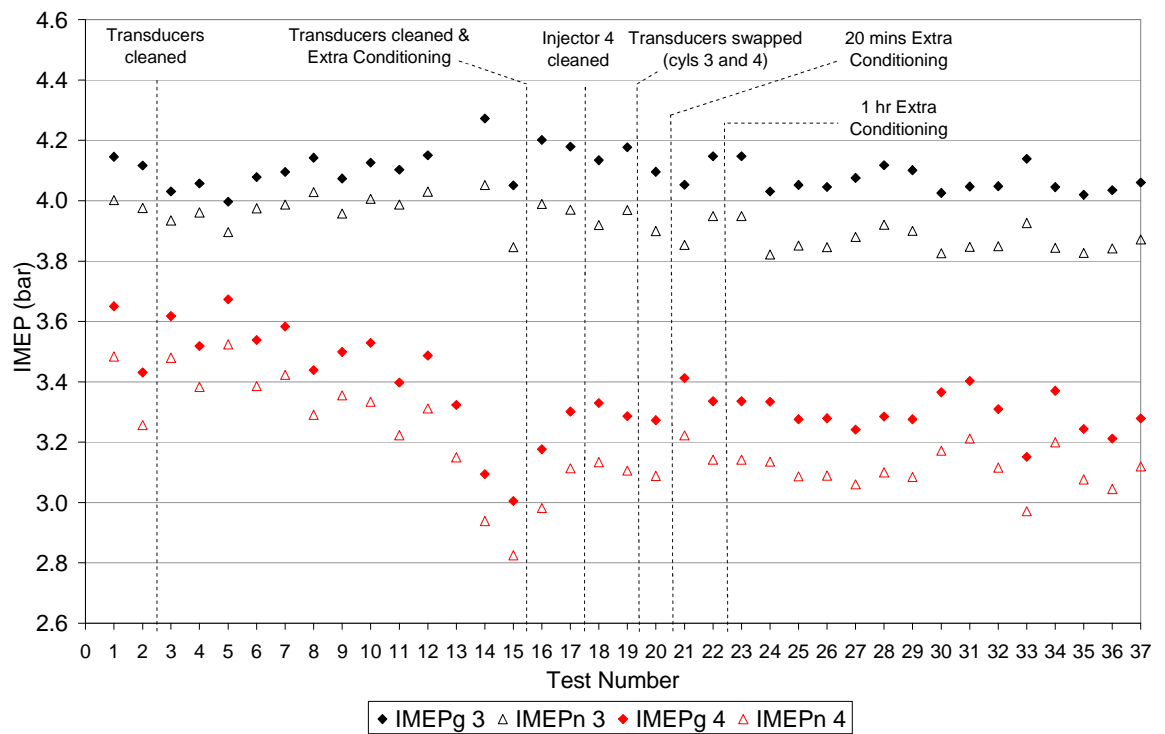


Figure 6.4: Gross (g) and net (n) IMEP variation over 20 month period for standard test point. Note data was collected in discrete testing periods and as such the number of tests are not equally spaced temporally

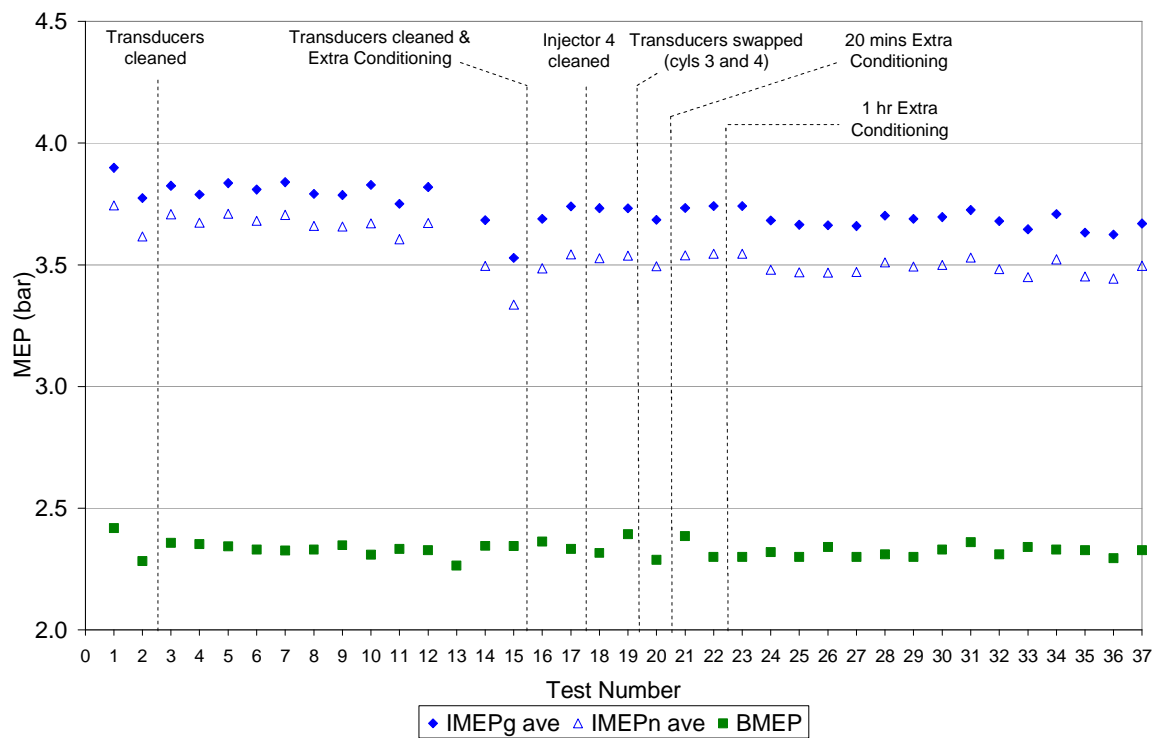


Figure 6.5: Average IMEP from cylinders 3 and 4 and BMEP over 20 month period for standard test point. Note data was collected in discrete testing periods and as such the number of tests are not equally spaced temporally

CHAPTER 7

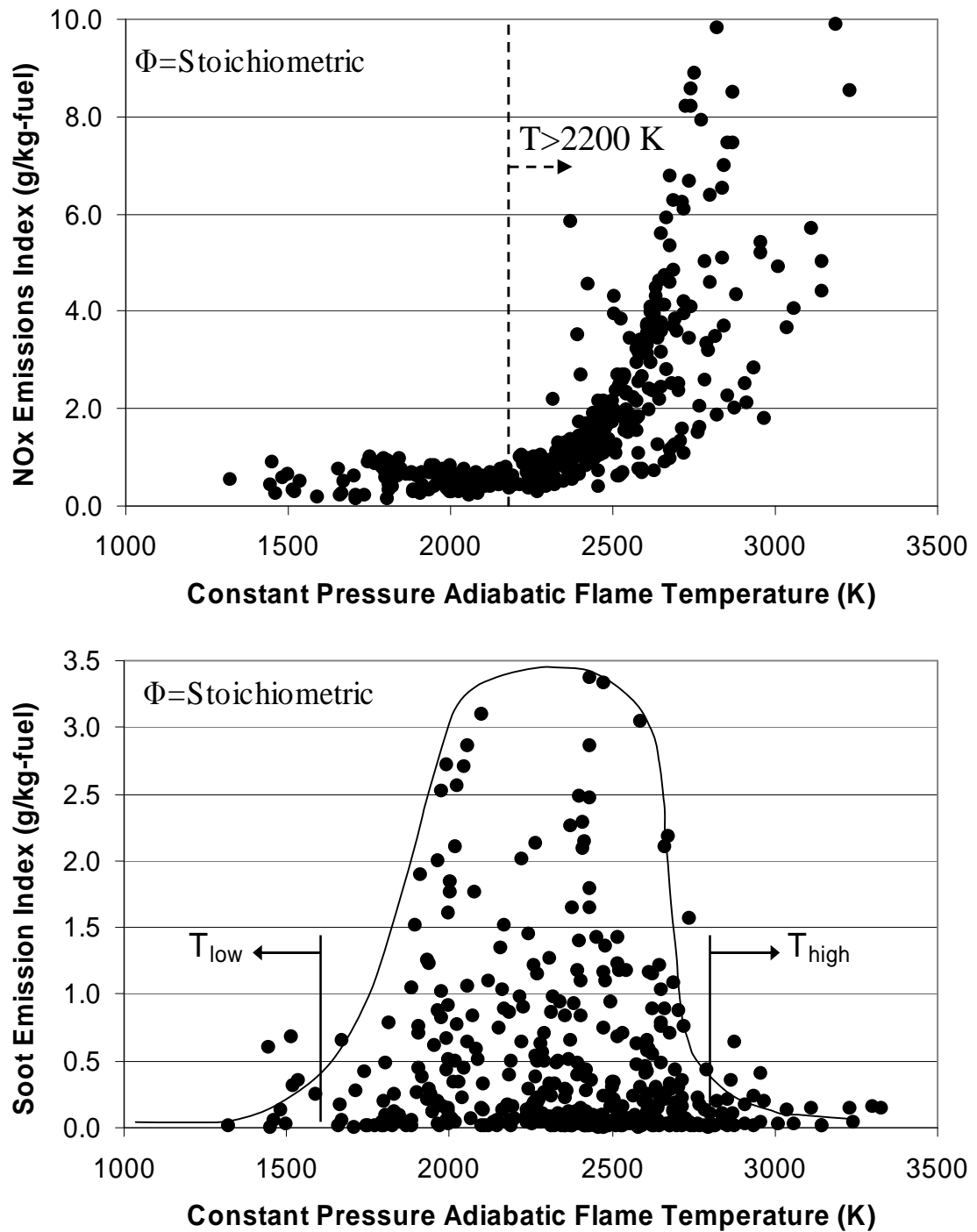


Figure 7.1: Relationship between NO_x (top) and Soot (bottom) emissions indices against constant pressure adiabatic flame temperature calculated using the Olikara and Borman equilibrium routines [81] based on stoichiometric fuel-air equivalence ratio.

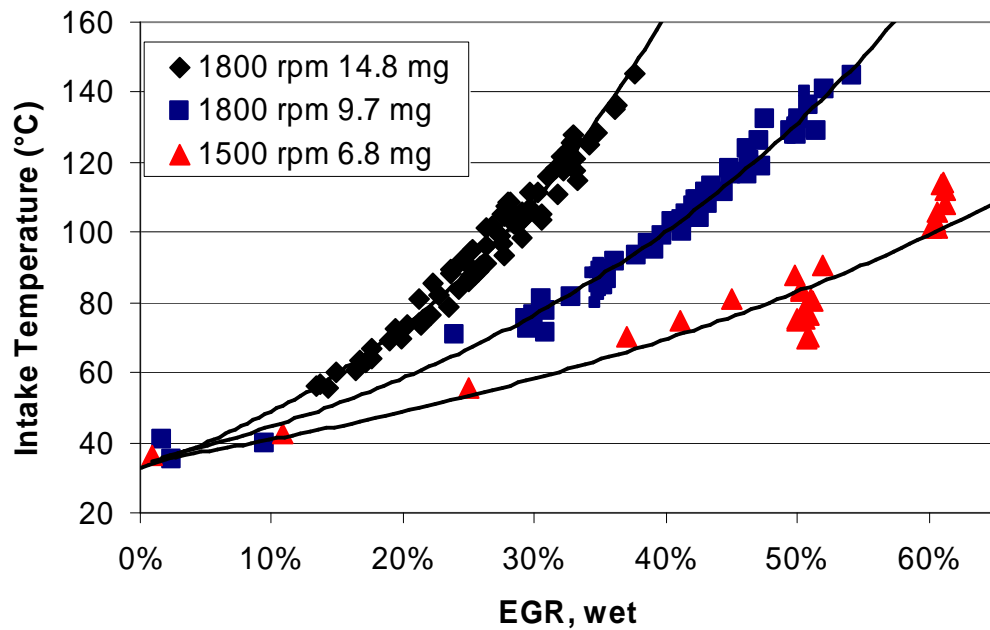


Figure 7.2: Dependence of intake temperature on EGR fraction at given fuelling rates

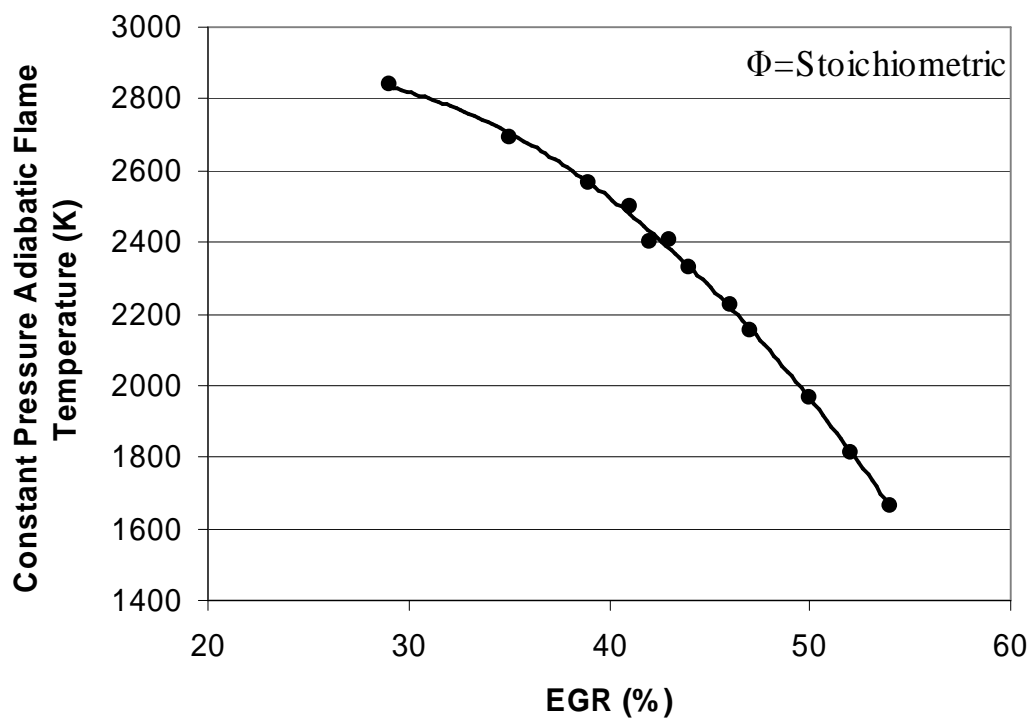


Figure 7.3: Effect of EGR on calculated adiabatic flame temperature based on stoichiometric fuel-air equivalence ratio. Data at 1800 rpm 9.7 mg/stk/cyl SOI -5°ATDC 600 bar fuel rail pressure

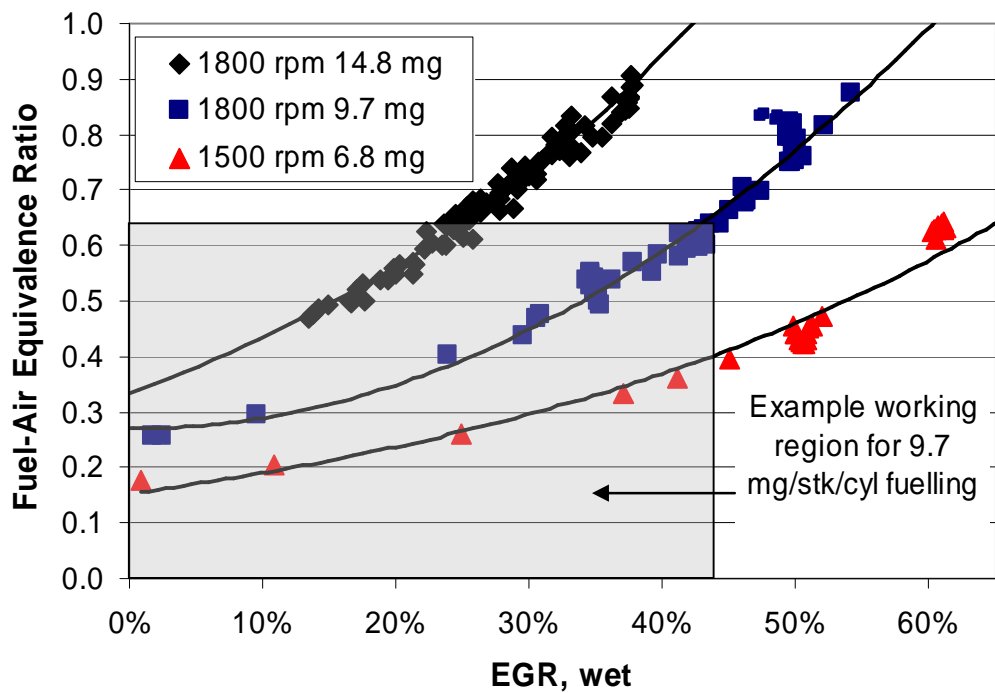


Figure 7.4: Displacement effect of EGR causing increase in overall equivalence ratio

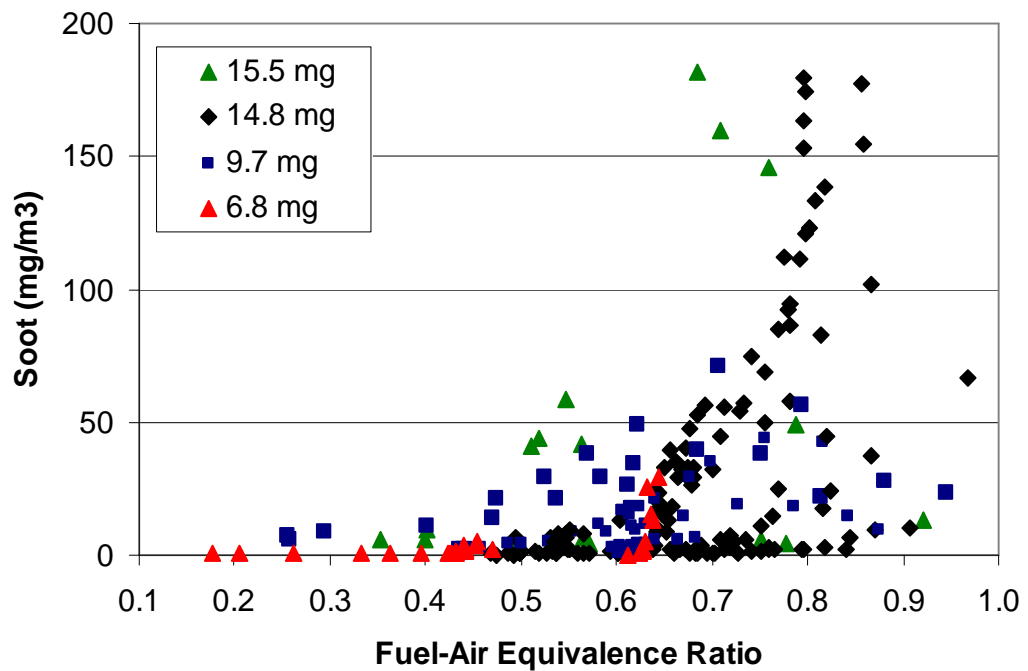


Figure 7.5: Soot concentration against fuel-air equivalence ratio for a range of fuel quantities. Data at 1500 rpm and 1800 rpm.

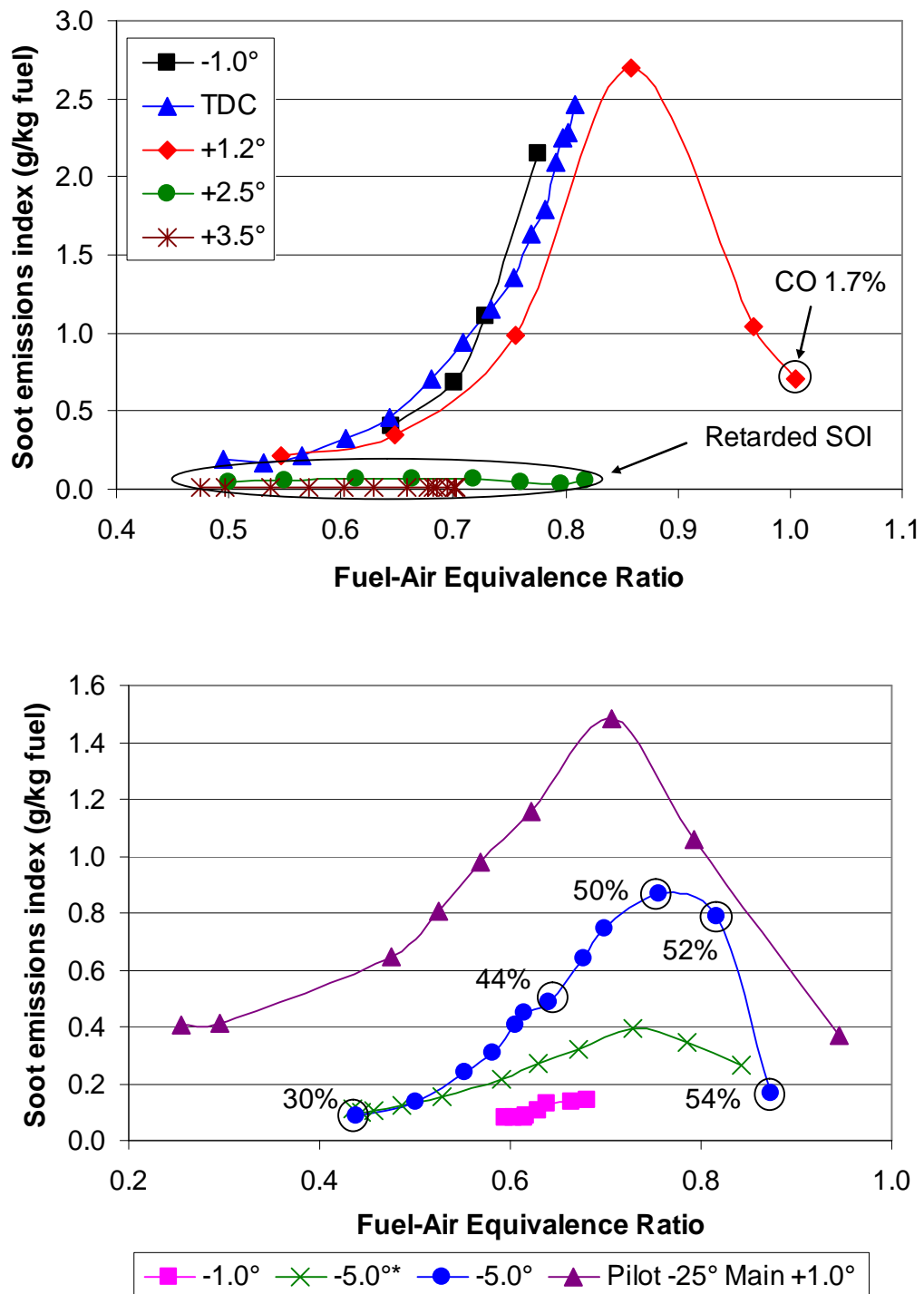


Figure 7.6: Soot against fuel-air equivalence ratio. Top: 1800 rpm 14.8 mg 600 bar rail pressure. Bottom: 1800 rpm 9.7 mg 600 bar rail pressure. Legend entries give the SOI, * indicates intake throttled. Labelled points indicate EGR rate along soot response.

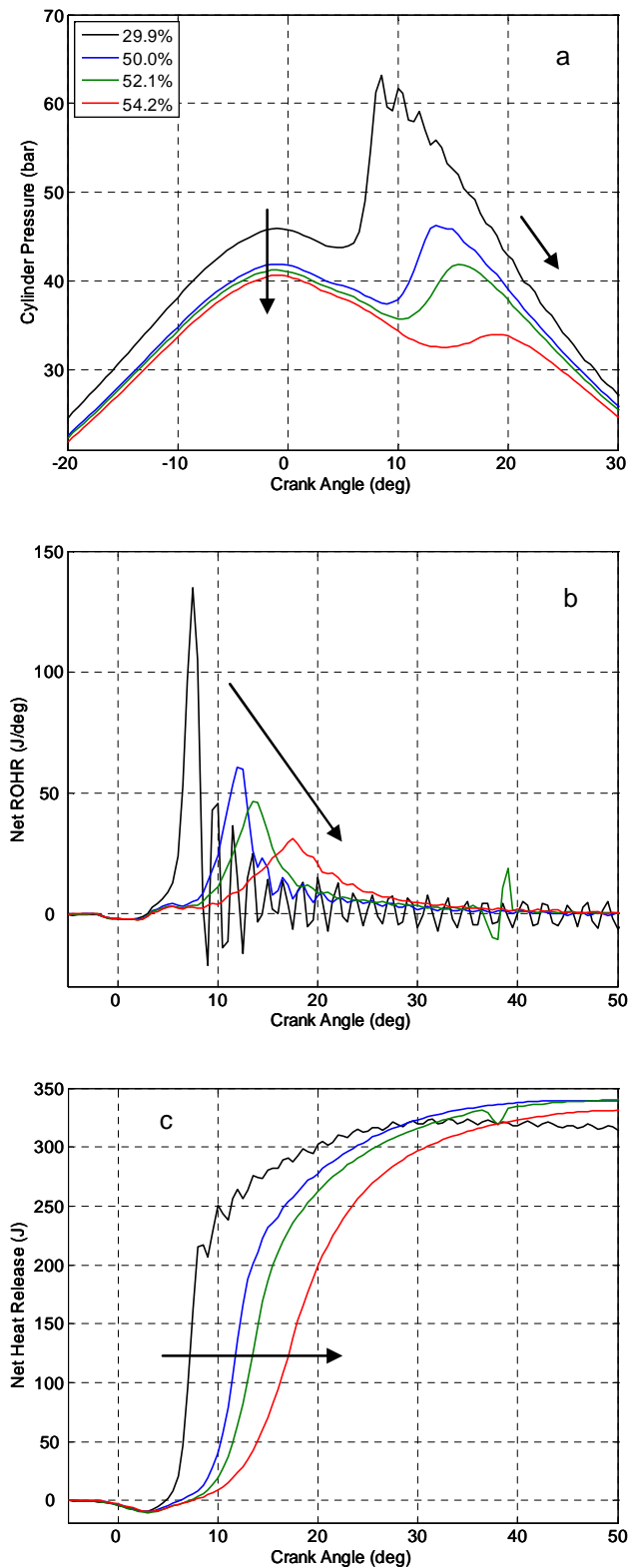


Figure 7.7: In-cylinder analysis at SOI of -5°ATDC, 1800 rpm 9.7 mg 600 bar rail pressure for different EGR rates. A) Cylinder pressure (bar), b) Net rate of heat release (J/°), c) Cumulative net heat release (J). Arrows indicate effect of increasing EGR

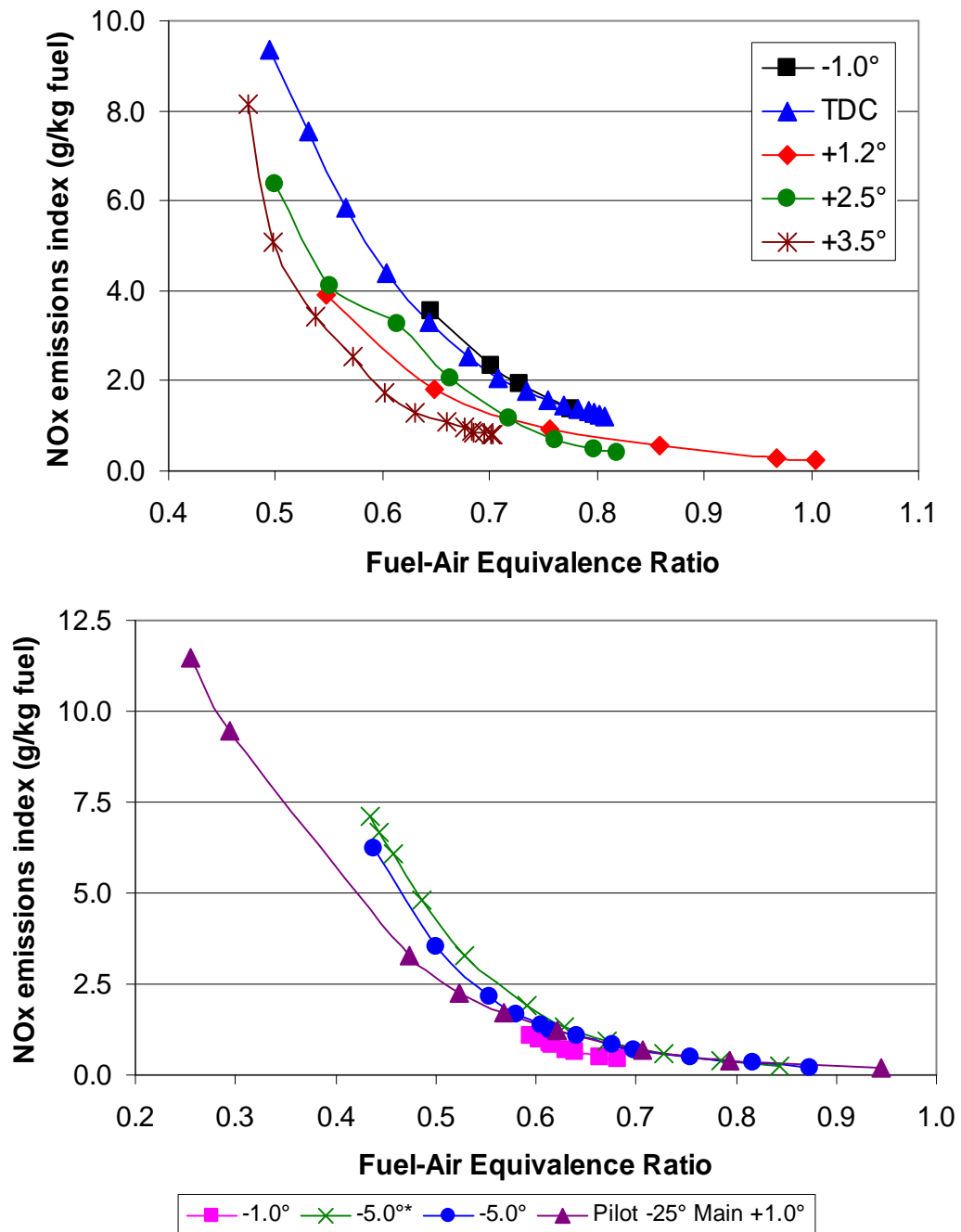


Figure 7.8: NO_x against fuel-air equivalence ratio. Top: 1800 rpm 14.8 mg 600 bar rail pressure. Bottom: 1800 rpm 9.7 mg 600 bar rail pressure. Legend entries give the SOI, * indicates intake throttled.

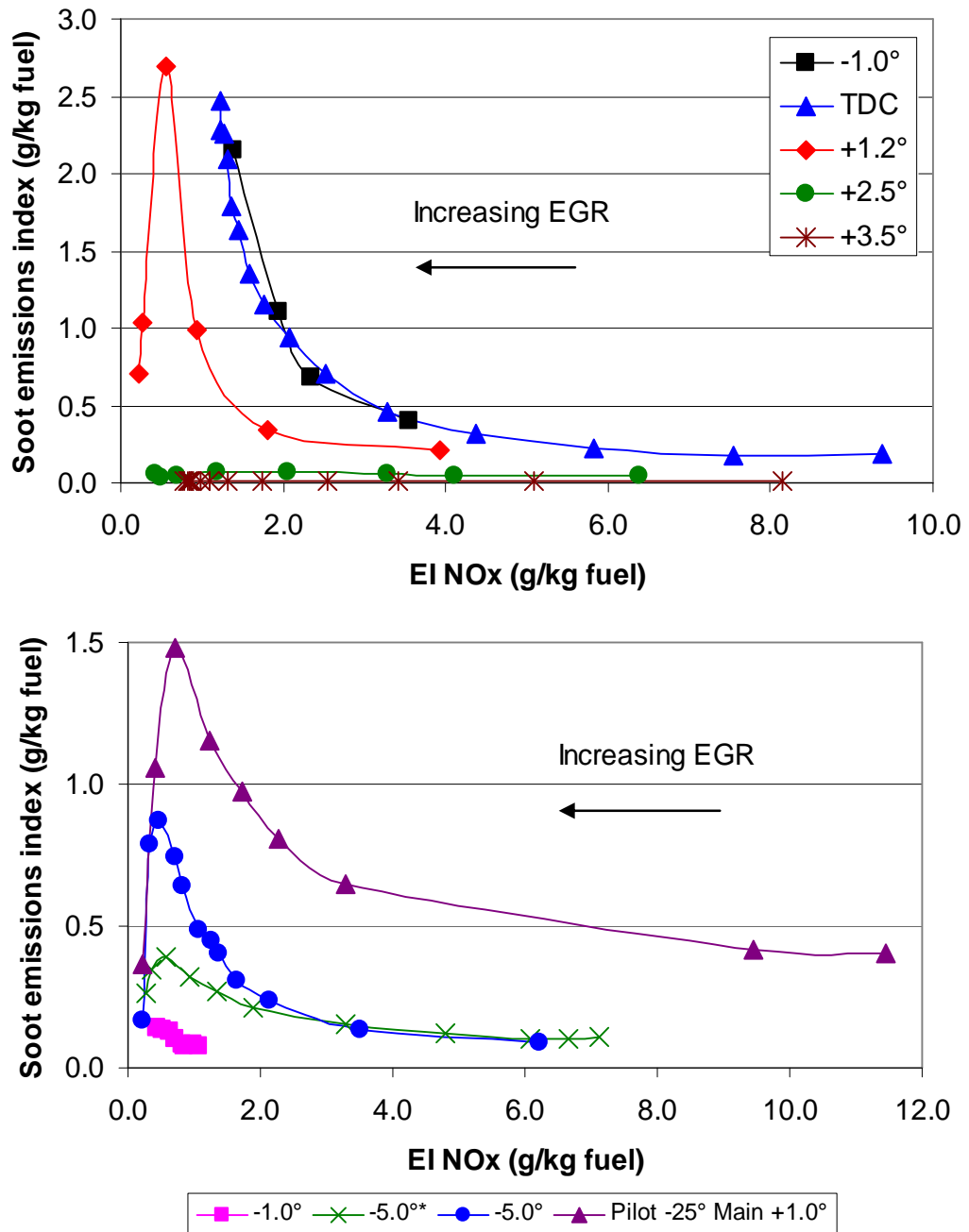


Figure 7.9: NO_x-soot trade-off for fixed injection timings (EGR sweeps). Top: 1800 rpm 14.8 mg 600 bar rail pressure. Bottom: 1800 rpm 9.7 mg 600 bar rail pressure. Legend entries give the SOI, * indicates intake throttled

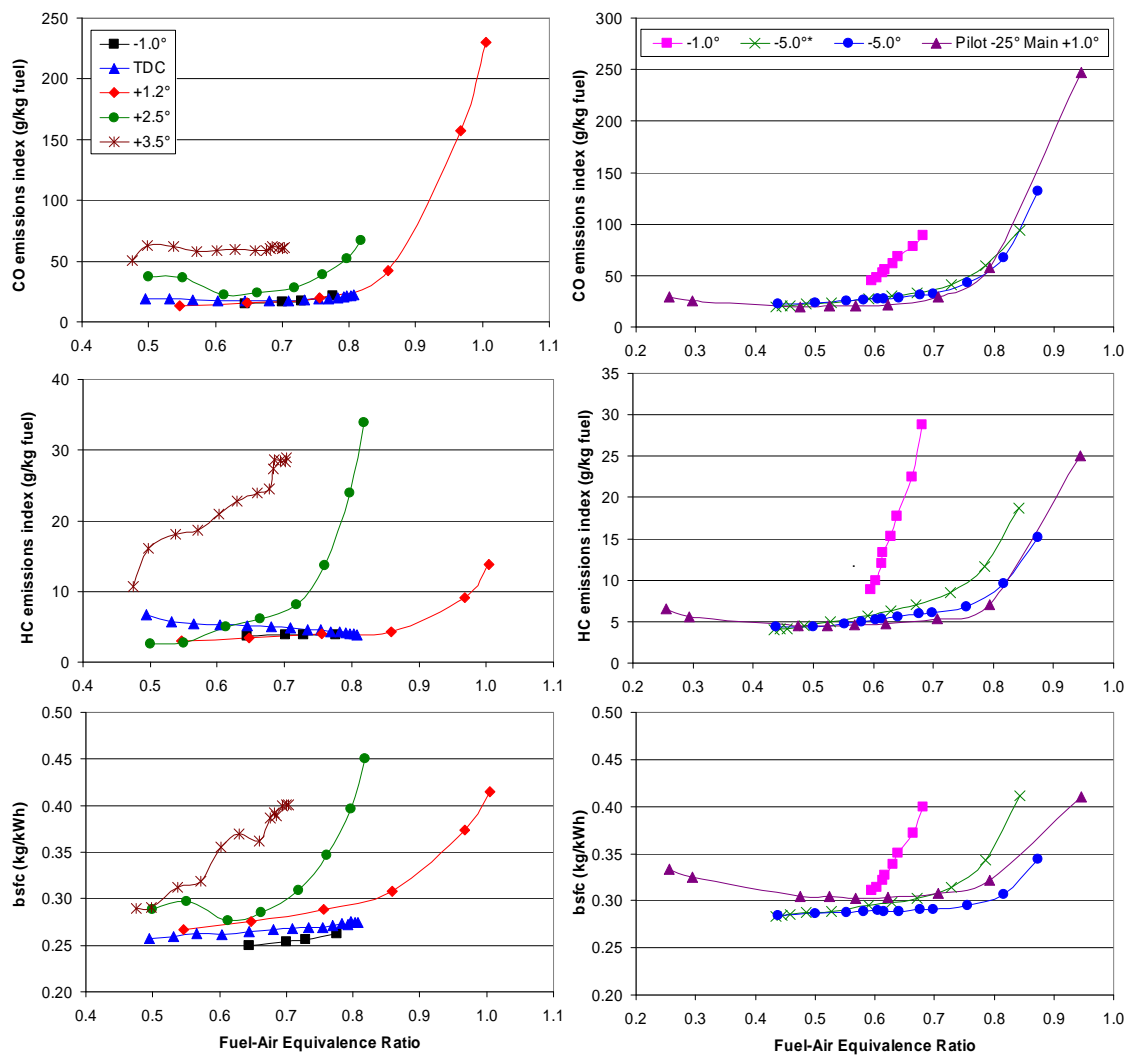


Figure 7.10: Response of CO and HC emissions and bsfc against fuel-air equivalence ratio. Left: 1800 rpm 14.8 mg 600 bar rail pressure. Right: 1800 rpm 9.7 mg 600 bar rail pressure. Legend entries give the SOI, * indicates intake throttled

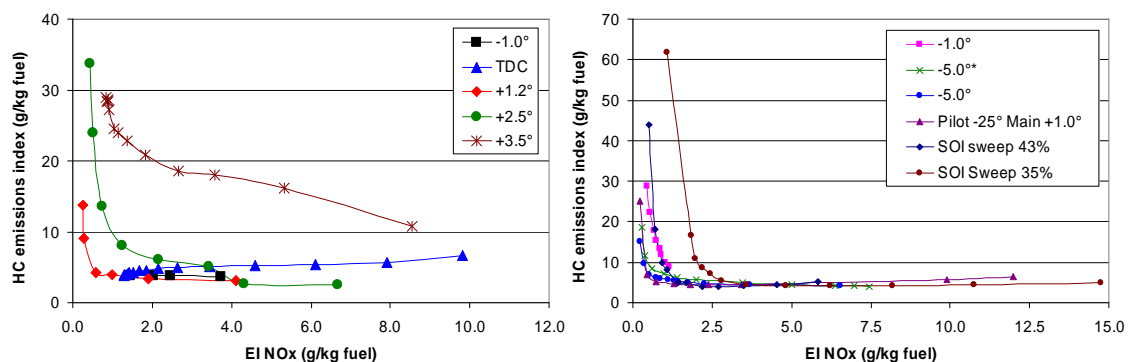


Figure 7.11: NO_x -HC trade-off with equivalence ratio. Left: 1800 rpm 14.8 mg 600 bar rail pressure. Right: 1800 rpm 9.7 mg 600 bar rail pressure. Legend entries give the SOI or EGR rate, * indicates intake throttled

CHAPTER 8

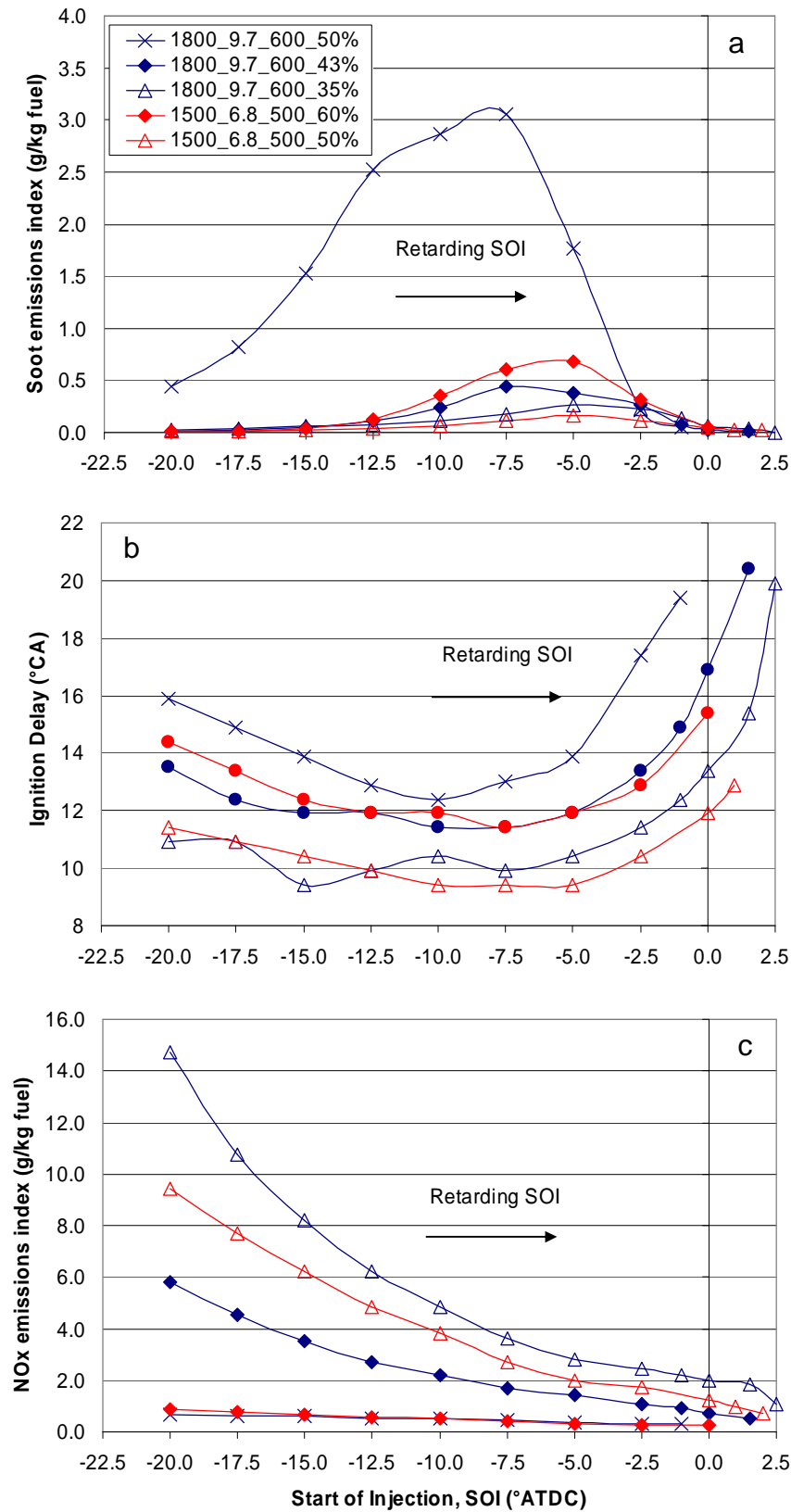


Figure 8.1: Dependence of (a) Net soot output, (b) ignition delay, and (c) NO_x emissions on injection timing. Legend entries give engine speed (rpm), fuel injection quantity (mg/stk/cyl), fuel rail pressure (bar), and EGR rate. Note single injections only

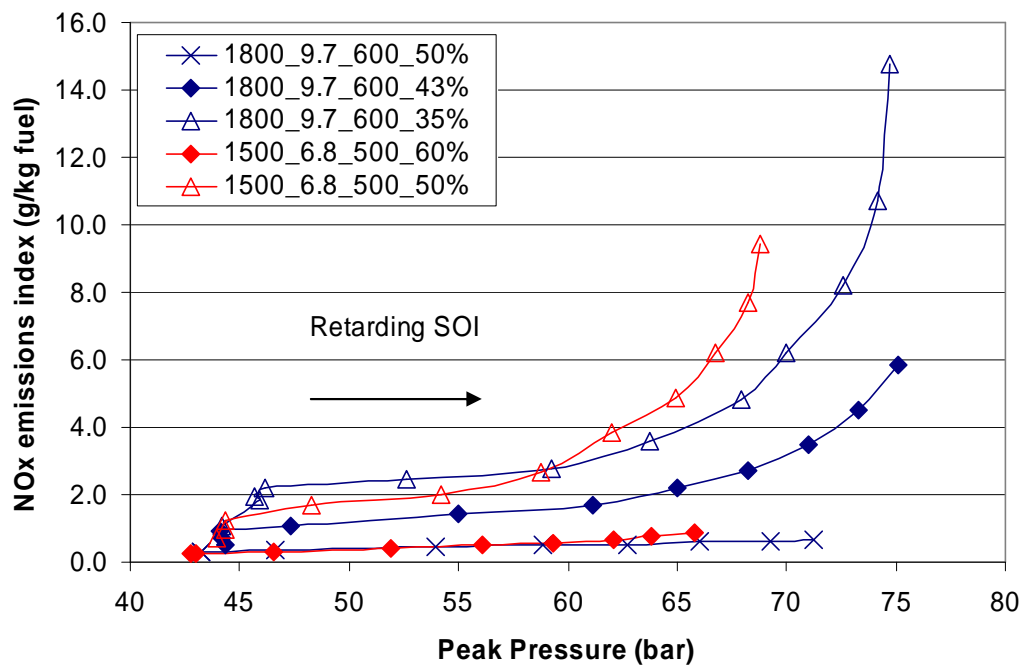


Figure 8.2: Dependence of NO_x on peak in-cylinder pressure. Legend entries give engine speed (rpm), fuel injection quantity (mg/stk/cyl), fuel rail pressure (bar), and EGR rate. Note single injections only

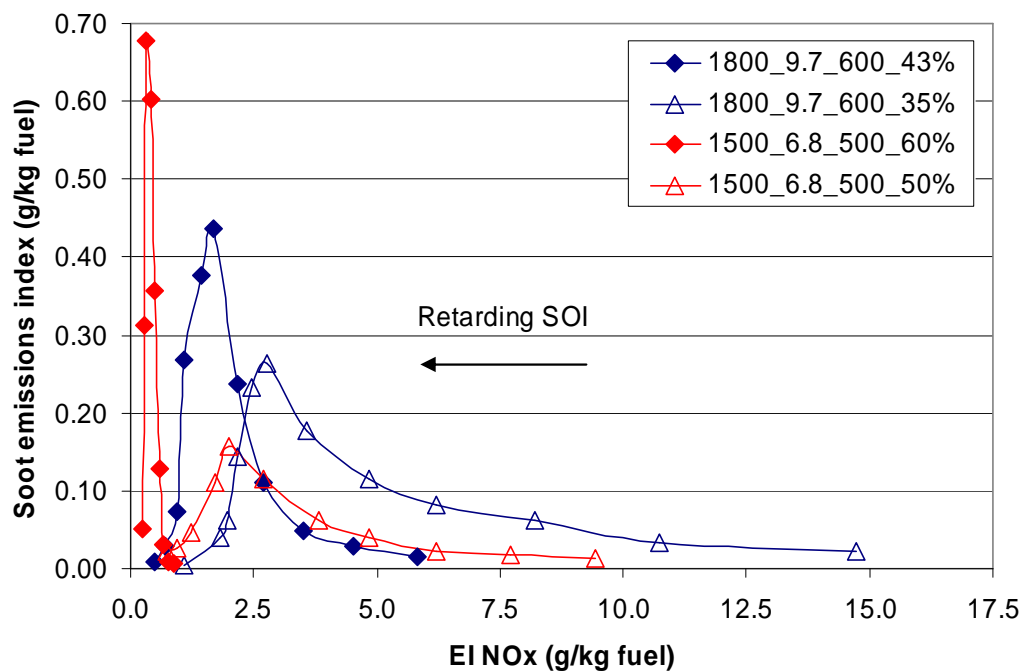


Figure 8.3: NO_x -soot trade-off for injection timing sweeps. Legend entries give engine speed, fuel injection quantity, and EGR rate. 1800_9.7_50% data removed to allow clearer scale. Note single injections only

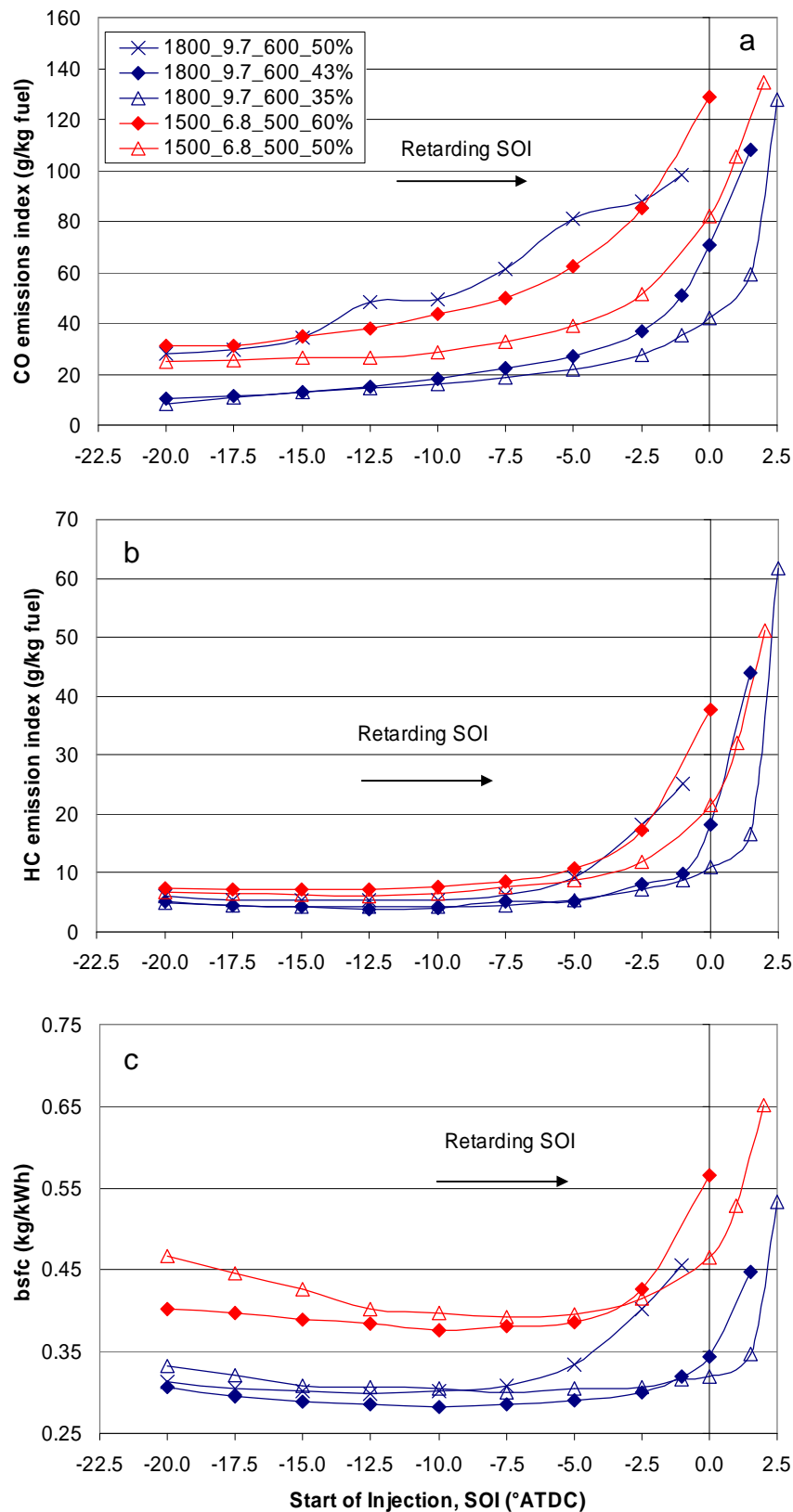


Figure 8.4: Effect of (a) CO emissions, (b) HC emissions, and (c) brake specific fuel consumption on injection timing. Legend entries give engine speed (rpm), fuel injection quantity (mg/stk/cyl), fuel rail pressure (bar), and EGR rate. Note single injections only

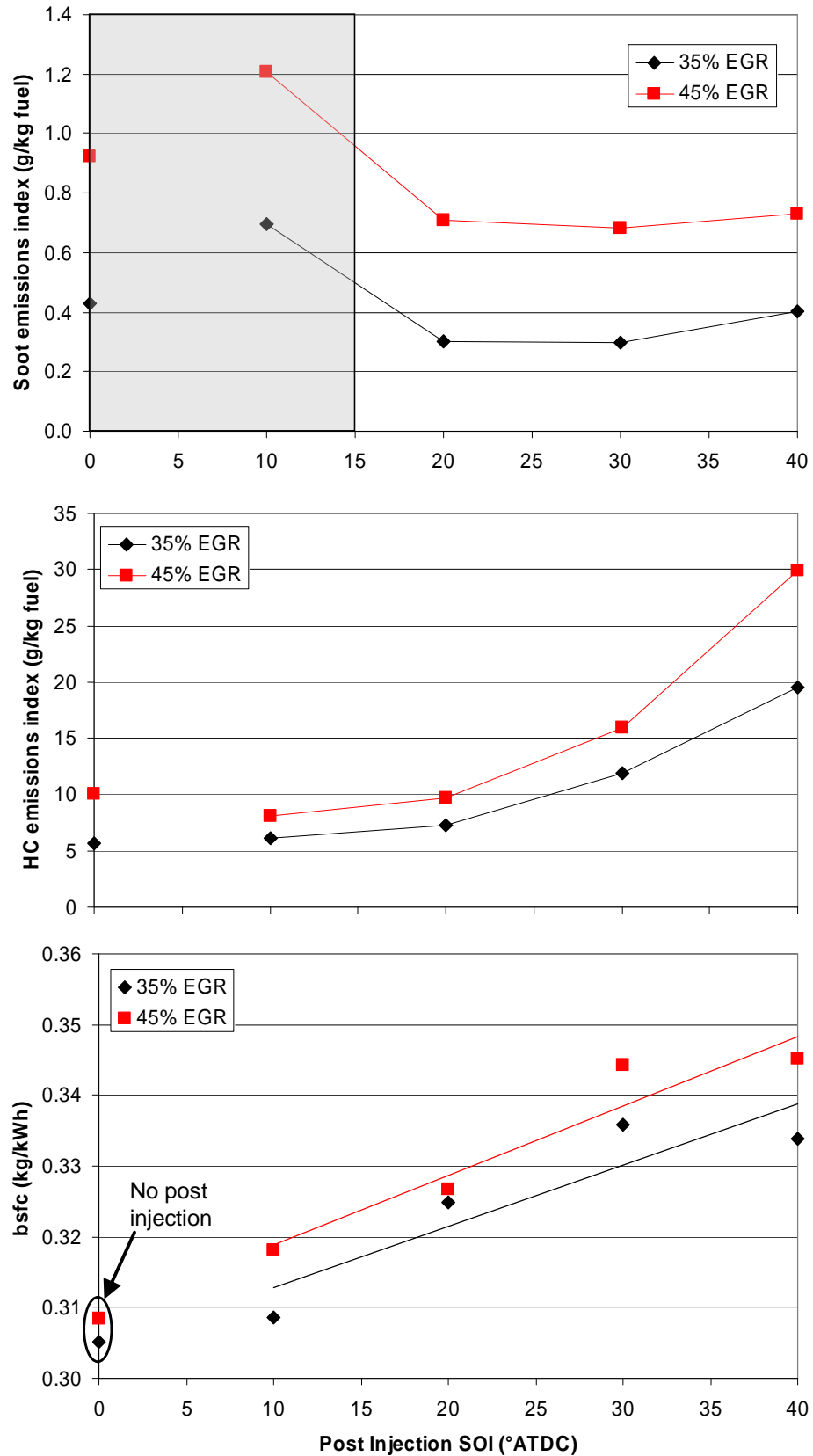


Figure 8.5: Effect of post injection timing on soot and HC emissions and bsfc for pilot-plus-main injections. 1800 rpm Pilot -25°ATDC 0.8 mg Main +1.0°ATDC (quantity adjusted to maintain constant 9.7 mg total fuel flow) 600 bar rail pressure. Shaded area highlights general zone resulting in no soot reduction relative to baseline. Data plotted at 0°ATDC correspond to no post injection event

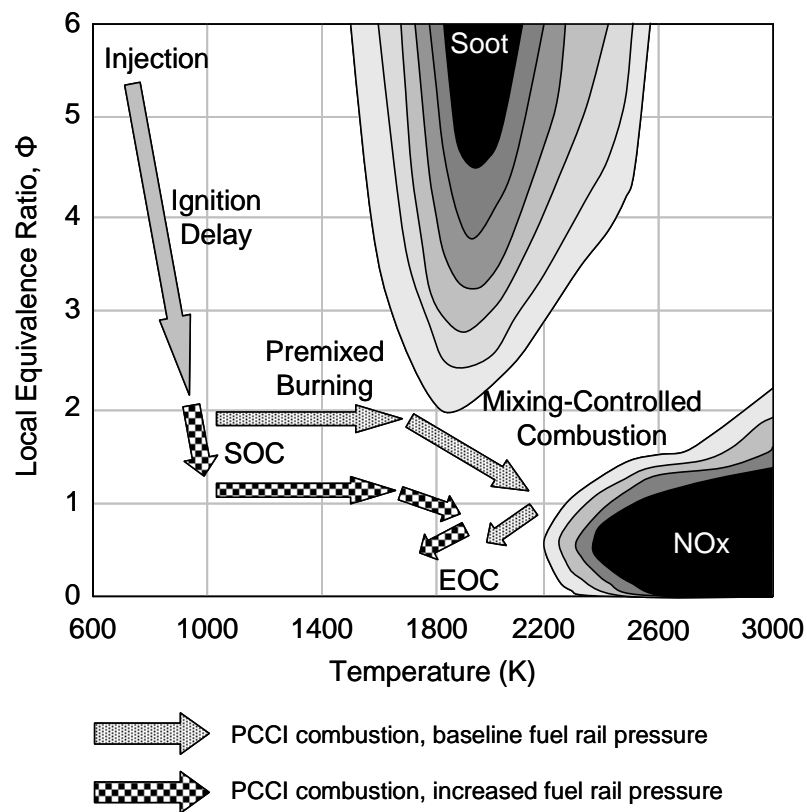


Figure 8.6: Qualitative Φ -T map illustrating effect of increasing fuel rail pressure on proposed paths taken by typical fuel parcels for a generic PCCI combustion strategy

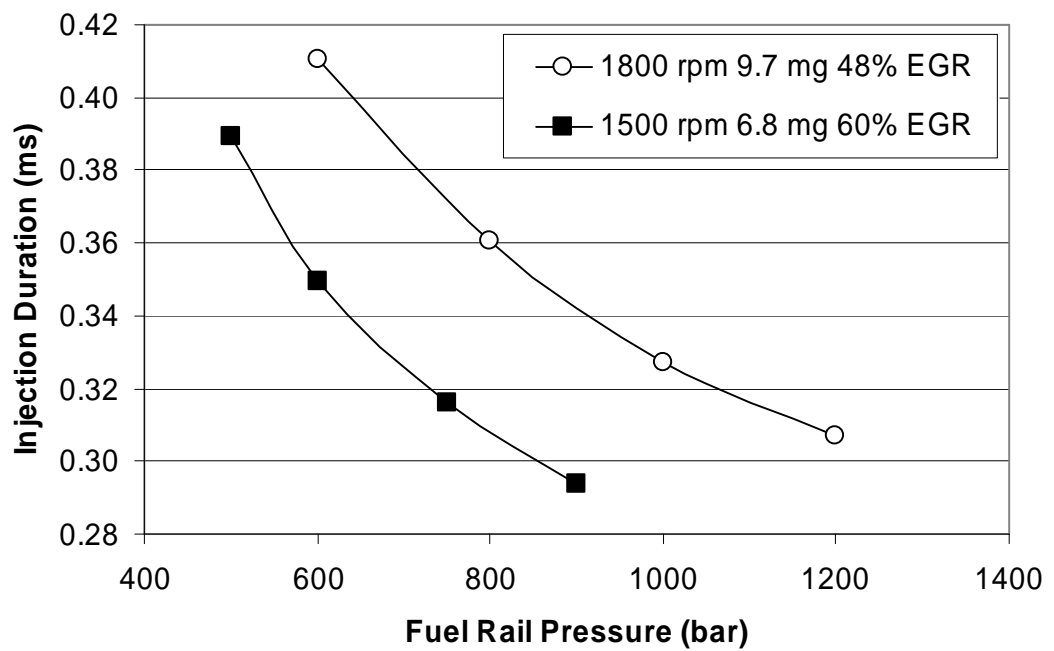


Figure 8.7: Reduction of injection duration with increasing rail pressure (data from INCA)

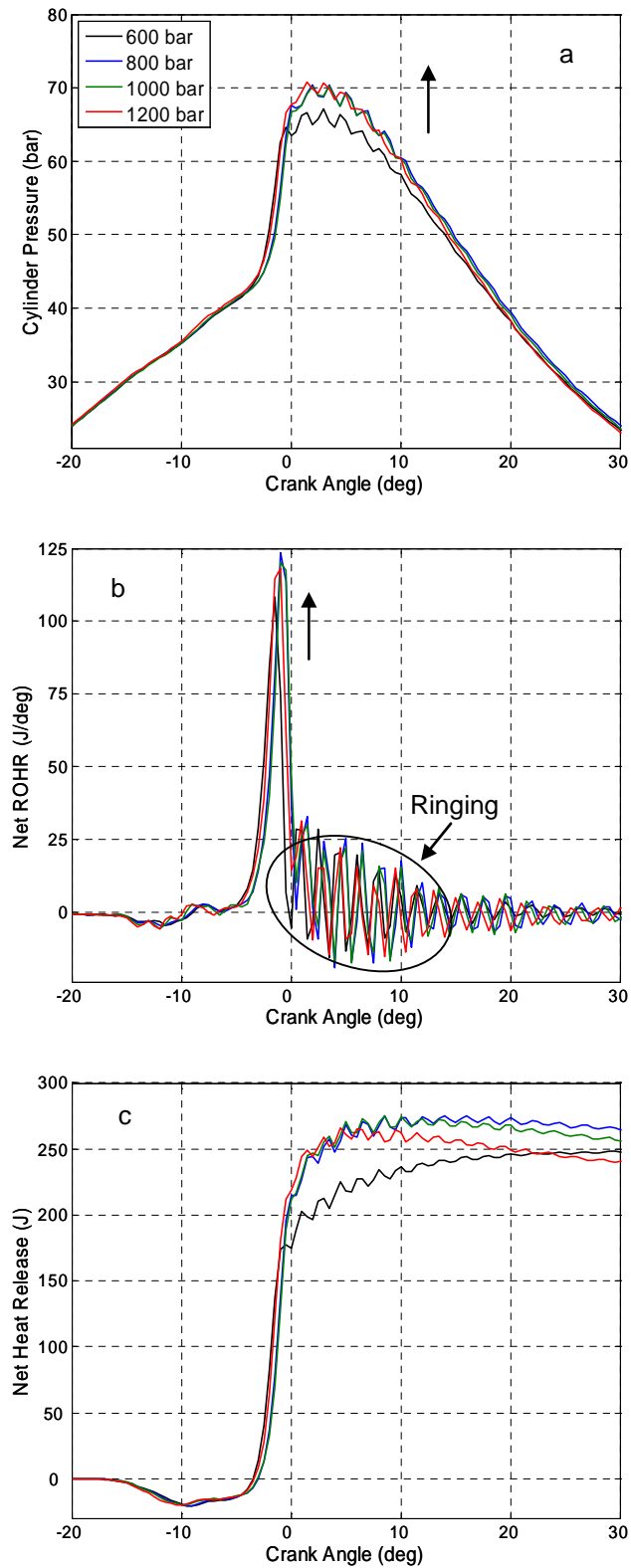


Figure 8.8: In-cylinder analysis at SOI of -17.5°ATDC, 1800 rpm 9.7 mg EGR 48% a) Cylinder Pressure (bar), b) Net rate of heat release (J/°), c) Cumulative net heat release (J). Arrows indicate effect on combustion characteristics with increasing rail pressure.

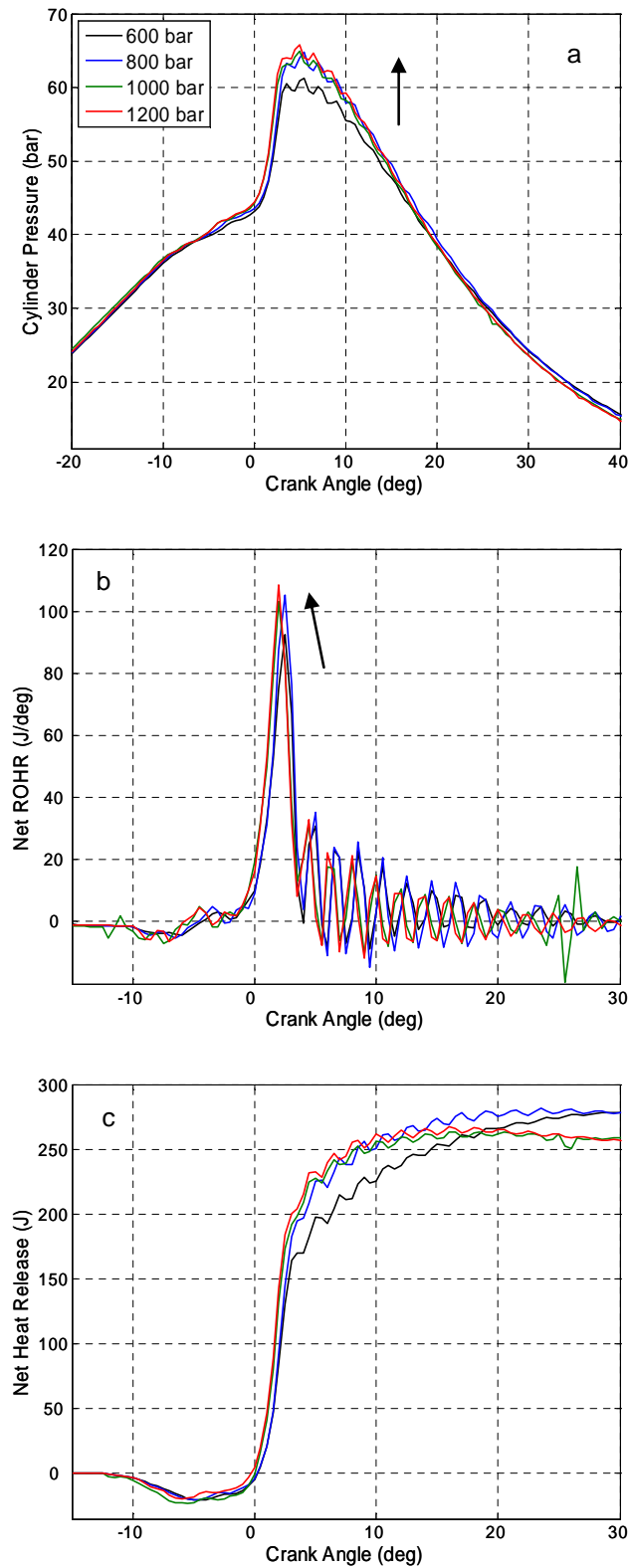


Figure 8.9: In-cylinder analysis at SOI of -12.5°ATDC, 1800 rpm 9.7 mg EGR 48% a) Cylinder Pressure (bar), b) Net rate of heat release (J/°), c) Cumulative net heat release (J). Arrows indicate effect on combustion characteristics with increasing rail pressure.

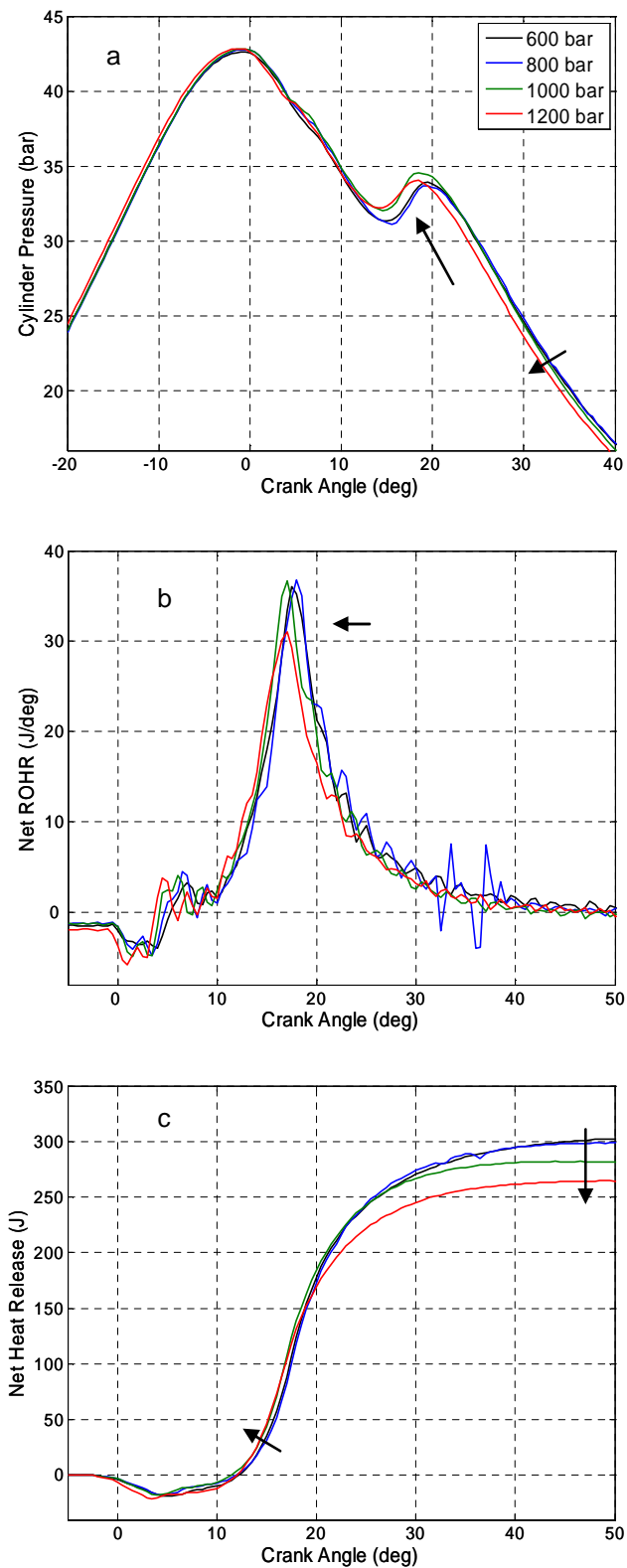


Figure 8.10: In-cylinder analysis at SOI of -2.5°ATDC, 1800 rpm 9.7 mg EGR 48% a) Cylinder Pressure (bar), b) Net rate of heat release (J/°), c) Cumulative net heat release (J). Arrows indicate effect on combustion characteristics with increasing rail pressure.

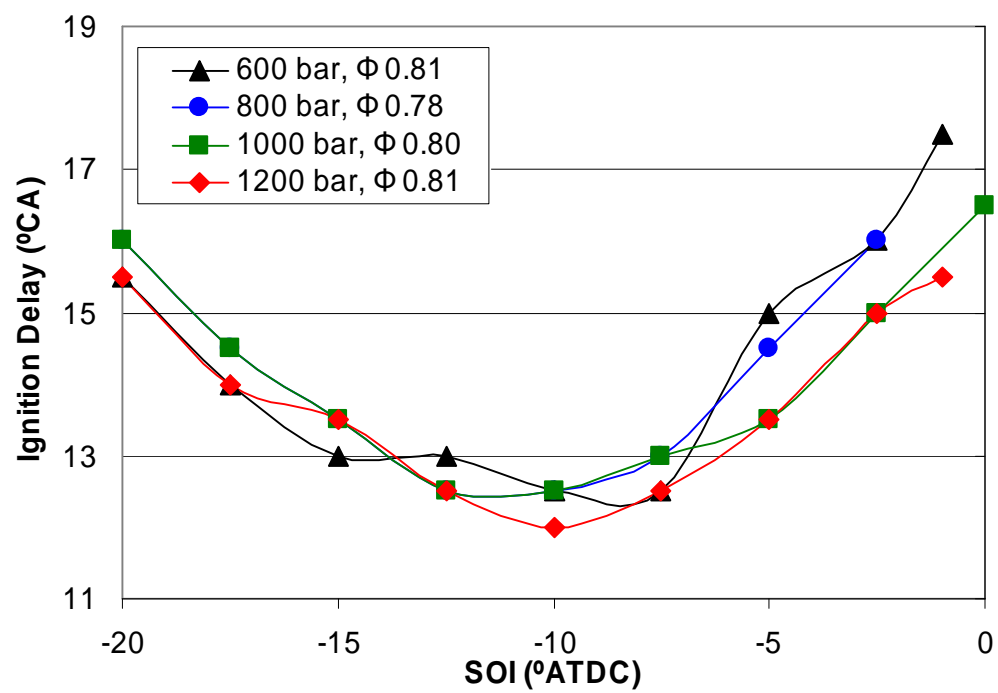


Figure 8.11: Effect of fuel injection pressure on ignition delay. Case B: 1800 rpm 9.7 mg 48% EGR. Legend entries give fuel rail pressure and average fuel-air equivalence ratio.

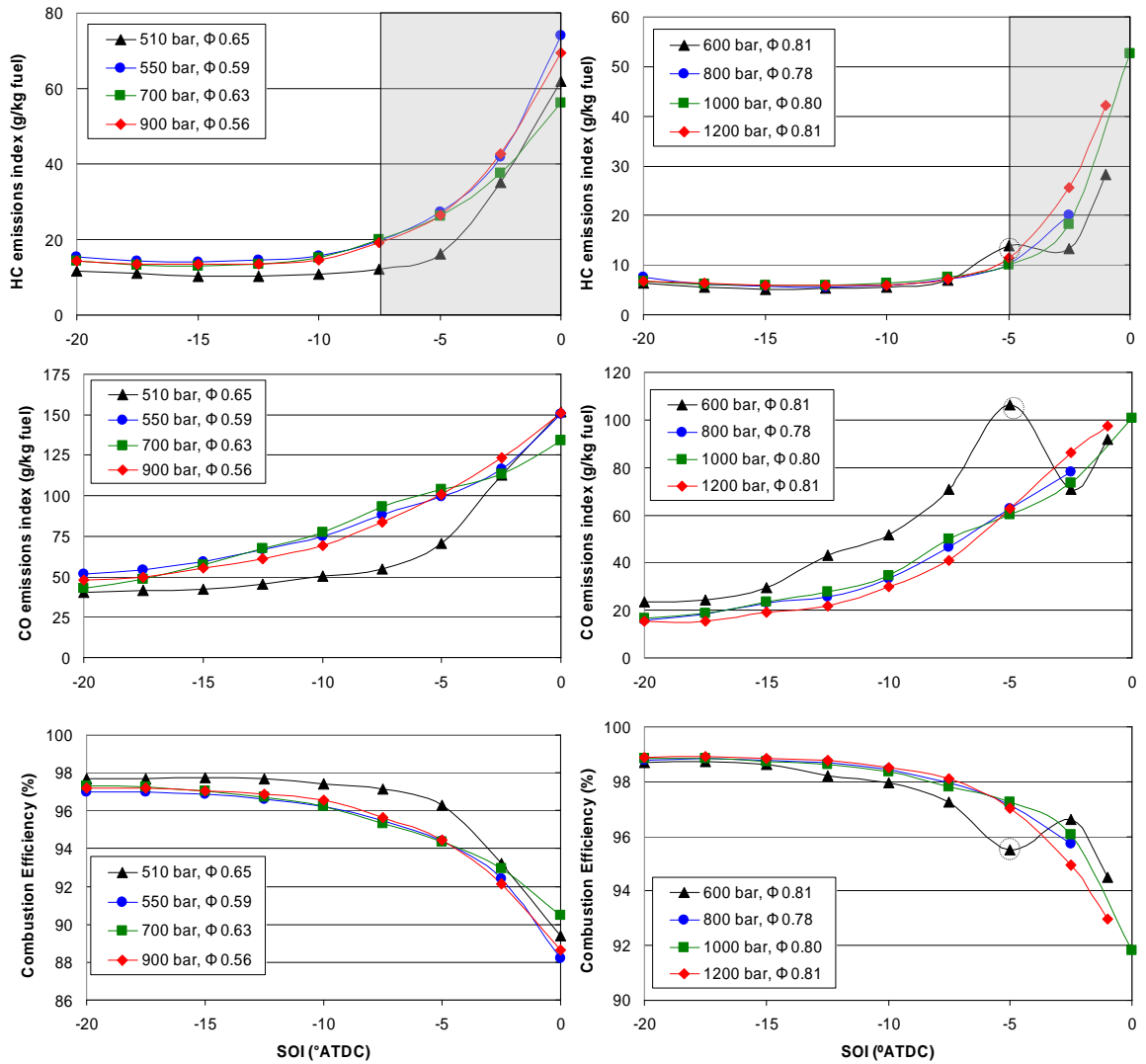


Figure 8.12: Effect of fuel rail pressure on CO and HC output and combustion efficiency. Left: Case A 1500 rpm 6.8 mg 60% EGR. Right: Case B 1800 rpm 9.7 mg 48% EGR. Legend entries give fuel rail pressure and average fuel-air equivalence ratio for that data set. Shaded areas represent regions of significantly deteriorating emissions.

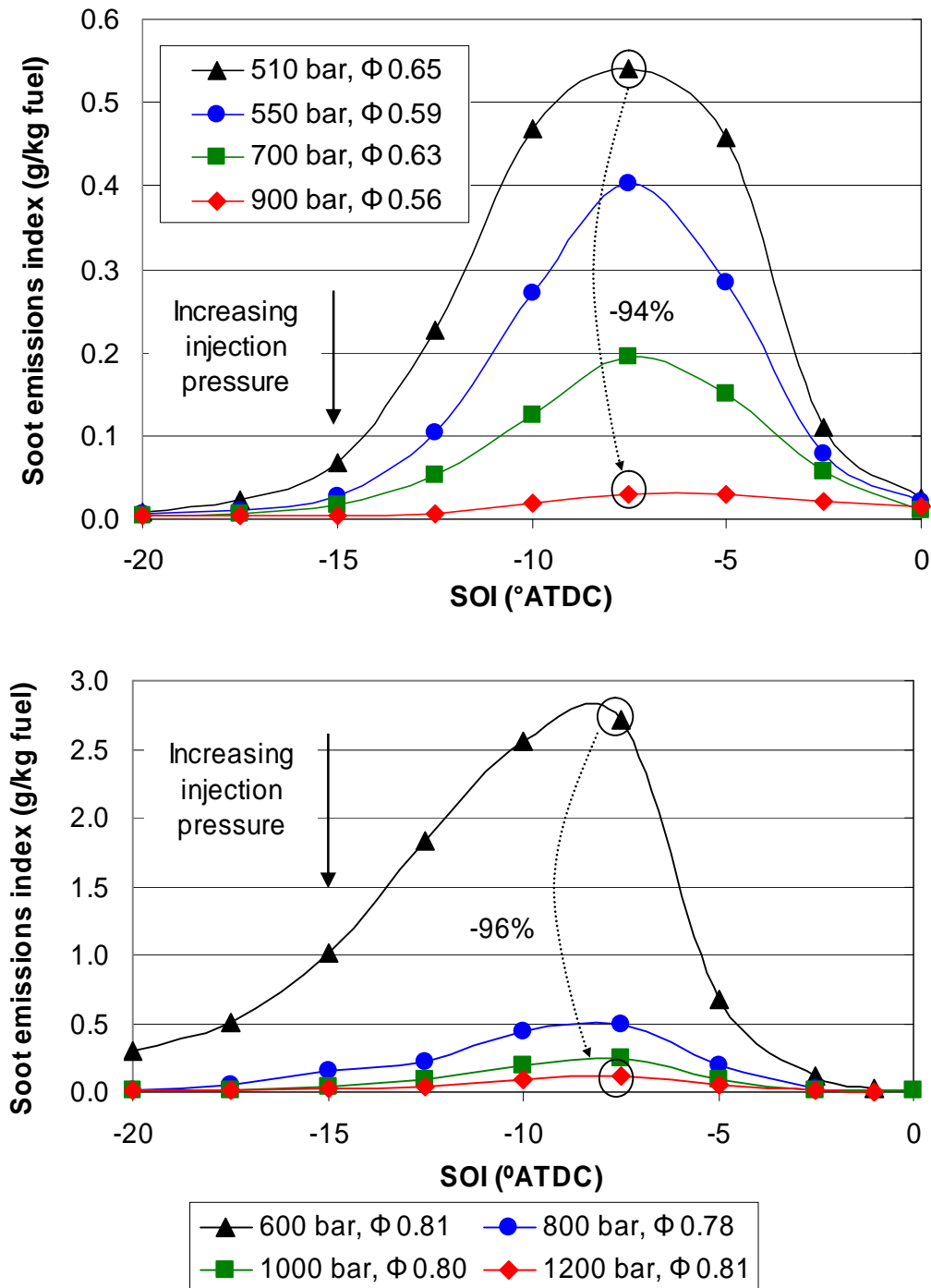


Figure 8.13: Effect of fuel injection pressure on soot emissions. Top: Case A 1500 rpm 6.8 mg 60% EGR. Bottom: Case B 1800 rpm 9.7 mg 48% EGR. Dotted arrows indicate soot reduction of peak values when increasing rail pressure from minimum to maximum values presented. Legend entries give fuel rail pressure and average fuel-air equivalence ratio for that data set.

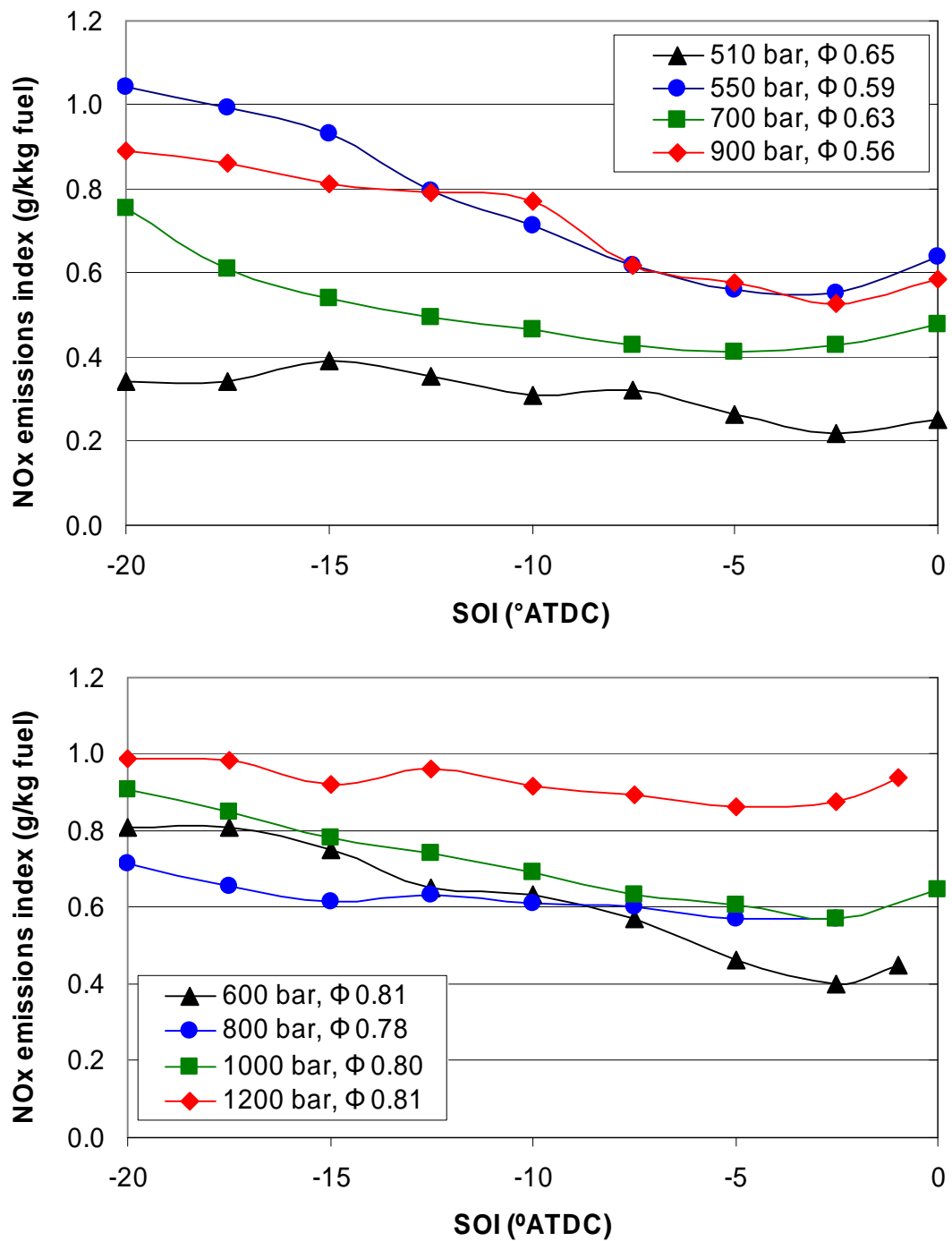


Figure 8.14: Effect of fuel injection pressure on NO_x emissions. Top: Case A 1500 rpm 6.8 mg 60% EGR. Bottom: Case B 1800 rpm 9.7 mg 48% EGR. Legend entries give fuel rail pressure and average fuel-air equivalence ratio for that data set.

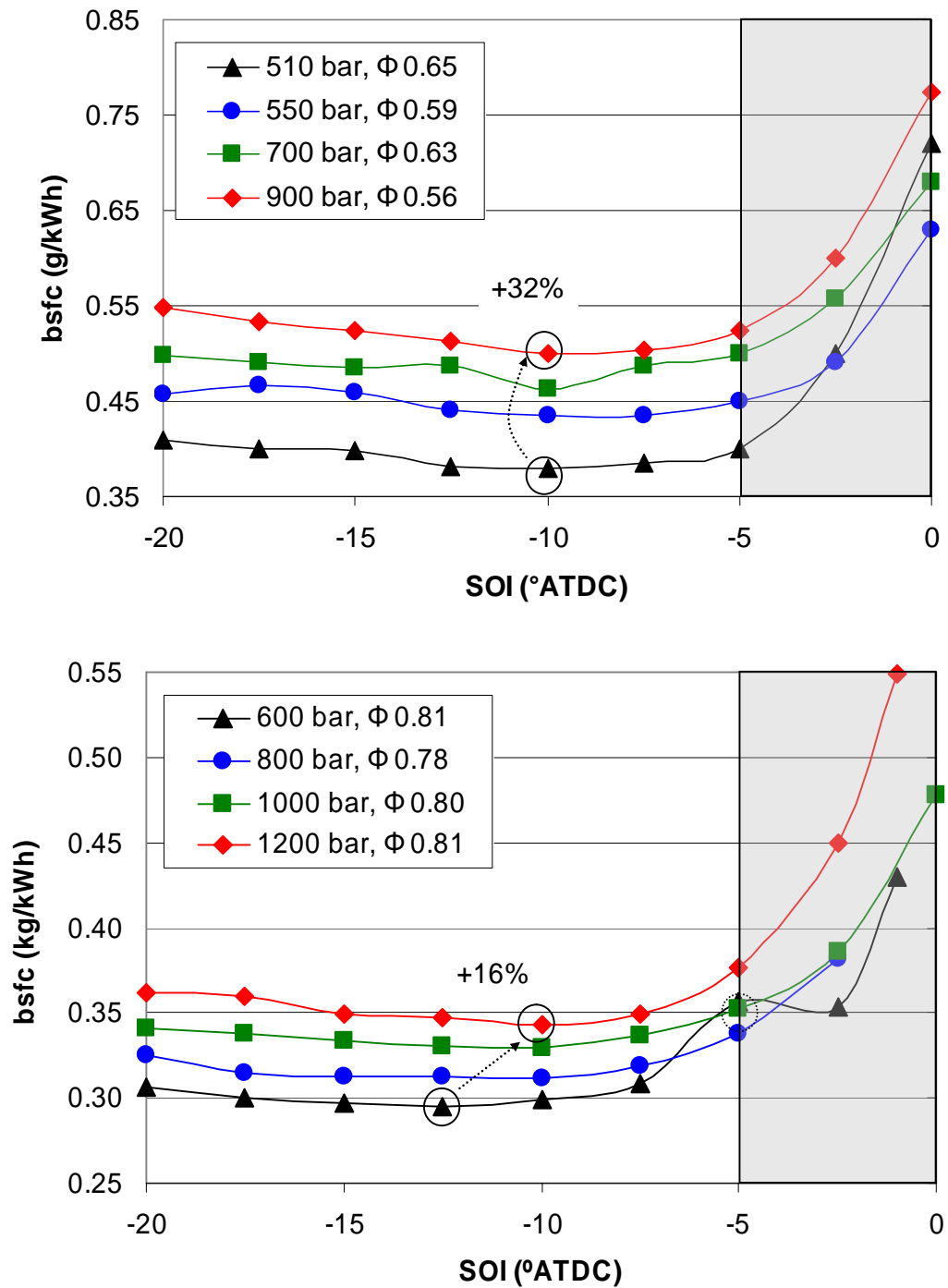


Figure 8.15: Effect of fuel injection pressure on bsfc. Top: Case A 1500 rpm 6.8 mg 60% EGR. Bottom: Case B 1800 rpm 9.7 mg 48% EGR. Dotted arrows indicate bsfc increase from minimum values when increasing rail pressure from minimum to maximum values presented. Shaded areas represent regions of significantly deteriorating fuel consumption. Legend entries give fuel rail pressure and average fuel-air equivalence ratio for that data set.

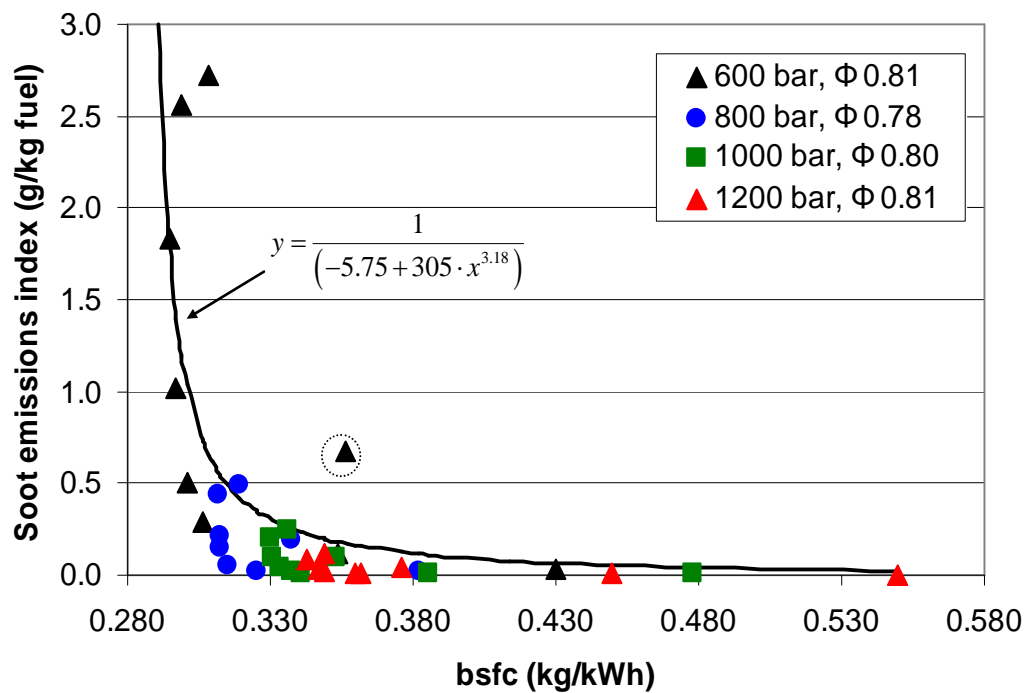


Figure 8.16: Soot-fuel consumption trade-off with varying injection timing and pressure. Case B: 1800 rpm 9.7 mg 48% EGR. Legend entries give fuel rail pressure and average fuel-air equivalence ratio for that data set. Labelled is the non-linear regressional model fitted to the data.

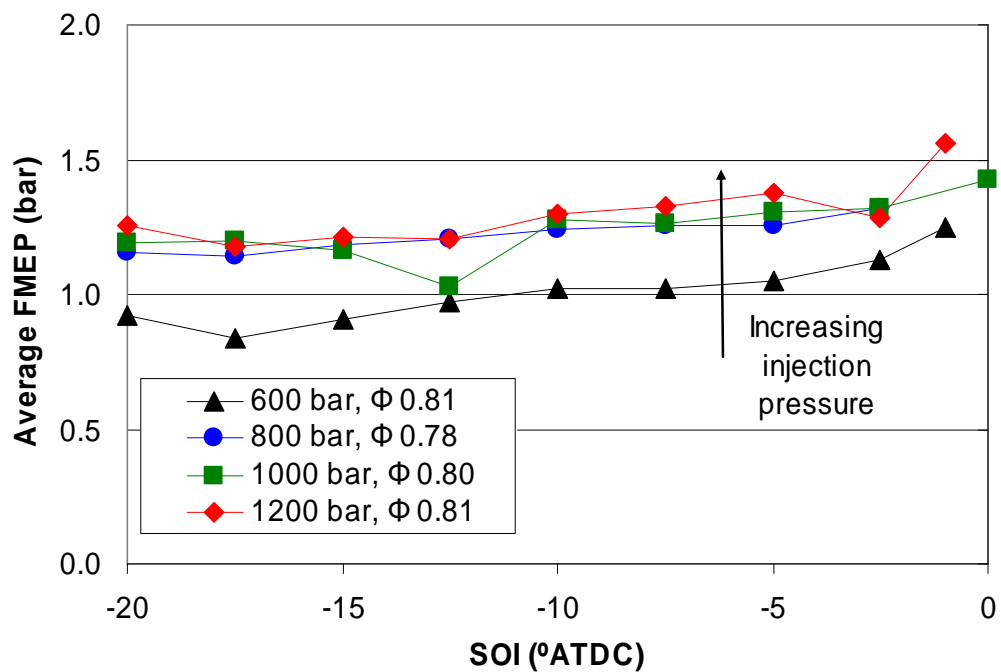


Figure 8.17: FMEP variation with injection pressure. Averaged values from cylinders 3 and 4. Data at 1800 rpm 9.7 mg 48% EGR. Legend entries give fuel rail pressure and average fuel-air equivalence ratio for that data set.

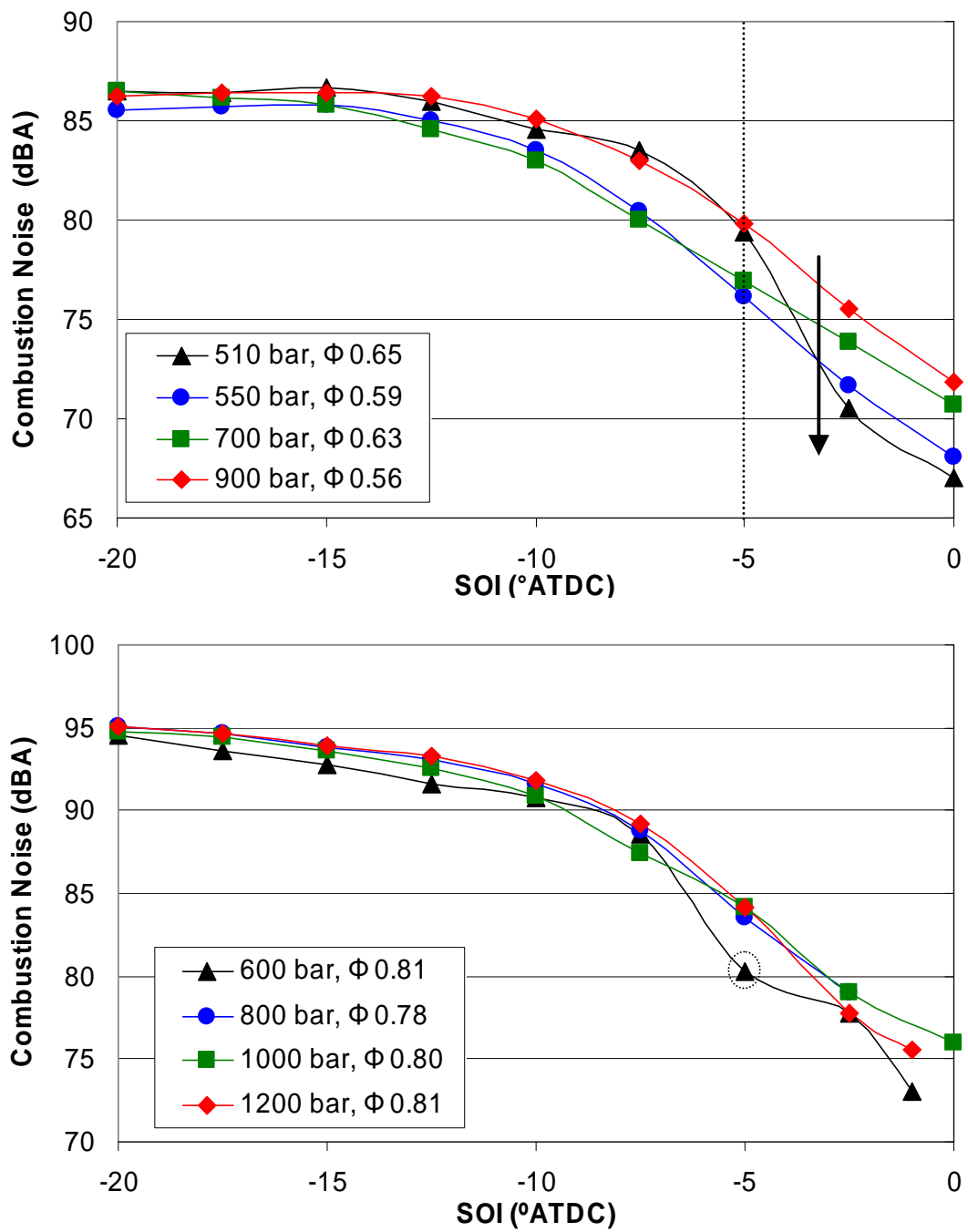


Figure 8.18: Effect of fuel injection pressure on combustion noise. *Top: Case A 1500 rpm 6.8 mg 60% EGR. Bottom: Case B 1800 rpm 9.7 mg 48% EGR. Legend entries give fuel rail pressure and average fuel-air equivalence ratio for that data set.*

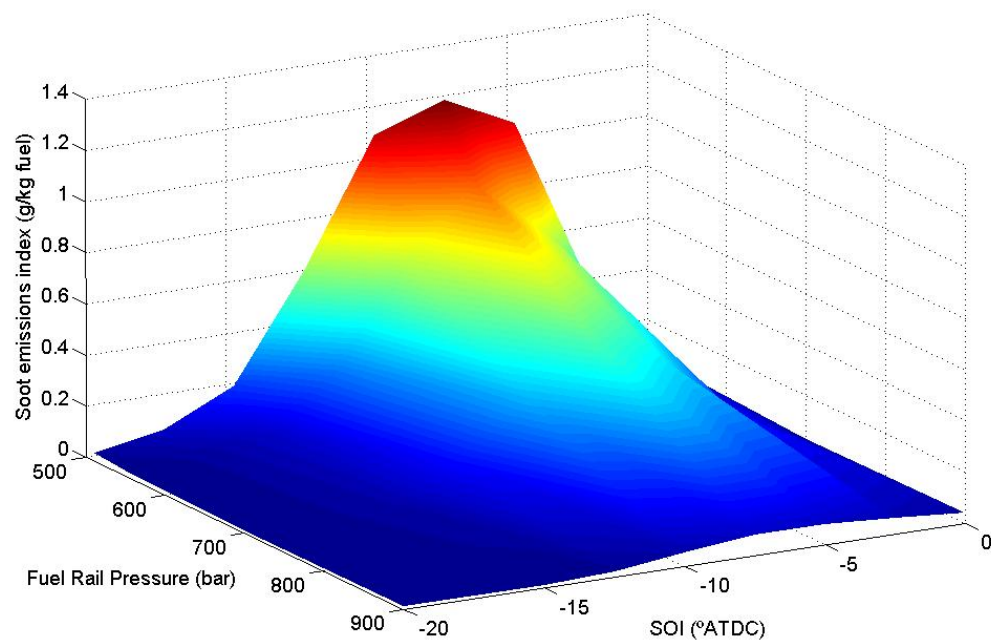


Figure 8.19: 3D Surface plot illustrating the non-linear dependence of soot emissions on fuel rail pressure and injection timing for case A (1500 rpm 6.8 mg 60% EGR)

CHAPTER 9

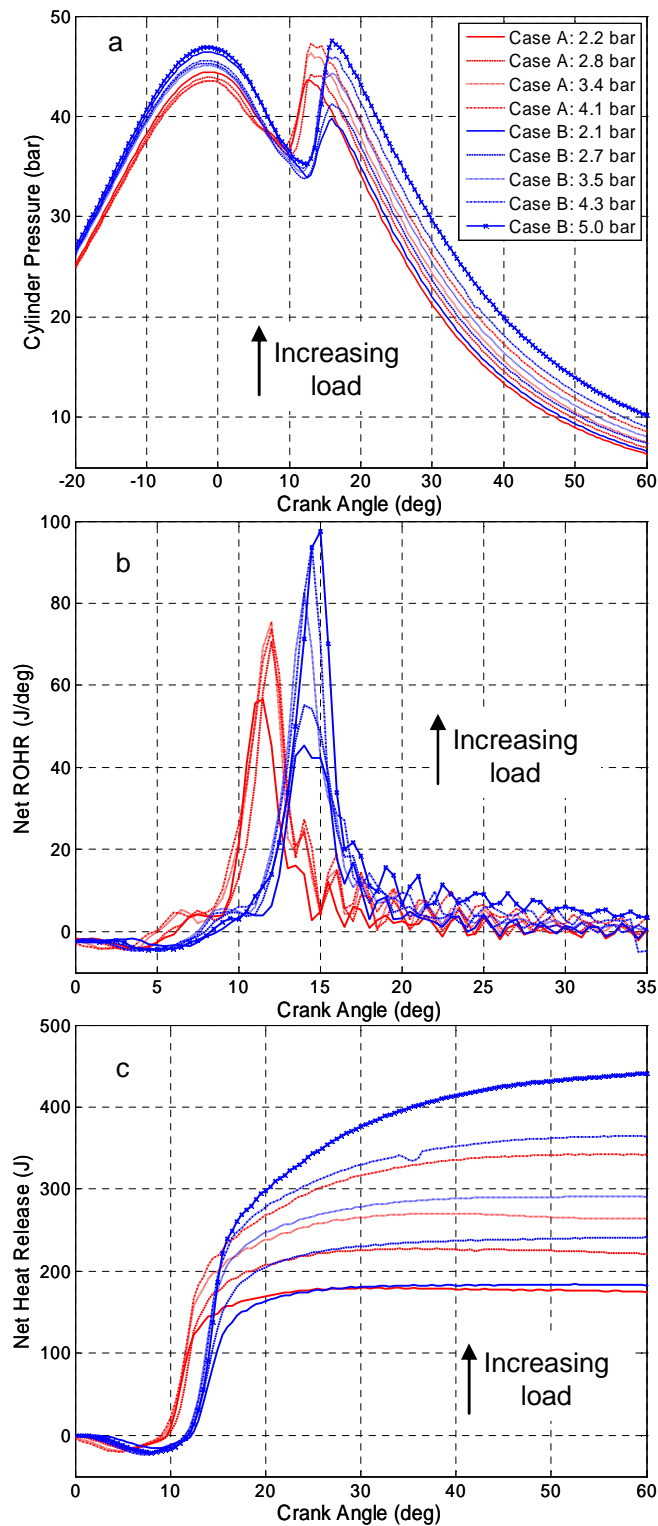


Figure 9.1: In-cylinder analyses for Cases A (red) and B (blue) with increasing loads at 550 bar fuel rail pressure. a) Cylinder Pressure (bar), b) Net rate of heat release ($\text{J}/^\circ$), c) Cumulative net heat release (J). Arrows indicate increasing load. Legend entries correspond to case and gross IMEP output

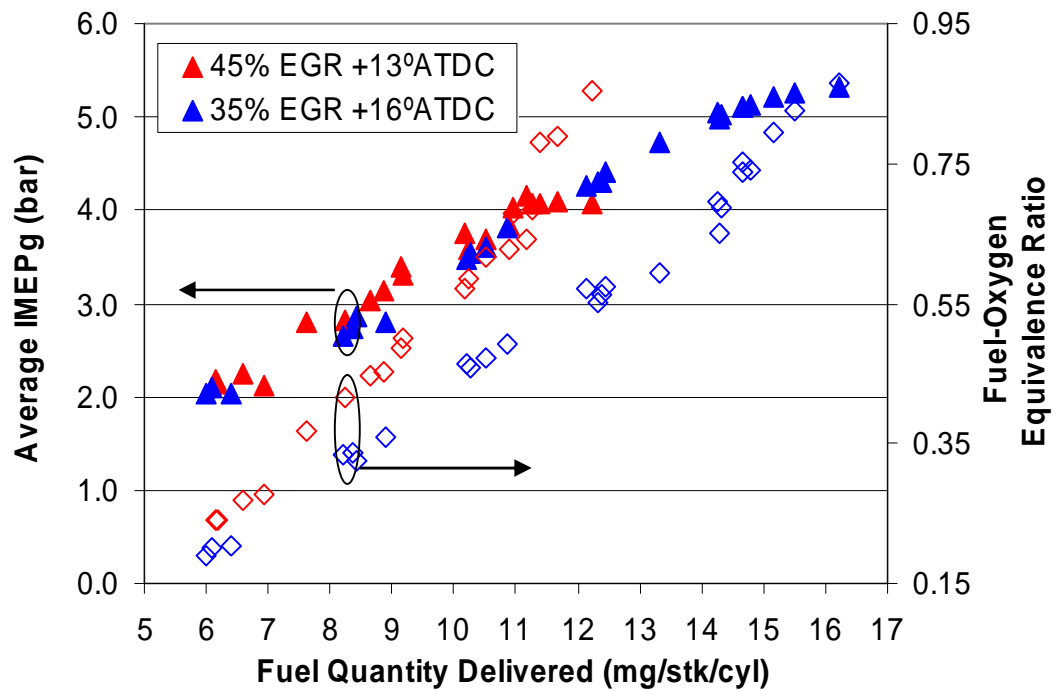


Figure 9.2: Effect on gross IMEP load output (solid) and fuel-oxygen equivalence (hollow) with increasing fuel quantity delivered at 1500 rpm. Average IMEP from cylinders 3 and 4. Case A (red): 45% EGR location of peak pressure +13°ATDC. Case B (blue): 35% EGR location of peak pressure +16°ATDC.

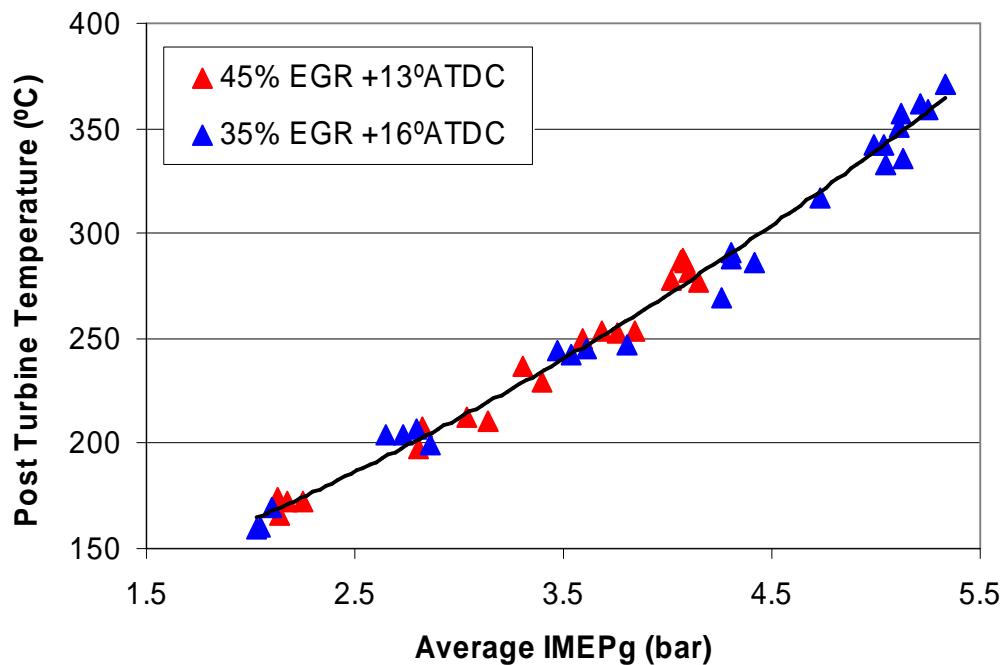


Figure 9.3: Relationship between gross IMEP (averaged between cylinders 3 and 4) and exhaust gas temperature post-turbine (bank B) at 1500 rpm. Legend entries give EGR rate and constant combustion phasing location (peak pressure), Case A (red), Case B (blue)

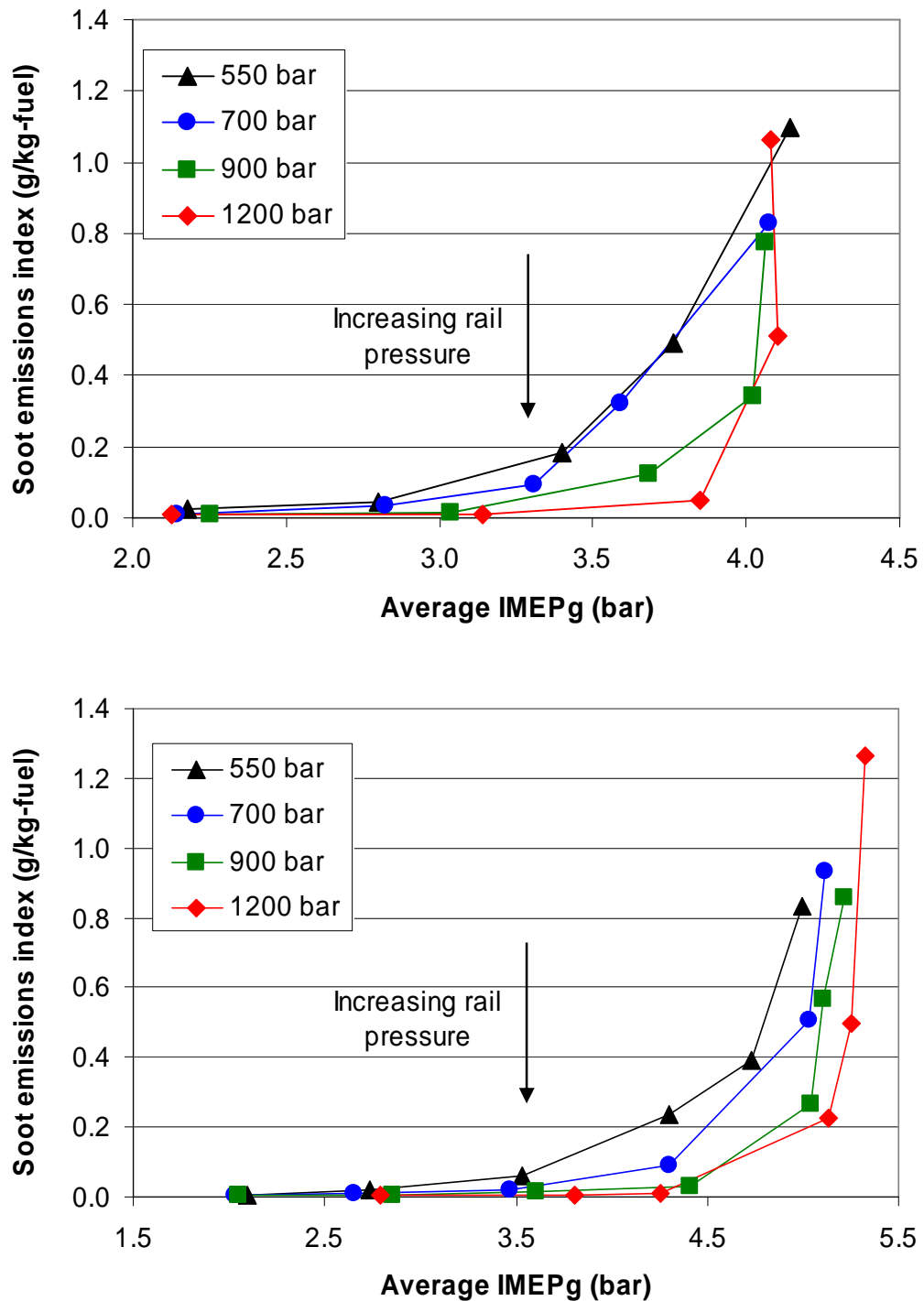


Figure 9.4: Effect on soot output with increasing load. Contours are for different fuel rail pressures at 1500 rpm. Average IMEP from cylinders 3 and 4. Top: Case A 45% EGR location of peak pressure +13°ATDC. Bottom: Case B 35% EGR location of peak pressure +16°ATDC

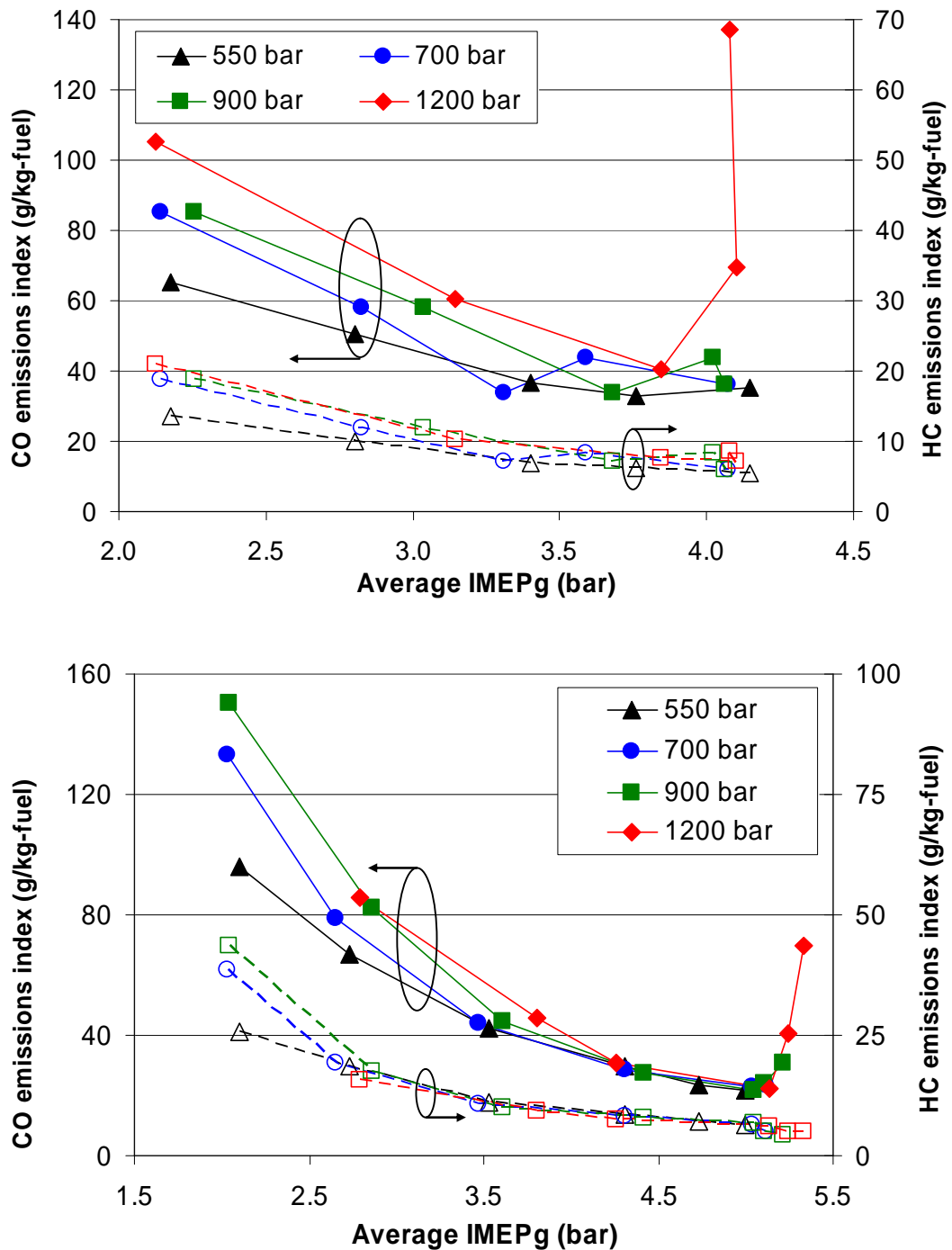


Figure 9.5: CO (solid) and HC (hollow) variation with increasing load at 1500 rpm. Average IMEP from cylinders 3 and 4. Top: Case A 45% EGR location of peak pressure +13°ATDC. Bottom: Case B 35% EGR location of peak pressure +16°ATDC

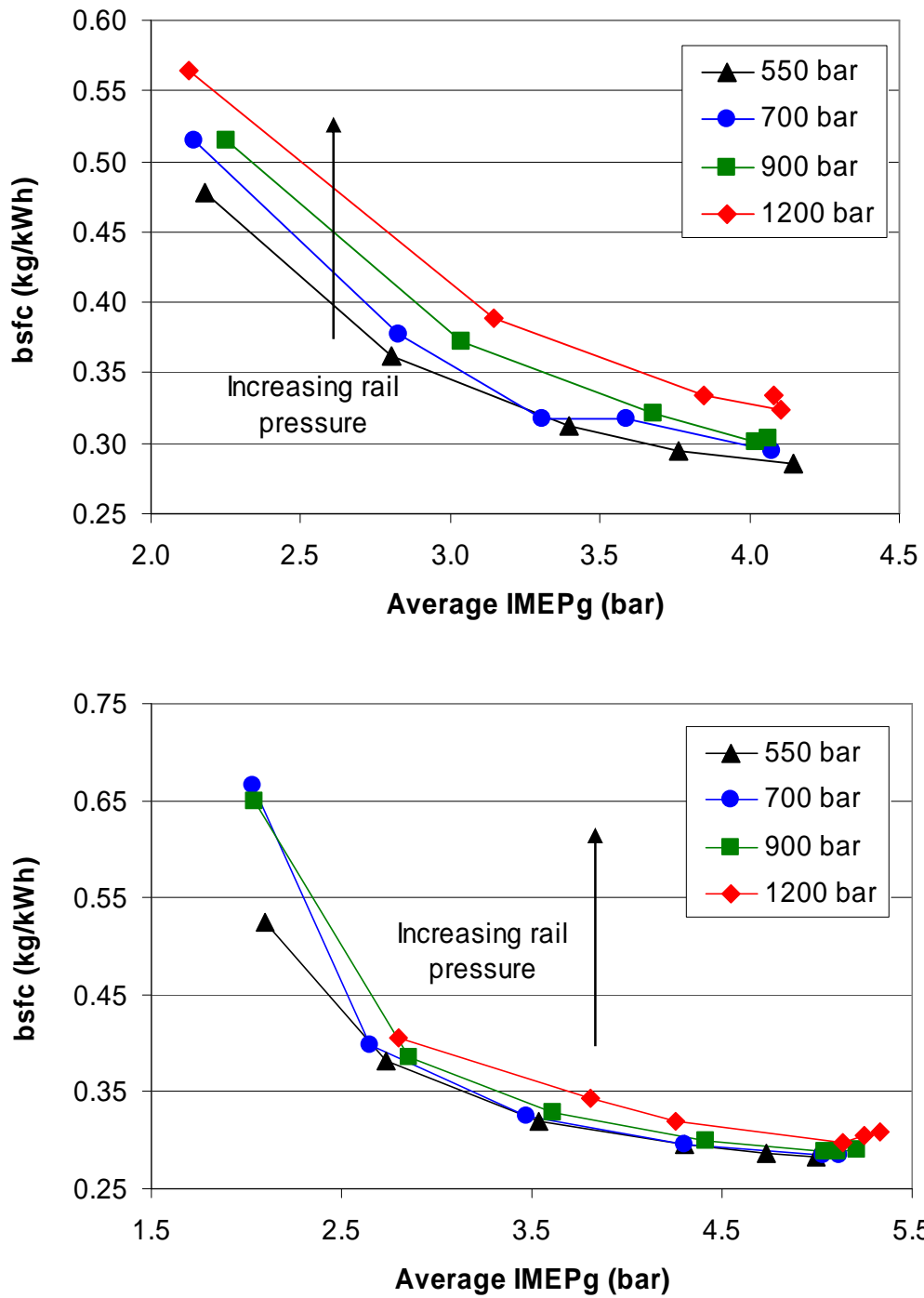


Figure 9.6: Effect on bsfc with increasing load for different rail pressures at 1500 rpm Average IMEP from cylinders 3 and 4. Top: Case A 45% EGR location of peak pressure +13°ATDC. Bottom: Case B 35% EGR location of peak pressure +16°ATDC

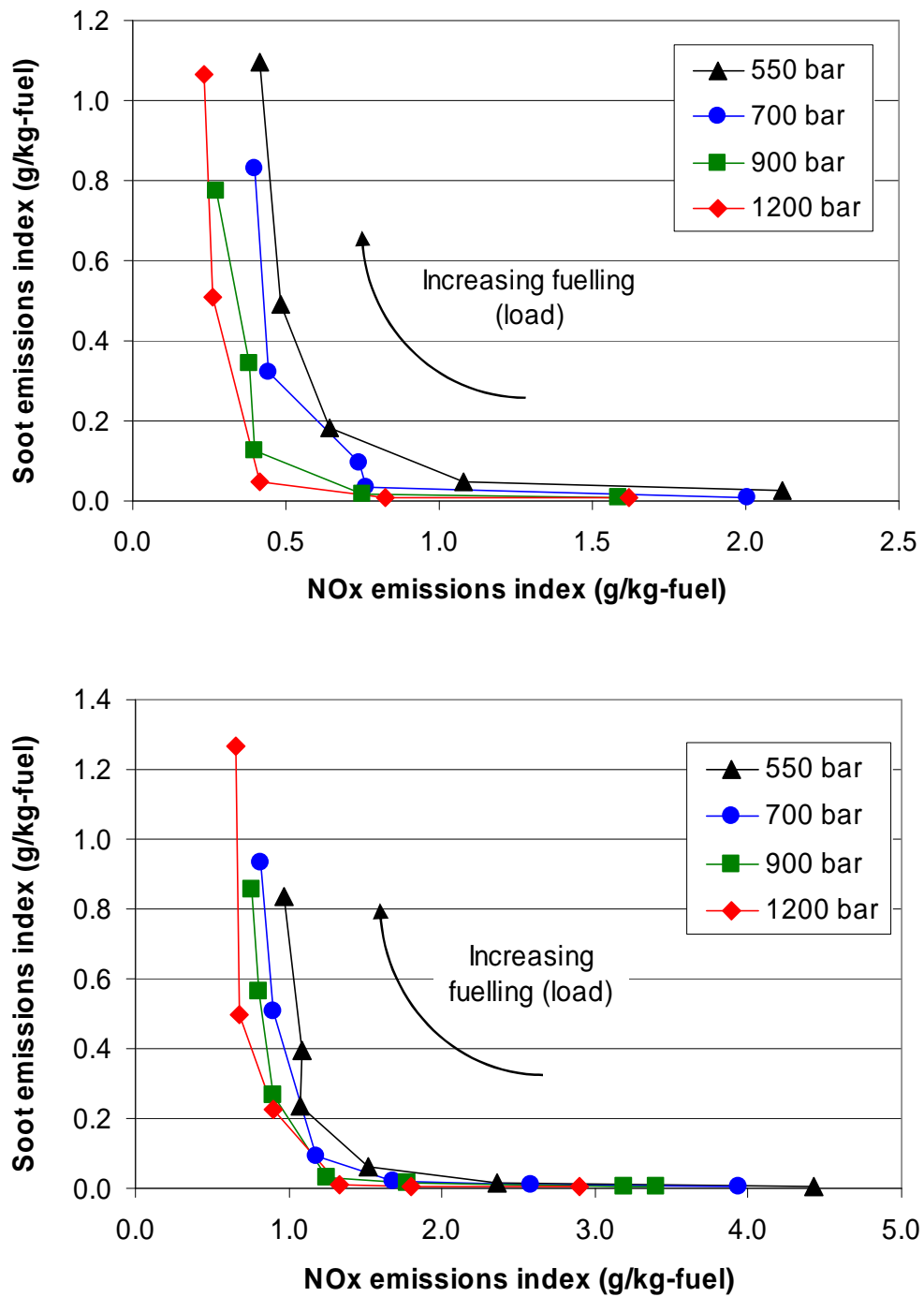


Figure 9.7: NO_x-Soot trade-off as load is increased at 1500 rpm. Top: Case A 45% EGR location of peak pressure +13°ATDC. Bottom: Case B 35% EGR location of peak pressure +16°ATDC

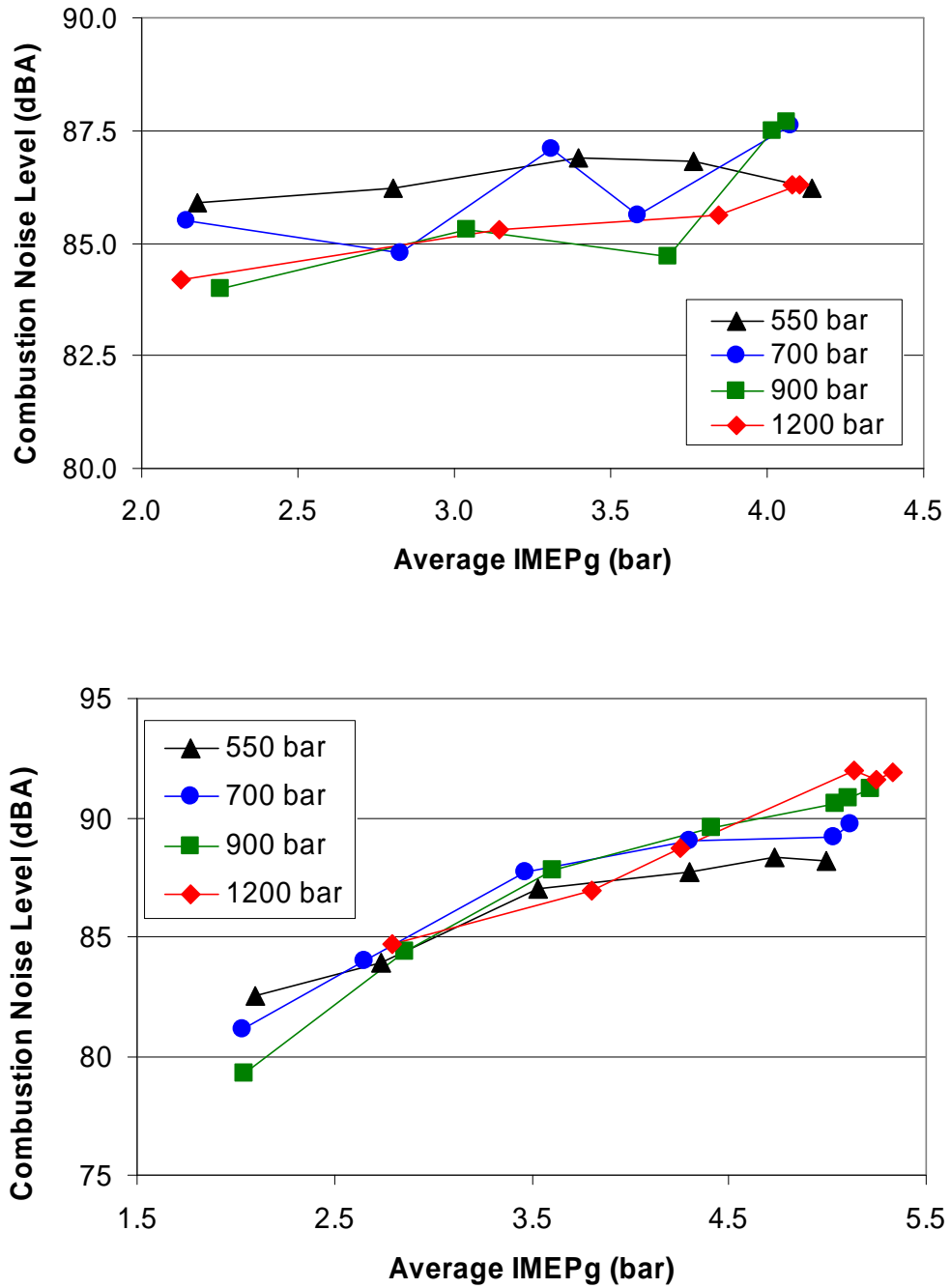


Figure 9.8: Effect on combustion noise level with increasing load for different rail pressures at 1500 rpm. Average gross IMEP from cylinders 3 and 4. Top: Case A 45% EGR location of peak pressure +13°ATDC. Bottom: Case B 35% EGR location of peak pressure +16°ATDC

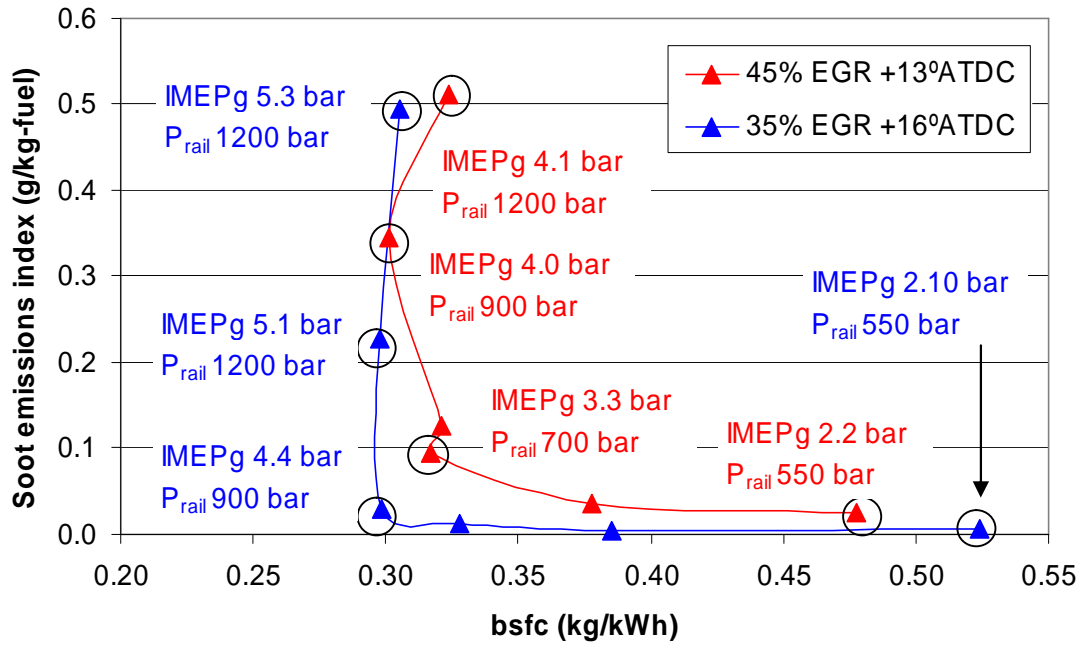


Figure 9.9: Summary soot-bsfc trade-off curves with soot minimised for bsfc values within 5% of the baseline value obtained at that IMEPg load output. Legend entries give EGR rate and constant combustion phasing location (peak pressure), Case A (red), Case B (blue).

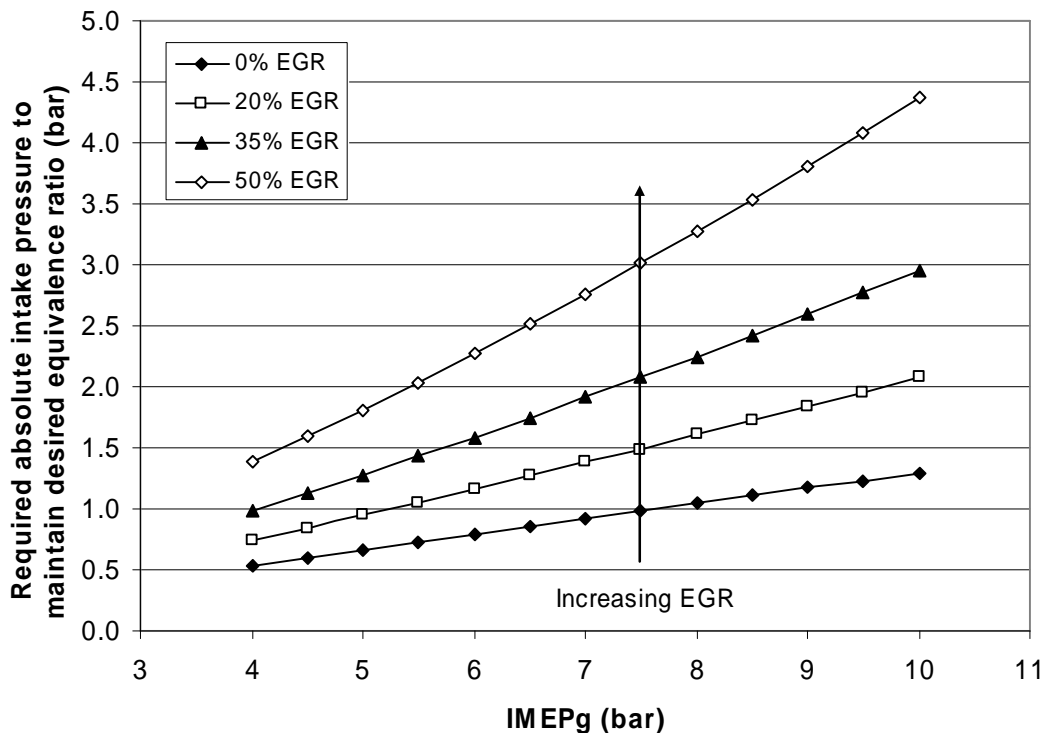


Figure 9.10: Required absolute intake pressure to maintain fuel-air equivalence ratio of $\Phi=0.7$ as a function of engine load. Assumed $\eta_{vol}=90\%$, $AFR_s=14.6$, $N=1500$ rpm, $T_{air}=35^\circ\text{C}$, T_{EGR} estimated through data extrapolation

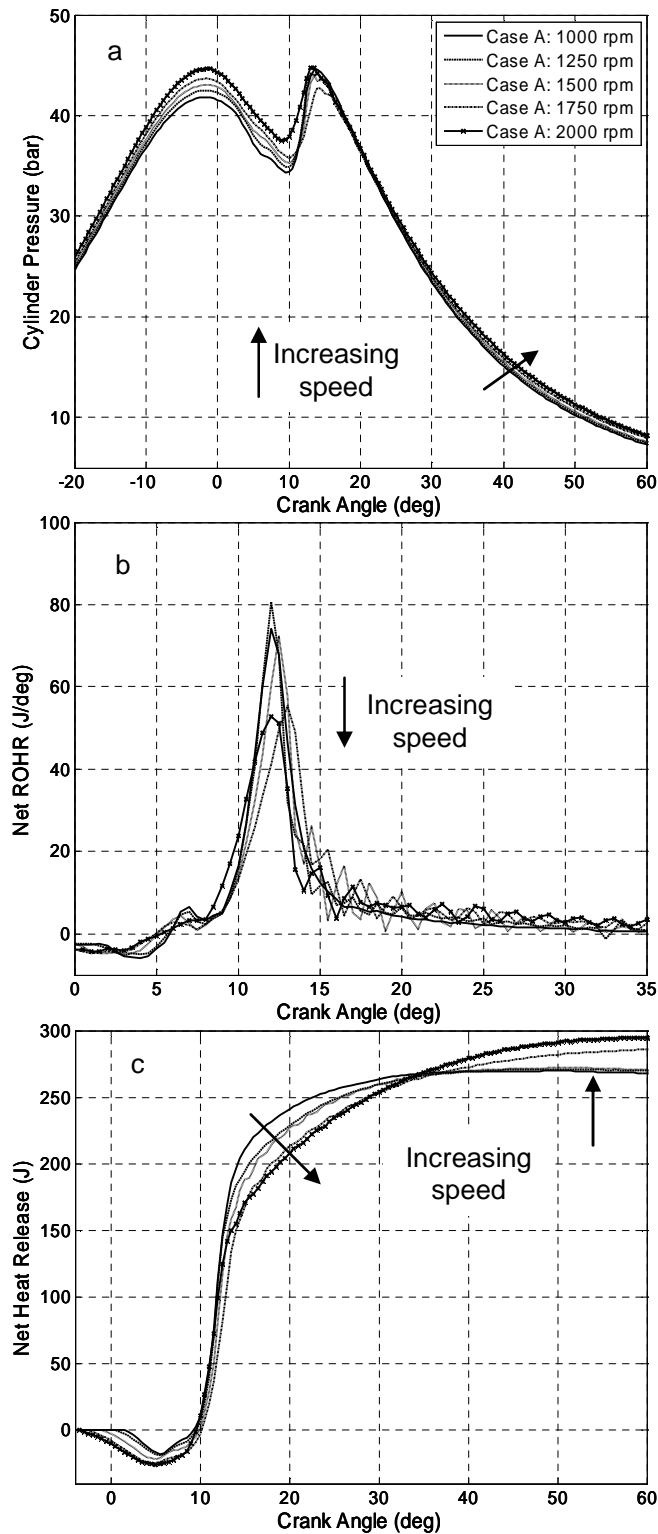


Figure 9.11: In-cylinder analyses at 2.5 bar BMEP with increasing speed at 550 bar fuel rail pressure. a) Cylinder Pressure (bar), b) Net rate of heat release ($J/^{\circ}$), c) Cumulative net heat release (J). Arrows indicate increasing speed. Legend entries correspond to case and engine speed.

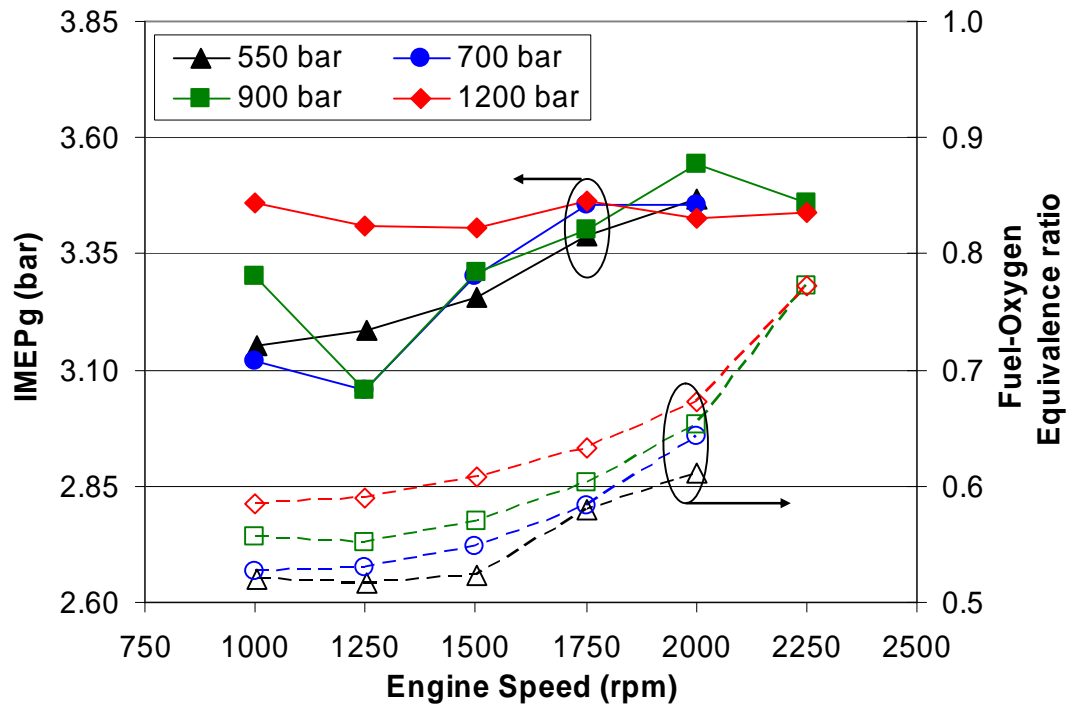


Figure 9.12: Effect on gross IMEP load output (solid) and fuel-oxygen equivalence (hollow) with increasing engine speed at 2.5 bar BMEP. Average IMEP from cylinders 3 and 4, 45% EGR location of peak pressure +13°ATDC

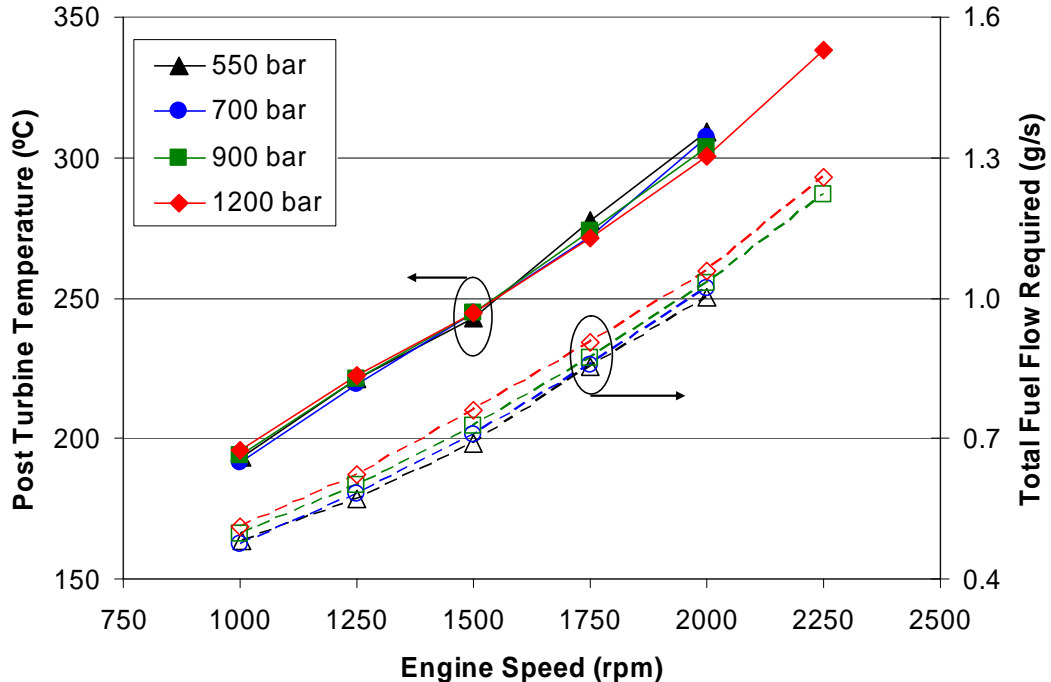


Figure 9.13: Dependence of exhaust gas temperature post-turbine (bank B) and total fuel required to maintain 2.5 bar BMEP load on engine speed, 45% EGR location of peak pressure +13°ATDC. Legend entries give fuel rail pressure.

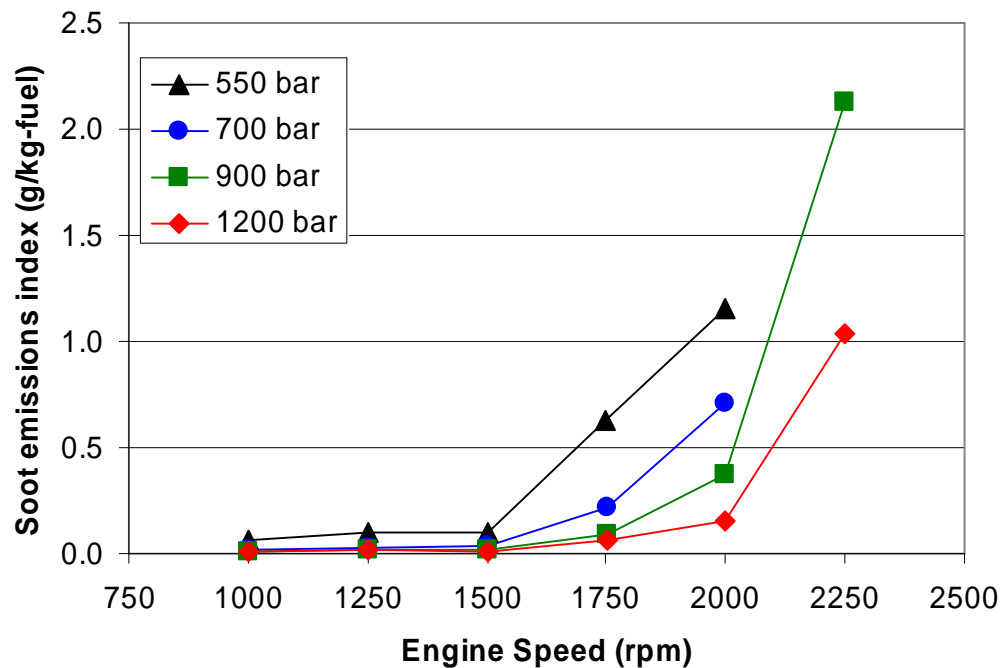


Figure 9.14: Effect on soot output with increasing speed. Contours are for different fuel rail pressures at 2.5 bar BMEP, 45% EGR location of peak pressure +13°ATDC.

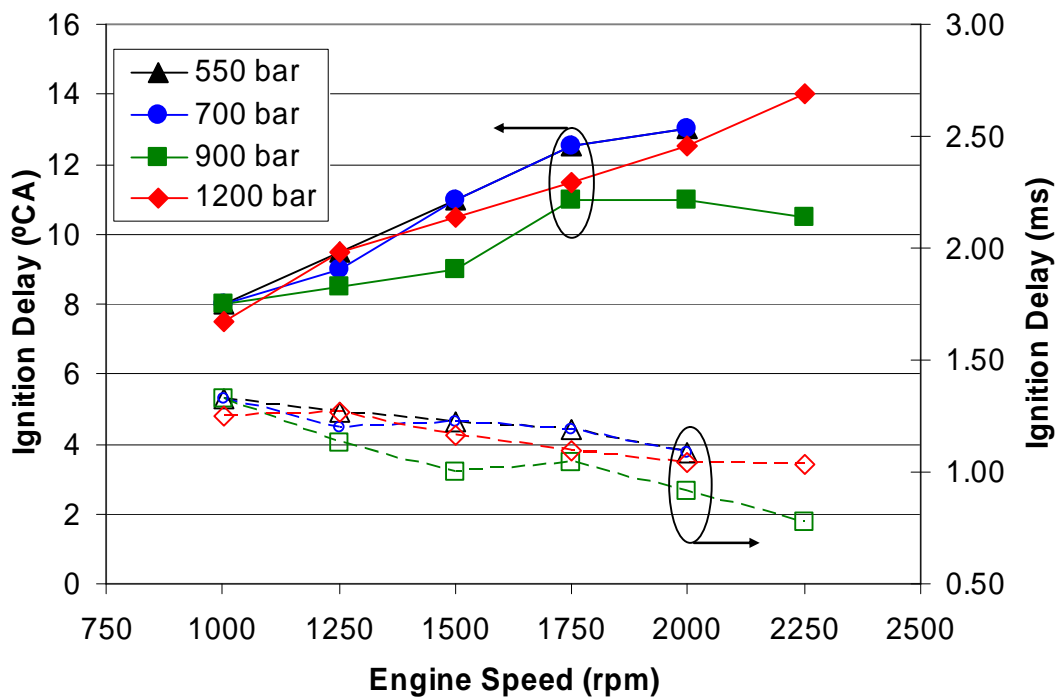


Figure 9.15: Effect on ignition delay in the crank domain (solid) and time domain (hollow) with increasing engine speed at 2.5 bar BMEP, 45% EGR location of peak pressure +13°ATDC

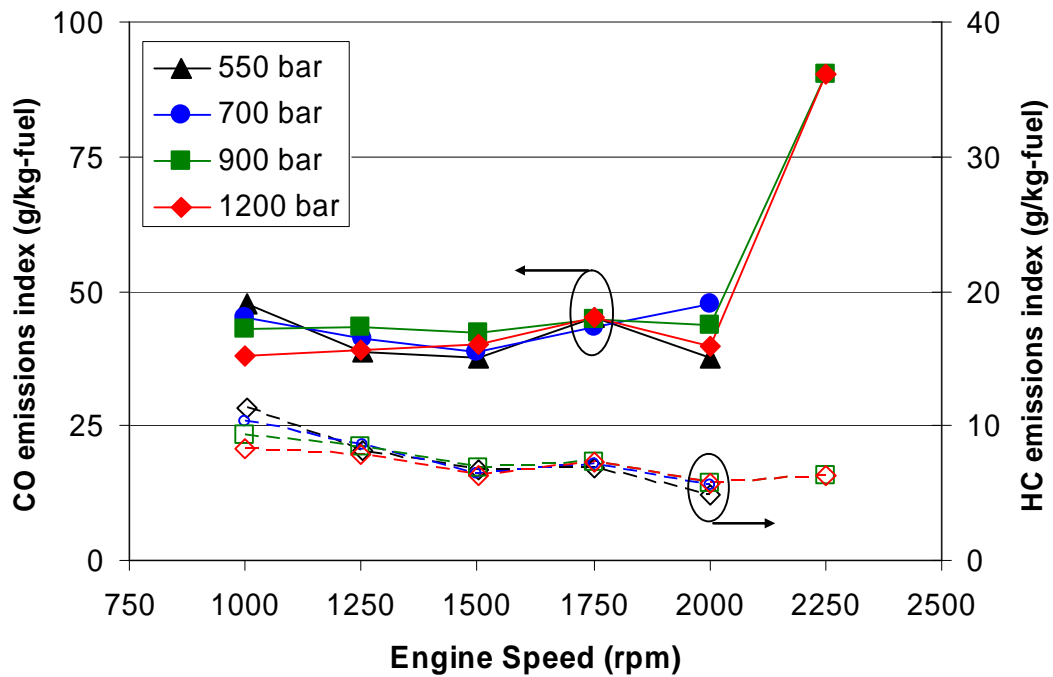


Figure 9.16: CO (solid) and HC (hollow) variation with increasing load at 1500 rpm, 45% EGR location of peak pressure +13°ATDC.

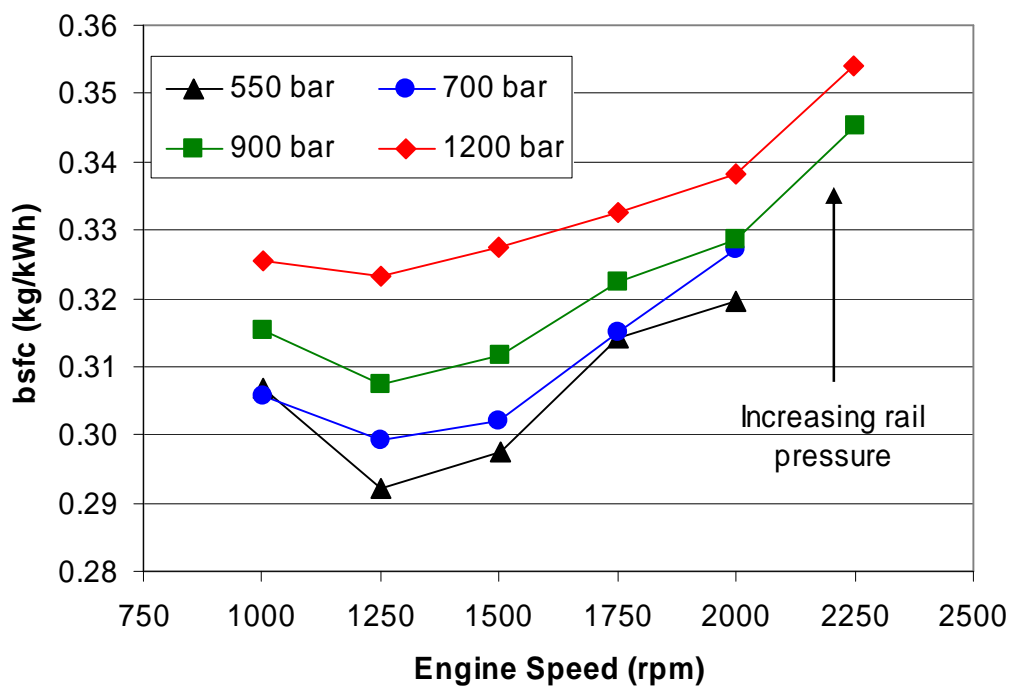


Figure 9.17: Effect on bsfc with increasing speed. Contours are for different fuel rail pressures at 2.5 bar BMEP, 45% EGR location of peak pressure +13°ATDC.

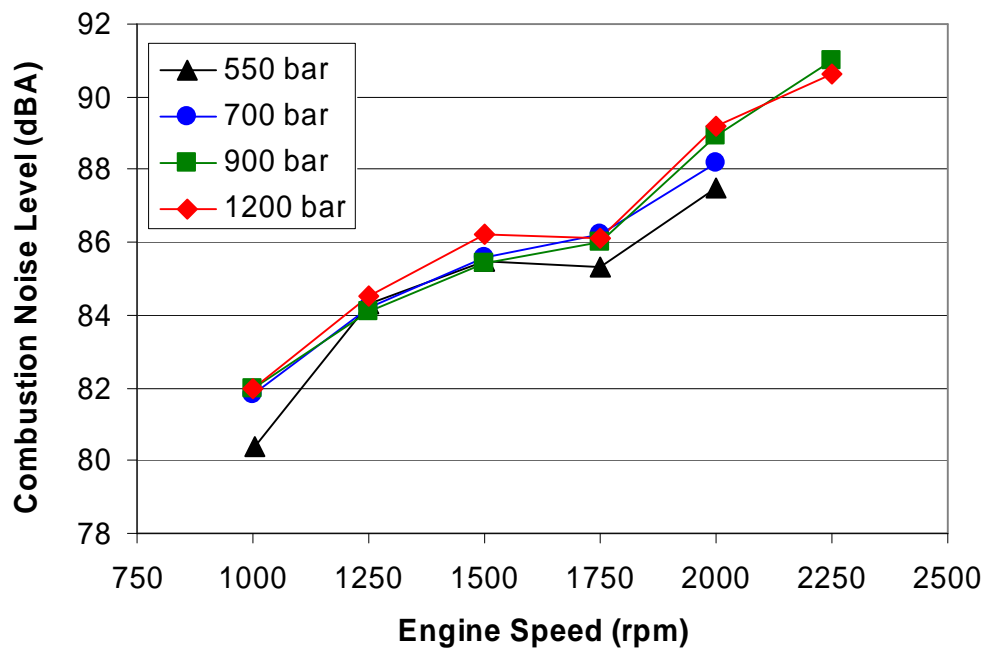


Figure 9.18: Effect on combustion noise level with increasing engine speed for different rail pressures at 1500 rpm, 45% EGR location of peak pressure +13°ATDC.

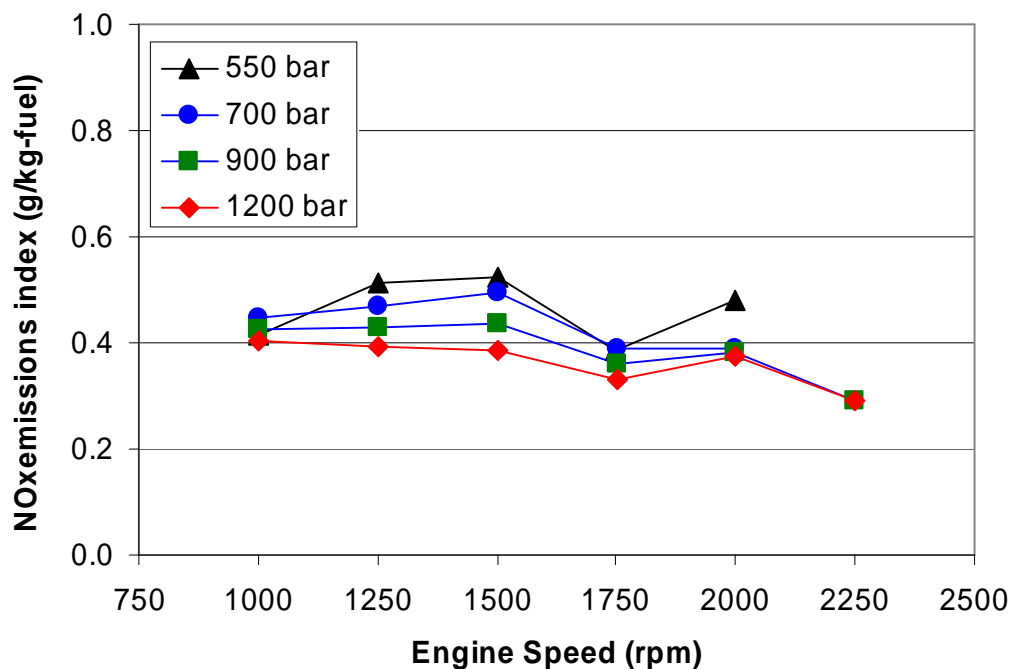


Figure 9.19: Effect NO_x emissions with increasing engine speed for different rail pressures at 1500 rpm, 45% EGR location of peak pressure +13°ATDC.

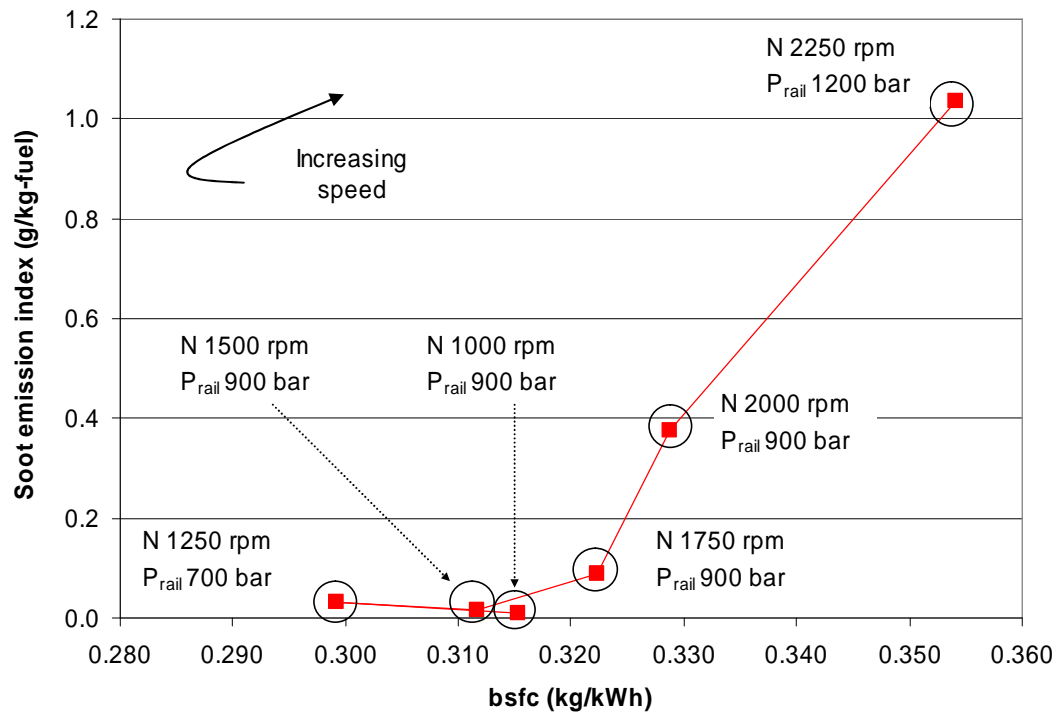


Figure 9.20: Summary soot-bsfc trade-off curve with soot minimised for bsfc values within 5% of the baseline value obtained at each engine speed for 2.5 bar BMEP load output. Labelled are the engine speed and fuel rail pressure for each point, 45% EGR location of peak pressure +13°ATDC.

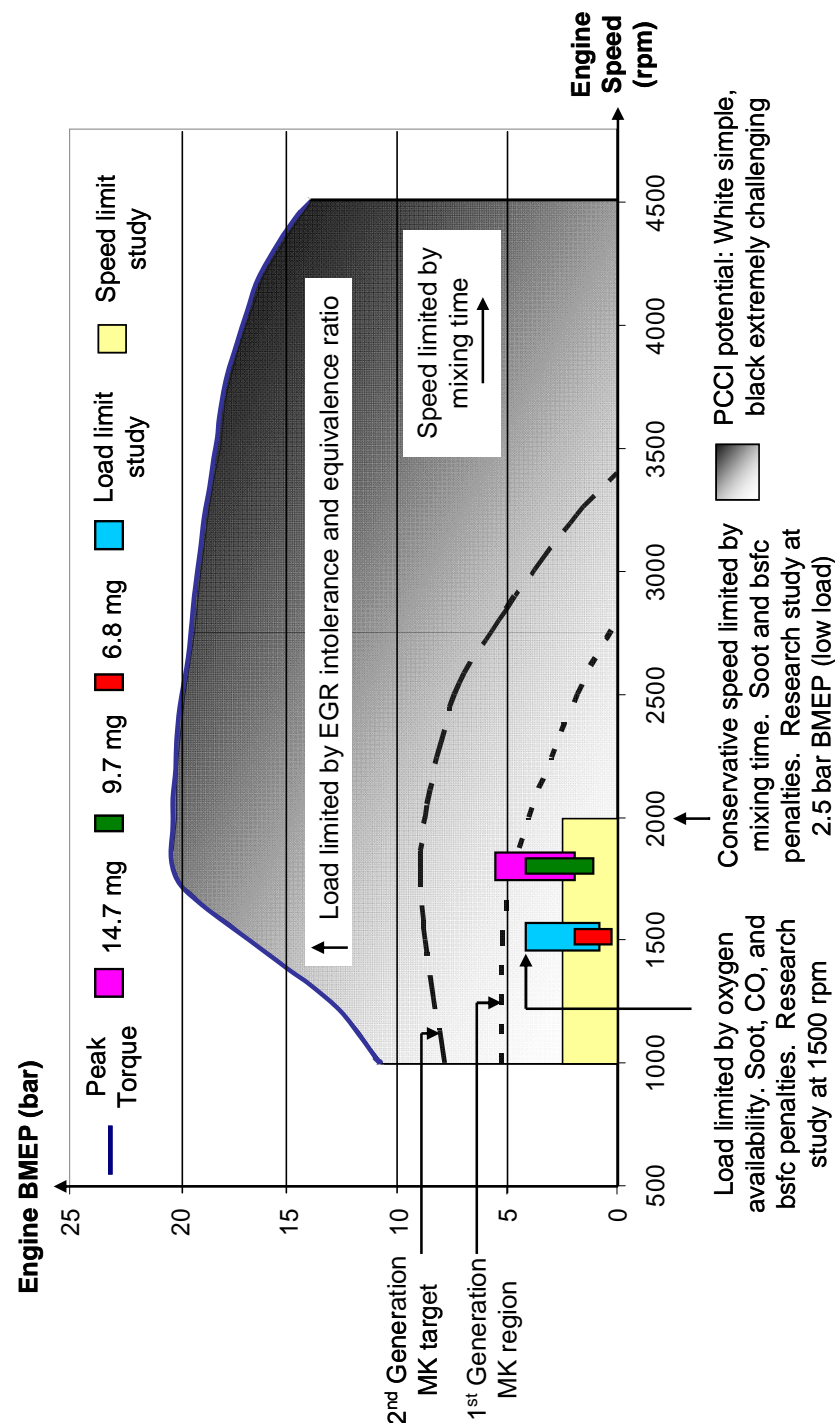


Figure 9.21: Speed and load operating regions and limits for PCCI combustion. Experiments carried out at operating conditions close to NEDC requirements. Labelled are the regions investigated in the current research study, the regions reported with Modulated Kinetics (MK), and the load and speed limits discovered. Fuelling rates are shown to indicate relative regions of data collected within the investigation, along with the peak torque of the engine. Shading gradient indicates the potential for exploiting PCCI combustion (white relatively simple, black extremely challenging/not possible)

CHAPTER 10

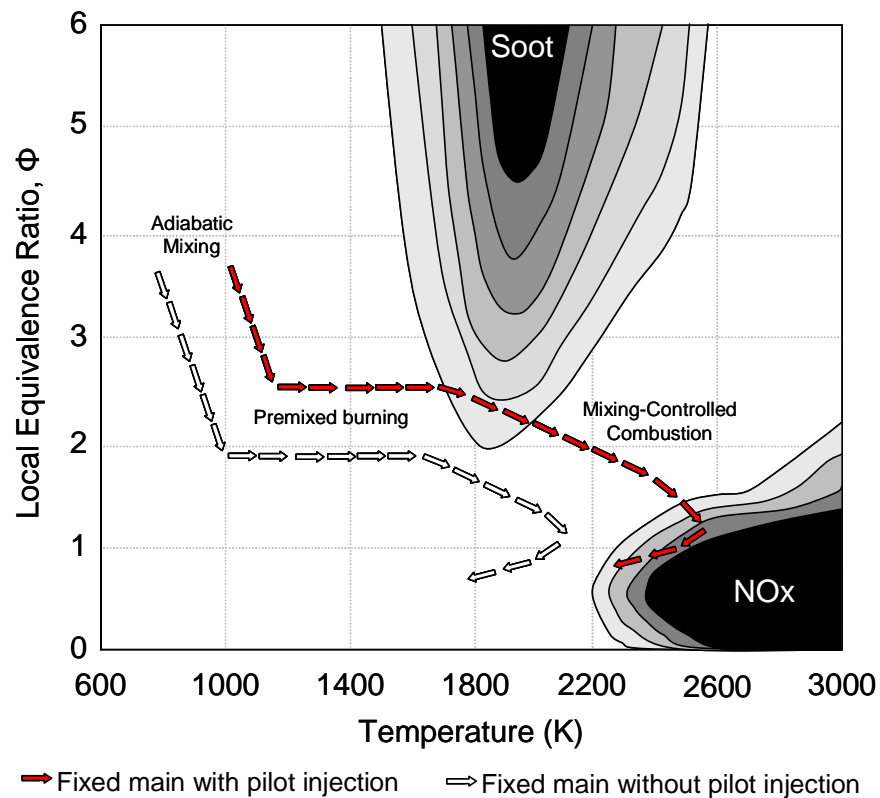


Figure 10.1: Qualitative representation of proposed paths taken by typical fuel parcels in the Φ - T plane during combustion for a fixed main injection of SOI around TDC with and without pilot injection. Note proposed paths for main fuel packets only.

Appendix 1: Conversion from “dry” to “wet” analysis

The following derivation details how the water removed from the exhaust stream is accounted for to calculate the true emission values. This method was originally devised by Jones [74] from which the following work was reproduced:

The molar fraction of species i given by the analysers has the majority of the water removed prior to analysis. The analyser outputs therefore give the “dry” fraction such:

$$\tilde{x}_i^* = \frac{n_i}{n_{\text{exhaust}} - n_{\text{H}_2\text{O}}} \quad (\text{A1.1})$$

The real “wet” composition, however, is given by:

$$\tilde{x}_i = \frac{n_i}{n_{\text{exhaust}}} \quad (\text{A1.2})$$

The mass fraction of water is calculated from the simplified combustion equation (Equation 4.1). The mass of water lost in the chiller is then given by:

$$m_{\text{H}_2\text{O}}(\text{lost}) = (x_{\text{H}_2\text{O}} - 0.0055) \cdot m_{\text{exhaust}} \quad (\text{A1.3})$$

Where 0.55% is the mass of water left found from the saturation limit at 5°C using a psychrometric chart (example given in Figure 10.2 on page 210).

The number of moles of water removed is therefore:

$$n_{\text{H}_2\text{O lost}} = \frac{m_{\text{H}_2\text{O lost}}}{\tilde{m}_{\text{H}_2\text{O}}} \quad (\text{A1.4})$$

Rearranging Equation (A1.1) and dividing by the total number of moles in the exhaust:

$$\frac{n_i}{n_{\text{exhaust}}} = \frac{\tilde{x}_i^* (n_{\text{exhaust}} - n_{\text{H}_2\text{O lost}})}{n_{\text{exhaust}}} \quad (\text{A1.5})$$

Combining equations (A1.2) and (A1.5):

$$\tilde{x}_i = \frac{\tilde{x}_i^* (n_{\text{exhaust}} - n_{\text{H}_2\text{O lost}})}{n_{\text{exhaust}}} \quad (\text{A1.6})$$

It follows that:

$$\tilde{x}_i = \frac{\tilde{x}_i^* \left(\frac{m_{exhaust}}{\tilde{m}_{exhaust}} - \frac{m_{H_2O \text{ lost}}}{\tilde{m}_{H_2O}} \right)}{\left(\frac{m_{exhaust}}{\tilde{m}_{exhaust}} \right)} \quad (A1.7)$$

And from the power trend line obtained from Figure 4.1 the conversion from “dry” to “wet” is given by:

$$\tilde{x}_i = \left(\frac{\tilde{x}_i^*}{0.141\lambda^{-1.02} + 1} \right) \quad (A1.8)$$

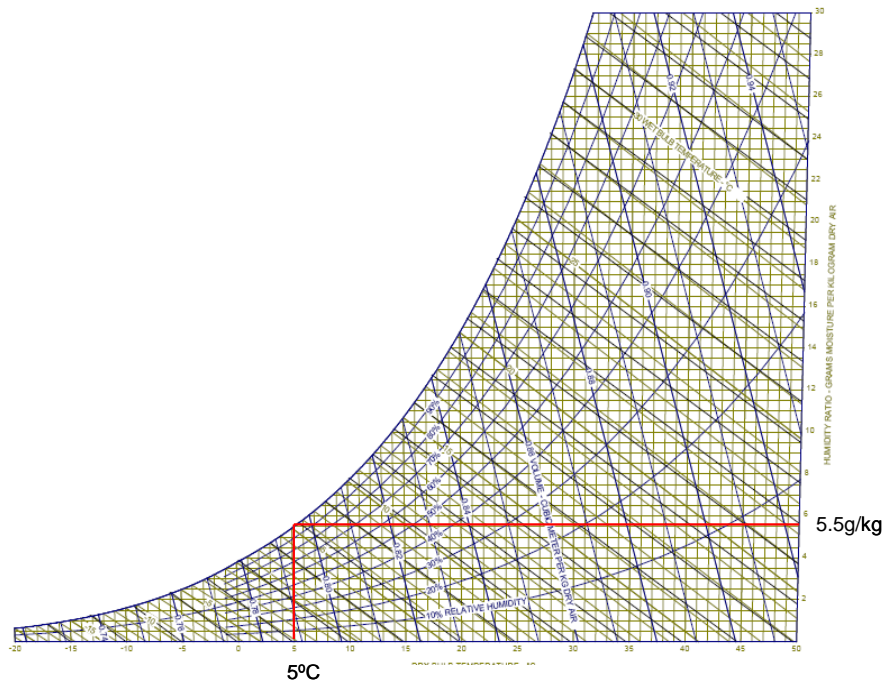


Figure 10.2: Example psychrometric chart [116] used to calculate fraction of water remaining in exhaust sample after the chiller unit

Appendix 2: Derivation of EGR fraction

The following derivation details how the definition of EGR rate obtained from the conservation of mass is calculated from engine exhaust and inlet CO₂ data:

$$EGR(\%) = \frac{\dot{m}_{EGR}}{\dot{m}_{man}} \cdot 100$$

$$\dot{m}_{man} = \dot{m}_{EGR} + \dot{m}_{atm}$$

$$(\dot{m}_{CO_2})_{man} = (\tilde{x}_{CO_2})_{man} \left(\frac{\tilde{m}_{CO_2}}{\tilde{m}_{man}} \right) (\dot{m}_{EGR} + \dot{m}_{atm})$$

$$(\dot{m}_{CO_2})_{EGR} = (\tilde{x}_{CO_2})_{exh} \left(\frac{\tilde{m}_{CO_2}}{\tilde{m}_{EGR}} \right) (\dot{m}_{EGR})$$

$$(\dot{m}_{CO_2})_{atm} = (\tilde{x}_{CO_2})_{atm} \left(\frac{\tilde{m}_{CO_2}}{\tilde{m}_{atm}} \right) (\dot{m}_{atm})$$

$$(\dot{m}_{CO_2})_{man} = (\dot{m}_{CO_2})_{EGR} + (\dot{m}_{CO_2})_{atm}$$

$$(\tilde{x}_{CO_2})_{man} \left(\frac{\tilde{m}_{CO_2}}{\tilde{m}_{man}} \right) (\dot{m}_{EGR} + \dot{m}_{atm}) = (\tilde{x}_{CO_2})_{exh} \left(\frac{\tilde{m}_{CO_2}}{\tilde{m}_{EGR}} \right) (\dot{m}_{EGR}) + (\tilde{x}_{CO_2})_{atm} \left(\frac{\tilde{m}_{CO_2}}{\tilde{m}_{atm}} \right) (\dot{m}_{atm})$$

$$(\tilde{x}_{CO_2})_{man} \left(\frac{\tilde{m}_{CO_2}}{\tilde{m}_{man}} \right) (\dot{m}_{EGR}) + (\tilde{x}_{CO_2})_{man} \left(\frac{\tilde{m}_{CO_2}}{\tilde{m}_{man}} \right) (\dot{m}_{atm}) =$$

$$(\tilde{x}_{CO_2})_{exh} \left(\frac{\tilde{m}_{CO_2}}{\tilde{m}_{EGR}} \right) (\dot{m}_{EGR}) + (\tilde{x}_{CO_2})_{atm} \left(\frac{\tilde{m}_{CO_2}}{\tilde{m}_{atm}} \right) (\dot{m}_{atm})$$

$$\left(\left(\frac{(\tilde{x}_{CO_2})_{man}}{\tilde{m}_{man}} \right) - \left(\frac{(\tilde{x}_{CO_2})_{atm}}{\tilde{m}_{atm}} \right) \right) \dot{m}_{atm} = \left(\left(\frac{(\tilde{x}_{CO_2})_{exh}}{\tilde{m}_{EGR}} \right) - \left(\frac{(\tilde{x}_{CO_2})_{man}}{\tilde{m}_{man}} \right) \right) \dot{m}_{EGR}$$

$$\dot{m}_{atm} = \dot{m}_{man} - \dot{m}_{EGR}$$

$$\left(\left(\frac{(\tilde{x}_{CO_2})_{man}}{\tilde{m}_{man}} \right) - \left(\frac{(\tilde{x}_{CO_2})_{atm}}{\tilde{m}_{atm}} \right) \right) (\dot{m}_{man} - \dot{m}_{EGR}) = \left(\left(\frac{(\tilde{x}_{CO_2})_{exh}}{\tilde{m}_{EGR}} \right) - \left(\frac{(\tilde{x}_{CO_2})_{man}}{\tilde{m}_{man}} \right) \right) \dot{m}_{EGR}$$

$$\left(\frac{(\tilde{x}_{CO_2})_{man}}{\tilde{m}_{man}} \right) \dot{m}_{man} - \left(\frac{(\tilde{x}_{CO_2})_{atm}}{\tilde{m}_{atm}} \right) \dot{m}_{man} - \left(\frac{(\tilde{x}_{CO_2})_{man}}{\tilde{m}_{man}} \right) \dot{m}_{EGR} + \left(\frac{(\tilde{x}_{CO_2})_{atm}}{\tilde{m}_{atm}} \right) \dot{m}_{EGR} =$$

$$\left(\frac{(\tilde{x}_{CO_2})_{exh}}{\tilde{m}_{EGR}} \right) \dot{m}_{EGR} - \left(\frac{(\tilde{x}_{CO_2})_{man}}{\tilde{m}_{man}} \right) \dot{m}_{EGR}$$

$$\left(\left(\frac{(\tilde{x}_{CO_2})_{exh}}{\tilde{m}_{EGR}} \right) - \left(\frac{(\tilde{x}_{CO_2})_{atm}}{\tilde{m}_{atm}} \right) \right) \dot{m}_{EGR} = \left(\left(\frac{(\tilde{x}_{CO_2})_{man}}{\tilde{m}_{man}} \right) - \left(\frac{(\tilde{x}_{CO_2})_{atm}}{\tilde{m}_{atm}} \right) \right) \dot{m}_{man}$$

Assuming $\tilde{m}_{man} = \tilde{m}_{EGR} = \tilde{m}_{atm}$;

$$\dot{m}_{EGR} = \left(\frac{(\tilde{x}_{CO_2})_{man} - (\tilde{x}_{CO_2})_{atm}}{(\tilde{x}_{CO_2})_{exh} - (\tilde{x}_{CO_2})_{atm}} \right) \dot{m}_{man}$$

$$EGR(\%) = \frac{\dot{m}_{EGR}}{\dot{m}_{EGR} + \dot{m}_{atm}} \cdot 100 = \frac{\dot{m}_{EGR}}{\dot{m}_{man}} \cdot 100 = \left(\frac{(\tilde{x}_{CO_2})_{man} - (\tilde{x}_{CO_2})_{atm}}{(\tilde{x}_{CO_2})_{exh} - (\tilde{x}_{CO_2})_{atm}} \right)$$

Appendix 3: Conversion Derivation of Equation 7.1

The total inlet flow is given by:

$$\dot{m}_{total} = \dot{m}_{air} + \dot{m}_{EGR} \quad (A3.1)$$

Inserting the definition used for EGR defined in Equation 4.19:

$$\dot{m}_{total} = \frac{\dot{m}_{air}}{(1 - EGR)} \quad (A3.2)$$

From the definition of fuel-air equivalence ratio it therefore follows that:

$$\dot{m}_{air} = \frac{AFRs \cdot \dot{m}_f}{\phi} \quad (A3.3)$$

Rearranging gives:

$$\phi(1 - EGR) = \frac{AFRs \cdot \dot{m}_f}{\dot{m}_{total}} \quad (A3.4)$$

The total mass of induced gas can be described by:

$$\dot{m}_{total} = \eta_{vol} \cdot \rho_i \cdot nV_s \cdot \frac{N}{2} \quad (A3.5)$$

Thus the final equation (7.1) is arrived at:

$$\phi = \frac{C}{(1 - EGR)} \quad (A3.6)$$

Where;

$$C = \frac{AFRs \cdot \dot{m}_f}{\eta_{vol} \cdot \rho_i \cdot nV_s \cdot \frac{N}{2}} \quad (A3.7)$$

Appendix 4: Estimated required intake pressure as a function of engine load for fixed fuel-air equivalence ratio

Assuming the air temperature downstream of the intercooler (heat exchanger) is fixed at a temperature of 35°C $c_p = 1.005 \text{ kJ / kg}$ for the intake fresh air [80].

Exhaust temperature is a function of engine load, but is also dependent on combustion phasing and combustion efficiency. Generally it increases with increased fuelling. Using experimental data recorded for the relatively retarded combustion phasing employed in Chapter 9 (~+13°ATDC), a relationship between fuel quantity required (kg/s) and gross indicated load output (bar) was obtained that could be extrapolated to higher loads:

$$\dot{m}_f = -6.24 \times 10^{-7} \cdot IMEP_g^2 + 2.18 \times 10^{-4} \cdot IMEP_g \quad (A4.1)$$

Note the correlation in A4.1 is relevant for the conditions stated only. An approximation of the temperature of the EGR gas to the intake manifold was then obtained. Here T_{EGR} represents the temperature (°C) of the exhaust gas downstream of the EGR cooler immediately upstream of the intake manifold:

$$T_{EGR} = -0.92 \cdot IMEP_g^2 + 50.2 \cdot IMEP_g + 44 \quad (A4.2)$$

Assuming the temperature of the compressed fresh air remains constant at 40°C, the mixture temperature in the intake manifold can be estimated by performing an enthalpy balance. The enthalpy of the air is given by:

$$\begin{aligned} H_{air} &= m_{air} \cdot c_{p_{air}} (T_{air} - T_{ref}) \\ H_{air} &= 1.005 \cdot m_{air} \cdot (T_{air} - 298) \end{aligned} \quad (A4.3)$$

The enthalpy of the EGR is given by

$$\begin{aligned} H_{EGR} &= m_{EGR} \cdot c_{p_{EGR}} (T_{EGR} - T_{ref}) \\ H_{EGR} &= m_{air} \cdot \left(\frac{EGR}{1 - EGR} \right) \cdot c_{p_{EGR}} \cdot (T_{EGR} - 298) \end{aligned} \quad (A4.4)$$

The enthalpy of the mixture in the intake manifold is thus given by:

$$\begin{aligned} H_{intake} &= m_{intake} \cdot c_{p_{intake}} (T_{intake} - T_{ref}) \\ &= H_{air} + H_{EGR} \\ &= m_{air} \cdot \left(c_{p_{air}} \cdot (T_{air} - 298) + \left(\frac{EGR}{1 - EGR} \right) \cdot c_{p_{EGR}} \cdot (T_{EGR} - 298) \right) \end{aligned} \quad (A4.5)$$

$c_{p_{EGR}}$ was calculated as a polynomial function of temperature [80] assuming the gas to be air. Rearranging to solve for the intake temperature:

$$T_{\text{intake}} = \left(\frac{\left(c_{p_{\text{air}}} \cdot (T_{\text{air}} - 298) + \left(\frac{EGR}{1 - EGR} \right) \cdot c_{p_{EGR}} \cdot (T_{EGR} - 298) \right)}{c_{p_{\text{intake}}} \cdot \left(1 + \left(\frac{EGR}{1 - EGR} \right) \right)} \right) + 298 \quad (\text{A4.6})$$

The intake temperature can now be estimated by inputting the desired fuel flow rate or IMEP_g. The intake density is calculated from the ideal gas law:

$$\rho_{\text{intake}} = \frac{p_{\text{intake}}}{R \cdot T_{\text{intake}}} \quad (\text{A4.7})$$

Rearranging equations A3.6 and A3.7 from Appendix 3 and substituting A4.7 the required intake pressure required for a given value of equivalence ratio is given by:

$$p_{\text{intake}} = \frac{AFR_s \cdot \dot{m}_f \cdot R \cdot T_{\text{intake}}}{\eta_{\text{vol}} \cdot \phi \cdot n V_d \cdot \frac{N}{2} \cdot (1 - EGR)} \quad (\text{A4.8})$$

Therefore the required intake pressure can be calculated for a desired rate of EGR and fuel-air equivalence ratio at a specified engine speed and load.